

Technische Universität München
Fakultät für Physik

Max-Planck-Institut für Physik
(Werner-Heisenberg-Institut)



PhD Thesis

Direct Observation of the Hosing Instability of a Long Relativistic Proton Bunch in the AWAKE Experiment

Direkte Beobachtung der Hosing-Instabilität eines langen
relativistischen Protonenpakets im AWAKE-Experiment

Mathias Julius Hüther

München, November 2020



TECHNISCHE UNIVERSITÄT MÜNCHEN
Fakultät für Physik

Max-Planck-Institut für Physik
(Werner-Heisenberg-Institut)

Direct Observation of the Hosing Instability of a Long
Relativistic Proton Bunch in the AWAKE
Experiment

Mathias Julius Hüther

Vollständiger Abdruck der von der Fakultät für Physik der Technischen Universität
München zur Erlangung des akademischen Grades eines

Doktors der Naturwissenschaften (Dr. rer. nat.)

genehmigten Dissertation.

Vorsitzende:

Prof. Dr. Laura Fabbietti

Prüfer der Dissertation:

1. Hon.-Prof. Dr. Allen Caldwell
2. Hon.-Prof. Dr. Frank Jenko

Die Dissertation wurde am 02.09.2020 bei der Technischen Universität München ein-
gereicht und durch die Fakultät für Physik am 20.11.2020 angenommen.

Post tenebras lux.
Motto of the City of Geneva

Abstract

In this thesis we report on the first direct experimental observation of the non-axisymmetric Hosing Instability of a long relativistic proton bunch propagating through a m-scale plasma with density $n_{pe} \sim 0.5 \cdot 10^{14} \text{ cm}^{-3}$ in the AWAKE experiment at CERN. Analyzing streak camera images, we observe a periodic oscillation of the proton bunch centroid with growing amplitude along the bunch. We calculate by means of a Fast Fourier Transform that the frequency of the oscillation is equal to the cold electron plasma frequency. Moreover, by capturing time-integrated radial proton bunch profiles, we show that the Hosing Instability develops along a characteristic plane in the bunch. We discuss the results of three-dimensional particle-in-cell simulations of the Hosing Instability performed in the OSIRIS code at similar parameters compared to our experiment in different propagation distances along the plasma and in different planes across the bunch.

By performing fits to the bunch centroid position in simulation and experiment, we show good agreement to the theoretical model of the Hosing Instability and give evidence for Coupled Beam Hosing, i.e. the coupling of the bunch centroid oscillation to the modulation of the bunch density due to the process of Seeded Self-Modulation via the plasma wakefields.

Furthermore, we show that in the case that the Self-Modulation process is not seeded, the occurrence of the Hosing Instability depends on the delay between the high-power laser pulse ionizing the Rubidium vapour and the arrival of the proton bunch. In this configuration, both events where the Self-Modulation Instability or the Hosing Instability (with and without coupling to the Self-Modulation process) develops can be observed. Eventually, we infer that the Hosing Instability can also be induced by a deliberate misalignment of the plasma channel with respect to the proton bunch trajectory.

Kurzfassung

In dieser Arbeit berichten wir im Rahmen des AWAKE-Experiments am CERN über die erstmalige direkte experimentelle Beobachtung der nicht-achsensymmetrischen Hosing-Instabilität eines langen relativistischen Protonenpakets, das durch ein Plasma der Dichte $n_{pe} \sim 0.5 \cdot 10^{14} \text{ cm}^{-3}$ propagiert.

Auf Streakkamerabildern beobachten wir eine periodische Oszillation des Schwerpunkts des Protonenpakets mit wachsender Amplitude entlang des Pakets. Mittels einer schnellen Fouriertransformation bestimmen wir, dass die Periode der Oszillation gleich der Schwingungsperiode der Plasmaelektronen ist. Durch die Analyse von zeitlich integrierten radialen Profilen der Protonenpakete zeigen wir, dass die Instabilität sich entlang einer charakteristischen Ebene im Protonenpaket entwickelt.

Wir diskutieren die Ergebnisse von dreidimensionalen Particle-in-Cell Simulationen der Hosing-Instabilität mit dem OSIRIS-Code unter gleichwertigen Bedingungen wie in unserem Experiment sowohl entlang des Plasmas als auch in verschiedenen Ebenen innerhalb des Protonenpakets.

Fits an die Schwerpunktsposition des Protonenpakets in der Simulation und im Experiment zeigen eine gute Übereinstimmung mit dem theoretischen Modell der Hosing-Instabilität und belegen das Auftreten des Coupled Beam Hosing, der Kopplung der Schwerpunktsschwingung des Protonenpakets an die Dichtemodulation durch den Prozess der angeregten Selbstmodulation.

Schließlich zeigen wir, dass die Häufigkeit von Ereignissen mit der Hosing-Instabilität vom zeitlichen Abstand zwischen dem Rubidiumdampf ionisierenden Laserpuls und dem Protonenpaket abhängt. Dabei können sowohl die Self-Modulation-Instabilität als auch die Hosing-Instabilität (mit und ohne Kopplung zum Selbstmodulationsprozess) beobachtet werden. Außerdem kann das Wachstum der Hosing-Instabilität durch eine beabsichtigte falsche Ausrichtung des Plasmakanals zur Propagationsachse des Protonenpakets angeregt werden.

Contents

Abstract	7
Kurzfassung	9
Contents	11
List of Figures	15
List of Tables	19
1 Introduction to Plasma Based Particle Acceleration: Historical Overview and Motivation	21
1.1 Conventional Particle Acceleration	21
1.2 Plasma-Based Particle Acceleration	23
1.2.1 Laser Driven Wakefield Acceleration	23
1.2.2 Particle Driven Wakefield Acceleration	24
1.3 Structure of the Thesis	26
2 Theoretical Description of Plasma Wakefields and Instabilities	27
2.1 Definition of Plasma	27
2.2 Linear Theory of Plasma Wakefields	29
2.3 Plasma Instabilities	32
2.3.1 The Current Filamentation Instability	32
2.3.2 The Self-Modulation Instability	32
2.3.3 The Hosing Instability	35
2.3.4 Coupled Beam Hosing	38
2.4 Seeding of the Self-Modulation Process of a Long Proton Bunch with a Short Electron Bunch	42
3 The AWAKE Experiment	47
3.1 Layout of the Experiment and its Components	48
3.1.1 The AWAKE Experimental Facility	48
3.1.2 The Proton Beam Line	49
3.1.3 The Ionizing Laser System	50
3.1.4 The Laser Beam Dumps	52
3.1.5 The Vapour Source	55
3.1.6 Proton Beam Diagnostics	55
3.1.7 The Laser Line for the Electron Gun	57

3.1.8	The Electron Beam Line and Electron Diagnostics	60
3.2	AWAKE Run 2	61
4	Laser Ablation Studies for Beam Dump Foils	63
5	Hosing Instability Simulations with OSIRIS	69
5.1	OSIRIS	69
5.2	Initial Bunch Parameters	70
5.3	Simulation Results	71
5.3.1	Bunch Centroid Oscillation and its Frequency	71
5.3.2	Fit of Bunch Centroid Equation to Simulation Data	77
5.3.3	Angle Scan	82
5.3.4	Time-Integrated Radial Bunch Charge Distribution	88
5.4	Comparison to Hosing Instability Simulations Without Seed of the Self-Modulation Process	89
6	Experimental Results – Part 1: Observation of the Hosing Instability with Seed of the Self-Modulation Process	93
6.1	Streak Camera Data Evaluation and Background Estimations	93
6.1.1	Streak Camera Raw Data	94
6.1.2	Background Subtraction	95
6.1.3	Bunch Trajectory and Centre of Gravity of Plasma Off Events	96
6.2	Bunch Characterisation	97
6.3	Characterisation of Hosing and Self-Modulation	101
6.3.1	Integrated Signal and Bunch Centroid Position	103
6.3.2	The Fourier Transform of Streak Camera Data	106
6.4	Analysis of Hosing Instability Events with Seed of the Self-Modulation Process	108
6.4.1	Dependence of the Hosing Instability Growth on the Bunch Population	110
6.4.2	Symmetry of the Events with Respect to the Bunch Propagation Axis	111
6.4.3	Bunch Centroid Oscillation Frequency	112
6.5	Radial Diagnostic of the Hosing Instability	117
6.5.1	Determination of the Plane of the Hosing Instability Growth	118
6.6	Fit of the Bunch Centroid Displacement Equation to the Experimental Data	122
6.7	Comparison of the Experimental Results to the Simulation Results	129
7	Experimental Results – Part 2: Observation of the Hosing Instability without Seed of the Self-Modulation Process	131
7.1	Effects of the Delay between Ionizing Laser Pulse and Proton Bunch	131
7.2	Analysis of Hosing Instability Events without Seed of the Self-Modulation Process	133

7.3 Hosing Instability Induced by a Misalignment of the Proton Bunch with Respect to the Plasma Column	141
8 Conclusions and Outlook	147
Glossary	151
Acknowledgements	157
Bibliography	159
Appendices	167
A Publications	167
B Technical Drawings	173

List of Figures

1	Charge separation by a proton bunch driver propagating through plasma	31
2	Schematic visualisation of the growth of the Self-Modulation and the Hosing Instability	34
3	Number of exponentiations and normalized centroid position along the bunch according to Equation 2.27 for an SPS-like proton bunch	37
4	Factors μ and ν as well as the ratio $\frac{N_{HI}}{N_{SMI}}$ at different plasma densities	38
5	Comparison between coupled and uncoupled beam hosing	39
6	Schematic of the Self-Modulation seeding scheme by a co-propagating short electron bunch at the centre of the long proton bunch	42
7	Effective charge distribution along the proton bunch for seeding with a short electron bunch	43
8	Parallel and perpendicular wakefields according to Equation 2.47 for a long proton bunch and an electron seed bunch	45
9	Schematic of the Self-Modulation seeding scheme by a co-propagating short electron bunch at the head of long proton bunch	46
10	Situation of the AWAKE experiment within the CERN accelerator complex	47
11	Overview of the AWAKE facility	48
12	General layout of the AWAKE experiment	49
13	Schematic overview of the components and beam lines of the AWAKE laser system	51
14	Photo of the AWAKE laser room	53
15	Technical drawing of laser beam dump LBDP2	54
16	Integration of the laser beam dump LBDP2 into the proton beam line	54
17	Photo of the vapour source in the AWAKE tunnel	55
18	Beam paths of laser beams inside the box of the in-air compressor and the third harmonic generation stage	58
19	Design of the in-air double-pass grating compressor	59
20	Schematic of the third harmonic generation stage for the conversion of IR to UV	60
21	Layout for AWAKE Run 2 experiments	61
22	Set-up for the measurements of laser ablation rates	64
23	Microscope image of a hole ablated by high-power laser pulses of the AWAKE laser system on an Aluminium foil	65
24	Comparison between the ablation rates of experiments at MPP and the publication by Wynne and Stuart	67

List of Figures

25	Initial proton bunch for OSIRIS simulations	71
26	Slices of the charge distribution of 3D simulation results in OSIRIS in the plane perpendicular to the Hosing Instability seed	72
27	Slices of the charge distribution of 3D simulation results in OSIRIS in the plane of the Hosing Instability seed	73
28	Comparison of the slices of the charge distribution in perpendicular planes after a propagation distance of 10.10 m through plasma	74
29	Bunch centroid displacements after different propagation distances through plasma in the planes of the Hosing Instability seed and perpendicular to it as well as the corresponding Discrete Fourier Transforms of the centroid oscillation	75
30	Integrated signals along the bunch after different propagation distances through plasma in the planes of the Hosing Instability and the corresponding Discrete Fourier Transforms of the signal	77
31	Fit of Equation 2.30 to the centroids determined from the OSIRIS simulation after a different propagation distances through plasma	81
32	Evolution of different fit parameters in Equation 2.30 along the plasma	82
33	Slices of the charge distribution of 3D simulation results in OSIRIS along different planes across the charge distribution of the simulated bunch after a propagation distance of 8.08 m through plasma	83
34	DFT power spectrum of the centroid displacement and peak intensities for different angles	84
35	Fits of Equation 2.30 to the bunch centroid projection in different planes across the charge distribution of the simulated bunch with fixed coupling constant	86
36	Dependence of the oscillation amplitude on the angle of the projection for fixed coupling constant	87
37	Dependence of the coupling constant on the angle of the projection	87
38	Time-integrated radial charge distribution of the simulated p^+ -bunch after different propagation distances through plasma	88
39	Initial proton bunch for OSIRIS-Simulations of the Hosing Instability without seed of the Self-Modulation process	89
40	Slices of the charge distribution of 3D simulation results in OSIRIS for a proton bunch without seeding the Self-Modulation process	90
41	Bunch centroid displacements after different propagation distances in plasma for a proton bunch with Hosing Instability seed but without seeding the Self-Modulation process	91
42	Correction of the non-linear streak camera time axis to a linear time axis in different time windows	94
43	Continuous and hot pixel background on streak camera images	96
44	Plasma off events in the 211 ps and 1134 ps streak camera time window of proton bunches with low and high bunch population	98

45	Gaussian fits of the longitudinal and radial bunch charge distribution of the proton bunch shown in Figure 44d	100
46	Comparison of events with bunch rotation mechanism off and on	101
47	Streak camera images of Hosing and Self-Modulation events under similar conditions with low and high proton bunch population	102
48	Integrated signals and bunch centroid displacements for the low bunch population events shown in Figure 47	104
49	Projection of focused and defocused protons onto the streak camera slit	104
50	Streak camera image of Hosing event with marked centroid positions	105
51	DFTs of the integrated signals and the centroid displacements for the HI and the SSM events shown in Figure 48	107
52	Streak camera image and bunch centroid of a Hosing event from the data set acquired in the 509 ps streak camera time window	109
53	Histogram of the maximum displacements of the bunch centroid from the plasma off trajectory	111
54	Histograms of the area ratios of the bunch centroid from the plasma off trajectory	112
55	DFT of the bunch centroid displacements for different data sets	114
56	Normalized centroid oscillation frequencies for events shown in Figure 55	116
57	Time-integrated radial proton bunch profiles acquired at the imaging stations for different events	121
58	Orientation of the plane of the Hosing Instability growth for the events gathered in the 211 ps streak camera time window with low and high p^+ -bunch population	121
59	Fits of the bunch centroid equation (Equation 2.30) to the experimentally determined centroids for the low and high bunch population events shown in Figures 47a and 47c	124
60	Events with low and high coupling constant from the high bunch population data set and fits of Equation 2.30 to their centroid oscillations	127
61	Events with lowest and highest p from the high bunch population data set and fits of Equation 2.30 to their centroid oscillations	128
62	Event with negative R^2 from the high bunch population data set and fit of Equation 2.30 to the centroid oscillation	129
63	Events with Hosing Instability at different delays between ionizing laser pulse and proton bunch	132
64	Normalized centroid oscillation frequencies for Hosing Instability events at different delays between ionizing laser pulse and proton bunch	135
65	Streak camera image, centroid displacement, laser alignment and time-integrated radial proton bunch profiles for different events at 1000 ns delay between ionizing laser pulse and proton bunch	138
66	Fits of the bunch centroid displacements (Equation 2.30) to the experimentally determined centroids for the events shown in Figure 65b and Figure 65c	139

List of Figures

67	Streak camera images and fits to the bunch centroid oscillation for two different Hosing Instability events with 4000 ns delay between ionizing laser pulse and proton bunch	140
68	Effects of the plasma column position on the development of the Hosing Instability	144
69	Orientation of the planes of the Hosing Instability growth determined from the time-integrated radial proton bunch profiles for events with deliberately misaligned laser position in one direction	145
70	Plasma skin depth in dependence on plasma density	146
71	Appearance and temporal distribution of pre-bunches before the main proton bunch	149
72	Appearance of the long-wavelength mode of the Hosing Instability	150

List of Tables

I	Overview of different foils used for the beam dump foil ablation studies . . .	63
II	Experimental parameters used at MPP and in the publication by Wynne and Stuart	65
III	Results of the ablation studies	66
IV	Normalization to plasma units in OSIRIS	69
V	Initial parameters for the fit of Equation 2.30 to the centroid oscillation determined from simulation data	78
VI	Longitudinal and radial proton bunch sizes for different SPS beams determined from Gaussian fits	100
VII	Frequency resolution and maximum bandwidth for a purely sinusoidal signal at different streak camera time windows used in AWAKE	106
VIII	Overview of the experimental parameters of the data sets for the Hosing Instability characterisation with seed of the Self-Modulation process . . .	109
IX	Maximum displacements of the bunch centroid from the plasma off trajectory	110
X	Area ratios determined from the centroid displacements	111
XI	Initial parameters for the fit of Equation 2.27 to the experimentally determined centroid oscillation	122
XII	Resulting fit parameters of the fits to the bunch centroid modulation according to Equation 2.27	125
XIII	Overview of the experimental parameters of the data sets for the Hosing Instability characterisation without seed of the Self-Modulation process at different delays between ionizing laser pulse and proton bunch	134
XIV	Frequency ranges for the determination of the DFT peaks at different delays between ionizing laser pulse and proton bunch	136
XV	Overview of the experimental parameters of the data set for the study of the Hosing Instability seed by a deliberate misalignment of the proton bunch with respect to the plasma column	145

1 Introduction to Plasma Based Particle Acceleration

Historical Overview and Motivation

1.1 Conventional Particle Acceleration

The development of particle accelerators was one of the most important technical achievements extending the frontiers of modern physics during the last century. The enormous success in the search for new particles and related new physics would not have been possible without the continuous increase of the energies of the colliding particles.

Since the development of the first scientific apparatus for electron acceleration, the famous Braun tube, by F. Braun in 1897 [1], the main principle of particle accelerators remained unchanged for many decades. Charged particles emitted from a cathode are accelerated through electric fields to reach higher velocities and accordingly gain more energy. Magnetic fields are applied to keep the particles on their desired trajectories.

The first large-scale linear machines reaching particle energies up to the MeV-range were the Cockcroft-Walton accelerator [2] and the Van-der-Graff generator [3], both developed in the early 1930s. At the same time, the first circular machines, like e.g. the cyclotron, have been built. The size of the machines has been further increased in the following years. For the acceleration of electrons, linear accelerators (LINACs), have been developed. The world's longest and most powerful LINAC, reaching electron (and positron) energies up to 50 GeV, is the Stanford Linear Collider (SLC) at SLAC, Menlo Parc, California, USA, put into operation in 1989 (for an overview see e.g. [4]).

In Europe, the foundation of the European Nuclear Research Center CERN (Conseil européen pour la recherche nucléaire) in 1954 in Geneva, Switzerland, led to a concentration of research resources in particle acceleration and collider physics. The Proton Synchrotron (PS, 1959) and its extension the Super Proton Synchrotron (SPS, 1976) were the leading machines in proton (p^+)/antiproton acceleration and in establishing the physics of the Standard Model in the 1970–1980s (e.g. the discovery of W and Z bosons). Also at CERN, the Large Electron-Positron Collider (LEP) [5] started operating in 1989 and reached a center-of-mass collision energy of up to 209 GeV in its final stage (LEP2). Its successor machine, the Large Hadron Collider (LHC), is the largest particle accelerator ever built. It is able to accelerate p^+ -bunches to energies up to 7 TeV, resulting in centre-of-mass energies in p^+p^+ -collisions of 14 TeV. The discovery of the Higgs boson in 2012, predicted already in 1966 by P. Higgs et al. (Noble prize in physics in 2013), was the impressive proof of the validity of the Standard Model of particle

physics.

Nevertheless, there are still plenty of questions beyond the Standard Model to be answered, like e.g. the search for Supersymmetry (SUSY) or dark matter. Besides observation and detection of cosmic particles, particle accelerators will play the major role for a systematic search under well-defined conditions.

The main disadvantage of hadron-hadron colliders, like the LHC, compared to lepton-lepton colliders is the high hadronic background in collisions, making a precise reconstruction of the large number of quarks and gluons interacting in these collision processes very difficult. Leptons, however, are considered to be point-like particles. Therefore, lepton-lepton collisions give much clearer event signatures and they are much better for precision measurements. Hence, it is very likely that the next particle accelerator to be built will again be a lepton-lepton collider.

Charged particles moving on circular trajectories emit synchrotron radiation. As the energy loss of the charged particle ΔE_S per turn with radius r_S is inversely proportional to the fourth power of its rest mass m_0 [6],

$$\Delta E_S \propto \frac{E^4}{r_S m_0^4 c^8}, \quad (1.1)$$

acceleration of electrons (e^-) or positrons in circular accelerators gets very inefficient above certain energies.¹ Hence, to accelerate electrons to energies needed to study non-standard model processes, it is more efficient to accelerate them linearly.²

State-of-the-art conventional linear accelerators, however, have an upper limit of the acceleration gradient due to the limited electric field in their radio-frequency (RF) cavities. Applying more than about 100 MV/m leads to electric breakdown of those accelerating RF-structures. As there is yet no promising technical solution known to significantly overcome this limitation, the only way to increase the energies of the accelerated particles is to extend the acceleration length. For example, to accelerate an electron to 100 GeV, a machine of at least one kilometre length is necessary.³ Accelerating electrons and positrons up to the TeV-scale would require machines of several kilometres length, presumably to be built in tunnels, which makes their construction very complicated and expensive.

There are several designs for future colliders proposed and under discussion within the High Energy Physics community. The most promising machine currently planned is the Compact Linear Collider (CLIC) at CERN [7], which could be operational around 2040. It would be an electron-positron collider reaching centre-of-mass energies up to 3 TeV and acceleration gradients up to 100 MeV/m. According to current planning, it would be built in stages from 11 km up to a final length of 50 km. A rough preliminary cost estimate is around 6–7 billion CHF for the first stage [8]. Moreover, there are well-engineered

¹For protons ($m_p = 1836m_e$) this is no real limitation as the emitted radiation is by a factor of about $1836^4 = 1.1 \cdot 10^{13}$ lower than for electrons.

²The LEP, mentioned above, was already limited by Synchrotron radiation: At its maximum centre-of-mass energy (209 GeV) the energy gain per round trip equals the energy loss due to Synchrotron radiation.

³The acceleration gradient of the SLC (also mentioned above) is “only” about 20 MeV/m [4].

plans for an International Linear Collider (ILC), presumably to be built in Japan, with a length of 31 km (plus 2 damping rings, each of them with 6.7 km circumference). The ILC is supposed to have superconducting accelerating cavities and aims for centre-of-mass energies up to 500 GeV in acceleration gradients of 31.5 MeV/m [9]. However, currently the final decision on its construction is postponed by the Japanese government.

Furthermore, design studies for another project at CERN, the Future Circular Collider (FCC) are ongoing [10]: An about 80–100 km long circular accelerator either as hadron-hadron collider (similar to the LHC) aiming for collision energies up to 100 TeV or as electron-electron collider (similar to LEP) with centre-of-mass energies in the range of 90–400 GeV or even as electron-proton collider.

All projects have in common that due to their enormous size and the resulting costs, their realization requires large resources. Only within the scope of the next decade, the final decision on their construction will be taken.

Therefore, new and fundamentally different concepts, like e.g. plasma-based particle acceleration, are a very promising alternative to conventional accelerator designs for linear acceleration of electrons or positrons.

1.2 Plasma-Based Particle Acceleration

In general, two main approaches for particle acceleration in plasma wakefields can be distinguished: Laser Driven Wakefield Acceleration (LWFA) and Particle Driven Wakefield Acceleration (PWFA).

1.2.1 Laser Driven Wakefield Acceleration

In 1979, a pioneering proposal was presented by T. Tajima and J. M. Dawson, the “Laser Electron Accelerator” [11]. They suggested to excite wakes of plasma oscillations using the ponderomotive force of high-intense electromagnetic pulses (i.e. laser pulses). Electrons are injected into these wakefields, trapped and accelerated in gradients up to the multi-GeV/m scale. The prerequisites for realizing their theoretical concept were established by the further development of broadband, high-intense, ultra-short pulse lasers in the 1980s. After the development of Chirped Pulse Amplification (CPA) by D. Strickland and G. Mourou in 1985 [12] (both awarded with the Nobel Prize in Physics in 2018), the main restriction for high-power laser pulses, the optical damage on laser mirrors, could be overcome. Soon the required lasers with pulse energies up to the TW-regime had been available. The first experimental realizations of plasma based acceleration were published by Amironov et al. [13] and Kitagawa et. al. [14] in 1992 and by Clayton et al. [15] in 1993. They showed the acceleration of externally injected electrons up to 9.1 MeV in gradients of about 0.7 GeV/m. Already in 1995, Modena et al. [16] reported on the acceleration of electrons in gradients of more than 100 GeV/m.

Due to the relatively compact size and the rather cheap experimental set-ups compared to conventional machines, LWFA soon became a very promising research field at many institutes and laboratories all over the world. Plenty of different design concepts (e.g.

gas jets from nozzles, discharge capillaries, gas cells) and injection techniques (e.g. self injection, colliding-pulse injection, shock-front injection, ionisation injection) have been developed within the last decades. The main challenges to compete with the beam quality of conventional accelerators are still the relatively large energy spread of the accelerated electrons as well as the rather low bunch charge. Nevertheless, there are already remarkable results on reducing the energy spread of the accelerated beams. In 2004, three research groups (Mangles et al. [17], Geddes et al. [18] and Faure et. al [19]) showed that they were able to lower the energy spread to a level of just a few percent. The emittance of beams produced by laser wakefield accelerators is about comparable to that produced in conventional accelerators. Normalized transverse emittance values down to $0.2 \pi \text{ mm} \cdot \text{mrad}$ have been shown (e.g. at electron energies up to 245 MeV [20]). In 2019, Gonsalves et al. showed the acceleration of 5 pC of electrons to 7.8 GeV over a length of 20 cm using the Berkeley Lab Laser Accelerator (BELLA) (peak power 0.85 PW) [21]. There are several new laser wakefield accelerators planned, e.g. the framework of the Extreme Light Infrastructure Project (ELI) contains also funding for laser wakefield accelerator research [22].

1.2.2 Particle Driven Wakefield Acceleration

It was proposed by Chen et al. in 1985 [23] that not only laser pulses, but also an e^- -bunch could be used as a drive beam for creating the necessary wakefields to accelerate particles. Just three years later, this concept was first proven by Rosenzweig et al. [24] at Argonne National Laboratories. They probed the wakefields of a 21 MeV e^- -bunch propagating through plasma by measuring the energy of a witness bunch behind the driver. The theoretically predicted variation between accelerating and decelerating fields behind the drive bunch could be experimentally observed.

In 2007, Blumenfeld et al. [25] showed at SLAC that they were able to double the energy of some of the electrons of a 42 GeV e^- -beam on a distance of less than one metre in an e^- -driven plasma wakefield accelerator. This corresponds to an acceleration gradient of 52 GeV/m and the energy gain is comparable to the energy gained by an electron over the 3 km distance of the SLAC LINAC that produced the drive bunch.

The higher the energy carried by the drive bunch, the higher the absolute amount of energy that can be transferred to the witness bunch. As p^+ -bunches can be accelerated to much higher relativistic masses γm_0 than e^- -bunches, p^+ -bunches can carry substantially higher energies per bunch ($\gamma = (1 - \frac{v^2}{c^2})^{-\frac{1}{2}}$ is the Lorentz factor). Therefore, it would be more favourable to use p^+ -bunches instead of e^- -bunches as drivers. For example, a p^+ -bunch from PS (bunch energy $E = 25 \text{ GeV}$, bunch population $N_b = 3 \cdot 10^{11} p^+$) carries an energy of 1.2 kJ, a p^+ -bunch from SPS ($E = 400 \text{ GeV}$, $N_b = 3 \cdot 10^{11} p^+$) 19.2 kJ and a p^+ -bunch from LHC ($E = 7 \text{ TeV}$, $N_b = 1.2 \cdot 10^{11} p^+$) even 135 kJ. A SLAC-like e^- -bunch ($E = 28.5 \text{ GeV}$, $N_b = 2 \cdot 10^{10} e^-$) carries only 91.2 J. Moreover, a 1 PW-laser pulse with a pulse length of 100 fs does also not carry more than 100 J. This emphasises that p^+ -bunches are the more promising drivers when aiming for the highest possible energy gain in a single plasma stage.

Therefore, in 2009, A. Caldwell et al. [26] described how to realize a p^+ -driven plasma wakefield accelerator in a single acceleration stage design. This work laid the foundation for the later AWAKE experiment at CERN.

In order to effectively drive wakefields with a p^+ -bunch, the longitudinal bunch size needs to be on the order of the plasma wavelength λ_{pe} (see Chapter 2.1). For a plasma with an electron charge density of about $7 \cdot 10^{14} \text{ cm}^{-3}$, this would correspond to $\lambda_{pe} \approx 1.2 \text{ mm}$. Contrary to this prerequisite, all large conventional p^+ -accelerators have bunch lengths of several centimetres, e.g. the SPS bunches have a root mean square (RMS) length of about 12 cm, the fully accelerated bunches at LHC 7.5 cm [27]. As it is yet not possible at these plasma densities to shorten the bunch size to a length close to λ_{pe} by any bunch rotation mechanism, AWAKE relies on the Self-Modulation-Instability (SMI) in a plasma [28] (see Chapter 2.3.2). Due to the electro-magnetic response of the surrounding plasma, the initially long p^+ -bunch is subject to radial periodic focusing and defocusing fields and finally transforms into a train of short micro-bunches separated by λ_{pe} . Seeding this Self-Modulation (SM) process with a sharp ionization front allows to control the start point of the process within the bunch and to achieve an event-to-event phase stability for e^- -injection. This technique is referred to as Seeded Self-Modulation (SSM) [29].

In 2018, AWAKE measured the periodical focusing and defocusing plasma wakefields acting on a relativistic p^+ -bunch by investigating the radial [30] and longitudinal [31] bunch charge modulation at different plasma densities. Moreover, AWAKE proved the ability to control and reproduce the phase of the SSM [32]. To probe the wakefields and to show the feasibility of the general concept of e^- -acceleration, AWAKE demonstrated the external injection of witness electrons into the wake. Electrons with a charge in the pC-range were accelerated to energies up to 2 GeV [33] in 10 m of plasma, limited by the injection scheme.

During its growth, however, the SMI has to compete with another plasma instability with similar growth rate, the Hosing Instability (HI), resulting from a small transverse displacement of the p^+ -bunch propagation axis from the centre of the plasma channel, from initial noise in the p^+ -bunch or from plasma axial asymmetries. Seeding the SM process as in AWAKE, strongly suppresses the growth of the HI [34].

However, in case the growth of the HI overcomes the SM growth, the centroid of the p^+ -bunch starts to oscillate across the bunch propagation axis with increasing amplitude along the bunch and along the plasma, resulting in a break-up of the micro-bunch structure. A significantly larger growth of the HI compared to the SM process would drastically reduce the useful acceleration length in a plasma-wakefield accelerator and would not have made the above described e^- -acceleration results of AWAKE possible.

The observation and description of the HI has already been shown for a laser pulse propagating through plasma, e.g. by [35]. Also the HI of a long p^+ -bunch in plasma and the coupling to the self-modulation process was already discussed in detail in theoretic publications, e.g. by C. Schroeder et al. [36], but it has so far never been unambiguously observed in experiment.

The subject of this thesis is the first observation and documentation of the HI of a long p^+ -bunch propagating through plasma in the context of AWAKE. In order not

to jeopardize the efforts in the further development of p^+ -driven PWFA a much closer understanding of the HI (e.g. the effects on longer plasma sources) is of essential interest.

1.3 Structure of the Thesis

As just mentioned, in this thesis, we show the first experimental observation of the HI of a p^+ -bunch and discuss its appearance under different experimental conditions as well as its growth inside the plasma.

The following Chapter 2 gives a short theoretical introduction to the definition and description of a plasma, the generation of plasma wakefields and the fundamental physics behind the SM processes and the HI.

In Chapter 3, we give an overview of the different parts of the AWAKE experiment, the set-up and its most important components. We focus especially on the acquisition of streak camera (SC) images of the p^+ -bunch from optical transition radiation (OTR), mainly used for the analysis of the SM process and the HI. Special attention lies on my main contributions to the experimental set-up of AWAKE, the third-harmonic generation (THG) stage for frequency conversion of the infrared laser pulse into an ultraviolet laser pulse used for the electron source photo-cathode as well as on the movable Aluminium (Al) foil beam dumps for the high-power laser pulse.

Chapter 4 gives a brief overview of laser ablation studies for the design of these high-power laser beam dumps.

Chapter 5 is dedicated to give a short overview of simulation results on the HI performed with the particle-in-cell (PIC) code OSIRIS showing the growth of the HI along the plasma and in different planes across the bunch with respect to the plane of the HI seed.

In Chapter 6, we present the first part of the analysis of SC images to describe the experimental observation of the HI while the SM process is seeded. Therefore, we explain how to calculate the bunch centroid and how to determine its modulation frequency. Moreover, we perform and interpret fits to the displacements of the p^+ -bunch centroids and analyze time-integrated radial bunch profiles acquired from two-screen imaging stations (IS).

We continue in Chapter 7 with the observation of the HI at varying delays between the ionizing laser pulse and the p^+ -bunch, i.e. without seed of the SM process. Furthermore, we describe different processes that can influence the development of the HI, e.g. the alignment of the p^+ -bunch trajectory with respect to the plasma channel.

Chapter 8 gives a general conclusion, an outlook to open questions that still need to be answered and an overview of possible further studies on the HI.

2 Theoretical Description of Plasma Wakefields and Instabilities

2.1 Definition of Plasma

Colloquially, a plasma is often called the fourth state of matter: A gas which is fully ionized and which consists of core ions and their free electrons. For us, this description is far from being sufficient. Therefore, we describe a neutral plasma as a state of matter, which is characterized by the following properties:

The matter is at least partially ionized and the number of negatively and positively charged particles is about similar, i.e. $N_e \sim N_i$. This is referred to as quasi-neutrality. Furthermore, the collective behaviour of the particles is dominated by their electromagnetic interaction. Collisions and thermodynamic processes are subordinated effects. Assuming a displacement x of a single plasma electron by a force \vec{F} , the surrounding background electrons rearrange to re-establish quasi-neutrality of the plasma. The displaced plasma electron is then affected by a restoring force

$$F_{res} = m_e \ddot{x} = eE = -\frac{n_0 e^2}{\epsilon_0} x \quad (2.1)$$

and starts to oscillate harmonically. Here, m_e denotes the electron rest mass, e the elementary charge, ϵ_0 the vacuum permittivity, E the electric field and n_0 the plasma electron density.

For cold electrons¹, the resonance frequency of this harmonic oscillation, called plasma angular frequency, is given by

$$\omega_{pe} = 2\pi f_{pe} = \sqrt{\frac{n_0 e^2}{\epsilon_0 m_e}}. \quad (2.2)$$

Hence, ω_{pe} (and therefore also the plasma frequency f_{pe}) depends only on n_0 .

A charged test particle inserted into a quasi-neutral plasma is shielded by the rearrangement of their surrounding particles. Outside a sphere with radius

$$\lambda_D = \sqrt{\frac{\epsilon_0 k_B T_e}{n_0 e^2}} \quad (2.3)$$

¹In this context, cold means that we can neglect the thermal velocity of the electrons $v_{e,th} = \sqrt{\frac{k_B T_e}{m_e}}$, where k_B is the Boltzmann constant and T_e the plasma electron temperature.

the plasma seems to be still quasi-neutral. This sphere is called Debye sphere and its radius Debye length. Moreover, we assume that on the timescales of the rearrangement the mobility of the ions is negligible. To maintain the condition of quasi-neutrality the plasma size has to be much larger than the Debye sphere and therefore the number of particles $N_D = \frac{4}{3}\pi\lambda_D^3 n_e$ inside the Debye sphere has to fulfil the condition $N_D \gg 1$. Assuming a cold electron temperature $k_B T_e \sim 4$ eV for a plasma with $n_0 = 0.5 \cdot 10^{14} \text{ cm}^{-3}$ (as used in our HI experiments), the Debye length is about $2 \mu\text{m}$ and the Debye sphere contains about 1700 particles.

Propagation of Waves in Plasma

An electrostatic wave (or Langmuir wave) propagating through a cold plasma with a phase velocity v_{ph} has a dispersion relation $\omega = \omega_{pe}$ and a plasma wave number

$$k_{pe} = \frac{\omega_{pe}}{v_{ph}}. \quad (2.4)$$

The group velocity $v_{gr} = \frac{\partial\omega}{\partial k_{pe}} = 0$.

An electromagnetic (EM) wave, e.g. a laser pulse, propagating through a plasma, however, is subject to dispersion. Its dispersion relation is given by

$$\omega^2 = \omega_{pe}^2 + k_{EM}^2 c^2, \quad (2.5)$$

where k_{EM} is the wave number of the EM wave in vacuum. This allows to determine the phase velocity v_{ph} and group velocity v_{gr} of an EM wave inside the plasma [37]

$$v_{ph} = \frac{\omega}{k} = \frac{c}{\sqrt{1 - \frac{\omega_{pe}^2}{\omega^2}}} = \frac{c}{\eta} \quad (2.6)$$

and

$$v_{gr} = \frac{\partial\omega}{\partial k} = c \sqrt{1 - \frac{\omega_{pe}^2}{\omega^2}} = c\eta \quad (2.7)$$

with the plasma refractive index $\eta = \sqrt{1 - \frac{\omega_{pe}^2}{\omega^2}}$.

Hence, two different plasma regimes can be distinguished: For $\omega_{pe} < \omega$ the plasma refractive index is real and an external EM wave can propagate freely through the plasma as the response of the plasma electrons is slower than the group velocity of the EM wave. For $\omega_{pe} > \omega$ however, η becomes imaginary and the EM wave becomes evanescent. It is reflected by the plasma within the collisionless plasma skin depth $k_{pe}^{-1} = \frac{c}{\omega_{pe}} = \frac{\lambda_{pe}}{2\pi}$, where λ_{pe} is the plasma wavelength.

A plasma in which EM waves can propagate is called underdense plasma, a plasma which reflects EM waves is referred to as overdense plasma.

As ω_{pe} depends only on the plasma density n_0 , a plasma with $n_b < n_0$ is overdense with respect to a particle beam with density n_b and underdense for $n_b > n_0$.

The plasma in AWAKE and for our HI studies is an overdense plasma ($n_b < n_0$) with respect to the p^+ -bunch ($n_b = 4 \cdot 10^{12} \text{ cm}^{-3}$ for a Gaussian p^+ -bunch with $N_b = 3 \cdot 10^{11} p^+$,

longitudinal bunch size $\sigma_z = 12$ cm and radial bunch size $\sigma_r = 200$ μm). For a plasma density $n_0 = 0.5 \cdot 10^{14}$ cm^{-3} , the plasma frequency $f_{pe} = 63.4$ GHz and the collisionless plasma skin depth is 0.75 mm. In the following, we use the plasma skin depth instead of the Debye length in order to describe distances inside the plasma.

Similarly to Equation 2.4, we can define the wave number of a beam particle with mass m_b as [36]

$$k_b = \sqrt{\frac{n_b e^2}{m_b \epsilon_0 c^2}}. \quad (2.8)$$

In order to simplify the further calculations, similarly to [36], we define a wave number²

$$\hat{k}_\beta = \frac{k_b}{k_{pe}} \cdot \sqrt{\frac{1}{2\gamma}} = \sqrt{\frac{m_e}{m_p} \cdot \frac{n_b}{n_0}} \cdot \sqrt{\frac{1}{2\gamma}}. \quad (2.9)$$

The Wave-breaking Field

Plasmas can sustain very high electric fields, which make them a very interesting medium for particle acceleration. The upper limit of an electric field in a plasma depends on the maximum amount of plasma electrons, which can be displaced by a certain distance inside the plasma and is given by the non-relativistic cold wave-breaking field [38]

$$E_{wb} = \frac{cm_e \omega_{pe}}{e}. \quad (2.10)$$

The maximum acceleration gradient in plasma depends again only on the plasma electron density n_{pe} and can be estimated as

$$E_0 \left[\frac{\text{V}}{\text{m}} \right] = 96 \sqrt{n_{pe} [\text{cm}^{-3}]}. \quad (2.11)$$

Therefore, in a plasma with AWAKE baseline parameters ($n_0 = 7 \cdot 10^{14}$ cm^{-3}) electric field gradients up to 2.5 GV/m can be reached.

2.2 Linear Theory of Plasma Wakefields

In this section, we describe a linear theory of wakefields in plasma. The validity of this linear theory is met as long as the charge density perturbation induced by the wakefields is small compared to the total plasma electron density n_{pe} . The 2D cylindrical charge distribution of the particle beam n_b is given by

$$n_b(\zeta, r) = n_{b0} \cdot n_{b\parallel}(\zeta) \cdot n_{b\perp}(r) \quad (2.12)$$

²The wave number \hat{k}_β is calculated from the beam betatron wave number $k_\beta = k_{pe} \sqrt{\frac{m_e}{m_p}} \sqrt{\frac{n_b}{n_0}} \sqrt{\frac{1}{2\gamma}}$ by normalizing to the plasma frequency, i.e. $\hat{k}_\beta = \frac{k_\beta}{k_{pe}}$.

where $n_{b\parallel}(\zeta)$ denotes the normalized longitudinal and $n_{b\perp}(r)$ the normalized radial charge density. The charge density of the bunch is given by $n_{b0} = n_b(\zeta = 0, r = 0)$ and $\zeta = ct - z$ is the spatial coordinate in the co-moving bunch frame.

According to [39, 40], the longitudinal and radial wakefields $W_z(\zeta, r)$ and $W_r(\zeta, r)$ can be expressed by

$$W_z(\zeta, r) = n_{b0} \frac{e}{\epsilon_0} \int_{-\infty}^{\zeta} n_{b\parallel}(\zeta') \cos(k_{pe}(\zeta - \zeta')) d\zeta' \cdot R(r) \quad (2.13)$$

and

$$W_r(\zeta, r) = n_{b0} \frac{e}{k_{pe}\epsilon_0} \int_{-\infty}^{\zeta} n_{b\parallel}(\zeta') \sin(k_{pe}(\zeta - \zeta')) d\zeta' \cdot \frac{dR(r)}{dr}. \quad (2.14)$$

The transverse component $R(r)$ and its spatial derivative $dR(r)/dr$ in Equation 2.13 and 2.14 are given by

$$\begin{aligned} R(r) &= k_{pe}^2 K_0(k_{pe}r) \int_0^r r' n_{b\perp}(r') I_0(k_{pe}r') dr' \\ &\quad + k_{pe}^2 I_0(k_{pe}r) \int_r^\infty r' n_{b\perp}(r') K_0(k_{pe}r') dr' \end{aligned} \quad (2.15)$$

and

$$\begin{aligned} \frac{dR(r)}{dr} &= -k_{pe}^3 K_1(k_{pe}r) \int_0^r r' n_{b\perp}(r') I_0(k_{pe}r') dr' \\ &\quad + k_{pe}^3 I_1(k_{pe}r) \int_r^\infty r' n_{b\perp}(r') K_0(k_{pe}r') dr' \end{aligned} \quad (2.16)$$

with I_0 , I_1 and K_0 , K_1 the zeroth and first order modified Bessel functions of the first and second kind, respectively.

For the on-axis case ($r = 0$), the transverse component $R(0)$ and hence the longitudinal wakefields become maximal and Equation 2.15 reads

$$R(0) = k_{pe}^2 \int_0^\infty r' n_{b\perp}(r') K_0(k_{pe}r') dr'. \quad (2.17)$$

The radial wakefields are zero on-axis as $dR(0)/dr = 0$ and reach their maximal value for $r = \sigma_r$.

When a relativistic p^+ -bunch is propagating through a neutral plasma, the free electrons in the plasma are displaced and afterwards attracted by the positive charge of the bunch particles. The plasma electrons are accelerated towards the bunch propagation axis gaining kinetic energy from the electric fields of the bunch and overshoot across the propagation axis of the bunch.

As the plasma ions have significantly higher masses than electrons, it takes much longer for ions than for electrons to be accelerated in the same electric fields. As the density of the drive bunch is much smaller than the plasma density ($n_b \ll n_{pe}$), on the timescales discussed here ($\sim 1/\omega_{pe}$), the ion motion can be considered to be negligible and we can assume a purely stationary ion background.

Now, the electrons, which have overshoot across the bunch propagation axis, are pulled back by the ions remaining around the centre. They gain again kinetic energy and overshoot to the other side of the bunch propagation axis. This leads to a periodic oscillation of the plasma electrons with a period of $2\pi/\omega_{pe}$, the plasma wake. Hence, the wavelength of this periodic oscillation is equal to λ_{pe} .

Figure 1 schematically visualizes this charge separation inside the plasma caused by a p^+ -bunch driver. For a negatively charged test particle (or for an e^- -witness bunch) the longitudinal electric field inside the bubble is decelerating in the leading half, whereas it is accelerating in the trailing half of the bubble. The radial electric field is focusing in the centre of the bubble, whereas it is defocusing in its first and last quarter. Thus, in order to accelerate electrons over longer distances they have to be injected into the focusing and accelerating phase of the wake, i.e. within a quarter of a plasma wavelength. Therefore, the longitudinal size of the witness bunch should be shorter than $\lambda_{pe}/4$. For a Gaussian bunch, the condition for optimal longitudinal bunch length is given by [41]

$$k_{pe}\sigma_z = \sqrt{2}. \quad (2.18)$$

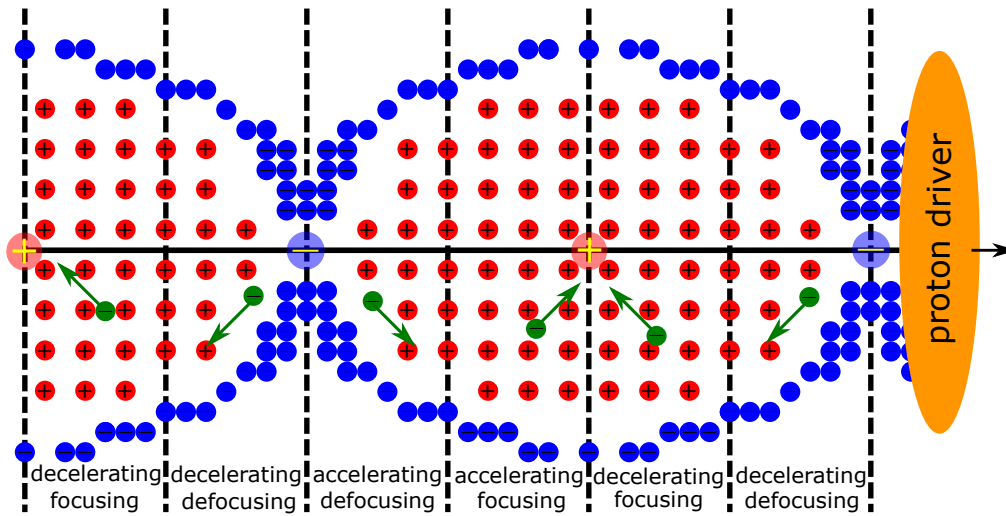


Figure 1: Charge separation by a p^+ -bunch driver (orange, bunch length $L_b \approx \lambda_{pe}/2$) propagating through a neutral plasma. The plasma electrons (blue) are expelled from the bunch propagation axis. Afterwards, they are attracted back to the axis, overshoot and start oscillating with a period of $2\pi/\omega_{pe}$ along the axis. The much heavier ions (red) can be considered as immobile.

The arrows indicate the direction of movement of an injected negatively charged test particle (green). Efficient electron acceleration is only possible in focusing and accelerating phases of the wake.

2.3 Plasma Instabilities

In plasmas, various kinds of longitudinal and transverse instabilities can appear. These instabilities can either grow randomly from noise or from inhomogeneous conditions inside the plasma. Moreover, instabilities can be seeded externally, e.g. by a non-axisymmetric drive bunch or a sudden change of the plasma conditions. In plasmas which interact with charged particle beams (or more general, in counter-streaming plasmas) the predominant instabilities are referred to as two-stream instabilities.

In the following section, we focus only on those plasma instabilities, which are important for AWAKE.

2.3.1 The Current Filamentation Instability

While the condition for the optimal longitudinal p^+ -bunch size is given by Equation 2.18, another condition can be stated for the optimal radial bunch size in order to avoid the bunch to break up into filaments due to the Current Filamentation Instability (CFI) [42]. The return current inside the bunch is shielded by the plasma electrons within a plasma skin depth $k_{pe}^{-1} = c/\omega_{pe}$. In order to ensure the return current to flow outside the bunch, its transverse size σ_r has to fulfil the condition

$$\frac{c}{\omega_{pe}} > \sigma_r \quad (2.19)$$

or equivalently

$$k_{pe}\sigma_r < 1. \quad (2.20)$$

This avoids that currents inside the p^+ -bunch repel each other and amplify non-uniformities inside the bunch, which would lead to a break-up of the bunch structure into filaments of larger current density. This effect was observed experimentally, e.g. by Allen et al. [43].

2.3.2 The Self-Modulation Instability

The Self-Modulation Instability (SMI) is an axi-symmetric transverse two-stream plasma instability. An initially long p^+ -bunch (or more general, particle bunch) with bunch length $L_b \gg \lambda_{pe}$ propagating through plasma is subject to a process that periodically modulates the transverse bunch density into a train of equally spaced micro-bunches, separated by a period on the order of λ_{pe} (see Figure 2a). Co-propagating initial seed wakefields start to periodically focus and defocus protons in the front of the bunch, i.e. regions with higher and lower charge density are created. As the strength of the wakefields is proportional to the charge density, charges get more focused in regions where the density is already higher and the wakefield amplitude increases. Regions, however, in which the protons are already defocused and thus their density is lower, drive lower wakefields. Hence, the entire process is driven resonantly and leads to the periodical modulation of the bunch structure.

In general, the SMI can grow from low amplitude wakefield noise driven by the unmodulated p^+ -bunch. The growth of the instability starts somewhere at the beginning of the p^+ -bunch, at a position unknown in the experiment. Therefore, there is no reproducibility of the modulation phase on an event-to-event basis. The initial seed level depends on the noise level in the bunch. In order to overcome this randomness, the instability needs to be seeded externally, for example with a sharp rising edge in the p^+ -bunch charge distribution. This could be done either with a pre-shaped half-cut Gaussian p^+ -bunch, which is very difficult to produce in conventional particle accelerators or, like in AWAKE, with a sharp rise in the plasma density distribution caused by the ionisation front created by a high-power laser pulse co-propagating with the p^+ -bunch. The modulation of the p^+ -bunch caused by this seeding technique is referred to as Seeded Self-Modulation (SSM) [29].

Besides those approaches, also seeding with a charged particle beam, e.g. an e^- -bunch, would be a possible concept (see [44] and Appendix A). A short e^- -bunch co-propagating within the long p^+ -bunch with $n_{b,e^-} \sim n_{b,p^+}$ leads to a distinct reduction in the effective charge density distribution. Hence, it leads to the sharp rise of the charge density needed to provide large enough initial seed wakefields in the rear part of the p^+ -bunch. A detailed discussion on this concept is subject of Section 2.4.

Furthermore, seeding the SM process overcomes the development of other two-stream instabilities with similar growth rates, like the HI (see Section 2.3.3).

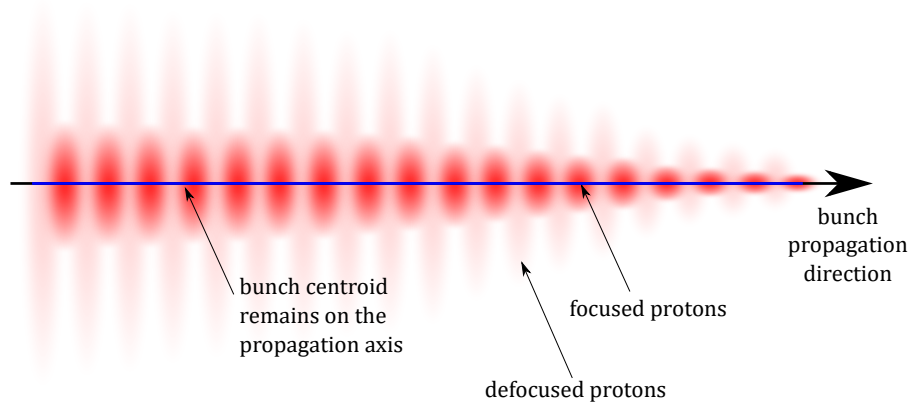
According to Schroeder et. al. [45], we can calculate the bunch radius perturbation r_1 due to the SMI for a bunch with flat-top radial profile and $r(z, \zeta = 0) = \delta r \Theta(z)$ and $r(z = 0, \zeta) = \delta r$, where Θ denotes the Heaviside step function. It is given by

$$\frac{r_1}{\delta r} = \frac{3^{1/4}}{\sqrt{8\pi N_{SMI}}} e^{N_{SMI}} \cos \left[\frac{\pi}{12} - k_{pe}(\zeta - \zeta_0) - \frac{1}{\sqrt{3}} N_{SMI} \right] \quad (2.21)$$

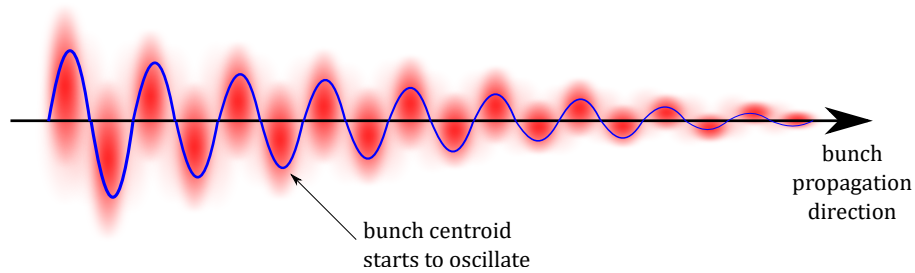
with the number of exponentiations

$$N_{SMI} = \frac{3^{3/2}}{4} \left[2\nu \hat{k}_\beta^2 k_{pe}^3 (\zeta - \zeta_0) z^2 \right]^p, \quad (2.22)$$

$p = \frac{1}{3}$ and $\nu = 4I_2(k_{pe}r_0)K_2(k_{pe}r_0)$. The term proportional to $k_{pe}(\zeta - \zeta_0)$ in N_{SMI} indicates the growth of the instability along the bunch, the term proportional to $(k_{pe}z)^2$ the growth along the plasma. The start point of the instability growth along ζ is described by ζ_0 .



(a) A long p^+ -bunch ($L_b \gg \lambda_{pe}$) propagating through plasma is subject to the SMI. Periodic focusing and defocusing forces are acting on the bunch resulting in a modulation of the bunch charge distribution into a train of micro-bunches separated by λ_{pe} . The centroid of the p^+ -bunch remains on the bunch propagation axis.



(b) A long p^+ -bunch with a non-axisymmetric distribution of the bunch charge propagating through plasma is subject to the HI. It results from the non-axisymmetric coupling between the p^+ -bunch transverse position and the focusing force induced by the plasma wakefields. The bunch centroid starts to oscillate periodically with an oscillation wavelength of λ_{pe} and with growing amplitude along the bunch and the plasma.

Figure 2: Schematic visualisation of the growth of the SMI (a) and the HI (b)

2.3.3 The Hosing Instability

Similarly to the SMI described in the section above, the Hosing Instability (HI) is also a transverse two-stream instability. It is akin to the Beam Break-Up (BBU) instability in conventional particle accelerators and was first described for an e^- -bunch in a pre-formed hollow plasma in 1991 by Whittum et. al [46]. First, they consider the case where an e^- -bunch with axi-symmetric shape is propagating through the plasma (equilibrium case). The plasma electrons are expelled by the e^- -bunch radially symmetric to the outside of the propagation axis and a channel of remaining immobile ions is formed.

Now, they introduce a small centroid perturbation Δx_c on the e^- -bunch distribution. The e^- -bunch is hence no longer propagating in the centre of the plasma channel, which then induces a shift of the channel wall by $-\Delta x_c$. The expelled electrons in the boundary region of the ion channel respond to the change of the charge distribution by a harmonic oscillation. This oscillation can now couple to the perturbation in the charge distribution of the e^- -bunch. It results in a harmonic oscillation of the bunch centroid with increasing amplitude along the plasma and the bunch.

The HI of an e^- -bunch in the blow-out regime of a plasma wakefield accelerator is analytically and numerically studied by [47]. They show that the growth of the HI is affected by the e^- -beam parameters and that the growth rate is much lower for a bunch driving wakefields than for a bunch in a pre-formed plasma channel (as discussed in [46]).

An analogous effect for lasers propagating through plasma, laser hosing, was also investigated, e.g. by [35]. The mathematical description of laser hosing and the HI of a particle bunch is very similar.

The mitigation of the HI in plasma wakefield accelerators is yet an important subject of analytical and numerical work, e.g. see [34] or [48].

So far, the HI of a long p^+ -bunch propagating through an overdense plasma as shown in Figure 2b and its suppression is extensively discussed, e.g. by [36], but has not yet been unambiguously observed in experiments, possibly due to the following reasons: The propagation distances in plasma in previous experiments might have been too short to observe a large enough growth of the HI and the experiments have been designed in a way that the growth of the HI is suppressed. Moreover, the observation of wiggles or kinks in the transverse bunch structure might be caused by poor alignment between the beam trajectory and the plasma column and a relation of the observed effect to the growth of the HI might have been difficult to establish.

Furthermore, positively charged bunches are in general less sensitive to the growth of the HI as there is no blow-out regime and there is no uniform focusing force. Contrary to that, negatively charged beams are more sensitive as they can reach the blow-out regime with focusing by the ion column.

In the narrow bunch limit, i.e. $k_{pe}\sigma_r \ll 1$, the equation of the beam centroid evolution along z is given by [34]

$$\frac{\partial^2 x_c}{\partial z^2} = k_\beta^2 \int_{-\infty}^{\zeta} n_{\parallel}(\zeta') k_{pe} (x_c(\zeta') - x_c(\zeta)) \sin(k_{pe}(\zeta - \zeta')) d\zeta', \quad (2.23)$$

where x_c denotes the position of the bunch centroid. From Equation 2.23, we can derive the following equations [34, 36]:

$$\frac{\partial^2 x_c}{\partial z^2} - k_\beta^2 \frac{\delta n_{pe}}{n_0} x_c = k_\beta^2 x_w \quad (2.24)$$

$$\frac{\partial^2 x_w}{\partial \zeta^2} + k_{pe}^2 x_w = k_{pe}^2 x_c n_{||} \quad (2.25)$$

$$\frac{\partial^2 \left(\frac{\delta n_{pe}}{n_0} \right)}{\partial \zeta^2} + k_{pe}^2 \frac{\delta n_{pe}}{n_0} = -k_{pe}^2 n_{||}. \quad (2.26)$$

Equations 2.24 – 2.26 are a set of second order differential equations of a driven harmonic oscillation. From Equation 2.24, we can infer that the beam centroid x_c is oscillating with an angular frequency of $k_\beta \sqrt{\frac{\delta n_{pe}}{n_0}}$ along z and from Equation 2.25 that the wake centroid x_w is oscillating with k_{pe} in ζ . By resonant coupling of Equation 2.24 to 2.25, a regime for the growth of the HI can be provided. Equation 2.26 describes the coupling of the beam density $n_{||}(\zeta) = r_b^2(z=0, \zeta)/r_b^2(\zeta)$ to the harmonic oscillation in $\delta n_{pe}/n_0$, i.e. the plasma wakefield.

To resonantly drive an oscillation, either the wake centroid has to oscillate close to k_{pe} or the beam centroid close to k_β . The former case ($x_w \sim k_{pe}$) is referred to as short pulse regime, the latter ($x_c \sim k_\beta$) as long pulse regime.

Similarly to the bunch radius perturbation due to the SMI, the asymptotic solution for the bunch centroid displacement x_c due to the HI is calculated by Schroeder et al. in [36]. They assume an ultra-relativistic rigid long p^+ -bunch with a transversely flat-top distribution propagating through an overdense cold fluid plasma, an immobile ion background and no external seed of the SMI, i.e. a transversely constant p^+ -bunch size. Similarly to Equations 2.21 and 2.22, x_c is given by

$$\frac{x_c}{\delta_c} = \frac{3^{1/4}}{\sqrt{8\pi N_{HI}}} e^{N_{HI}} \cos \left[\frac{\pi}{12} - k_{pe}(\zeta - \zeta_0) - \frac{1}{\sqrt{3}} N_{HI} \right] \quad (2.27)$$

with the number of exponentiations

$$N_{HI} = \frac{3^{3/2}}{4} \left[\mu \hat{k}_\beta^2 k_{pe}^3 (\zeta - \zeta_0) z^2 \right]^p, \quad (2.28)$$

$p = \frac{1}{3}$ and $\mu = 2I_1(k_{pe}\sigma_r)K_1(k_{pe}\sigma_r)$ a factor describing the effect of the plasma return current. Here, the initial modulation of the beam centroid δ_c is again expressed by the initial conditions $r(z, \zeta = 0) = \delta_c \Theta(z)$ and $r(z = 0, \zeta) = \delta_c$. As in the SMI case, the term $\propto k_{pe}(\zeta - \zeta_0)$ describes the growth of the HI along the bunch, the term $\propto (k_{pe}z)^2$ its growth along the plasma.

The number of exponentiations of the HI along ζ according to Equation 2.28 is shown in Figure 3a for an AWAKE-like p^+ -bunch with different bunch populations and plasma densities. As expected, N_{HI} is the larger, the higher the bunch population and the

higher the plasma density. Along the bunch, N_{HI} continues to increase but with decreasing slope. As Equations 2.27 and 2.28 only describe the asymptotic solution of the differential equations 2.24 – 2.26, the approximation is less accurate for small values of $k_{pe}\zeta$ and becomes even non physical in the limits $z \rightarrow 0$ or $(\zeta - \zeta_0) \rightarrow 0$. Moreover, the

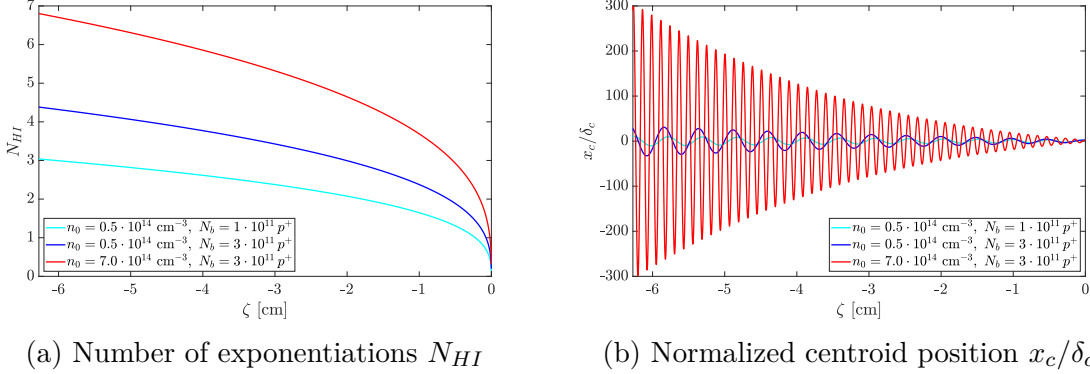


Figure 3: N_{HI} according to Equation 2.28 (a) and x_c/δ_c along the bunch according to Equation 2.27 (b) for an SPS-like p^+ -bunch with parameters where the HI is experimentally observed ($n_0 = 0.5 \cdot 10^{14} \text{ cm}^{-3}$, $N_b = 3 \cdot 10^{11} p^+$, $z = 10 \text{ m}$ (dark blue); $n_0 = 0.5 \cdot 10^{14} \text{ cm}^{-3}$, $N_b = 1 \cdot 10^{11} p^+$, $z = 10 \text{ m}$ (cyan), see Chapter 6) and for AWAKE baseline parameters (red).

model eventually overestimates the growth as it does not contain a possible saturation of the growth, which is observed in the experiment.

In Figure 3b, the normalized centroid position along ζ for a p^+ -bunch oscillating due to the HI is plotted for the same plasma parameters as in Figure 3a. In the experiment, the centroid oscillation can be determined from SC images (see Chapter 6). According to Equation 2.27, the oscillation frequency of the bunch centroid is equal to f_{pe} and thus the oscillation is faster for a higher plasma density than for a lower plasma density. Moreover, the amplitude of the oscillation is growing faster for larger N_{HI} . It can be seen from comparing the bunches with different N_b (but same n_0) that the phase of the oscillation also depends on N_b .

To compare the different numbers of exponentiations of the SMI and the HI, we can calculate the ratio of Equation 2.22 and Equation 2.28:

$$\frac{N_{HI}}{N_{SMI}} = \left(\frac{\mu}{2\nu} \right)^{\frac{1}{3}} = \left(\frac{1}{4} \cdot \frac{I_1(k_{pe}\sigma_r)K_1(k_{pe}\sigma_r)}{I_2(k_{pe}\sigma_r)K_2(k_{pe}\sigma_r)} \right)^{\frac{1}{3}} = \left(\frac{1}{4} \cdot R_{Bessel} \right)^{\frac{1}{3}}. \quad (2.29)$$

For $k_{pe}r_0 = 1$, the ratio of the Bessel functions is $R_{Bessel} \approx 1.54$ and $N_{HI}/N_{SMI} \approx 0.67$. This infers that the growth rates of the SMI and the HI are on the same order.

We can now calculate the dependence of the ratio N_{HI}/N_{SMI} on the plasma density. Figure 4 shows the values for μ and ν as well as the ratio of the number of exponentiations for a p^+ -bunch with $\sigma_r = 200 \mu\text{m}$ at plasma densities up to the AWAKE baseline density. We can conclude that N_{HI}/N_{SMI} reaches its maximum in the limit $n_0 \rightarrow 0$, but it remains below 1. From this limit, the ratio N_{HI}/N_{SMI} starts to decrease the higher the plasma

density is chosen. Thus, for the same initial seed level for the SMI and the HI, the growth of the SMI dominates over the growth of the HI.

This result, however, is difficult to be validated experimentally because the initial seed levels of both the SMI and the HI are unknown in the experiment and thus cannot be compared easily. We can only conclude from Figure 4 that at lower plasma densities it gets more likely that the HI dominates over the SMI. Therefore, we expect to see more events with the HI at lower than at higher plasma densities.

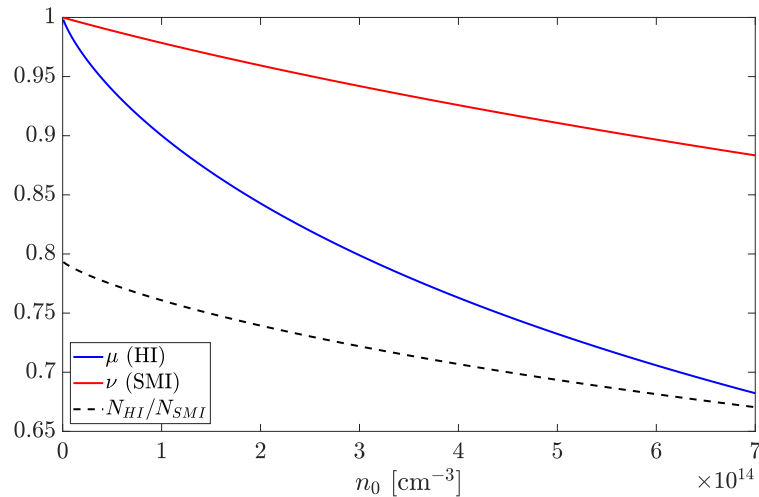


Figure 4: Factors μ and ν as well as the ratio $\frac{N_{HI}}{N_{SMI}}$ at different plasma densities.

2.3.4 Coupled Beam Hosing

Equation 2.27, discussed in the previous Section 2.3.3, only describes the growth of the HI. No additional growth of the SMI from an initial seed or from noise in the bunch structure is considered. Thus, there is no coupling to the wakefields and the centroid oscillations are symmetric with respect to $x_c/\delta_c = 0$.

In [36], Schroeder et al. also discuss the case where the SMI and the HI are seeded and growing simultaneously. Here, both instabilities can couple to each other via the plasma wakefields. This phenomenon is referred to as Coupled Beam Hosing (CBH). They state that in this case, the coupling of the SM process to the HI generates harmonics and that the amplitude of the beam hosing increases when compared to a simple growth of the HI without coupling. Moreover, the oscillations become asymmetric with respect to $x_c/\delta_c = 0$, i.e. the amplitude of the centroid oscillation is larger on one side of the bunch propagation axis than on the other.

In order to implement those additional effects, the harmonics and the asymmetry of the oscillation amplitudes, we modify Equation 2.27 to

$$\begin{pmatrix} x_c \\ \delta_c \end{pmatrix}_{coupled} = \begin{pmatrix} x_c \\ \delta_c \end{pmatrix}_{uncoupled} \cdot [1 + \varepsilon \cdot \sin(k_{pe}\zeta)], \quad (2.30)$$

where ε is a constant describing the strength of the coupling between the SMI and the HI. Figure 5a shows the centroid oscillation of a p^+ -bunch along $k_{pe}\zeta$ with $n_0 = 0.5 \cdot 10^{14} \text{ cm}^{-3}$

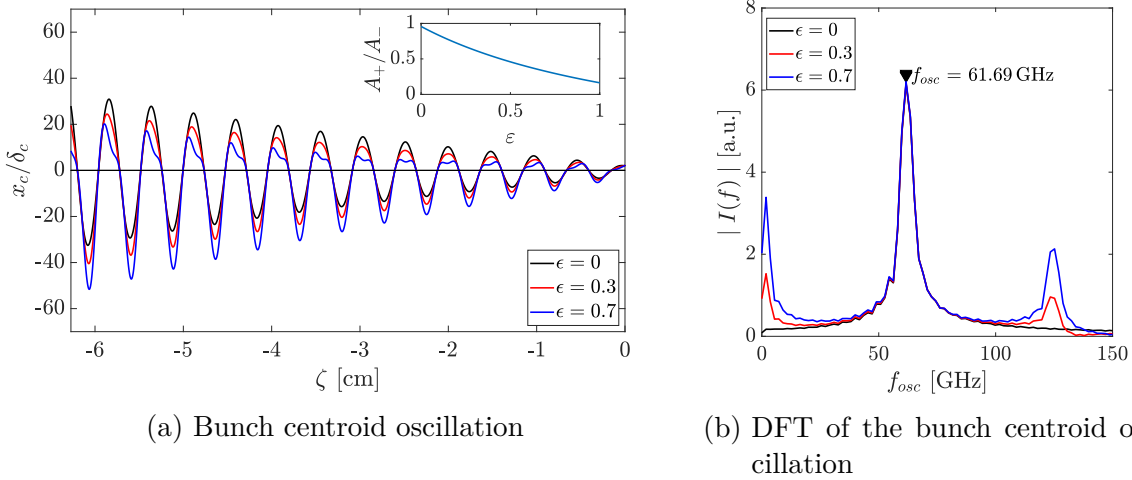


Figure 5: Comparison of the bunch centroid oscillation (a) and its DFT (b) between coupled and uncoupled beam hosing for an SPS-like p^+ -bunch with $n_0 = 0.5 \cdot 10^{14} \text{ cm}^{-3}$ and $N_b = 3 \cdot 10^{11} p^+$. The inlet in (a) shows the area ratio A_+/A_- in dependence of the coupling constant ε .

and $N_b = 3 \cdot 10^{11} p^+$ in the uncoupled case ($\varepsilon = 0$) and for two different coupling strengths ($\varepsilon = 0.3$ and $\varepsilon = 0.7$).

The plot confirms that for $\varepsilon = 0$ the oscillation is symmetric with respect to $x_c/\delta_c = 0$, whereas it becomes asymmetric for $\varepsilon > 0$. With increasing coupling constant ε , the oscillation amplitude gets higher on one side of the p^+ -bunch and more damped on the opposite side. The protons in the half of the oscillation period experiencing defocusing wakefields are further pushed away from the bunch propagation axis, whereas protons in the other half of the oscillation period experience the focusing forces by the SMI and reside closer to the axis. We discuss the effect of the focusing and defocusing phases of the wakefields on the asymmetry due to the coupling in more detail in the context of the PIC simulations in Chapter 5.

To have a measure which can be easily applied to the experimental SC data, we define the area ratio A_+/A_- , i.e. the ratio between the areas enclosed by the trajectory of the bunch centroid above and below the bunch propagation axis. To neglect whether the larger centroid displacement and thus the larger enclosed area is above or below the bunch propagation axis, we define that $A_+/A_- \in [0; 1]$. In case $A_+/A_- > 1$, we take the inverse value A_-/A_+ as area ratio. The inlet in Figure 5a shows the dependence of the area ratio on the coupling constant ε for the range $\zeta \in [-6.27; 0]$. Note, this range corresponds to the temporal size of the 211 ps SC time window (see Sections 3.1.6 and 6.3.2). The oscillation is cut in between a full oscillation period and therefore, $A_+/A_- < 1$ for $\varepsilon = 0$. Only when the range covers exactly full oscillation periods, $A_+/A_- = 1$ for a symmetric oscillation. As expected, the stronger the coupling, i.e. the more asymmetric the event, the smaller the area ratio.

The Discrete Fourier Transform

To determine the frequency of the bunch centroid modulation f_{osc} , we use the Discrete Fourier Transform (DFT). It is a transformation from a finite temporal signal $F(N)$ with equally spaced samples (e.g. the pixels of a SC image or the data points of a simulation) to its corresponding frequency spectrum $\tilde{F}(K)$ and is given for a signal with length M by [49]

$$\tilde{F}(K) = \sum_{N=0}^{M-1} F(N) \exp\left(-2\pi i \frac{KN}{M}\right) \quad (K = 0, \dots, M-1) \quad (2.31)$$

and an inverse transform

$$F(N) = \frac{1}{M} \sum_{K=0}^{M-1} \tilde{F}(K) \exp\left(2\pi i \frac{KN}{M}\right) \quad (N = 0, \dots, M-1). \quad (2.32)$$

As the length of the underlying signal is finite (for the SC used in AWAKE 512 pixel for all time windows), the frequency resolution Δf has to be discrete as well. This is referred to as bin discretisation of the DFT and its size in the frequency domain is given by

$$\Delta f = \frac{1}{M\Delta t} = \frac{1}{T_{streak}}, \quad (2.33)$$

where Δt corresponds to the size of a single data point or a pixel of the SC image in the time domain and T_{streak} to the SC time window or the size of a simulation window.

In order to artificially increase the sample length of the signal, the image can be zero padded, i.e. the length of the signal M is extended by adding zeros at the end of the sample.

To be able to use the Fast Fourier Transform (FFT) algorithm, the sample length M of the temporal signal has to fulfill

$$M = 2^n \quad \text{with } n \in \mathbb{N} \quad (2.34)$$

after the zero padding. It is important to note that zero padding of a signal does not enhance the frequency resolution of the DFT, but increases the interpolation density between two sample points [49], i.e. it increases the precision of finding the position of an isolated peak in the spectrum.

According to Equation 2.33, a better frequency resolution can be achieved by increasing T_{streak} . However, there is a bandwidth limit by the resolution of the signal in the time-domain. The Nyquist sampling theorem requires that the sampling rate has to be at least twice the maximum frequency to be resolved. Hence, for a sinusoidal signal the maximum frequency that can be resolved is given by

$$f_{max,sin} = \frac{M}{2T_{streak}}. \quad (2.35)$$

The DFT of the oscillations with different coupling strengths presented in Figure 5a with a sample length of 512 and a zero padding to $n = 14$ (same parameters as for experimental data) is shown in Figure 5b. We observe a clear peak in the DFT power spectrum at $f_{osc} = 61.7$ GHz with a similar amplitude and width for all plotted values of ε . This frequency is close to the plasma frequency $f_{pe}(n_0 = 0.5 \cdot 10^{14} \text{ cm}^{-3}) = 63.7$ GHz and differs by 2 GHz due to the resolution of the DFT. Moreover, for $\varepsilon \neq 0$ the DFT reveals peaks at $f_{osc} = 0$ and at the second harmonic $2f_{osc}$ with smaller amplitude than the main peak. The amplitude of these peaks increases for increasing ε . A more detailed discussion on the deviation between f_{osc} and f_{pe} is presented in Section 6.4.

These results infer that in the experiment we expect to see peaks in the DFT power spectrum of the signal of the bunch centroid oscillation near f_{pe} . Hence, we should be able to prove the relation $f_{osc}(n_0) = f_{pe}(n_0)$, similarly to the relation $f_{mod}(n_0) = f_{pe}(n_0)$ which has already been proven by [31] for the bunch charge modulation frequency f_{mod} due to the SM process.

2.4 Seeding of the Self-Modulation Process of a Long Proton Bunch with a Short Electron Bunch

In this section, we present a different seeding concept for the SM of a long p^+ -bunch using a short e^- -bunch. A schematic overview of the concept is shown in Figure 6. It has been discussed in the context of possible seeding methods for the upcoming AWAKE Run 2 (see Section 3.2).

A high-power laser pulse is ionizing the Rubidium (Rb) vapour and pre-forms a plasma column through which the long p^+ -bunch is propagating some ps after the laser pulse. A

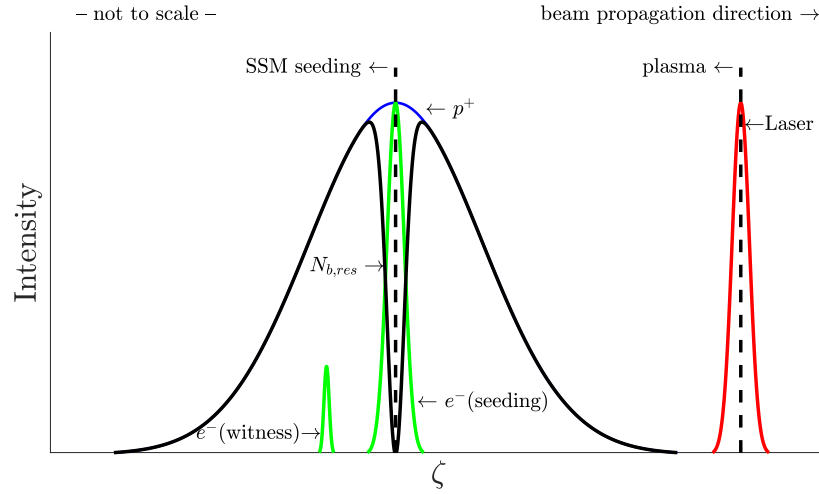


Figure 6: Schematic of the SM seeding scheme by a co-propagating short e^- -bunch at the centre of the long p^+ -bunch.

short e^- -bunch with a bunch population N_{b,e^-} on the order of the p^+ -bunch population N_{b,p^+} is co-propagating at the centre of the p^+ -bunch. This leads to a drop in the effective charge density distribution.

To simplify the following calculations, we assume that both bunches have a cos-shaped bunch distribution $N_{b,res}$. The effective longitudinal charge distribution $n_{b\parallel}$ along the p^+ -bunch is shown in Figure 7 and given by

$$n_{b\parallel}(\zeta') = \begin{cases} A_0 \cdot \sin\left(\frac{\pi \cdot (\zeta' + L)}{2(L-U)}\right) & \zeta' \in [-L, -U] \\ \frac{A_{min} - A_0}{2} \cdot \cos\left(\frac{\pi \zeta'}{U}\right) + \frac{A_{min} + A_0}{2} & \zeta' \in [-U, U] \\ A_0 \cdot \cos\left(\frac{\pi \cdot (\zeta' - U)}{2(L-U)}\right) & \zeta' \in [U, L] \\ 0 & \text{elsewhere.} \end{cases} \quad (2.36)$$

The longitudinal size of the p^+ -bunch is $2L$, the longitudinal size of the e^- -bunch is $2U$. The bunch population is assumed to be zero outside $[-L, L]$ for the p^+ -bunch and

2.4 Seeding of the SM Process of a Long Proton Bunch with a Short Electron Bunch

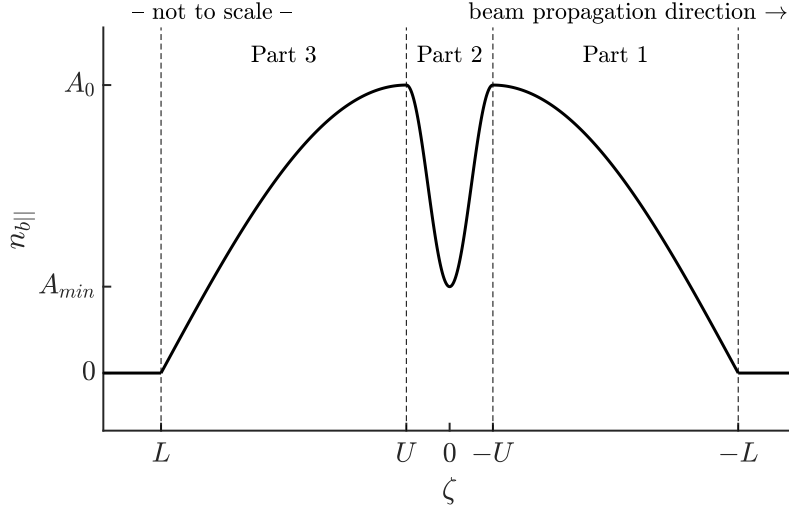


Figure 7: Effective charge distribution along the p^+ -bunch for seeding with a short e^- -bunch.

outside $[-U, U]$ for the e^- -bunch. Moreover, we assume that both bunches have radially the same extension.

Now, we calculate the wakefields driven by the separate parts of the p^+ -bunch (see Figure 7) by piecewise integrating Equations 2.13 and 2.14 along ζ . The leading part of the bunch ($-L < \zeta < -U$, Part 1) drives wakefields with a parallel component

$$E_{1,\parallel}(\zeta) = \begin{cases} 0 & \zeta < -L \\ \frac{A_0}{2k_{pe}} \left[-(C_+ + C_-) \left[\cos\left(\frac{\pi(\zeta+L)}{2(L-U)}\right) + \cos(k_{pe}(\zeta+L)) \right] \right] & \zeta \in [-L, -U] \\ \frac{A_0}{2k_{pe}} \left[-(C_+ - C_-) \sin(k_{pe}(\zeta+U)) + (C_+ + C_-) \cos(k_{pe}(\zeta+L)) \right] & \zeta > -U \end{cases} \quad (2.37)$$

and a perpendicular component

$$E_{1,\perp}(\zeta) = \begin{cases} 0 & \zeta < -L \\ \frac{A_0}{2} \left[(C_+ - C_-) \sin\left(\frac{\pi(\zeta+L)}{2(L-U)}\right) + (C_+ + C_-) \sin(k_{pe}(\zeta+L)) \right] & \zeta \in [-L, -U] \\ \frac{A_0}{2} \left[(C_+ - C_-) \cos(k_{pe}(\zeta+U)) + (C_+ + C_-) \sin(k_{pe}(\zeta+L)) \right] & \zeta > -U. \end{cases} \quad (2.38)$$

The parallel and perpendicular wakefield components in the part where the e^- -bunch is co-propagating with the p^+ -bunch ($-U < \zeta < U$, Part 2) are described by

$$E_{2,\parallel}(\zeta) = \begin{cases} 0 & \zeta < -U \\ \frac{A_1}{2k_{pe}} \left[(D_+ + D_-) \sin\left(\frac{\pi\zeta}{U}\right) - (D_+ - D_-) \sin(k_{pe}(\zeta+U)) \right] \\ \quad + \frac{A_2}{k_{pe}^2} \sin(k_{pe}(\zeta+U)) & \zeta \in [-U, U] \\ \frac{A_1}{2k_{pe}} \left[(D_+ - D_-) \sin(k_{pe}(\zeta-U)) - (D_+ - D_-) \sin(k_{pe}(\zeta+U)) \right] \\ \quad - \frac{A_2}{k_{pe}^2} \left[\sin(k_{pe}(\zeta-U)) - \sin(k_{pe}(\zeta+U)) \right] & \zeta > U \end{cases} \quad (2.39)$$

and

$$E_{2,\perp}(\zeta) = \begin{cases} 0 & \zeta < -U \\ \frac{A_1}{2} \left[(D_+ + D_-) \cos\left(\frac{\pi\zeta}{U}\right) - (D_+ - D_-) \cos(k_{pe}(\zeta + U)) \right] \\ \quad + \frac{A_2}{k_{pe}} [1 - \cos(k_{pe}(\zeta + U))] & \zeta \in [-U, U] \\ \frac{A_1}{2} [(-D_+ + D_-) \cos(k_{pe}(\zeta - U)) + (D_+ - D_-) \cos(k_{pe}(\zeta + U))] \\ \quad - \frac{A_2}{k_{pe}} [\cos(k_{pe}(\zeta + U)) - \cos(k_{pe}(\zeta - U))] & \zeta > U. \end{cases} \quad (2.40)$$

Finally, the wakefields of the last part ($U < \zeta < L$, Part 3) are given by

$$E_{3,\parallel}(\zeta) = \begin{cases} 0 & \zeta < U \\ \frac{A_0}{2k_{pe}} \left[(C_+ + C_-) \sin\left(\frac{\pi(\zeta-U)}{2(L-U)}\right) + (C_+ - C_-) \sin(k_{pe}(\zeta - U)) \right] & \zeta \in [U, L] \\ \frac{A_0}{2k_{pe}} \left[(C_+ + C_-) \cos(k_{pe}(\zeta - L)) + (C_+ - C_-) \sin(k_{pe}(\zeta - U)) \right] & \zeta > L \end{cases} \quad (2.41)$$

and

$$E_{3,\perp}(\zeta) = \begin{cases} 0 & \zeta < U \\ \frac{A_0}{2} \left[(C_+ - C_-) \cos\left(\frac{\pi(\zeta-U)}{2(L-U)}\right) + (-C_+ + C_-) \cos(k_{pe}(\zeta - U)) \right] & \zeta \in [U, L] \\ \frac{A_0}{2} \left[(C_+ + C_-) \sin(k_{pe}(\zeta - L)) + (-C_+ + C_-) \cos(k_{pe}(\zeta - U)) \right] & \zeta > L. \end{cases} \quad (2.42)$$

The constants in Equations 2.37 - 2.42 are given by

$$A_1 = \frac{A_{min} - A_0}{2} \quad (2.43)$$

$$A_2 = \frac{A_{min} + A_0}{2} \quad (2.44)$$

$$C_{\pm} = \frac{1}{2(L-U) \pm k_{pe}} \quad (2.45)$$

$$D_{\pm} = \frac{1}{\frac{\pi}{U} \pm k_{pe}}. \quad (2.46)$$

To get the final wakefield distribution along the bunch, we use the superposition theorem of waves in linear theory and add the different contributions of the bunch segments in every region. The resulting wakefields are then given by

$$E(\zeta) = \begin{cases} 0 & \zeta < -L \\ E_1(\zeta) \Big|_{\zeta \in [-L, -U]} & \zeta \in [-L, -U] \\ E_1(\zeta) \Big|_{\zeta \in [-U, U]} + E_2(\zeta) \Big|_{\zeta \in [-U, U]} & \zeta \in [-U, U] \\ E_1(\zeta) \Big|_{\zeta \in [U, L]} + E_2(\zeta) \Big|_{\zeta \in [U, L]} + E_3(\zeta) \Big|_{\zeta \in [U, L]} & \zeta \in [U, L] \\ E_1(\zeta) \Big|_{\zeta > L} + E_2(\zeta) \Big|_{\zeta > L} + E_3(\zeta) \Big|_{\zeta > L} & \zeta > L \end{cases}. \quad (2.47)$$

Figure 8 shows the resulting parallel and perpendicular wakefields for bunches with

2.4 Seeding of the SM Process of a Long Proton Bunch with a Short Electron Bunch

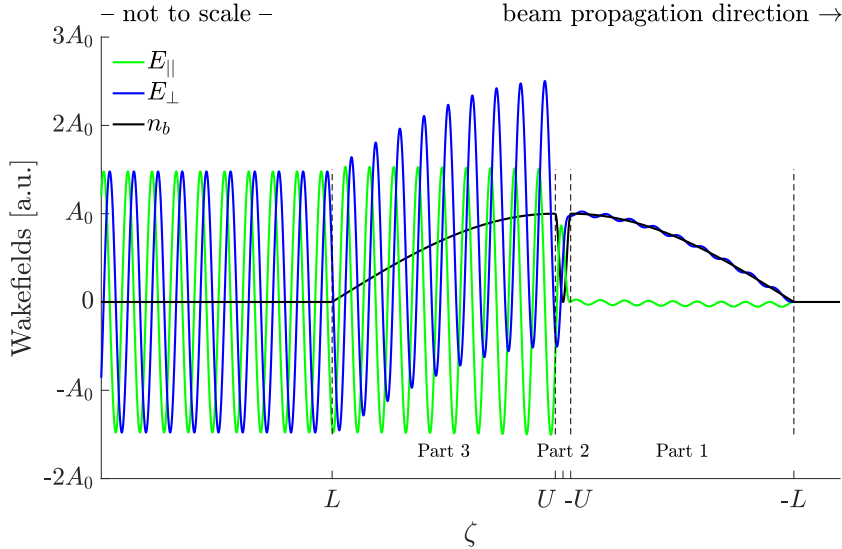


Figure 8: Calculated parallel and perpendicular wakefields $E_{\parallel}(\xi)$ and $E_{\perp}(\xi)$ according to Equation 2.47 for a long p^+ -bunch and an e^- -seed bunch with $\frac{U}{L} = \frac{1}{30}$, $\frac{U}{\lambda_{pe}} = 1.6$ and bunch populations $N_{b,p^+} = N_{b,e^-}$.

$\frac{U}{L} = \frac{1}{30}$ and $\frac{U}{\lambda_{pe}} = 1.6$ according to Equation 2.47. Part 1 of the p^+ -bunch ($-L < \zeta < -U$) which propagates through an already pre-formed plasma has a smooth profile. Here, the adiabatic response of the plasma dominates over the small amplitude wakefields. It leads to a globally focusing force by (partial) neutralisation of the bunch charges and thus to an increasing bunch density. Both effects can lead to a growth of the SMI (as opposed to the SSM) over long plasma distances.

Along the second and third part of the bunch large scale wakefields are driven. They are caused by the sudden change of the effective charge density at the position of the e^- -bunch and provide the seed for the SM process. The amplitude of the wakefields scales linearly with $A_0 - A_{min}$ and with the longitudinal size of the e^- -bunch $2U$. For parameters similar to AWAKE, the wakefields could reach values up the GV/m-scale. The concept presented here relies on the expectation that the wakefields driven by the first part of the p^+ -bunch are not sufficient to seed the growth of the SMI over the propagation length through plasma in AWAKE. Simulations by Kumar et al. [28] support this expectation. The growth of the SMI due to noise in the bunch, however, has to be estimated correctly and cannot be determined easily by simulations.

Experimental results of AWAKE [32] show that the initial noise level in the p^+ -bunch is high enough to almost fully modulate the charge distribution of the p^+ -bunch over a plasma length of 10 m. The position of the seed point, i.e. the position of the e^- -bunch might therefore be too late within the p^+ -bunch to overcome the seed level by noise at the front of the bunch. Hence, the concept described in this section would no longer provide the reproducibility of the modulation phase on an event-to-event basis needed for stable e^- -acceleration.

To overcome this limitation, in the upcoming AWAKE Run 2 (see Section 3.2) the

position of the co-propagating e^- -bunch will be moved close to the head of the p^+ -bunch (see Figure 9). Lotov et. al [50] determined numerically that due to the low initial

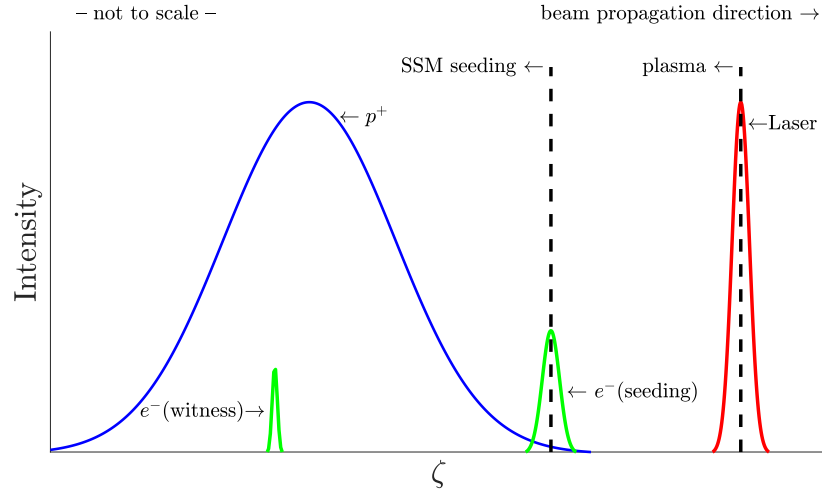


Figure 9: Schematic of the SM seeding scheme by a co-propagating short e^- -bunch at the head of a long p^+ -bunch.

noise fields in the SPS 10 MeV e^- -bunches with a length of 1 ps and a maximum current of 100 A would be sufficient to seed the SM process of the long p^+ -bunch.

3 The AWAKE Experiment

The AWAKE experiment is located at CERN and is a part of its accelerator complex (see Figure 10). It is a proof-of-principle experiment to study the physics and the tech-

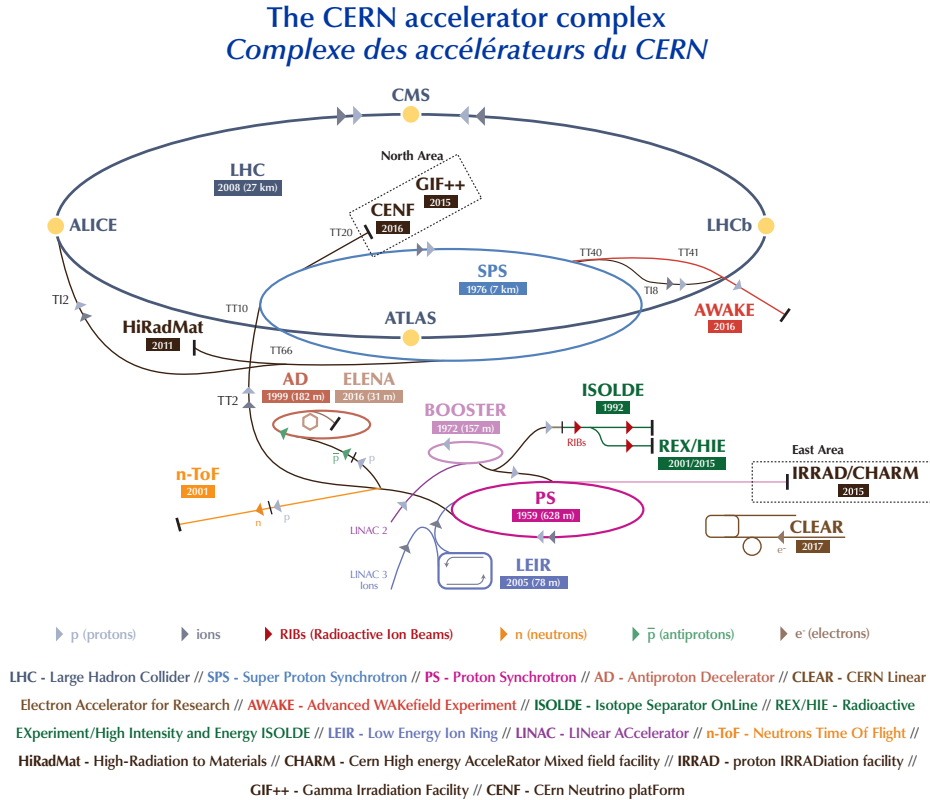


Figure 10: Situation of the AWAKE experiment within the CERN accelerator complex. The different p^+ -acceleration stages from LINAC2 to SPS are visualized. Figure: CERN

nical realization of plasma wakefield acceleration driven by a long p^+ -bunch. After its approval in 2013 (for the AWAKE Design Report see [51]), two years later the assembling of the experiment started in a cavern situated in a branch of the SPS tunnel (see Figure 11). The first scientific run period took place in December 2016. During three scientific run periods in 2017, AWAKE was able to measure the SSM of a p^+ -bunch and to investigate its physical properties, especially the modulation frequency of the p^+ -bunch in dependence of the plasma density as well as the radial defocusing of the protons [30, 31]. Furthermore, the event-to-event phase reproducibility of the SSM could be proven [32].

3 The AWAKE Experiment

After the commissioning of the UV-laser line to the photo-injector (see Section 3.1.7) as well as the e^- -gun and the e^- -spectrometer (see Section 3.1.8) end of 2017, AWAKE showed the first acceleration of externally injected electrons in a p^+ -driven plasma wake-field to energies up to 2 GeV [33].

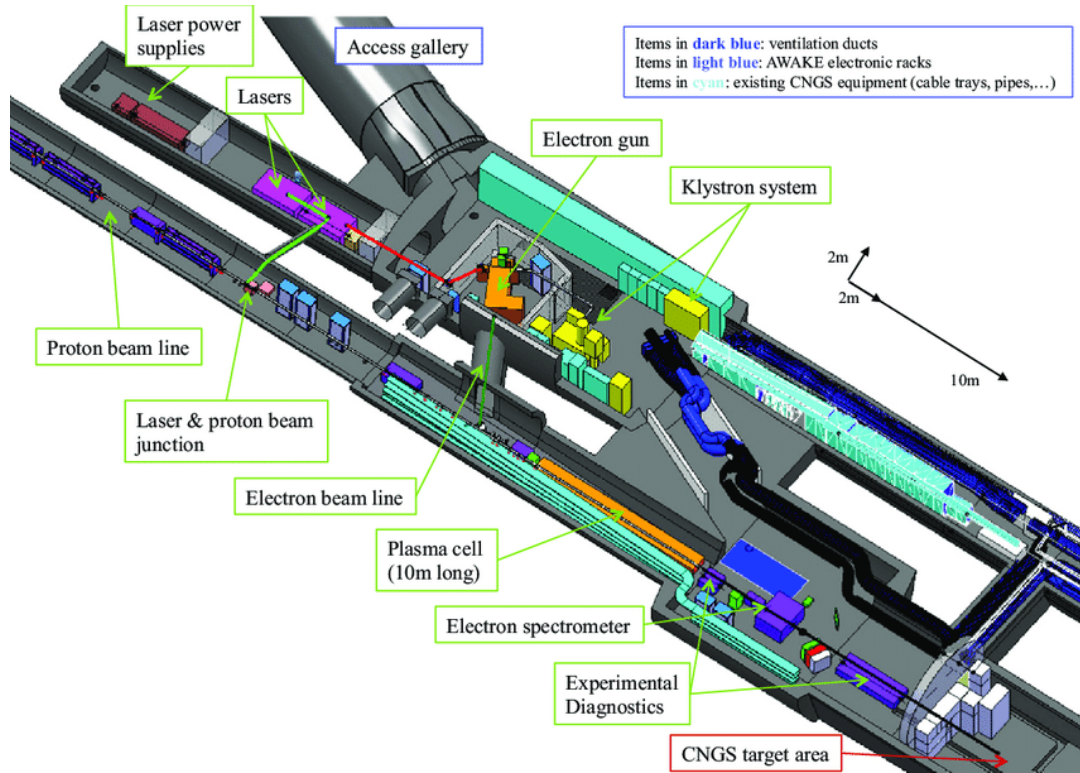


Figure 11: Overview of the AWAKE facility. Figure taken from [52].

3.1 Layout of the Experiment and its Components

The general set-up of AWAKE for studying the SSM and the HI is shown in Figure 12. In the following section we describe these main components of the AWAKE experiment. Hereby, we focus on the parts of the experiment needed for the observation and investigation of the HI, i.e. for gathering SC images of the p^+ -bunch. Moreover, my main additional contributions to the AWAKE experiment, the movable laser beam dumps and the third harmonic generation (THG) stage for the laser to the e^- -gun photo-cathode are discussed in more detail.

3.1.1 The AWAKE Experimental Facility

The AWAKE experiment is located at access point 4 of the SPS (BB4) close to the Prévessin site of CERN in the facilities of the former CERN Neutrinos to Gran Sasso (CNGS) Experiment. An about 800 m long access tunnel connects the experimental area

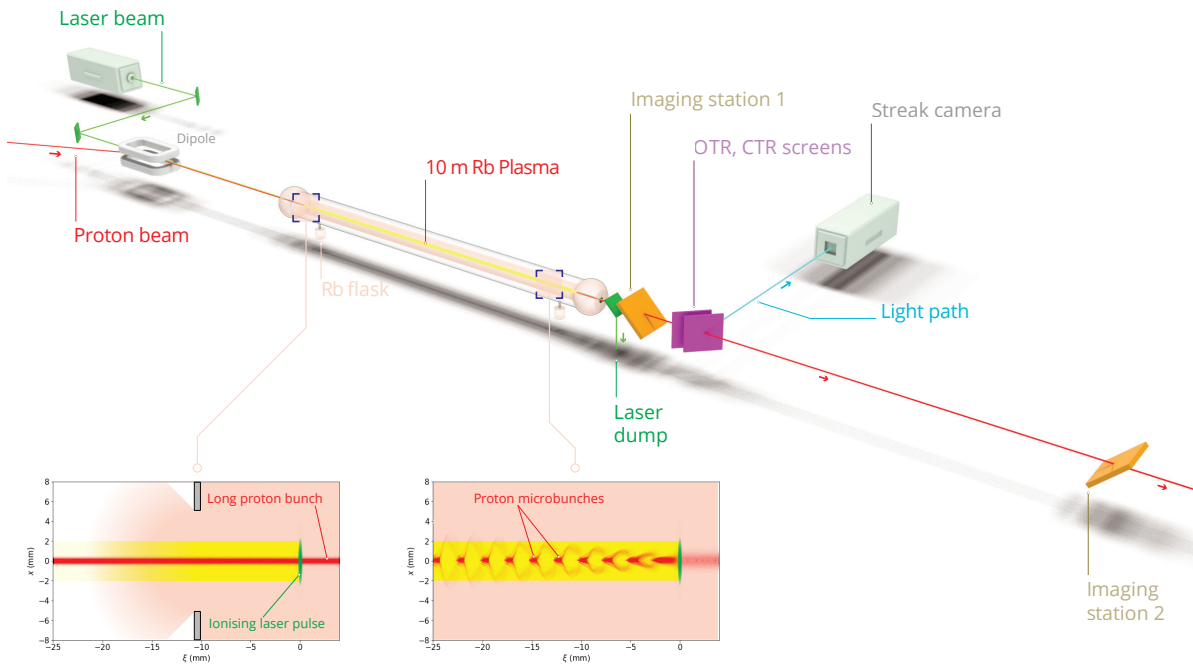


Figure 12: General layout of the AWAKE experiment for gathering SC images to investigate the SSM and the HI of a long p^+ -bunch. Figure: CERN

to the access point, which also hosts the AWAKE Control Center (ACC). The control room is about 40 m, the experimental area about 80 m below surface.

The experimental area (Figure 11) is divided into several access zones. The p^+ -beam line tunnel, connecting the AWAKE facility to the SPS, from where the protons are delivered. In the main AWAKE cavern, the vapour source (see Section 3.1.5) and the stations for the longitudinal and radial p^+ -bunch diagnostics (see Section 3.1.6) are installed. The former CNGS target area in a controlled radiation zone separated by a radiation protection wall is used as p^+ -beam dump. An over-pressurized clean room is hosting the high power laser system and its supplies (see Section 3.1.3). The SC is installed in a light-shielded room separated from the p^+ -beam line in order to avoid radiation effects or even damages. The e^- -gun (see Section 3.1.8) is installed in a radiation bunker, which is connected separately to the p^+ -beam line tunnel. Moreover, several technical installations required for operating the experiment are located in a rack gallery parallel to the target area and in a mezzanine above the e^- -gun. The e^- -spectrometer camera is placed in another light-shielded room in the rack gallery.

3.1.2 The Proton Beam Line

Protons delivered to AWAKE are accelerated in four stages: First by the CERN LINAC2 to about 50 MeV (0.31 c) [53], then by the BOOSTER to 1.4 GeV (0.91 c) [54] and subsequently by the Proton Synchrotron (PS) to 25 GeV (0.9993 c) [55]. The last acceleration

stage is the Super Proton Synchrotron (SPS) with a circumference of 6912 m. A single p^+ -bunch with a final energy of about 400 GeV (0.999998 c) is eventually coupled out by a kicker magnet and delivered through an about 800 m long transport beam line to the AWAKE facility. The different p^+ -acceleration stages before the p^+ -bunch is sent to AWAKE are visualized in Figure 10.

The SPS can provide p^+ -bunches with populations N_b in a range of $N_b = (0.5-3) \cdot 10^{11} p^+$. The repetition rate of the experiment depends on the length of the SPS super cycle.¹ The super cycle can contain up to two AWAKE cycles with a duration of 7.2 s [56]. During normal operation, the duration of an SPS super cycle is between $\sim 40-80$ s. Therefore, the maximum repetition rate for AWAKE is $\sim \frac{1}{20}$ Hz, but on most of the operation days either $\sim \frac{1}{30}$ Hz (two AWAKE cycles in the SPS super cycle) or $\sim \frac{1}{60}$ Hz (only one AWAKE cycle in the SPS super cycle).

In the standard beam configuration, the p^+ -bunches have a nearly Gaussian distribution with an RMS bunch length of $\sigma_z = 12$ cm and a radial RMS-size of $\sigma_{x,y} = 0.02$ cm. Assuming x and y to be independent, the longitudinal and transverse p^+ -bunch profiles are approximately given by [57]

$$\lambda_z = \lambda_{z,0} \cdot \left(1 - \frac{4z^2}{\sigma_z^2}\right)^\kappa \quad (3.1)$$

and

$$\lambda_{x,y} = \frac{1}{2\pi\sigma_x\sigma_y} \cdot \exp\left[-\left(\frac{x^2}{2\sigma_x^2} + \frac{y^2}{2\sigma_y^2}\right)\right], \quad (3.2)$$

where $\kappa \approx 1 - 2$ and $\lambda_{z,0}$ a normalization factor. Furthermore, a bunch rotation mechanism [52] shortening the RMS bunch length to about $\sigma_z = 6$ cm can be applied on the p^+ -bunches. In Chapter 6, we analyze SC images in order to characterize in more detail the incoming p^+ -bunches and discuss the difference in the bunch length for enabled and disabled bunch rotation mechanism.

3.1.3 The Ionizing Laser System

The ionizing laser for AWAKE is based on a commercial Titanium Sapphire (Ti:Sa) laser system from Amplitude Systems using the CPA technique to generate ultra-short, high-intensity laser pulses. A detailed description of the system can be found in [58]. Figure 13 gives a schematic overview of the different components and laser beam lines of the system described in this section, Figure 14 shows a photo of the AWAKE laser room.

The laser oscillator is an erbium-doped fiber oscillator with a wavelength of 1560 nm and a repetition rate of 88.173 MHz delivering 1 nJ pulses. By second harmonic generation (SHG), the desired operational wavelength of 780 nm is generated. It is followed by a stretcher module (gratings with 1500 lines/mm) introducing a chirp to the laser pulses

¹In order to match exactly the RF frequencies of the CERN accelerators, the length of an SPS super cycle is given in multiples of a basic period. The duration of a basic period is 1.2 s [56].

3.1 Layout of the Experiment and its Components

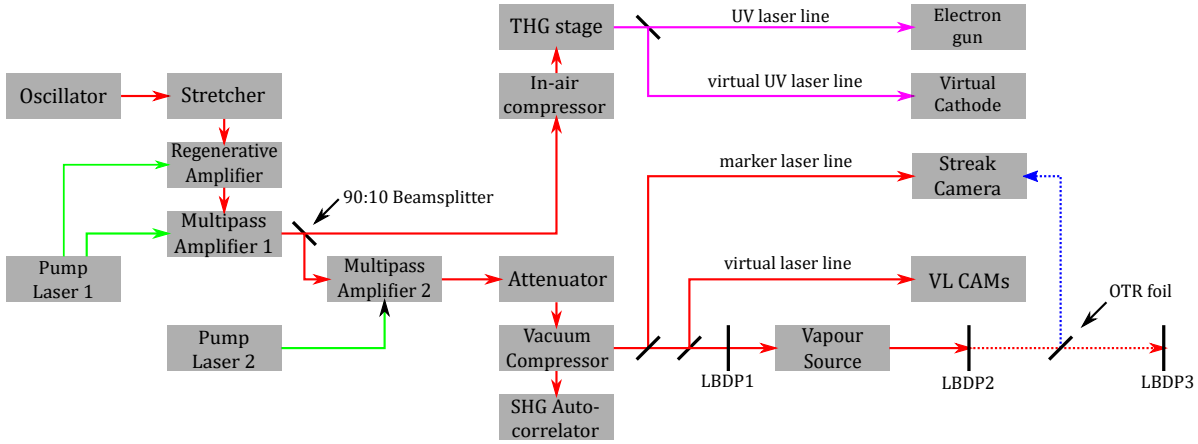


Figure 13: Schematic overview of the components and beam lines of the AWAKE laser system.

and elongating them from 100 fs to about 200 ps. In the subsequent regenerative amplifier module, single pulses are picked with a frequency of 10 Hz by a pair of Pockels cells and the pulse energy is increased to about 1 mJ. The laser pulses are then further amplified in two multi-pass amplifiers, pumped by a 2 J Nd:YAG laser system leading to a final pulse energy of up to 600 mJ. Those pulses are used for ionization of the Rb vapour and seeding of the SM process.

In order not to have fully amplified high-power laser pulses with a repetition rate of 10 Hz downstream the multi-pass amplifier (e.g. to avoid long-term damages on mirrors, compressor gratings and to reduce the ablation on the laser beam dumps) a dynamic delay is introduced to the timing of the pump laser pulses with which the YAG crystal is pumped. Normally, the crystal is pumped $\sim 1 \mu\text{s}$ after the laser pulse has passed the crystal. Only when a high-power pulse is requested (during normal operation once every ~ 30 s) the crystal is pumped on time so that the population inversion in the crystal has not yet decayed and the pulse is getting amplified.

After the first multi-pass amplifier stage, about 10% of the laser light is coupled out by a 90:10 beamsplitter and sent to the laser line leading to the e^- -gun (see Section 3.1.7). An attenuator consisting of a waveplate and Brewster polarizers allows to vary the laser pulse energy over a broad range. To shorten the stretched pulses again to about 120 fs by introducing the same negative amount of chirp previously introduced by the stretcher, a vacuum grating compressor is used. The resulting pulse length is determined by a SHG autocorrelator. The ionizing laser pulse is focused and transported in vacuum to the merging point with the p^+ -beam line, about 19.6 m upstream the vapour source. The laser beam focal point is about 6 m from the entry of the vapour source and the Rb vapour is ionized in a column of about 1 mm radius over the entire length of the vapour source.

For dumping the laser pulse, one massive and two thin-foil laser beam dumps are installed. These beam dumps are explained in more details in the following Section 3.1.4. Due to a jitter in the SC triggering system, it is difficult to determine the exact timing of the ionizing laser pulse with respect to the position of the p^+ -bunch on SC images.

Therefore, a marker laser beam line is installed [59]. The leakage of the first mirror after the vacuum compressor is used to couple out a small fraction of the ionizing laser pulse, which is sent to the streak room. The beam path is delayed by a motorized translation stage so that its optical path length matches the sum of the optical path length of the ionizing laser pulse and the OTR-light to the SC. The pulses are filtered down to energies which are no longer harmful to the SC and sent simultaneously, but spatially separated with the OTR-light on the SC slit (see Section 3.1.6). This enables to resolve the temporal correlation between the ionizing laser pulse and the p^+ -bunch. Moreover, changing the delay between the marker laser pulse and the ionizing laser pulse allows for marking time delays on SC images.

As it is not possible to monitor the laser beam profile inside the vapour source, a virtual laser line (VL) is set up in the p^+ -beam line tunnel. The beam profile of another small fraction of the ionizing laser pulse leaking through the next to last mirror before the vapour source is detected by three cameras at equal distances corresponding to the vapour source entry (VLCAM3), centre and exit (VLCAM5). The beam profile of this diagnostic beam in the virtual line can be assumed to be very similar to the beam profile of the ionizing laser beam at the corresponding distances inside the vapour source [60]. Since August 2017, a so called laser pulse cleaner consisting of two additional Pockels cells is installed inside the regenerative amplifier in order to remove pre-pulses up to a few ps before the high-power laser pulse. As a consequence, the maximum final pulse energy is reduced to about $E_{las} \sim 120$ mJ. A possible influence of the pulse cleaner on the observation of the HI is briefly discussed in Section 8.

During p^+ -beam operation, when the access to the AWAKE area is prohibited, the laser can be remotely controlled from the ACC.

3.1.4 The Laser Beam Dumps

As already mentioned in Section 3.1.3, in total three beam dumps for blocking the ionizing laser pulse are installed in AWAKE (see Figure 13). The most upstream one (LBDP1) is designed as a massive laser block which can be inserted into the p^+ -beam line downstream the laser-proton merging point before the vapour source. It is interlocked with the p^+ -extraction from the SPS so that the p^+ -beam cannot accidentally hit the dump. It mainly serves as a shutter to be able to have high-power pulses only in the beam line part upstream the vapour source. It is part of the laser safety system which ensures, when inserted, that the entire AWAKE experimental area is free of laser beams. The design of the other two beam dumps requires to be more advanced because they serve a different function. LBDP2 is located ~ 1.4 m downstream the vapour source to protect the sensitive OTR, CTR and IS foils as well as the SC against damage by a laser pulse. LBDP3, installed at the end of the beam line, protects the vacuum window separating the experimental area from the p^+ -beam dump. For the e^- -acceleration experiments starting in May 2018, the position of LBDP3 has been swapped with the position of the last IS2 so that the laser pulses are blocked before IS2. This enables the transverse p^+ -bunch profile to be measured at IS2 even in presence of high power laser pulses. In Figures 15 and 16, the design and the working principle of a laser beam dump (of



Figure 14: Photo of the AWAKE laser room. The round silver module in the foreground is the vacuum compressor. The oscillator and the amplifier stages for the high-power laser system as well as the in-air compressor and the THG stages for the e^- -gun laser line are located on the optical tables in the background.

type LBDP2 or LBDP3) are visualized based on the example of LBDP2. The laser beam dumps have to reflect the laser pulses while the p^+ -beam can pass through the dump. Therefore, on the one hand, the foils need to be as thin as possible to minimize the generation of radiation and secondary particles. On the other hand, the foils need to be thick enough to resist ablation by the high-power laser pulse over many events.

Ablation studies with various types of Al-foils (different tempers, alloys and thicknesses) were performed to determine the number of laser pulses acceptable before a shift of the foil is becoming necessary as the ablation might bore a hole in the foil. Based on this, a decision for a hard-tempered 200 μm thick Al-foil with 99% purity was made.² Detailed ablation studies on the choice of the laser beam dump foils and the number of high-power laser pulses acceptable without a risk for the downstream diagnostics are subject of Chapter 4.

The foils are mounted in a frame inside a vacuum vessel at an angle of 45° to deflect the incoming laser pulses to the inner wall of the vessel. Moreover, the foils need to be large enough to prevent scattered laser light to enter the vacuum pipe downstream the dump and possibly reach the optical diagnostics (OTR/CTR/IS foils, SC). This scattered light would appear as background light on the SC images and might even damage the SC optics. The frame, which holds the foil, is connected with a stepper-motor controlled spindle actuator. To monitor the current position of the foil, Linear Variable Differential Transformers (LVDTs) by Hottinger Baldwin Messtechnik are installed at each dump.

²Note, the fluence at the beam dump foil of LBDP2 is much higher than at the end of the beam line so that the number of high-power laser pulses accepted is less for LBDP2 than for LBDP3.

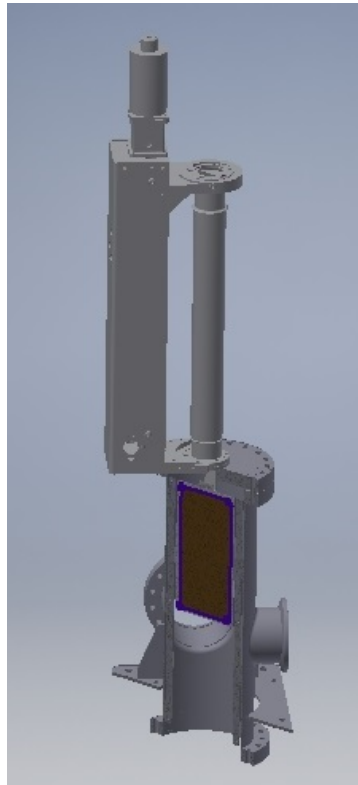


Figure 15: Technical drawing of LBDP2. For a better visualisation, a cut through the vacuum vessel is shown. Figure: T. Haubold, Max Planck Institute for Physics, Munich (MPP)

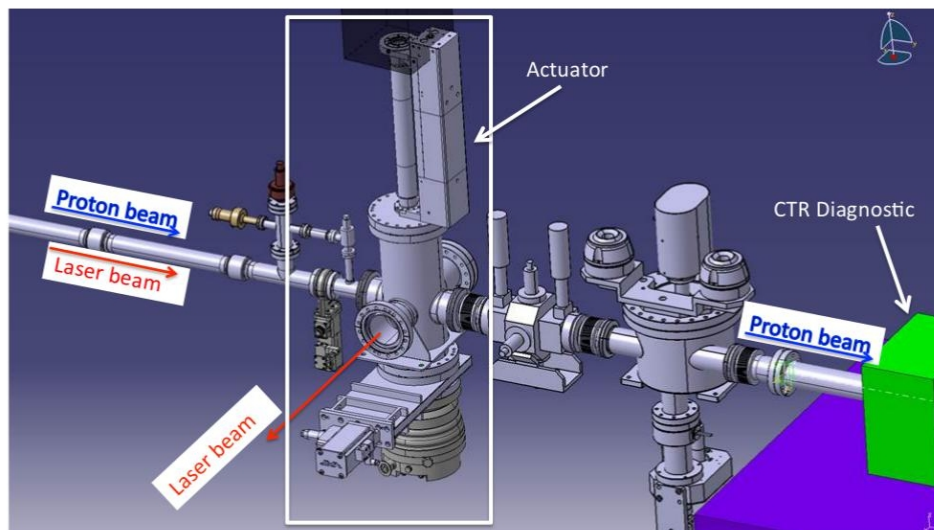


Figure 16: Integration of LBDP2 into the p^+ -beam line. Figure taken from [61].

LBDP3 contains also a wedge for laser propagation measurements, therefore the foil length is half the length of the foil installed in LBDP2.

Technical drawings of the beam dumps³ can be found in Appendix B.

3.1.5 The Vapour Source

The vapour source [62] (see Figure 17) is the core part of the AWAKE experiment. All relevant physical processes studied by AWAKE take place inside the plasma created in the vapour source. It consists of a 10 m long tube and an expansion volume at each side. Rb vapour is evaporated into the system in a temperature range adjustable between $T = 150^\circ\text{C} - 230^\circ\text{C}$. After ionization of the vapour by the high-power laser pulse, this provides the experimental conditions for a very uniform plasma (density and temperature uniformity better than 0.2%) for plasma densities in a range of $(0.5 - 10) \cdot 10^{14}\text{ cm}^{-3}$. Moreover, also linear plasma density gradients up to 20% between both ends of the vapour source can be set.

The vapour density (or more precisely, the vapour density length product) is measured with a fiber-based white-light interferometer [63] at both the upstream and the downstream end of the vapour source.



Figure 17: Photo of the vapour source in the AWAKE tunnel, view downstream to the experiment cavern. Image: M. Brice, CERN

3.1.6 Proton Beam Diagnostics

To obtain time-resolved diagnostics of the modulated p^+ -bunch, we detect the transition radiation (TR) emitted by the p^+ -bunch when passing through a foil. A relativistic

³Technical drawings by T. Haubold et al., MPP, Munich

3 The AWAKE Experiment

charged particle passing through a transition between two materials with different dielectric constants causes emission of transition radiation [64,65]. It is emitted in forward direction in a cone with opening angle $1/\gamma$ (forward radiation) and simultaneously also reflected by the surface of the transition material (backward radiation). The light emission caused by a p^+ -bunch propagating through a vacuum-metal boundary is prompt and its absolute intensity is given by [66]

$$I_{TR} = \frac{N_b^2 e^2 \gamma \omega_{pe,metal}}{3c}, \quad (3.3)$$

where $\omega_{pe,metal}$ is the metal equivalent electron plasma frequency. Hence, in our case, where all particles of the p^+ -bunch cross the transition zone, $I_{TR} \propto N_b^2$. For relativistic particles, the radiation wavelength is broadband, but at wavelengths shorter than the structure of the (micro)-bunches it is incoherent. The radiation in the visible light spectrum is referred to as optical transition radiation (OTR). It carries still enough information on the temporal and spatial structure of the p^+ -bunches for SC measurements. In a range around λ_{pe} (microwave bands), the radiation is emitted coherently and can be detected by microwave horn antennas and Schottky diodes. The coherent part in the radiation spectrum is called coherent transition radiation (CTR).

The detection of OTR and CTR is used for a time-resolved diagnostic of the p^+ -bunches in AWAKE [29,67].

For the OTR measurements, about 3.5 m downstream the exit of the vapour source, a 280 μm thick Silicon wafer coated with 1 μm mirror-finished Aluminium [31] (referred to as OTR-foil) can be inserted into the p^+ -beam line (see Figure 12). The emitted backward OTR-light is guided in free-space over ~ 16 m to the SC room using optical relay imaging, where it is then sent onto the slit of the SC (Hamamatsu Photonics, Model C10910-05).

Photons passing through the slit hit a photo-cathode (S20-ER), where they are converted proportional to their intensity into a number of electrons. Those electrons propagate through an accelerating mesh and into the electric field between two sweep electrodes. A temporally varying sweep voltage synchronized to the timing of the incoming photons deflects the electrons according to their arrival time by slightly changing angles. The electrons separated in time get separated in space and enter a micro-channel plate (MCP), where they are multiplied before they hit a phosphor screen. An ORCA-Flash4.0 CMOS camera gathers images of the light intensity distribution on the phosphor screen. This SC images show the transverse size of the beam over time. There are different possible time windows between 73 ps and 50 ns for the images. Table VII in Section 6.3.2 gives an overview of the different time scales and their maximum time and frequency resolution. For frequencies less than about 150 GHz, the p^+ -bunch modulation is directly visible on the SC images, whereas for higher frequencies Fourier analysis methods need to be applied in order to resolve the p^+ -bunch modulation frequency [29,67].

The SC is usually operated at slit widths between 10–50 μm , with an MCP gain in a range of 20–40 and with a 0.3 V trigger level. The slit is tilted with respect to the p^+ -bunch propagation axis by about -30° and the spacial calibration corresponds to

43.2 pixel/mm (0.0231 mm/pixel) [68]. A detailed explanation on the working principle of streak cameras from Hammamatsu Photonics can be found in [69].

In Chapter 6, we discuss in more detail the analysis and frequency resolution of the SC images.

The time-integrated radial p^+ -bunch distribution is determined from beam imaging stations [70] located upstream the vapour source, at the exit of the vapour source (IS1) and at the end of the beam line before the p^+ -beam dump (IS2). The distance between the entry of the vapour source to IS1 is ~ 12 m and the distance between IS1 and IS2 is ~ 8 m. The stations consist of movable foils (Al or Chromox (Cr_2O_3)) which can be inserted into the p^+ -beam line in order to generate OTR-light. CCD cameras are used for the detection of this time-integrated OTR-light. These cameras, which integrate over the entire beam profile, are called core cameras. Since summer 2017, additional cameras are installed which include a mask for the OTR-light emitted from the centre of the p^+ -bunch so that they block the intense center of the bunch. These halo cameras allow to study the radially defocused parts of the p^+ -bunch distribution.

The third diagnostic for the p^+ -beam in AWAKE is based on CTR [29]. While the p^+ -bunch crosses a second foil downstream the vapour source (the CTR-foil), coherent radiation is emitted with a frequency depending on the plasma density. This allows for a diagnostic of the bunch modulation frequency, especially at higher plasma densities, when the resolution of the SC becomes too low to fully resolve the p^+ -bunch modulation. The radiation is transported in cut-off waveguides and detected by Schottky diodes and different microwave horn antennas. To enhance the frequency resolution and to cover a broader spectrum, a frequency mixing technique [71] was developed.⁴

To determine the position of the p^+ -beam inside the SPS transport line, Beam Position Monitors (BPMs) are used. A detailed documentation of BPMs can be found in [72].

3.1.7 The Laser Line for the Electron Gun

The e^- -bunches to be accelerated in AWAKE are created at an UV photo-cathode. The UV-laser pulse hits the photo-cathode and punches out electrons from the cathode material. Below a certain laser wavelength the electrons can escape the material and get accelerated in an externally applied electric field. AWAKE uses Caesium telluride (Cs_2Te) with a quantum efficiency $QE = 12\%$ and a work function $\Phi_W = 4.66$ eV [73]. According to the theory of the photoelectric effect, an ideal wavelength to enable the electron to escape from the material while minimizing its initial kinetic energy (and therefore the e^- -beam emittance) can be calculated by minimizing

$$E_{kin,e^-} = \frac{hc}{\lambda_{max}} - e\Phi_W, \quad (3.4)$$

⁴In this thesis, however, no diagnostics based on CTR are used.

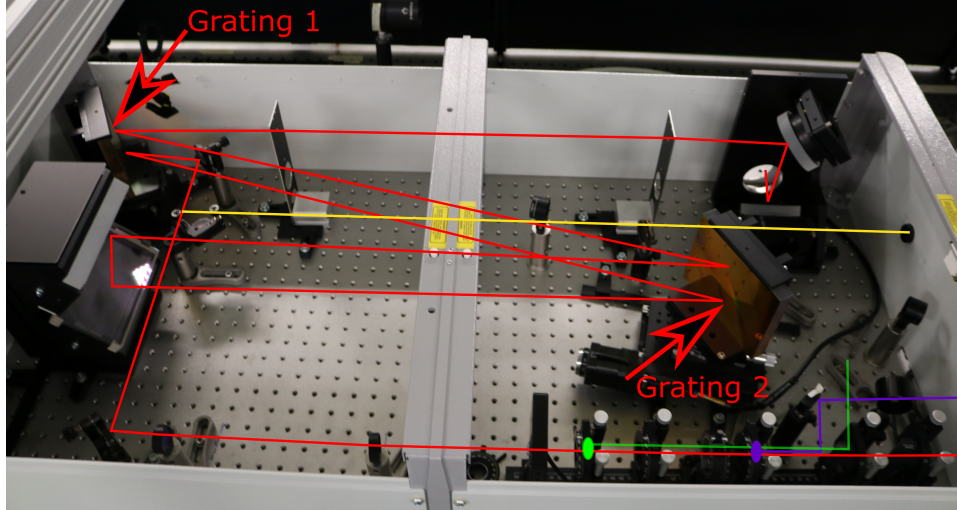


Figure 18: Beam paths of laser beams inside the box of the in-air compressor and the THG stage. The IR beam is depicted in red, the second harmonic in green and the third harmonic, i.e. the UV laser, in blue. The yellow line displays a diagnostic line for the IR-light to which the beam can be sent by flipping a mirror at the split point.

where h denotes the Planck constant.

For those parameters, the maximal wavelength is $\lambda_{max} = 266$ nm, a wavelength range which can be easily produced by THG out of the ionizing laser beam. Moreover, doing so, there is no need for complicated triggering as the delay between ionizing and photo-injector laser pulses can be adjusted simply by matching the optical path lengths of both beams.

In the following, we describe the generation of the UV-laser pulses from the ionizing laser beam. For more details see [74].

After the first multipass amplifier in the ionizing laser system (see Section 3.1.3) about 10% of the beam (~ 1 – 2 mJ) is coupled out using a beamsplitter. The laser pulses with a duration of about 11.2 ps are transported to a box, which contains the in-air compressor and the THG stage (photo see Figure 18). Figure 19 shows the design and the optical path lengths in the compressor as well as the positions of the optics inside the box.⁵ For the design of the compressor, we assume a spectral bandwidth of $\Delta\lambda_0 = \pm 20$ nm around the central wavelength $\lambda_0 = 780$ nm of the laser pulse. The pulse length τ should be reduced from about 160 ps to 10 ps. We use a double-path grating compressor with two gratings (1500 lines/mm each) and a roof mirror.

The IR-beam enters the box and is sent through a periscope (P), which increases the beam height by about 25 cm. Afterwards, the beam is sent to the first grating of the compressor (G1), which is tilted by the Littrow angle $\gamma_L = -28.7^\circ$ with respect to the axis normal to the surface of the grating (dashed line). On the grating, the first diffraction order is reflected to a second grating (G2), whereas all other orders are dumped. The path length of the different spectral components are different before they reach the

⁵Note, the beam enters the compressor box in the upper left corner on Figure 18, whereas it is entering the box on the lower left side on Figure 19.

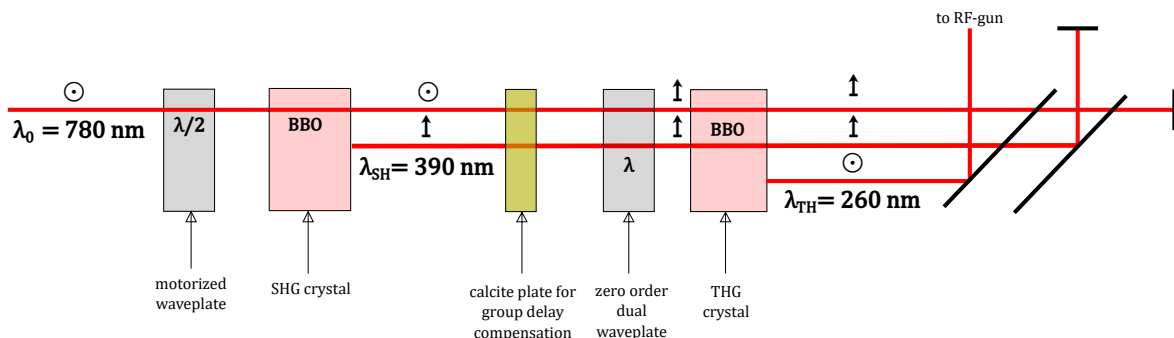


Figure 20: Schematic of the THG stage for the conversion of IR to UV. A horizontal polarization is denoted by \odot , a vertical polarisation by \uparrow .

pulse length of 5.2 ps is emitted.⁶ Both the IR and the blue beam are dumped inside the compressor box. The total efficiency of the THG stage is about 0.25 %, resulting in a pulse energy of the UV-pulse of about 200-400 nJ.

The UV-pulses are then sent through a beam expander consisting of two lenses ($f_1 = 100$ mm and $f_2 = 250$ mm). A periscope deflects the beam to a vacuum pipe, mounted on the ceiling of the laser room, in which it is transported to the e^- -bunker.

In order to reduce the emittance of the e^- -beam emitted from the cathode, the jitter of the UV-laser pulse needs to be reduced. Therefore, the UV-laser passes a motorized iris. To adjust the delay between the UV- and the ionizing laser pulse, a delay stage is installed. This allows also to control the timing of the e^- -bunch injection into the wake-fields along the p^+ -bunch. Before the beam is finally focused onto the photo-cathode, the beam passes a motorized filter wheel which allows the intensity of the beam to be adjusted. The maximum pulse energy at the entry of the vacuum pipe to the photo-cathode is about 100 nJ, i.e. over the total 24 m long path of the UV-pulse between the compressor box and the photo-cathode the energy losses are about 60%.

By sending the UV-light through a beamsplitter in front of the vacuum window, a small fraction of the light is coupled out and sent to a virtual beam line with a CCD camera installed at an equal distance to the photo-cathode. This virtual photo-cathode is used for diagnostics of the beam profile, the beam size, its remaining jitter and for the determination of its position on the photo-cathode.

3.1.8 The Electron Beam Line and Electron Diagnostics

The e^- -bunches are accelerated from the RF-cathode through a booster structure and merged with the p^+ -bunch (on axis and side injection) upstream the vapour source. A 40 MW clystron is installed to provide the necessary power for the e^- -gun and the booster structure. The e^- -bunch energy at the injection point is about 16 MeV, the charge per

⁶The difference to the ideal wavelength on the photo-cathode is $\Delta\lambda = 6$ nm. Hence, the kinetic energy ΔE_{kin} of the emitted electrons at the photo-cathode differs by about 0.11 eV from the optimal value.

e^- -bunch between 0.1–1 pC and the normalized emittance (RMS) 2 mm·mrad [76]. The bunch length can be adjusted by changing the pulse length of the UV-laser pulses by varying the distance d_{G1-G2} between the gratings of the in-air compressor (see Section 3.1.7).

After the electrons are accelerated in the wakefields of the p^+ -bunch, they are bent out by a magnet at the end of the beam line before LBDP3. The electrons are sent to a light-emitting chromox screen and this light is transferred to a spectrometer camera in a light-shielded room in the rack gallery. A quadrupol magnet is installed before the spectrometer in order to enable focusing to different energy ranges. For details on the e^- -spectrometer and its calibration see [77, 78].

3.2 AWAKE Run 2

In 2019 and 2020, no scientific run periods of AWAKE requiring p^+ -beams from CERN are possible due to the Long Shutdown 2 (LS2) of the CERN Accelerator Complex. This time is used to upgrade and improve the AWAKE experiment for the upcoming AWAKE Run 2, expected to start at the earliest in late 2021. Moreover, it is planned to begin with the dismantling of the former CNGS target area (see Figure 11 and Section 3.1.1) in order to expand the experimental cavern for AWAKE.

The layout of the experiment for Run 2 is shown in Figure 21. AWAKE will use two vapour sources, a first one (~ 10 m including a density step) to self-modulate the p^+ -bunch up to the saturation of the SM process and a second one (also ~ 10 m) to accelerate the e^- -bunches. This set-up has the advantage that e^- -bunches can be injected

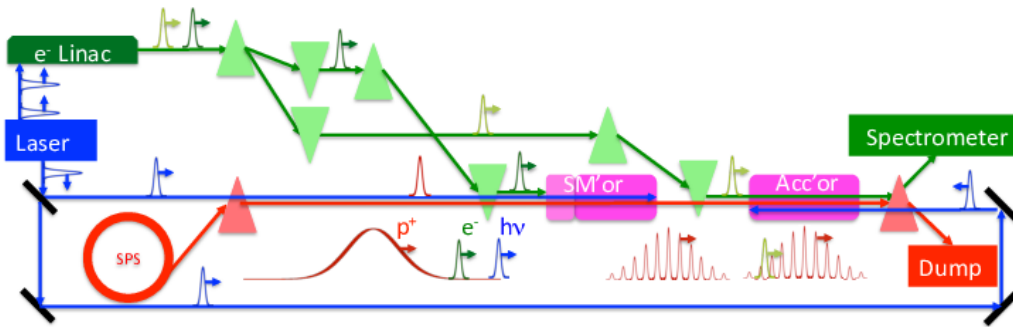


Figure 21: Layout for AWAKE Run 2 experiments. Figure taken from [79].

in between the two vapour sources and therefore into the wakefields of an already fully modulated p^+ -bunch structure. However, the seed process of the SM has to be different compared to Run 1. In order to seed the SM along the entire p^+ -bunch with a high phase reproducibility, the seeding is provided by a short e^- -bunch preceding the p^+ -bunch (see Section 2.3.2 and Appendix A). The plasma is created already ahead of the p^+ -bunch by a high-power laser pulse ionizing a Rb vapour so that the p^+ -bunch propagates inside

3 The AWAKE Experiment

both vapour sources entirely through pre-formed plasmas.

The scientific focus will be on preserving the low energy spread of the e^- -bunches through beam loading and matching of the beam to the ion column focusing force [79].

4 Laser Ablation Studies for Beam Dump Foils

Ablating a hole with the ionizing laser pulse in one of the beam dump foils might cause damage to the sensitive diagnostics downstream of LBDP2 or to the vacuum window at the end of the beam line after LBDP3 (see Section 3.1.4). In order to minimize this risk, the ablation properties of the foils have to be experimentally investigated. As mentioned above, the thickness D of the foils should be chosen as thin as possible in order to minimize the radiation impact on the downstream diagnostics and still thick enough to dump the number of high-power laser pulses of a scientific run period without the need for exchanging the foils. Therefore, we perform studies on the ablation rates of different possible foil types in order to experimentally determine the foils to be used and the number of high-power laser pulses allowed before shifting the foil becomes necessary. The foil material is decided to be Aluminium as the foils need to be installed in the high vacuum inside the AWAKE p^+ -beam line. In Table I, the five foils to be investigated in the ablation study and their different alloys, tempers and thicknesses are listed. All foils have a size of 25 mm \times 25 mm and are produced by Goodfellow. The experiments

alloy	temper	thickness D [μm]
Al 99%	hard	200
Al 99%	half-hard	380
Al 7075	T6	400
Al 99%	half-hard	1000
Al 6082	T6	1000

Table I: Overview of different foils used for the beam dump foil ablation studies.

were performed between October and December 2015 at MPP, before the ionizing laser was relocated to the AWAKE tunnel. An overview of the foils as well as the laser and vacuum parameters in our ablation studies at MPP can be found in Table II (left-hand side).

Figure 22 shows the experimental set-up for the ablation experiments. The foil to be studied is mounted at 45° with respect to the incoming laser beam in a vertically movable holder inside the laser vacuum vessel. The laser light is ablating the foil, gets reflected and is eventually dumped at a beam block outside the laser vessel (see Figure 22a). After N high-power laser pulses, the amount of material ablated from the foil is large enough to create a hole through which the laser light can propagate to a defusing screen. Now, a CCD camera (AVT Manta G-031 B) can detect the transmitted light which appears

4 Laser Ablation Studies for Beam Dump Foils

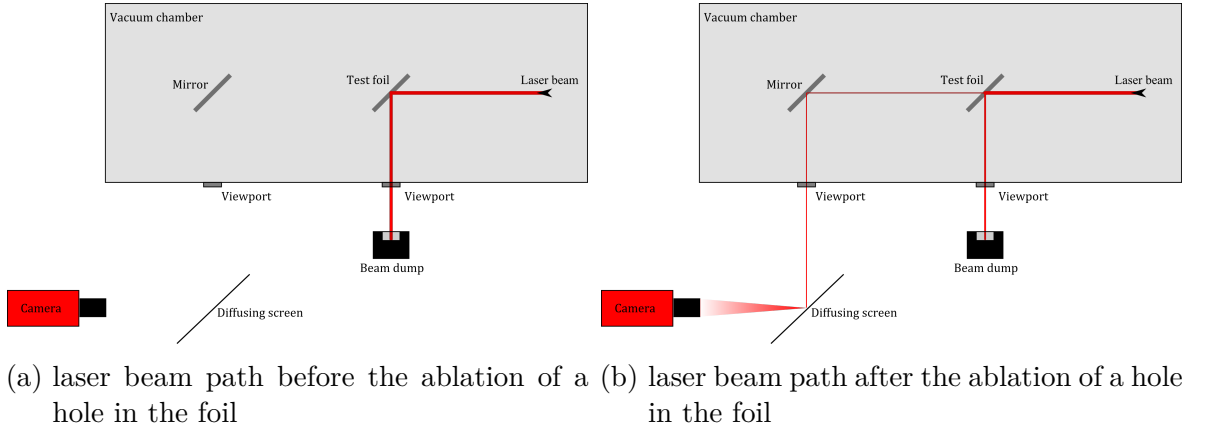


Figure 22: Set-up for the measurements of laser ablation rates at MPP.

on the screen (see Figure 22b). We count the number of laser pulses necessary to ablate a hole in the foil and repeat the experiment at another position on the foil. The number of high-power laser pulses needed to bore a hole is averaged over the number of ablated holes and the average ablation rate \bar{R}_A per high-power laser pulse

$$\bar{R}_A = \frac{D}{\bar{N}} \quad (4.1)$$

is computed.

The results for \bar{N} and \bar{R}_A (including their standard deviations $\Delta\bar{N}$ and $\Delta\bar{R}_A$) are summed up in Table III. The thicker foils with $D = 1000 \mu\text{m}$ have the lowest measured \bar{R}_A , whereas \bar{R}_A is higher for foils with only 200–400 μm thickness. It is clear that the ablation rate R_A may not be constant as the number of laser pulses increases. An ablation rate is only well defined for laser spot size areas A_{spot} large when compared to the hole depth d , i.e. large aspect ratios A_{spot}/d . When this is not the case, as in our experiment, material may not leave the exposed ablation area and contributes to an increase of the number of laser pulses it takes to bore a hole and thus decreases the measured \bar{R}_A . Hence, our measurements only reflect simple averages of the ablation rates obtained by boring a hole through a foil of given thickness D .

The hardness of the temper also influences \bar{R}_A . Foils with temper hard have a lower \bar{R}_A than foils with temper half-hard. Moreover, 99% Al is more resistant to high-power laser pulses than Al alloys (Al 7075, Al 6082).

To better understand the ablation process, we examine the structure of the ablated holes. As an example, Figure 23 shows an image of an ablated crater by $N = 1289$ high-power laser pulses on the foil Al 99% hard 200 μm under a microscope. The laser beam is coming from the right-hand side and hits the foil mounted at 45° with respect to the laser beam path resulting in an oval shape of the ablation crater. A large amount of the material ablated by the laser pulses is deposited on the opposite side of the incoming beam and forming a ridge.

It is interesting to note that the foils with temper half-hard tend to form a clear dark halo around the ablation crater with a diameter of about twice the size of the crater,

	MPP	Wynne/Stuart
material/alloy	Al (99%, 7075, 6082)	Al 7075
foil thickness [μm]	200 – 1000	1000 (depths measured $\leq 150 \mu\text{m}$)
pulse length [fs]	120	150
repetition rate [Hz]	max. 10	10^3
wavelength [nm]	780	810
fluence on target [J/cm^2]	6.57 ± 2.2	0.2 – 17
pulse energy [mJ]	7.20 ± 0.16	max. 1.5
beam diameter [μm]	530 ± 45	150
vacuum pressure [mbar]	10^{-5}	1.3×10^{-2}

Table II: Experimental parameters used at MPP and in the publication by Wynne and Stuart [80].

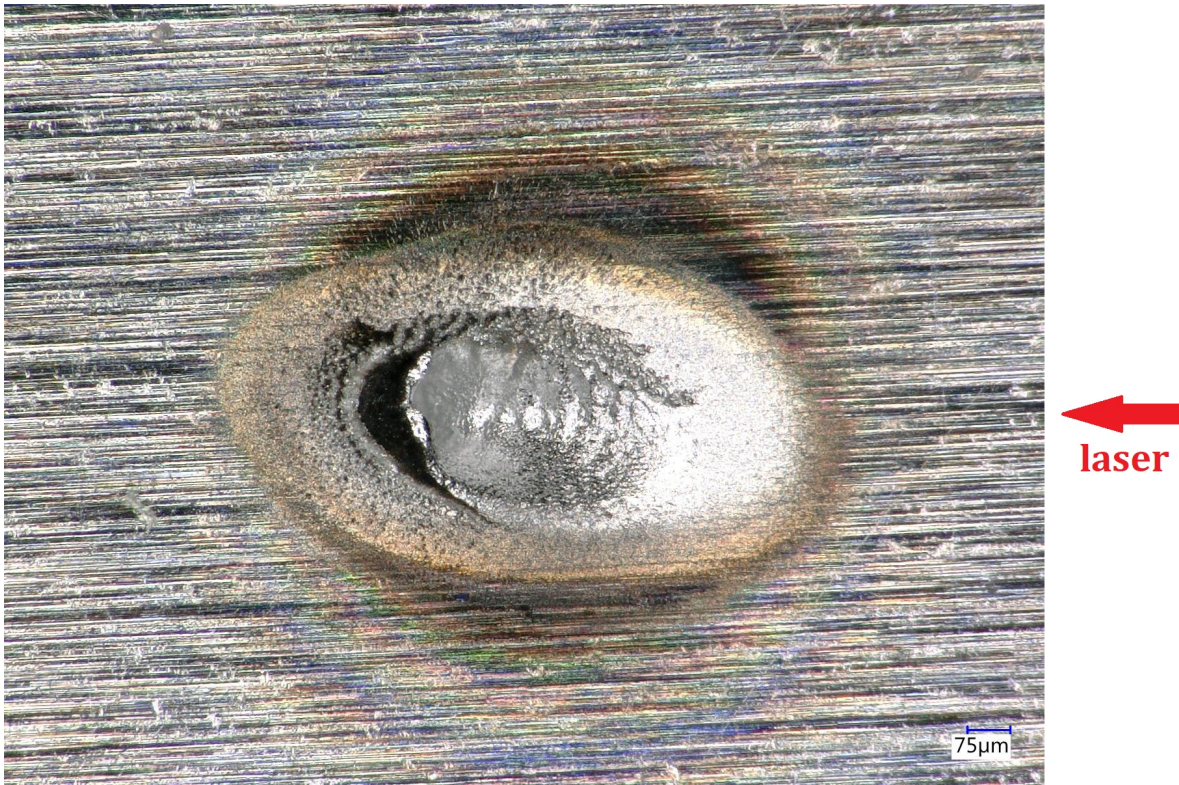


Figure 23: Microscope image of a hole ablated by $N = 1289$ high-power laser pulses of the AWAKE laser system on a foil ($200 \mu\text{m}$ Al 99% hard) mounted at an angle of 45° with respect to the incoming laser pulses. The laser pulses ablate an oval crater with a soft slope on the side of the incoming beam and deposit material to a steep ridge on the opposite side (dark region on the left-hand side of the crater). The hole, through which the laser light is eventually transmitted to the camera, is located at the bottom of the crater, but is too small to be discernible on the image.

4 Laser Ablation Studies for Beam Dump Foils

foil	ablated holes	$\bar{N} \pm \Delta\bar{N}$	$\bar{R}_A \pm \Delta\bar{R}_A$ [nm/pulse]
Al 99% hard 200 μm	9	1283 ± 139	156 ± 19
Al 99% half-hard 380 μm	9	1749 ± 177	217 ± 24
Al 7075 T6 400 μm	9	1536 ± 89	260 ± 16
Al 99% half-hard 1000 μm	9	9852 ± 856	102 ± 10
Al 6082 T6 1000 μm	3	7324 ± 1288	137 ± 29

Table III: Results of the ablation studies: Number of pulses \bar{N} required to ablate a hole and average ablation rate \bar{R}_A including their standard deviations.

whereas for foils with temper hard or T6 no or only a very vague shiny halo (as in Figure 23) is visible.

We compare our ablation rates to the results from Wynne and Stuart [80], who measured the ablation rates of Al for different laser pulse fluences and durations, ambient pressures and hole depths. The series of measurements closest to our experimental conditions are obtained for a wavelength of 810 nm (compared to 780 nm in our experiment) and 150 fs (compared to 100–120 fs in our experiment). They only measured foils of 1000 μm thickness, Al alloy 7075 and holes up to a depth of 150 μm . Moreover, the angle of incidence is 0° . The parameters of the experiments in the publication of Wynne and Stuart can be found on the right-hand side of Table II.

Figure 24 shows the \bar{R}_A measured at MPP (only for foils of thicknesses in the range of 200–400 μm) and for three different fluences the \bar{R}_A computed by numeric integration of R_A at a certain hole depth d taken from the publication by [80]. With a fluence of 6.6 J/cm^2 in the MPP experiments we can deduce that the values for \bar{R}_A measured are in the same range as those measured in well defined conditions by Wynne/Stuart.

For our study, we conclude that even though the foil Al 99% half-hard has the lowest \bar{R}_A of all tested foils ($\bar{R}_A = (102 \pm 10) \text{ nm/pulse}$), the average ablation rate is not low enough to justify the use of a 1000 μm thick foil. Thus, we decide to use the foil Al 99% hard 200 μm , which is a factor of five thinner but has only an about 1.5 times higher average ablation rate ($\bar{R}_A = (156 \pm 19) \text{ nm/pulse}$).

To include a sufficient safety margin, we decide to limit the number of high-power laser pulses per foil position to 600 on LBDP2 and 3000 on LBDP3 and shift the foils afterwards by $\sim 3 \text{ mm}$. It is important to note that the beam dump event counter only counts high-power laser pulses where the dynamic delay of the laser is set on time (see Section 3.1.3). The low power pulses with a pulse energy below 10 mJ do not have enough energy to ablate material from the foil and can therefore be neglected.

A change of the laser focusing to a focus further downstream in the vapour source in May 2017 resulted in a higher fluence on LBDP2. Therefore, by then we reduced the number of acceptable high-power laser pulses per foil position to 250 on LBDP2.

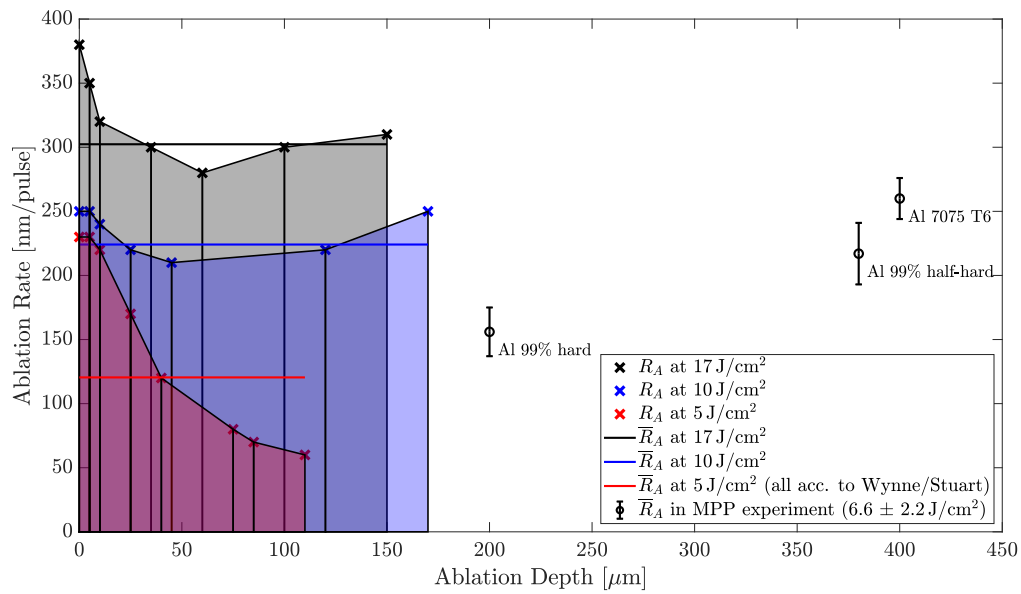


Figure 24: Comparison between the ablation rates of experiments at MPP (for foils up to 400 μm) and the publication by Wynne and Stuart [80]. \bar{R}_A is computed for three different fluences by numeric integration of R_A at certain hole depths d taken from the publication.

5 Hosing Instability Simulations with OSIRIS

5.1 OSIRIS

To compute the time-dependent behaviour of extended complex systems, which contain many particles interacting with each other (as given in our experimental situation), even the most modern and most effective supercomputers can not provide the needed computational power. Therefore, we need to model such physical systems by introducing macroparticles and use PIC codes with a high level of parallelization in order to take advantage of the computational capacity of such supercomputers.

In this thesis, we analyze and discuss the results of HI simulations performed by Mariana Moreira and Jorge Vieira from Instituto Superior Técnico (IST) Lisbon with the OSIRIS code [81, 82] at parameters similar to those of the experiment. In this chapter we already introduce and use some of the main analysis methods we also apply to the experimental results presented in Chapter 6.

OSIRIS is a fully relativistic, object-oriented PIC code, widely used for simulations in plasma based accelerator science which supports three-dimensional simulation modes. In OSIRIS, all physical quantities are normalized to plasma units which only depend on the plasma density n_{pe} . We denote quantities in plasma units by a hat (e.g. a plasma angular frequency in plasma units by $\hat{\omega}_{pe}$). Table IV gives an overview of the used normalization. To guarantee the numerical stability of the electromagnetic solving scheme,

physical quantity	symbol	normalization
time	\hat{t}	$\omega_{pe}^{-1} = \sqrt{\frac{\epsilon_0 m_e}{n_0 e^2}}$
space	\hat{x}	$k_{pe}^{-1} = \frac{c}{\omega_{pe}}$
mass	\hat{m}	m_e
velocity	\hat{v}	c
energy	\hat{W}	$m_{sp} c^2$
momentum	\hat{p}	$m_{sp} c$
charge	\hat{q}	e
electric field	\hat{E}	$E = \frac{m_e c \omega_{pe}}{e}$

Table IV: Normalization to plasma units in OSIRIS. Note, m_{sp} denotes the mass of a particle of a certain species, e.g. m_e for electrons or m_p for protons.

the Courant condition $C \leq 1$, which determines the length of a simulation step $\Delta\hat{t}$, has to be fulfilled. For a three-dimensional simulation C is given by

$$C = \Delta\hat{t} \sqrt{\sum_{i=1}^3 \frac{1}{\Delta\hat{x}_i}}. \quad (5.1)$$

Here, $\Delta\hat{x}_i = \hat{L}_i/N_{it}$ is the length of a single grid cell and \hat{L}_i the length of the simulation box in the i -th dimension. For all simulation results shown in this thesis, C is chosen to be 0.7, which is a good trade-off between time step length against simulation stability. The maximum number of necessary iterations is then given by $N_{it} = \hat{t}_{max}/\Delta\hat{t}$, where \hat{t}_{max} is the last time step in the simulation.

In general, simulations in normalized plasma units have to be scaled by n_{pe} , which allows to interpret the results for different plasma densities. By varying the value of n_{pe} , however, all other physical quantities depending on the choice of n_{pe} (e.g. the bunch propagation length in plasma or the bunch density) are changing accordingly.

5.2 Initial Bunch Parameters

We perform full 3D OSIRIS simulations of a p^+ -bunch with similar parameters as in the AWAKE experiment that are capable of covering the effects of the HI in transverse planes along the bunch without limitations by rotational or cylindrical symmetries. In the simulations, both the SM process and the HI are seeded and the initial simulation parameters correspond to the experimental parameters of the HI events shown in Chapter 6. This is necessary because the noise levels present in the experiment are unknown parameters. Seeding both instabilities also reduces the length over which the simulation has to run in order to observe the HI and SM interaction. Therefore, the simulation results are not meant to describe the exact interaction as expected in the experiment, but only to reveal the general characteristics and features of the HI.

The scaling factor for the simulation, the plasma density, is set to $n_{pe} = 0.5 \cdot 10^{14} \text{ cm}^{-3}$. This corresponds to a simulation window of $L_{x_1} \times L_{x_2} \times L_{x_3} = 10.5 \text{ cm} \times 0.9 \text{ cm} \times 0.9 \text{ cm}$ and a plasma length of $L_p = 1010.5 \text{ cm}$ along the x_1 -axis.

The relativistic ionisation front, which seeds the SM process in the experiment, is represented by a cut in the SPS-like p^+ -bunch profile at $t = 100 \text{ ps}$ ahead of its centre. The seed of the HI is obtained by an initially small harmonic oscillation of the bunch centroid in the x_1x_2 -plane with an amplitude of $\delta x_2 = 0.01 k_{pe}^{-1} = 7.5 \mu\text{m}$ and a wavelength of $2\pi/k_{pe}$. It is important to note that although the seed level is an unknown experimental parameter and thus has to be chosen in the simulation input file based on estimations, the growth rate of the HI along the bunch and the plasma is independent from the seed level.

The bunch population (for the entire bunch, not only the simulated part) is $N_b = 1.8 \cdot 10^{11} p^+$. This parameter is in between the two experimentally studied p^+ -bunch populations $N_b \sim 1 \cdot 10^{11} p^+$ and $N_b \sim 3 \cdot 10^{11} p^+$.

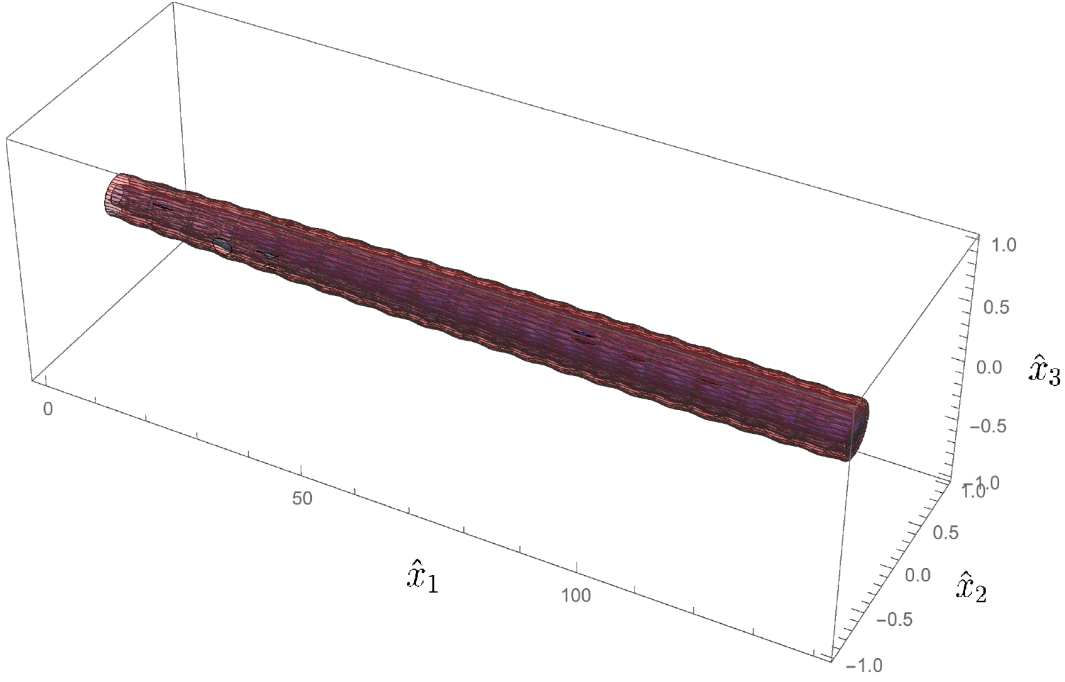


Figure 25: Initial shape of the SPS-like p^+ -bunch for the OSIRIS simulations according to Equation 5.2. The seed for the HI is obtained by the harmonic oscillation of the centroid visible as wiggles on the bunch profile, the seed of the SM process is obtained by the initial wakefields driven by a sharp cut in the bunch profile at $\hat{x}_1 = 135 c/\omega_{pe}$. Figure by courtesy of M. Moreira.

The initial beam profile (Figure 25) is given by [83]

$$n_b(x_1, x_2, x_3) = \begin{cases} 0 & \text{for } x_1 < 0 \\ \exp\left(\frac{-(x_1 - h_p - \Delta\tau)^2}{2\sigma_{x_1}^2} + \frac{-((x_2 - 0.01 \cdot \sin(x_1))^2 + x_3^2)}{2\sigma_r^2}\right) & \text{for } 0 \leq x_1 \leq h_p \\ 0 & \text{for } x_1 > h_p \end{cases} \quad (5.2)$$

with $\sigma_{x_1} = 12.0$ cm, $\sigma_{x_2} = \sigma_{x_3} = \sigma_r = 200$ μm , $\Delta\tau = -100$ ps $\cdot c = -3.0$ cm and $h_p = 10.2$ cm.

5.3 Simulation Results

5.3.1 Bunch Centroid Oscillation and its Frequency

Figures 26 and 27 show slices of the simulated charge distribution along the p^+ -bunch at six equally spaced propagation distances in plasma in the x_1x_3 -plane (no HI seed) and the x_1x_2 -plane where the HI is seeded. Those slices are akin to the charge distribution of the p^+ -bunch along the slit obtained from SC images in the experiment.

5 Hosing Instability Simulations with OSIRIS

In the plane perpendicular to the HI seed (Figure 26), the charge distribution remains symmetric about the bunch propagation axis. No signs for a growth of the HI are visible. The slices of the charge distribution of the bunch along the plasma show all the char-

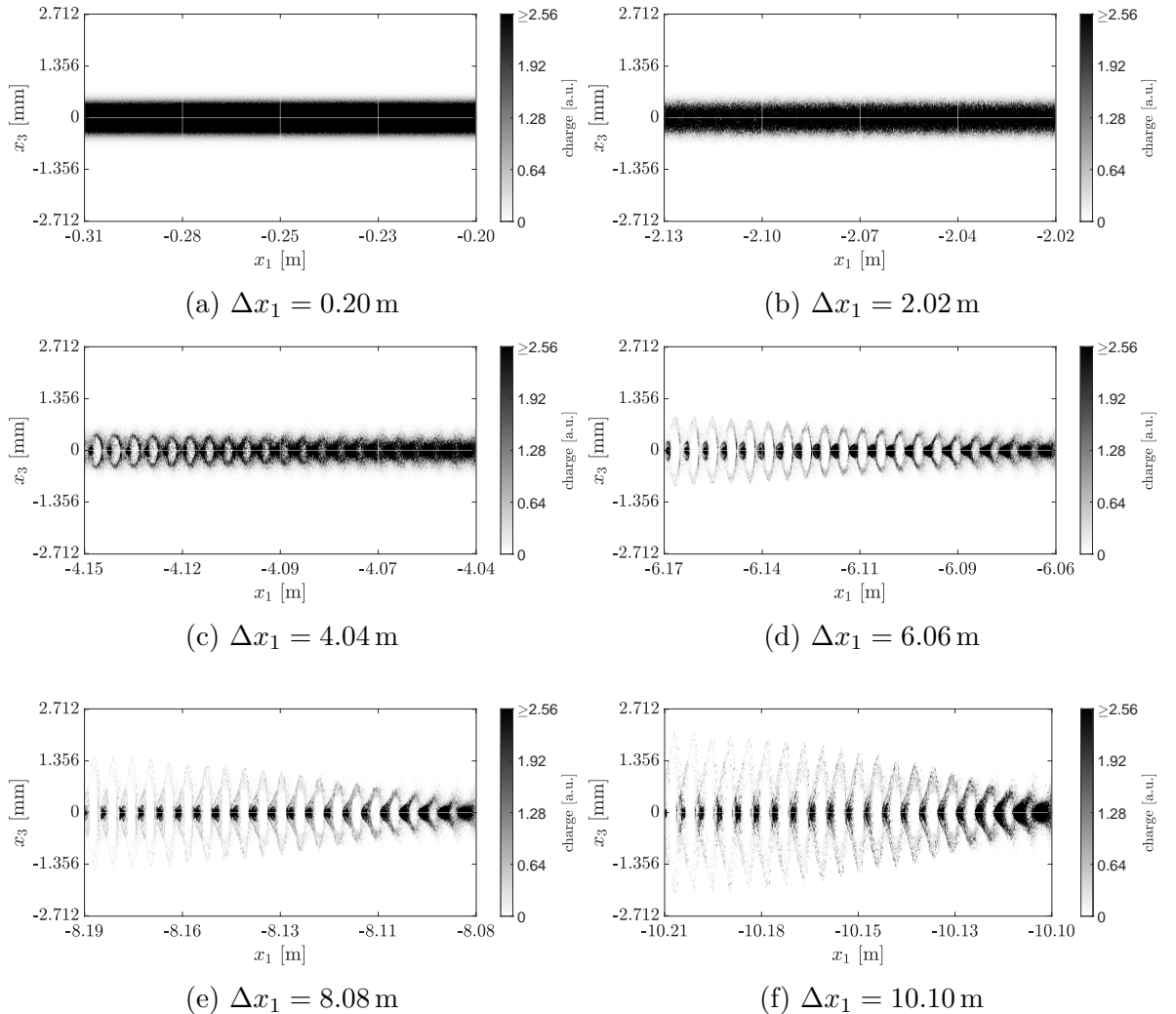


Figure 26: Slices of the charge distribution of 3D simulation results in OSIRIS in the plane perpendicular to the HI seed (x_1x_3 -plane) for an SPS-like p^+ -bunch after propagation distances Δx_1 through plasma with $n_{pe} = 0.5 \cdot 10^{14} \text{ cm}^{-3}$.

acteristics of SSM. The density modulation is periodically growing along the bunch and the plasma due to the periodical focusing and defocusing wakefields. The initially long p^+ -bunch is transformed into a train of short micro-bunches with a longitudinal size of λ_{pe} .

In the plane, in which the HI is seeded (Figure 27), however, we observe that the slices of the charge distribution of the p^+ -bunch are no longer axi-symmetric. After ~ 4 m, it becomes clearly visible that the protons are strongly displaced on one side of the x_2 -axis, whereas on the opposite side the protons remain close to the bunch propagation axis.

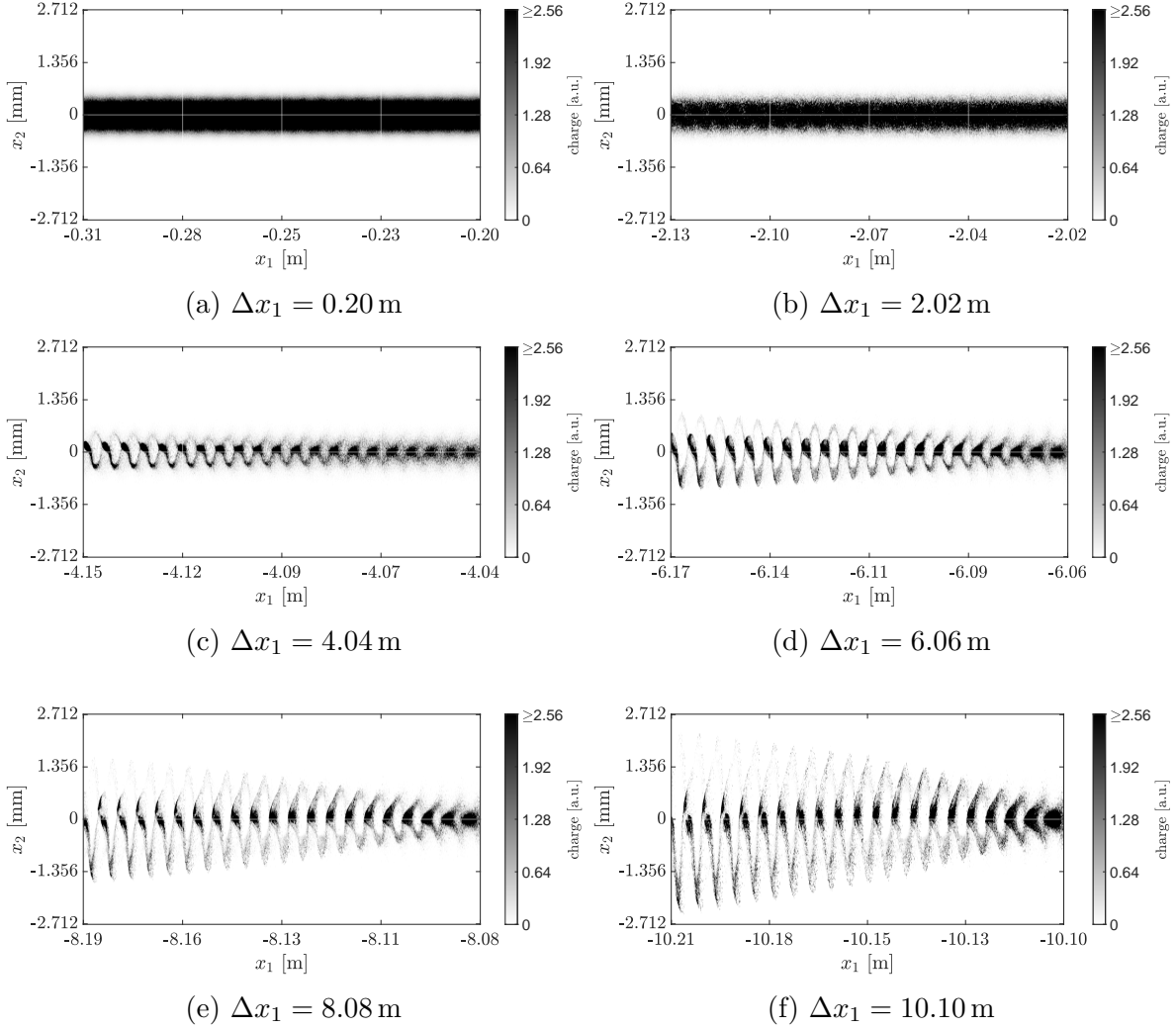


Figure 27: Slices of the charge distribution of 3D simulation results in OSIRIS in the plane of the HI seed (x_1x_2 -plane) for an SPS-like p^+ -bunch after propagation distances Δx_1 through plasma with $n_{pe} = 0.5 \cdot 10^{14} \text{ cm}^{-3}$.

At the end of the plasma, the structure of the beamlets has been fully broken up into two parts and the overall charge distribution is distinctively asymmetric with respect to the beam axis. Obviously, the growth of the HI influences the growth of the SM in this plane.

For a better understanding of the asymmetry which arises in the HI plane, Figure 28 shows an enlarged plot of the slices through the rear part of the p^+ -bunch charge distribution in the x_1x_2 - and x_1x_3 -plane after a propagation distance of $\Delta x_1 = 10.10$ m through plasma. It allows to compare the phase of the modulation and the oscillation in perpendicular planes. The protons experiencing the defocusing phase of the wakefields in the x_1x_3 -plane (SM) are the ones that are further displaced from the x_2 -axis. The protons in the focusing phase of the wakefields in the x_1x_3 -plane, however, remain close to the x_2 -axis in the HI plane. This coupling between the growth of the SM process and

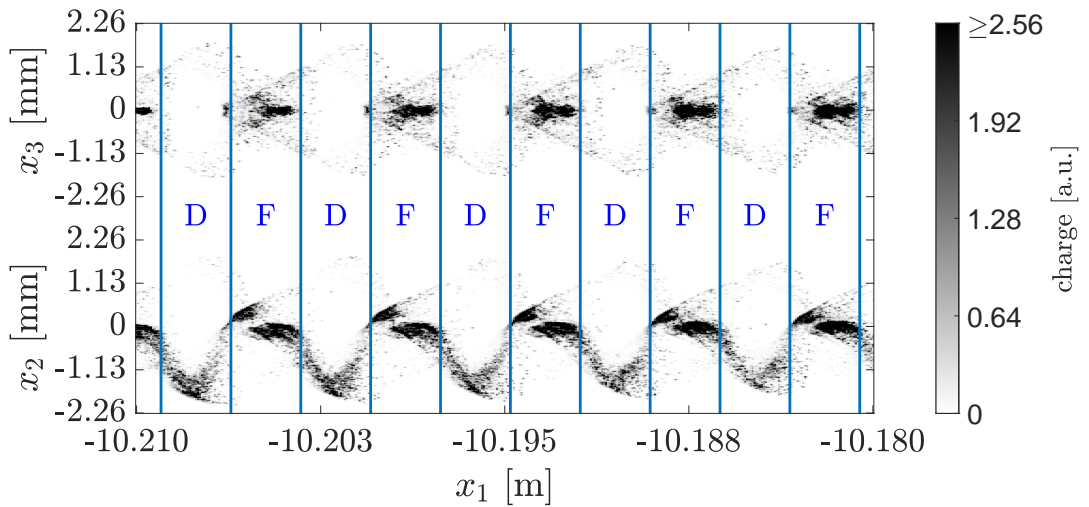


Figure 28: Comparison of the slices of the charge distribution in perpendicular planes after a propagation distance of $\Delta x_1 = 10.10$ m through plasma. The protons in the focusing phase (F) remain close to the bunch propagation axis in the x_1x_2 -plane. The protons that are strongly displaced in the x_1x_2 -plane are in the defocusing phase (D) of the wakefields.

the HI then results in the already theoretically discussed asymmetric charge distribution, which is the major characteristic for CBH (see Section 2.3.4).

Now, we compute the centroid of the charge distribution along the bunch. The simulations have the advantage that this can be done in different transverse planes and after different propagation distances through plasma, whereas in the experiment we are limited to a fixed plasma length and to the projection on the plane of the SC slit.

The left side of Figure 29a shows the displacement of the bunch centroid (similarly to Figure 5a) after different propagation distances through plasma. The centroid of the bunch is oscillating with growing amplitude along the bunch and along the plasma. For $\zeta \gtrsim -5$ cm, the modulation is almost symmetric with respect to the center axis, before it becomes distinctly asymmetric for smaller ζ (area ratios A_+/A_- as small as 0.16). The maximum displacement is 1.68 mm after 10.10 m of plasma. As described above,

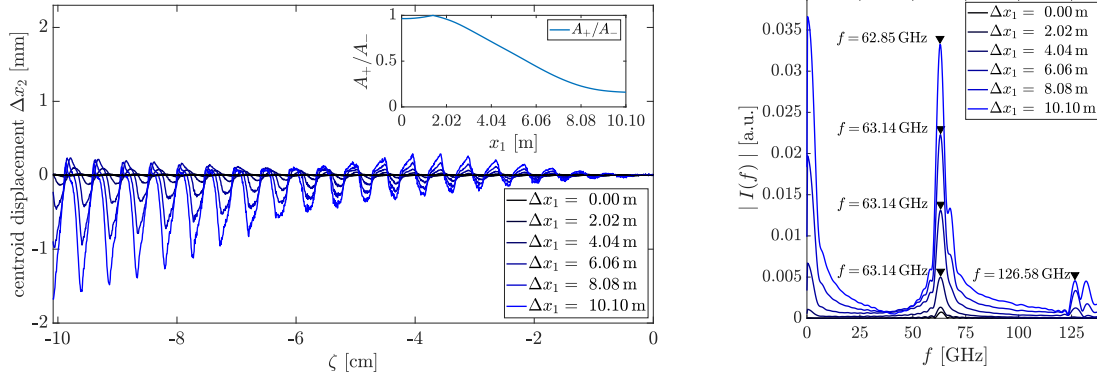
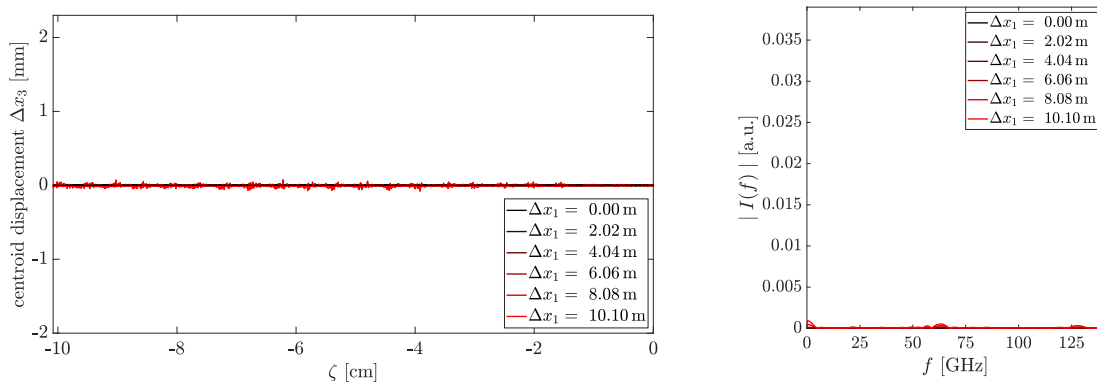
(a) Bunch centroid displacement along the x_1x_2 -plane and its DFT(b) Bunch centroid displacement along the x_1x_3 -plane and its DFT

Figure 29: Bunch centroid displacements after propagation of a distance of Δx_1 through plasma (left-hand side) in the plane of the HI seed (x_1x_2 -plane) (a) and in the plane perpendicular to the HI seed (x_1x_3 -plane) (b). The corresponding DFTs of the centroid oscillation are presented on the right-hand side. The inset in (a) shows the area ratio dependency on the propagation distance through plasma.

this asymmetry indicates that the growth of the HI couples to the growth of the SM process of the bunch (CBH) in the x_1x_2 -plane.

In the plane perpendicular to the HI seed (see Figure 29b, left-hand side), however, the centroid position is only fluctuating due to noise and on average there is no centroid displacement visible. The bunch centroid moves symmetrically along the bunch propagation axis.

On the right-hand side of Figure 29, we show the DFT of the centroid position along the bunch both in the HI plane (similarly to Figure 5b) and in the SM plane. As the temporal size of the simulation window corresponds to 336.14 ps, the size of the DFT bins in the frequency domain is 2.97 GHz.

For the HI plane of the bunch, there is a distinct maximum in the frequency distribution (see Figure 29a, right-hand side) around 63 GHz (for Δx_1 up to 8.08 m at $f = 63.11$ GHz and for $\Delta x_1 = 10.10$ m to 62.82 GHz). Moreover peaks with lower amplitude at the second harmonics ($2f_{osc} \sim 126$ GHz) as well as higher harmonics (not shown in the plot) of f_{osc} are visible in the spectrum. As expected (see Figure 5b), the amplitude of those peaks in the DFT spectrum is increasing along the plasma for a larger asymmetry due to the growing HI.

For the plane in which only the SM process is seeded (Figure 29b, right-hand side), there is no significant peak in the DFT spectrum exceeding the noise level around f_{osc} or any of the harmonics. This gives evidence that a clear peak in the DFT spectrum of the centroid oscillation in a specific plane along the bunch can be used as a criterion to distinguish the appearance of the HI compared to pure SSM.

For $n_{pe} = 0.5 \cdot 10^{14} \text{ cm}^{-3}$, the normalized DFT of the centroid oscillation function leads to $f_{osc}/f_{pe}(n_{pe}) = 0.994 \pm 0.047$ for Δx_1 up to 8.08 m and to $f_{osc}/f_{pe}(n_{pe}) = 0.989 \pm 0.046$ at the plasma exit ($\Delta x_1 = 10.10$ m). In the given uncertainties only the DFT bin discretisation is considered and no systematic error is included.

These results show that within the frequency resolution of the DFT (see Section 2.3.4) the centroid oscillation frequency is equal to the plasma frequency, $f_{osc}(n_{pe}) = f_{pe}(n_{pe})$.

In Figure 30, we present the integrated signal (sum over all pixels in every column along the bunch) in the x_1x_2 -plane for different propagation distances Δx_1 through plasma (left-hand side) and the corresponding DFTs of the signal (right-hand side). In the integrated signal along the bunch, which is almost constant at the plasma entry, also a modulation along the plasma starts to evolve. The modulation is getting larger for higher plasma propagation distances and reaches a full modulation depth already after ~ 4 m. The peaks in the frequency spectrum of the charge density modulation are at the same frequencies as in the calculation of the centroid oscillation frequency (Figure 29, right-hand side). The DFT in the perpendicular x_1x_3 -plane shows the same features, therefore it is not presented here. Hence, the PIC simulations confirm the theoretically expected result

$$f_{mod}(n_{pe}) = f_{osc}(n_{pe}) = f_{pe}(n_{pe}). \quad (5.3)$$

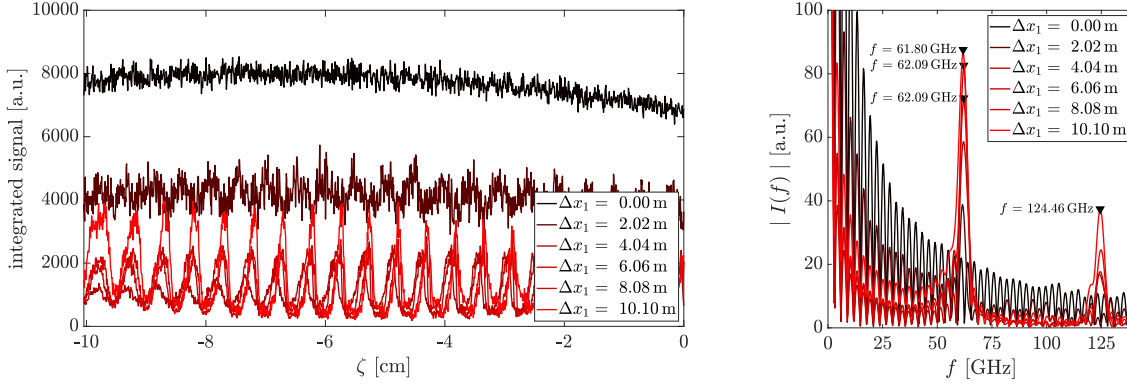


Figure 30: Integrated signals along the bunch after propagation of a distance Δx_1 through plasma (left-hand side) in the plane of the HI seed (x_1x_2 -plane). The corresponding DFTs of the signals are presented on the right-hand side. Note, the integrated signals and the DFTs in the x_1x_3 -plane give almost the identical results and are therefore not shown in the figure.

More features of the DFT and the small deviations from f_{pe} due to the DFT bin discretisation are discussed in more detail in Chapter 6, when analyzing the DFT of the experimentally determined p^+ -bunch centroids.

5.3.2 Fit of Bunch Centroid Equation to Simulation Data

Nonlinear Least Square Fits and the Goodness of Fit

Based on the theoretical description of the HI described in Section 2.3.3, we perform nonlinear least square fits of the bunch centroid displacement Δx_c in the plane of the HI seed directly extracted from the simulation data. For that, we use the Trust Region Algorithm of the MATLAB Curve Fitting Toolbox.

To determine the goodness of the fit (GoF), we calculate the coefficient of determination, also referred to as R^2 -parameter [84]. It is defined by

$$R^2 = 1 - \frac{S_{S,reg}}{S_{S,tot}} \quad \text{with } R^2 \in [-\infty; 1]. \quad (5.4)$$

For a set of data points $y = [y_1, y_2, \dots, y_{n \in \mathbb{N}}]$, the sum-of-squares of the total error is given by

$$S_{S,tot} = \sum_{i=1}^n (y_i - \bar{y})^2 \quad (5.5)$$

and the sum-of-squares from the regression model by

$$S_{S,reg} = \sum_{i=1}^n (y_i - y_{reg})^2 \quad (5.6)$$

with \bar{y} the mean of y and y_{reg} the data points obtained by the regression.

In general, the closer the computed R^2 to 1, the better the goodness of the fit¹. For

¹Note that in general R^2 does not prove that there is any correlation between the model and the data.

$R^2 = 1$, the non-linear fit shows perfect agreement with the data, whereas for $R^2 = 0$, the fit matches the data as well as a horizontal line at the average of the data, i.e. the null hypothesis. In case R^2 is negative², the fit to the data is even worse than the null hypothesis. The limit of R^2 above which the fit can be considered to match to the model depends on the expected correlation between the data and the fit. In this thesis, we mainly compare R^2 -values for different types of fits to qualify the fit results and not to accept or reject any hypothesis.

Fit parameters

We fit Equation 2.30 to the centroid positions along the bunch as shown in Figure 29a at 50 positions along the plasma. The first of the three fits is performed with only one (ζ_0), the second with two (ζ_0, ε) and the third with three (ζ_0, ε, p) independent fit parameters. Contrary to experimental data, in simulations we are able to analyze the evolution of the centroids along the plasma. This is important because we can also analyze propagation distances where the evolution of the HI growth is in a less (or more) non-linear regime than in the experiment and thus estimate where the theoretical model of CBH is valid and where it reaches its limitations. In the case that the initial seed level in the experiment is lower than in the simulation, we expect to see features on the SC images that are observed in the simulation at shorter propagation distances than 10 m.

It is important to note that the length of the simulated bunches ($\zeta \sim 10$ cm) is longer than on the SC images ($\zeta \sim 6$ cm in the 211 ps time window) so that a larger part of the highly oscillating rear part of the bunch with ($\delta x_{c,max} \gg r_0$) and with more distinct asymmetry is resolved. Here, we can also observe features which appear later in the bunch, e.g. long wavelength hosing (see Chapter 8).

Moreover, the simulation data are smoother and less noisy than SC images. Furthermore, we also know the initial seed level δ_c of the HI, which is introduced by the initial small harmonic oscillation of the bunch centroid in the x_1x_2 -plane with an amplitude of $0.01 k_{pe}^{-1} = 7.5 \mu\text{m}$. Therefore, in this section, we fix the value for δ_c and do not use it as a fit parameter, whereas it is kept as fit parameter when fitting to experimentally determined centroids. The resulting trust regions and the start points for the fit parameters

fit parameter	ζ_0	ε	p
start point	0	0	0.333
upper limit	—	5	1
lower limit	—	−5	0

Table V: Initial parameters for the fit of Equation 2.30 to the centroid oscillation determined from simulation data: Start points, upper and lower limits for the trust regions. Note, in order for a more stable simulation at high Δx_1 , the limit $|\varepsilon| = 5$ is different than for the experimental fits (see Table V). This limit, however, is not reached for any of the fits.

² R^2 is the name of a common quantity and gets negative for $\frac{S_{S,req}}{S_{S,tot}} > 1$ (see Equation 5.4). It is not the square of a number and thus $R^2 < 0$ does not violate the rules of math.

are given in Table V.

Fit Results

In Figure 31, the results of the fits are shown after 4.04 m, 6.06 m, 8.08 m, and at the end of the plasma (10.10 m). Figure 32 gives an overview of the evolution of the fit parameters for all 50 positions along the plasma.

In the fits with only one parameter ζ_0 (Figure 31a), the fit at $\Delta x_1 = 4.04$ m matches the frequency of the oscillation, whereas the amplitude starts to get too high for $\zeta \lesssim -6$ cm. The fit cannot reflect the asymmetry of the signal any longer since $\varepsilon = 0$ (no coupling), which leads to a large deviation between fit and data. For $\zeta \lesssim -8$ m, this results in a fit amplitude which is higher than the oscillation at the side where the protons are focused and in a too low amplitude on the side of the defocused protons.

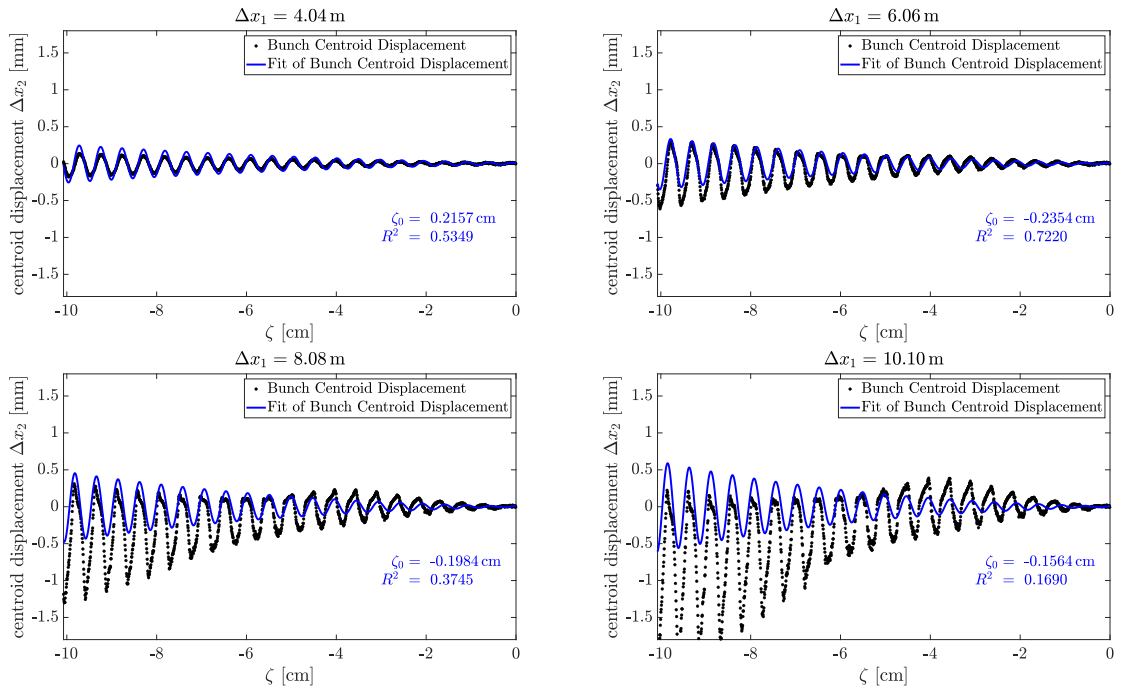
Adding the coupling constant ε to the fits (Figure 31b) does not enhance the quality of the fit for $\Delta x_1 = 4.04$ m indicating that the coupling between the HI and the SM process via the plasma wakefields does not yet play an important role at this distance in plasma. However, now we observe a good agreement between the simulation data and the fit for $\Delta x_1 = 6.06$ m and $\Delta x_1 = 8.08$ m, where the asymmetry of the oscillation is dominant. The fit can now take into account the coupling between the SSM and the HI. For $\Delta x_1 = 10.10$ m, however, the oscillation becomes highly nonlinear ($\Delta x_c \gg \sigma_r$) and the fit model breaks down (red areas on the right-hand side in all subfigures of Figure 32).

As a next step, we check the power law for $(k_{pe}^3 \zeta z^2)^{1/3}$ in N_{HI} (Equation 2.28) by introducing the exponent p in the number of exponentiations as an additional free fit parameter. The fits match the data much better for the entire range between ~ 3 m to ~ 8.5 m. The goodness of the fit reaches values up to 0.96 around 3 m (see Figure 32c). Only for $\Delta x_1 \gtrsim 8.5$ m the value for ε is rapidly increasing (see Figure 32a) so that the fit does not longer agree with the data. The values for p (see Figure 32b), however, are non-physical for $p \lesssim 3$ m (red areas on the left-hand side in all subfigures of Figure 32) as the HI seed by the harmonic oscillation is dominant and is fitted by the fit routine setting $p \approx 0$. For longer propagation in this plane, p starts to become physically meaningful and increases to the expected value $p = 1/3$ (see Section 2.3.4), where it stays nearly constant over the entire plasma length. Therefore, we do not take into consideration the results for $\Delta x_1 < 2.5$ m.

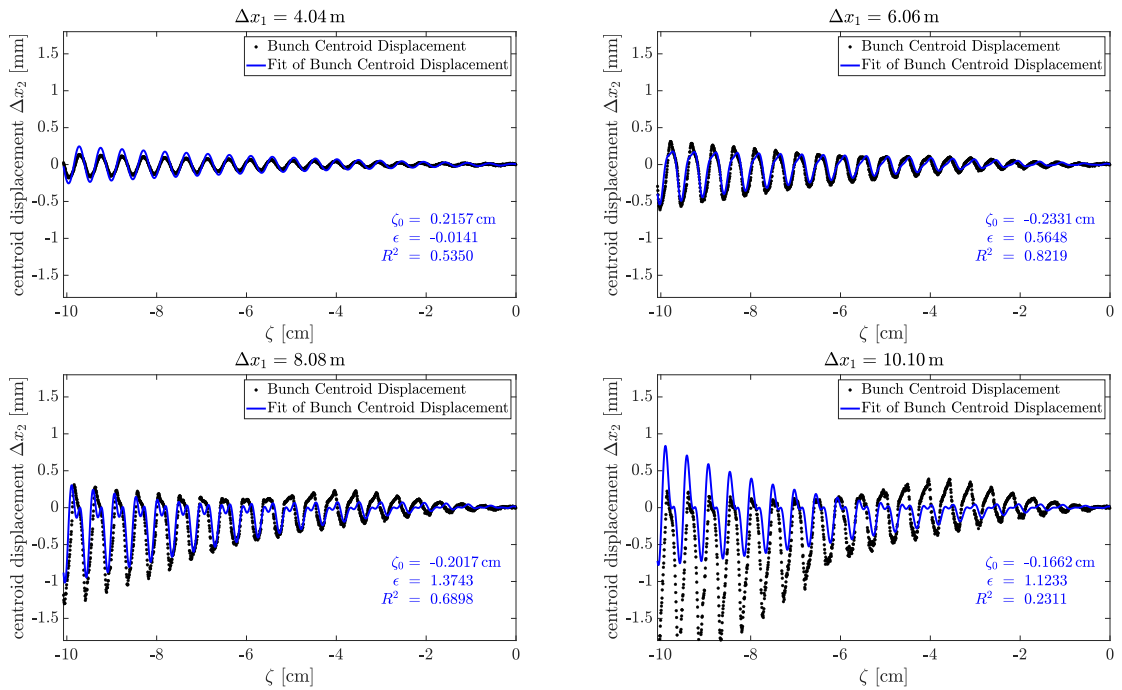
Here, it is already important to note that the asymmetry in the simulation after 10.10 m with $\Delta x_{c,max} > 1.5$ mm is much higher than it is ever observed in any of the events in the experiment (see Section 6.4.1), where the highest $\Delta x_{c,max}$ is about 0.6 mm. This implies that the initial seed values chosen in the fits are higher than in the experiment and that the results around ~ 6 – 8 m (where $\Delta x_{c,max} \sim 0.5$ – 1 mm) are closer to the regime which we observe in AWAKE.

The coupling constant ε (see Figure 32a) is small ($\lesssim 0.10$) for the first 4 m of plasma and then starts to increase with longer bunch propagation distance. This indicates that the coupling starts manifesting itself around ~ 4 m. After about 8.5 m, ε behaves differently in the fits with two and three fit parameters when the fit gets into a highly non-linear

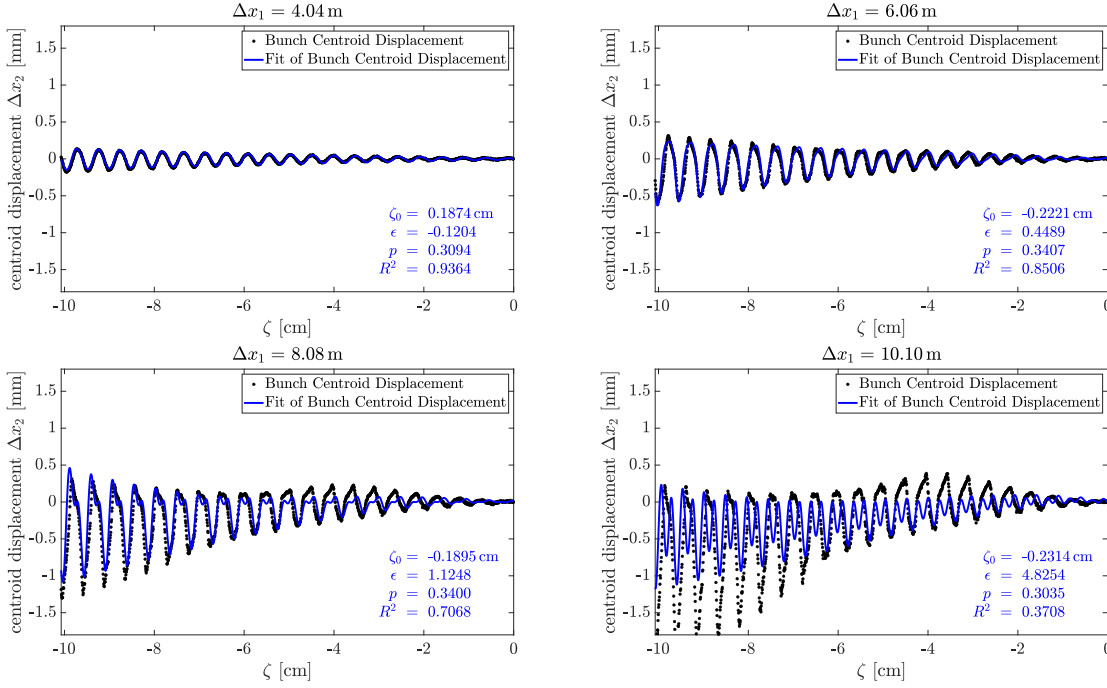
5 Hosing Instability Simulations with OSIRIS



(a) one fit parameter ζ_0 ($\delta_c = 0.01, \varepsilon = 0, p = 0.333$)



(b) two fit parameters ζ_0, ε ($\delta_c = 0.01, p = 0.333$)

(c) three fit parameters ζ_0, ε, p ($\delta_c = 0.01$)Figure 31: Fit of Equation 2.30 to the centroids determined from the OSIRIS simulation after a propagation distance Δx_1 through plasma.

regime ($\Delta x_c/\sigma_r \sim 18$). The coupling is decreasing for two fit parameters, whereas ε is rapidly increasing (up to ~ 5 after 10.10 m) for three fit parameters, which is caused by the strong asymmetry along the bunch and results in the appearance of non-physical minima between the oscillation periods (see fits at $\Delta x_1 = 10.10$ m). In our model, ε is meant to introduce an asymmetry which is small when compared to the bunch radius. The high values for ε and the occurrence of minima at the upper peaks of the oscillation after ~ 8.5 m are a sign that the model is no longer valid to describe the physical situation. For three fit parameters, the coupling is increasing much less (only up to ~ 1.5), which is caused by the higher value of p for $\Delta x_1 \gtrsim 8.5$ m. This is, however, still not a very accurate physical description of the coupling.

The goodness of fit (Figure 32c) reaches the best value ($R^2 = 0.96$) around $\Delta x_1 \sim 5$ m regardless of the number of fit parameters. This can be interpreted as the growth of the HI remaining in a linear growth regime around this propagation distance ($\Delta x_c/\sigma_r \sim 1$). For larger Δx_1 the goodness of fit decreases for all numbers of fit parameters, though with different strength. For two and three fit parameters, the GoF decreases to about $R^2 \sim 0.5$, whereas for only one fit parameter R^2 decreases much faster to $R^2 = 0.3$ after $\Delta x_1 = 8.5$ m of plasma, when the growth gets too non-linear. For most of the range between ~ 3.5 m and ~ 8.5 m, however, the GoF is above 0.7.

We can summarize that the fits to the simulation data confirm the model of CBH introduced in Section 2.3.4. It should be accurate to describe the experimental results as long

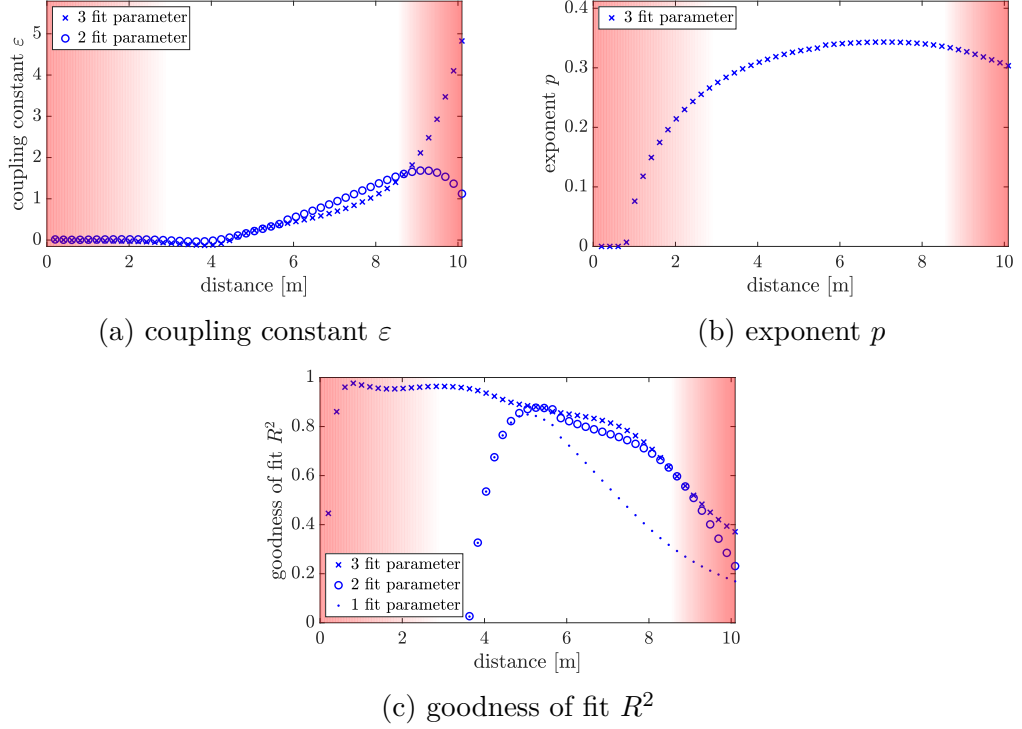


Figure 32: Evolution of different fit parameters in Equation 2.30 along 10.10 m of plasma. The red areas indicate regions where the fit model is not valid.

as the asymmetry (or non-linearity) is not dominating over the oscillation (i.e. $\varepsilon \lesssim 1.5$). Moreover, we can establish the power law in $k_{pe}^3 \zeta z^2 = 1/3$, as theoretically predicted. Thus, we can well compare the fits of the experimental data with the simulation results in similar growth regimes, i.e. for similar $\Delta x_c / \sigma_r$.

5.3.3 Angle Scan

The three-dimensionality of the simulations enables us to make a series of slices through the p^+ -bunch charge distribution for different angles α with respect to the $x_1 x_2$ -plane. Slices at different angles can be representative of what is expected to be observed in the experiment when the angle at which the plane of the HI growth is oriented (see Figure 58) is not equal to the orientation of the SC slit.

The resulting slices after $\Delta x_1 = 8.08$ m of plasma are shown in Figure 33. The transition from the plane where the HI is seeded and CBH develops (Figure 33a, referred to as 0° -plane) to the plane of pure SSM (Figure 33g, referred to as 90° -plane) becomes clearly visible: While increasing α starting from 0° (Figure 33a), the asymmetry in the 2D bunch charge distribution due to the HI appears to become less and less dominant (Figures 33b and 33c), before it becomes completely symmetric at $\alpha = 90^\circ$ (SSM, Figure 33d). Increasing α further, the asymmetry starts to become more and more dominant again (Figures 33e and 33f), before we end up again at 180° in the plane of the HI (Figure

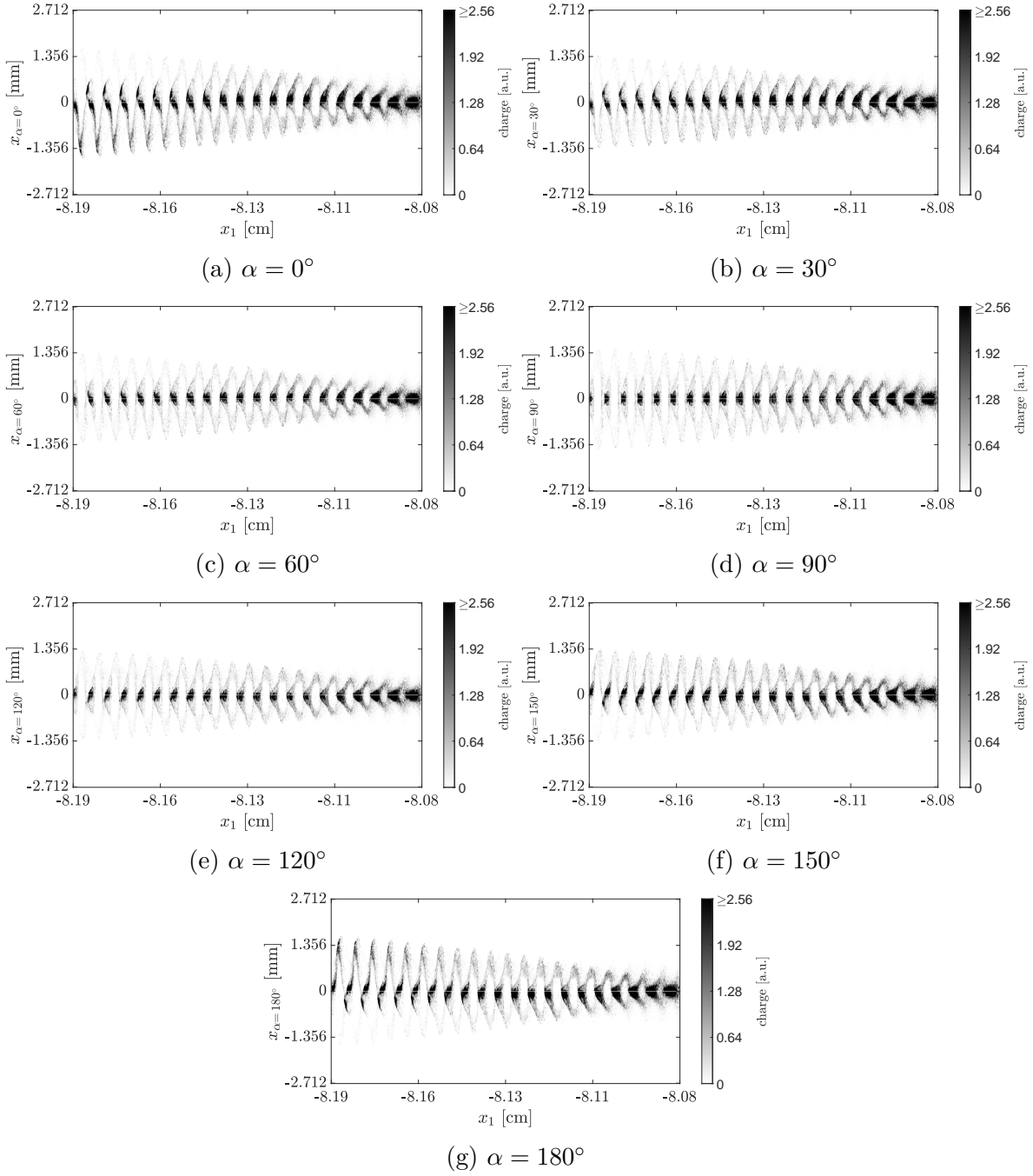


Figure 33: Slices of the charge distribution of 3D simulation results in OSIRIS along different planes x_α across the charge distribution of the simulated bunch after a propagation distance of $\Delta x_1 = 8.08$ m through plasma.

33g). Here, the distribution is mirrored to the 0° -plane, i.e. the protons further displaced from the bunch propagation axis are in the positive x_2 -direction. When we discuss the fits to the centroid at different angles later in this section, we observe that ε remains constant for all angles. Only the amplitude of the centroid oscillation increases, which then appears as a larger asymmetry in the charge distribution of the p^+ -bunch.

We can now calculate the DFT of the centroid displacement along the bunch for the different slices across the p^+ -bunch charge distribution along the different planes. In Fig-

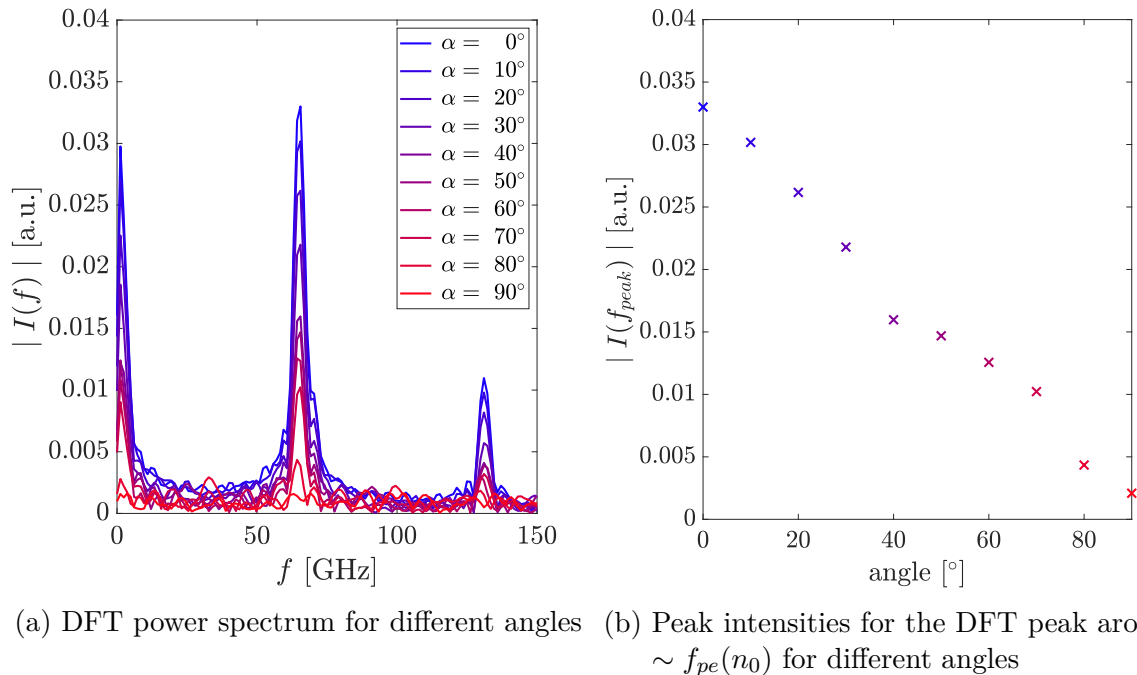


Figure 34: DFT spectrum of the centroid displacement (a) and peak intensities (b) for different angles $\alpha \in 0^\circ - 90^\circ$ with respect to the x_1x_2 -plane after a propagation distance $\Delta x_1 = 8.08$ m.

ure 34a, the results of the DFT of the centroid oscillation are plotted in angular steps of $\Delta\alpha = 10^\circ$. For $\alpha = 90^\circ$, no frequency peak higher than the noise level is visible. For $\alpha < 90^\circ$, a clear peak in the frequency spectrum appears close to f_{pe} . The strength of this peak decreases linearly until a minimum is reached for the 90° -plane (see Figure 34b). The behaviour is similar for steps of 10° from the 90° -plane to the 180° -plane (not shown in the plot).

It is important to mention that in the experiment the plane in which the HI develops is random and thus not necessarily in the plane at $\alpha = 0^\circ$ with respect to the SC slit orientation. The value for α is hence an unknown parameter in the experiment and possibly changing from event to event. The results from Figures 33 and 34 show, however, that the HI can also be observed on SC images for $\alpha \neq 0^\circ$ (unless $\alpha \sim 90^\circ$) and also that f_{osc} can be determined independently of α .

Moreover, in the experiment, the time-integrated radial bunch profiles (see Section 6.5)

are another diagnostic to detect the HI also in planes close to $\alpha = 90^\circ$ with respect to the SC slit orientation.

To further investigate the coupling constant ε in different planes with respect to the plane of the HI seed, we perform three different series of fits at a distance of $\Delta x_1 = 6.06$ m, the propagation distance at which $x_{c,max}$ is similar to what is observed in the experiment (see Chapter 6). In all of these fits, we keep the results of the fits in the 0° -plane for ζ_0 as fixed constants and set p to the now established value of $1/3$. In the first series of fits (Figure 35), we only use the amplitude δ_c as a single free fit parameter and fix ε to the fit results at $\alpha = 0^\circ$. In the second series (fits not shown), we keep ε as a free fit parameter and fix instead $\delta_c(\alpha) = \delta_c(0^\circ) \cdot \cos(\alpha)$. In the third series, we set $\delta_c = \delta_c(0^\circ)$ and use ε as free fit parameter (also not shown in a figure).

Contrary to the fits in Figure 31, where the centroid displacements are directly determined in the output of the simulation, the centroid displacements in the angle scan have to be calculated from the charge density in the simulation. This leads to a significantly higher noise in the signal of the centroid displacements.

The fits of the first series (see Figure 35) give good results as the bunch centroid oscillation matches well the data for all angles α . Figure 36 shows δ_c against the angle of the projection plane determined from the fits displayed in Figure 35 and gives evidence that the amplitude of the oscillation depends, as expected, on the angle of the projection and scales with

$$\delta_c(\alpha) = \delta_c(0^\circ) \cdot \cos(\alpha). \quad (5.7)$$

Keeping ε as a free fit parameter (second series of fits) returns almost constant values for ε for different angles ($\Delta\varepsilon \lesssim 0.05$, except for $\varepsilon = 90^\circ$, see Figure 37).

In both fits, the amplitude of the oscillation is decreasing the stronger, the closer the investigated plane gets to the 90° -plane. For planes around $\alpha = 90^\circ$, there is no centroid oscillation visible. Therefore, the fits do not give meaningful results for $\alpha = 90^\circ$ and we cannot determine a meaningful value for ε . The signal is purely dominated by noise which thus returns low values for R^2 .

The third series of fits, however, does in general not give any reasonable results ($R^2 < 0.2$ for $\alpha > 30^\circ$).

The series of fits infers that the theoretically expected cos-dependence can be established and that ε is conserved for a rotation along α . Furthermore, we can conclude that the coupling strength is a universal feature of the oscillation at a certain propagation distance in plasma, regardless of the plane of the slice. Therefore, we can also determine the coupling constant ε for HI events where the orientation of the SC slit is not in the plane of the HI growth (except for $\alpha \sim 90^\circ$). Moreover, this means that it is in general also possible to determine the initial seed level δ_c of the HI from the experimental data, when the angle between the SC slit and the plane of the HI growth is known.

5 Hosing Instability Simulations with OSIRIS

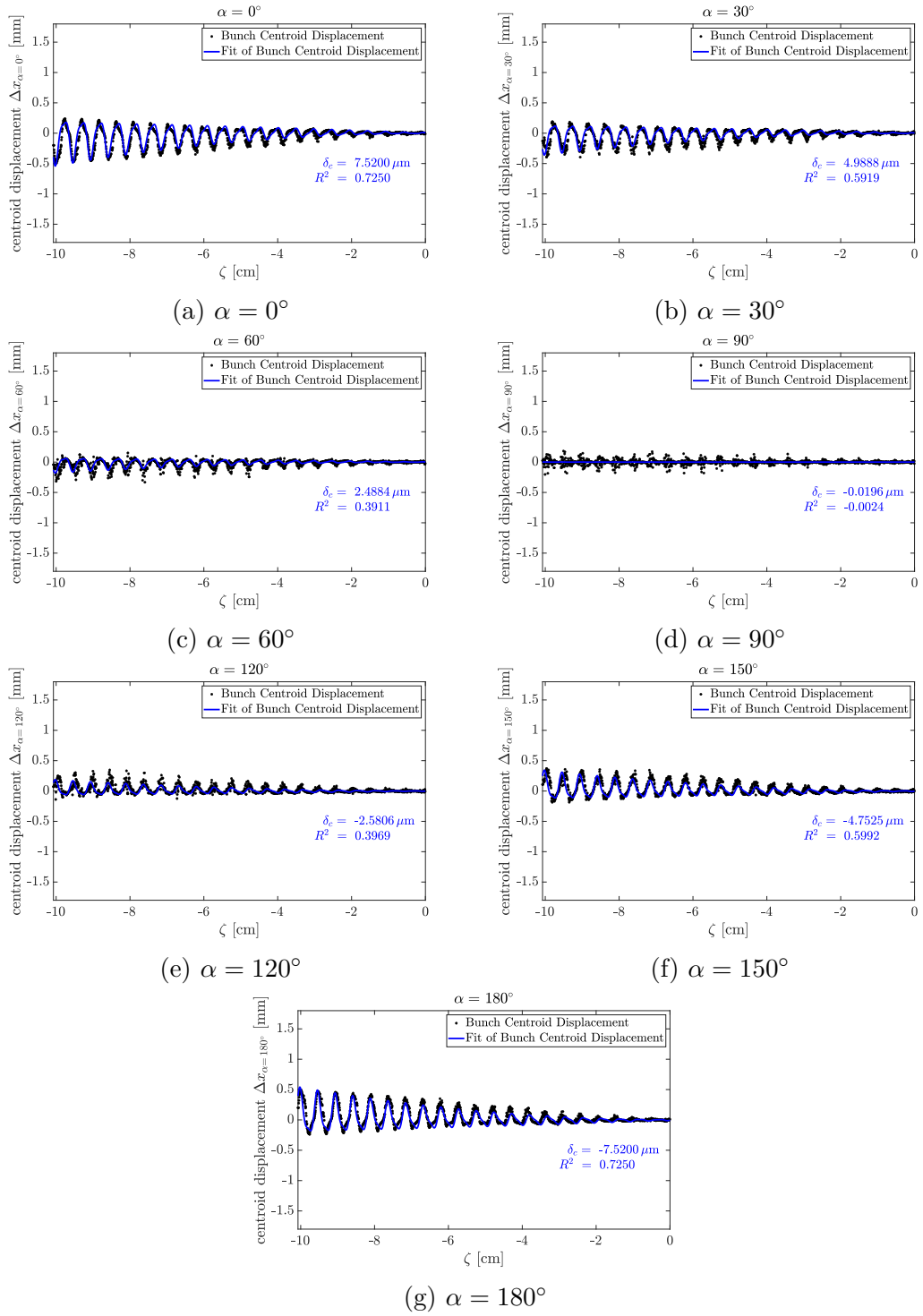


Figure 35: Fits of Equation 2.30 to the bunch centroid projection along different planes x_{α} across the charge distribution of the simulated bunch after a propagation distance of $\Delta x_1 = 6.06$ m through plasma with fixed coupling constant $\varepsilon = 0.5648$.

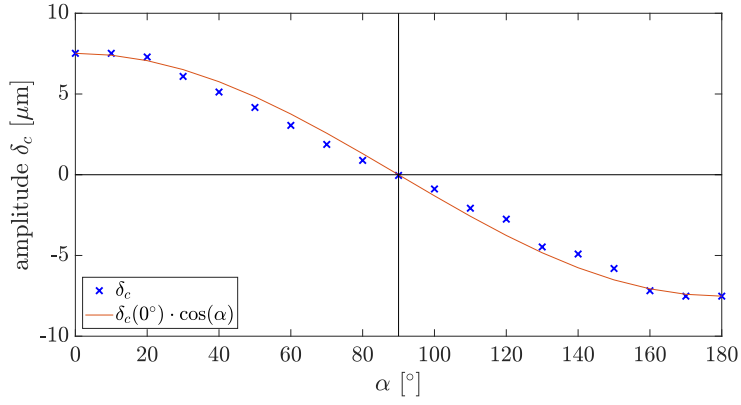


Figure 36: Dependence of the oscillation amplitude δ_c on α for fixed coupling constant $\varepsilon = 0.5648$

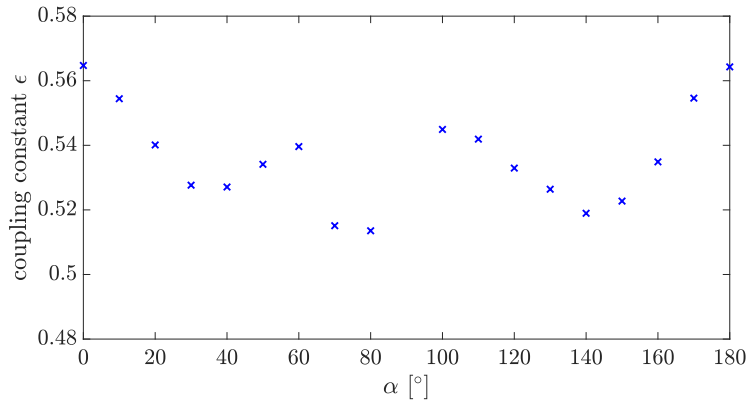


Figure 37: Dependence of the coupling constant ε on α for fits with free fit parameter ε and $\delta_c(\alpha) = \delta_c(0^\circ) \cdot \cos(\alpha)$.

5.3.4 Time-Integrated Radial Bunch Charge Distribution

The simulation data also allow to analyze the time-integrated radial bunch charge distributions which is akin to gathering time-integrated radial profiles of the p^+ -bunch with the two IS installed in AWAKE (see Section 6.5)³.

The distributions are shown in Figure 38 at the plasma entry ($\Delta x_1 = 0.20$ m), after $\Delta x_1 = 5.05$ m and at the end of the plasma ($\Delta x_1 = 10.10$ m). After 5.05 m, the radial

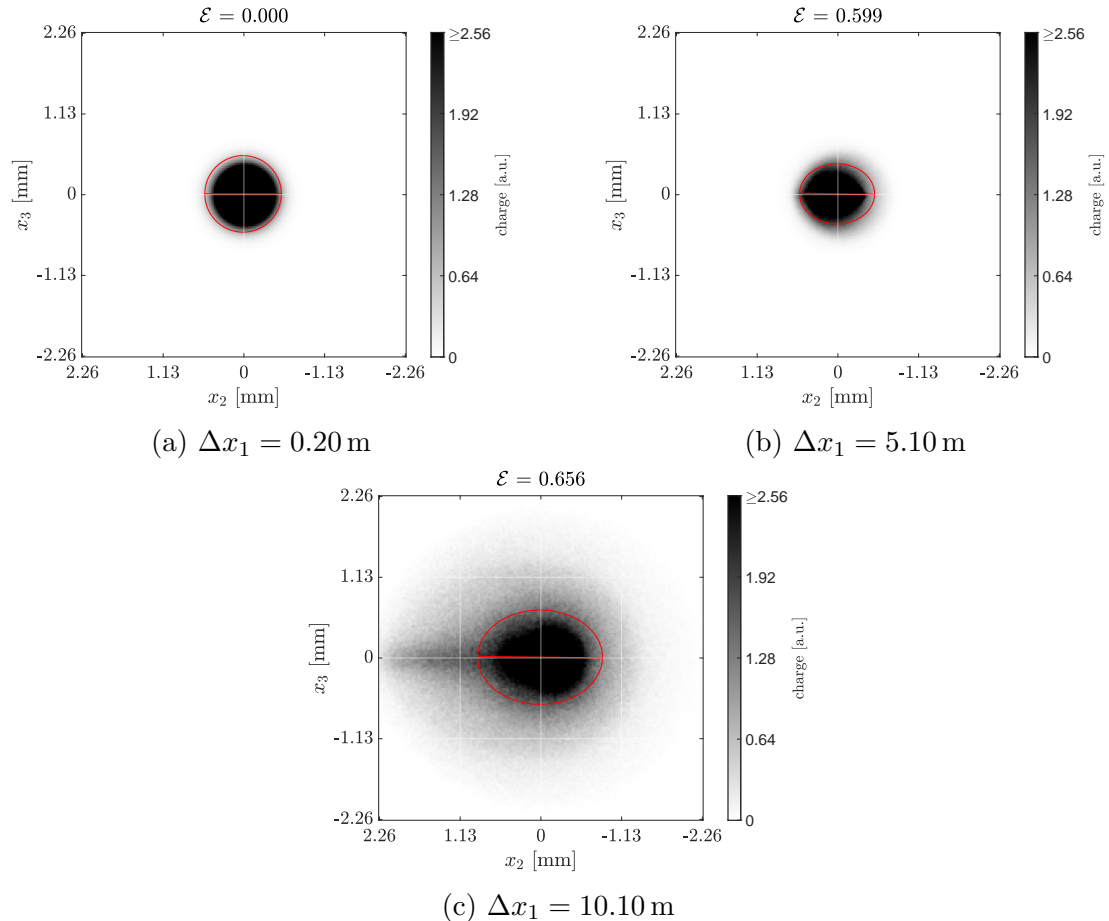


Figure 38: Time-integrated radial charge distribution of the simulated p^+ -bunch in the x_2x_3 -plane after propagation distances of 0.20 m (a), 5.05 m (b) and 10.10 m (c) through plasma.

bunch shape is still nearly radially symmetric and centered around the bunch propagation axis (0,0), whereas after 10.10 m a clear elongation of the radial bunch profile along the x_2 -axis (i.e. along the orientation of the HI seed) becomes clearly visible.

As in our experimental situation the orientation of the HI has to be revealed from the IS, we need to define a measure of the asymmetry of the profiles and find an algorithm to

³Note, in the experiment however, the radial bunch profile is time-integrated along the entire p^+ -bunch, including its unmodulated leading part, whereas in the simulation only the simulated part of the bunch (see Figure 25) is taken into account for the time-integration. This should, however, not change the general features of the shapes of the bunch profiles.

determine the orientation of the privileged HI plane. Therefore, we calculate the contour line along the time-integrated radial bunch profile at 25% of the maximum intensity and fit an ellipse onto the remaining two-dimensional isosurface. The major axis of this ellipse with eccentricity⁴ $\mathcal{E} \in [0; 1]$ then can be used to define the orientation of the privileged HI plane. We can then compare the eccentricity of the ellipses of different events in order to compare the asymmetry of the time-integrated radial bunch profiles. These ellipses and their major axes are depicted in red in Figure 38. As expected, the orientation of the major axes is parallel to the x_2 -axis, i.e. the orientation of the HI seed and the eccentricity is increasing along the plasma.

5.4 Comparison to Hosing Instability Simulations Without Seed of the Self-Modulation Process

In order to prove that the observed asymmetries of the p^+ -bunch centroid after propagation through plasma result from the coupling of the HI to the growth of the SM process, we compare our results to another simulation where only the HI (and no SM process) is seeded. The input p^+ -bunch for this simulation is shown in Figure 39. The

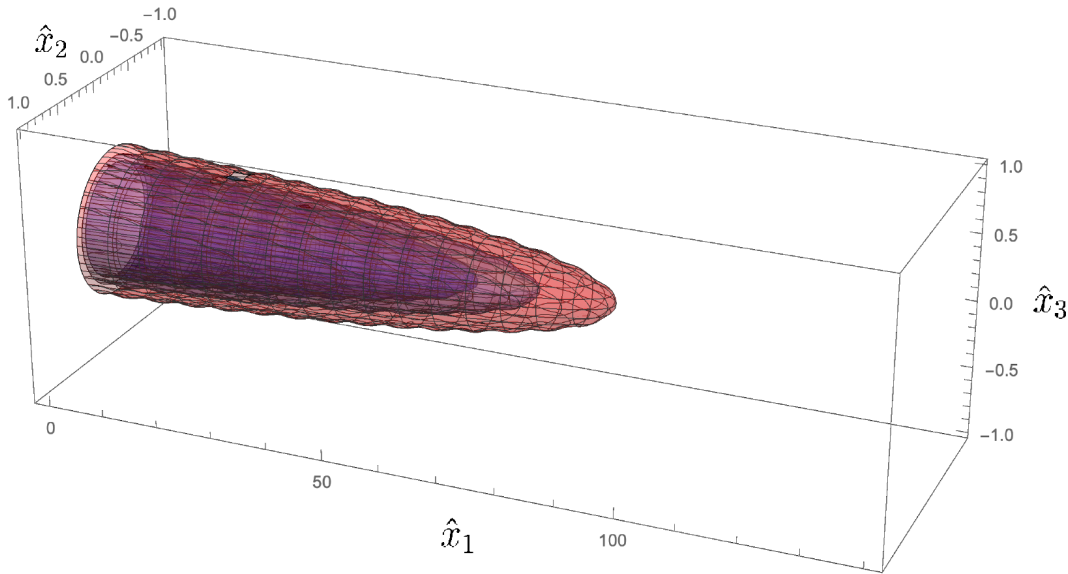


Figure 39: Initial shape of the SPS-like p^+ -bunch for the OSIRIS simulations of the HI without seed of the SM process. The seed for the HI is obtained by the harmonic oscillation of the centroid visible as wiggles on the bunch profile. Image by courtesy of M. Moreira.

input parameters of the bunch are similar to the parameters stated in Section 5.2 except that we simulate only the front part of an SPS-like p^+ -bunch and the simulation window is chosen to be only $L_{x_1} \times L_{x_2} \times L_{x_3} = 10.5 \text{ cm} \times 0.3 \text{ cm} \times 0.3 \text{ cm}$. There is no cut in the beam profile which would provide the seed wakefields for the growth of the SM process.

⁴An ellipse with $\mathcal{E} = 0$ is a circle, the limit $\mathcal{E} \rightarrow 1$ a line.

5 Hosing Instability Simulations with OSIRIS

The HI is seeded equivalently by an harmonic oscillation with $\delta x_2 = 0.01 k_{pe}^{-1} = 7.5 \mu\text{m}$. Figure 40 shows the simulation results in the $x_1 x_2$ -plane, the plane of the HI seed. The most important conclusion we can make from the simulation is that we observe the bunch centroid oscillating symmetrically. The amplitude of the oscillation is lower than

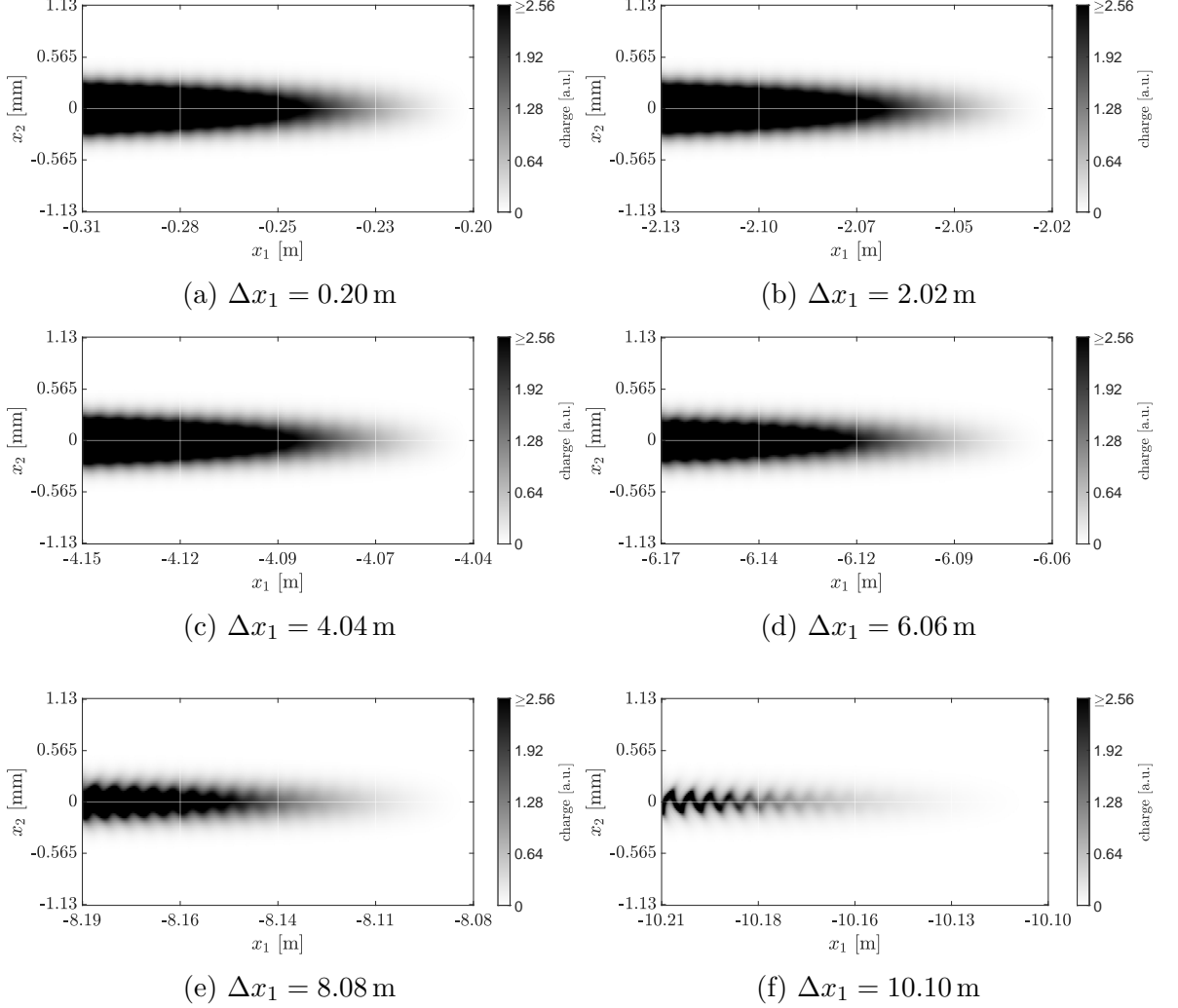


Figure 40: Slices of the charge distribution of 3D simulation results in OSIRIS for an SPS-like p^+ -bunch after propagation distances Δx_1 through plasma with $n_{pe} = 0.5 \cdot 10^{14} \text{ cm}^{-3}$ without seeding the SM process. Note, for a better visibility, the scaling of the x_2 -axis is only half as large as in Figures 26, 27 and 33.

in the case where also the SM process is seeded (see Figure 27). Furthermore, we determine the bunch centroid displacements after propagation of a distance Δx_1 in plasma (similarly to Figure 29a). In the Figure, we can see that for propagation distances $\zeta \gtrsim -4 \text{ cm}$ almost no growth of the oscillation amplitude is visible at all. The centroid position is dominated by the initial seed level of δx_2 . After about 4–6 m propagation through plasma, an exponential growth of the amplitude becomes

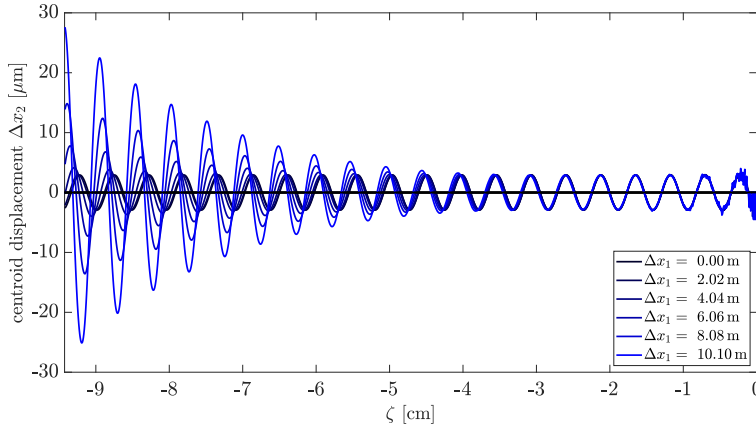


Figure 41: Bunch centroid displacements after propagation of a distance Δx_1 in plasma for an SPS-like p^+ -bunch with HI seed but without seeding the SM process. Note, the scaling of the Δx_2 -axis is different than in Figure 29a.

visible for $\zeta \lesssim -4$ cm, but with a much lower amplitude compared to the growth of the HI with seed of the SM process. A reason for this are the different shapes of the simulated bunches. In this simulation, the input is the rising edge of a Gaussian p^+ -bunch (see Figure 39), whereas we simulate the rear part of a Gaussian bunch cut 100 ps before its centre in the simulation of CBH. Therefore, the initial seed wakefields for the SM process are much lower (see e.g. Figure 8).

Taking a cut through the charge distribution in the $x_1 x_2$ -plane along the bunch, we also observe a periodic modulation, which is not caused by periodic focusing and defocusing forces along the bunch, but only by the bunch centroid moving out and back into the plane of the slice (not shown here).

Hence, the results prove that the asymmetry of the bunch centroid oscillation with respect to the bunch propagation axis is only a feature of the coupling of the HI growth to the SM process and cannot be observed in the case of the pure HI.

At the end of Chapter 6, we compare the experimental results and the predictions by the simulations (Section 6.7).

6 Experimental Results – Part 1

Observation of the Hosing Instability with Seed of the Self-Modulation Process

The experimental data presented in this thesis were collected in different scientific run periods of AWAKE between June 2017 and November 2018. For all events analysed, the nominal Rb vapour density is set to a range of $n_0 = (0.5 \pm 0.1) \cdot 10^{14} \text{ cm}^{-3}$. In this chapter, we assume that the Rb vapour is initially (i.e. at the time of the laser pulse transit) fully ionized in a column with a radius of $\sim 1 \text{ mm}$ by the high power laser pulse and that the protons are propagating entirely through this plasma column. This implies the assumption that by default all events are acquired with a well aligned set-up. Thus, the plasma density n_{pe} can be assumed to be equal to the neutral density n_{Rb} measured by interferometry. In this chapter, for all events, the timing of the ionizing laser pulse is chosen to be below $0.5 \sigma_z$ ahead of the centre of the p^+ -bunch, i.e. we seed the growth of the SM process.¹

As the characterisation of the HI in Chapters 6 and 7 is mainly based on SC images, we first define and describe the methods used to analyse the SC data and characterise the p^+ -bunches sent to AWAKE. We explain how to determine the centroid of the p^+ -bunch and identify the oscillation of the bunch centroid as the typical signature of the HI in comparison to events with SSM or SMI as already inferred by the simulation results in Chapter 5. Moreover, we show that the centroid oscillates at the plasma frequency and that the growth rate of the HI depends on the p^+ -bunch population. Furthermore, we study the integrated radial p^+ -bunch distribution determined from the IS (see Section 3.1.6) and identify the plane in which the HI develops along the p^+ -bunch. By fitting Equation 2.30 to the experimentally determined p^+ -bunch centroids, we give evidence for the coupling between the SM process and the HI.

6.1 Streak Camera Data Evaluation and Background Estimations

The aim of this section is to establish the methods for evaluating the SC data (see Section 3.1.6) and to describe the parameters of the incoming p^+ -bunches into the plasma. As

¹Note, contrary to here, in Chapter 7, we analyse the development of the HI without seeding the SM process, i.e. the growth of the SMI and the HI compete with each other.

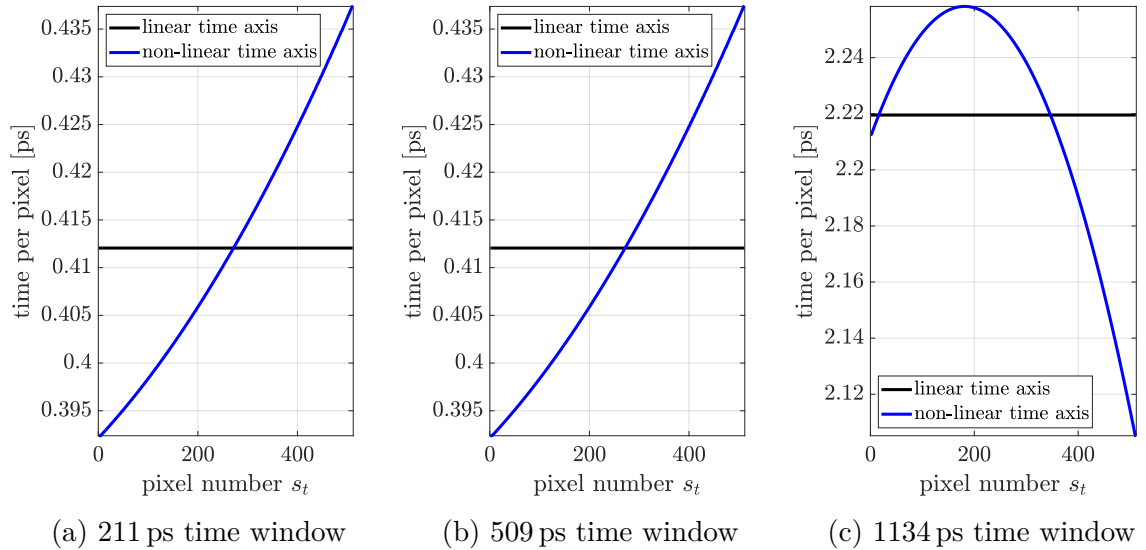


Figure 42: Correction of the non-linear SC time axis to a linear time axis in different time windows.

there are no diagnostics for the p^+ -bunches installed before the vapour source, we assume that the p^+ -bunch parameters are equal to the measured parameters of p^+ -bunches after propagation through Rb vapour (i.e. no plasma in the source).

6.1.1 Streak Camera Raw Data

The SC raw data are arrays with a size of $S_t \times S_r = 512 \times 672$ pixels, where S_t is the size in the temporal and S_r in the radial dimension of the image, respectively. The images have a 16-bit depth, i.e. the pixels counts $I_{pix}(s_t, s_r)$ are within the range $[0; 65535]$, where (s_t, s_r) define the coordinates of a specific pixel of the image.

As mentioned in Section 3.1.6, OTR-photons arriving through the slit of the SC onto its photo-cathode are converted into a number of electrons proportional to the intensity of the incoming light. The sweep voltage applied between the sweep electrodes then deflects the electrons, which arrive at different times and leave the streak tube with slightly different angles, before they are sent to the MCP. Therefore, the time axes of the resulting SC images are non-linear, which leads to non-constant time intervals per pixel. This effect has to be corrected in order to display the SC images with a linear time axis. Thus, the time per pixel is linearized by an interpolation algorithm, distributing the original pixel counts from a non-linear grid onto a grid with constant steps. Figure 42 shows the time per pixel along the temporal axis of the SC before (i.e. as given by the SC manufacturer) and after the linearization for the three different SC time windows used in the analysis. All SC images shown in this thesis are corrected to linear time axes. The Point Spread Function (PSF) of the imaging system is measured using a Ronchi ruling, i.e. a mask with well known grid distances. The resulting optical resolution is given by the FWHM of the Green's function and is about 0.187 mm [68]. The conversion from pixels to their corresponding length units on the OTR-foil is given by 1 pixel =

0.0231 mm for the spatial axis of the SC image, regardless of the SC time window. Hence, the width of the PSF is about 8 pixels.

6.1.2 Background Subtraction

Continuous Background

All SC images have a background that needs to be subtracted before being further analysed. It is mainly caused by the bias level of the CCD camera mounted in the SC system, i.e. an artificially electronic offset introduced to ensure that the analog to digital converter always reads positive values [85]. Moreover, there is an additional background by the readout-noise and the dark current of the CCD. Potential remaining stray light in the dark room, where the SC is placed, can also lead to a background signal on the camera.

It can be shown from background images with no p^+ -beam and no (marker) laser that this background is constant over time and only fluctuating randomly. It is, however, varying for different choices of time window, slit width and MCP gain. To reduce the noise level in this continuous background, we average at least 20 background images for every data set and for every SC setting. This averaged continuous background is then subtracted from all SC images before any analysis. Figure 43a shows as an example (for MCP gain 30 and slit width 20 μm) the remaining pixel counts of a background image after subtraction of the continuous background. On average, the remaining pixel count in the data set of the background images fluctuates by about ± 5 and the sum of all remaining pixel counts of the image fluctuates on the order of $\pm 10^4$. Hence, the contribution of this background fluctuations can be neglected as they are randomly distributed across the image and thus average out when calculating the centroid of the image in Section 6.3.1. For most of the background images analysed, the highest pixel count of a single pixel of the image is below 100.

Hot Pixel Background

In presence of the p^+ -beam, however, the background becomes higher due to interaction of the protons with material in the p^+ beam-line upstream the OTR-diagnostics (e.g. section separation windows, irises or LBDP2) causing secondaries and an activation of these materials. This background can be analysed by taking a SC image a few ns after the p^+ -beam (Figure 43b is an example for MCP gain 30 and slit width 20 μm). It can be seen that on average this radiation background is also randomly distributed across the image and results in small groups of pixels where the measured intensity is very high, often up to the pixel saturation count. These pixels are referred to as “hot pixels”. The incidence of these hot pixels depends on the p^+ -bunch population. Due to their randomness and the high locally confined intensity, it is not possible to reasonably subtract or filter this hot pixel background. Even though, in presence of protons, pixel counts up to camera saturation are reached, the effect has no periodic features and av-

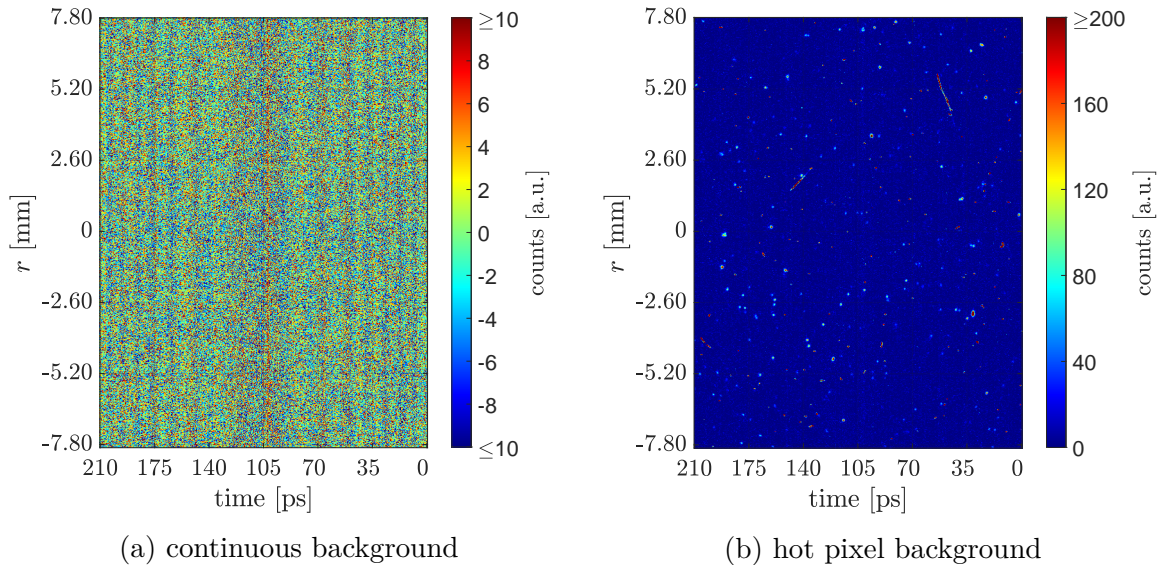


Figure 43: (a) Remaining pixel counts of a background image after subtraction of the averaged continuous background. The remaining background fluctuations are randomly distributed across the image. (b) Background taken a few ps after a p^+ -bunch. Hot pixels are appearing randomly across the image. Note, in this image the continuous background is already subtracted.

erages out while calculating the bunch centroid position on the SC image. Thus, it only increases the noise in the modulation of the p^+ -bunch centroid, but does not effect the main conclusions in this thesis. Summing up all pixel values, the counts of the hot pixels are $\sim 5 - 10\%$ when compared to a typical p^+ -event.

To ensure a good displayability of the SC images for events with different charges and to reduce the effect of hot pixels, the maximum value of the chosen colour map scales with the pixel count of the image after subtraction of the continuous background.² This means that the colour scale is saturated above a certain value, specified on each image. Moreover, we do no longer display negative pixels counts, which appear due to the subtraction of the continuous background. However, it is important to note that the choice of the colour scale has no influence on the analysis and is only conducive to enhance the way of displaying the SC images shown in this thesis.

6.1.3 Bunch Trajectory and Centre of Gravity of Plasma Off Events

To calculate the centroid of the p^+ -bunch as a function of time (i.e. column by column on the SC images), we analyze SC images of bunches propagating entirely through vapour (referred to as plasma off events). Due to the aperture of the imaging optics in the optical path of the OTR-light, the radial field of view of the SC images is only about

²Unless mentioned otherwise, for streak images showing p^+ -bunches, the maximum value of the colour map is chosen as twice the maximum value out of all mean values along the spatial axes of the image, which is arbitrary, but scales well with the intensity depending on the p^+ -bunch population.

± 4 mm around its centre line. Therefore, we can remove the edges of the SC images which contain no other information than the background of the CCD camera. Moreover, the marker laser pulse, placed at the upper left edge of some images, has to be excluded from the analysis so that the additional pixel counts do not distort the calculation of the image centroid. In this first step of cropping, the outer 86 rows on each side of the spatial axis of the image are removed so that the remaining image size is $S_t \times S_r = 512 \times 500$ pixels.³

Now, we calculate the centroid of each column along the temporal dimension of the image and average over all columns. The radial position of this average defines the p^+ -bunch propagation axis on the image, i.e. the center of gravity axis of the p^+ -bunch charge distribution

$$C_{p^+} = \frac{1}{512} \sum_{s_t=1}^{512} \left(\frac{500}{2} + 0.5 - \frac{\sum_{s_r=1}^{500} I_{pix}(s_t, s_r) \cdot \left(\frac{500}{2} + 0.5 - s_r \right)}{\sum_{s_r=1}^{500} I_{pix}(s_t, s_r)} \right). \quad (6.1)$$

Based on this, the SC images are further cropped to a size of $S_t \times S_r = 512 \times 300$ so that C_{p^+} defines the centre of the SC image and the integrated charge distribution along the p^+ -bunch is symmetric with respect to the p^+ -bunch axis.

As the steering of the SPS p^+ -bunches varies slightly on a day-to-day basis, for every data set, we calculate an average position of C_{p^+} from a set of p^+ -bunch streak images without presence of plasma. All streak images showing events, where the plasma is turned on, are now cropped accordingly so that the center line of the images lies on C_{p^+} , i.e. the bunch centroids are centered on the averaged p^+ -bunch propagation axis of the corresponding plasma off events. This is especially important for making statements on the symmetry of the bunch charge distribution with respect to the p^+ -bunch propagation axis of an HI event. Applying this procedure to the background images shows that C_{p^+} lies on the bunch centroid with a standard deviation of less than 3 pixel = 0.07 mm, which is below the optical resolution limit of the SC.

6.2 Bunch Characterisation

We distinguish between three different p^+ -bunch populations requested from the SPS. In the following, bunches with a requested population of $N_b = 1 \cdot 10^{11} p^+$ are referred to as bunches with low population, bunches with requested $N_b = 2 \cdot 10^{11} p^+$ as bunches with medium population and bunches with requested $N_b = 3 \cdot 10^{11} p^+$ as bunches with high population. Within the same operation cycle (or operation day) the event-to-event fluctuation in the bunch population is usually below $\pm 10\%$ around its mean. The deviation from the requested p^+ -bunch population between different SPS operation cycles, however, is much higher, e.g. up to $\pm 0.5 \cdot 10^{11} p^+$ at high bunch population.

³Figure 44, discussed in more detail in the following section, gives examples for such cropped SC images of a p^+ -bunch propagating entirely through Rb vapour.

6 Experimental Results – Part 1

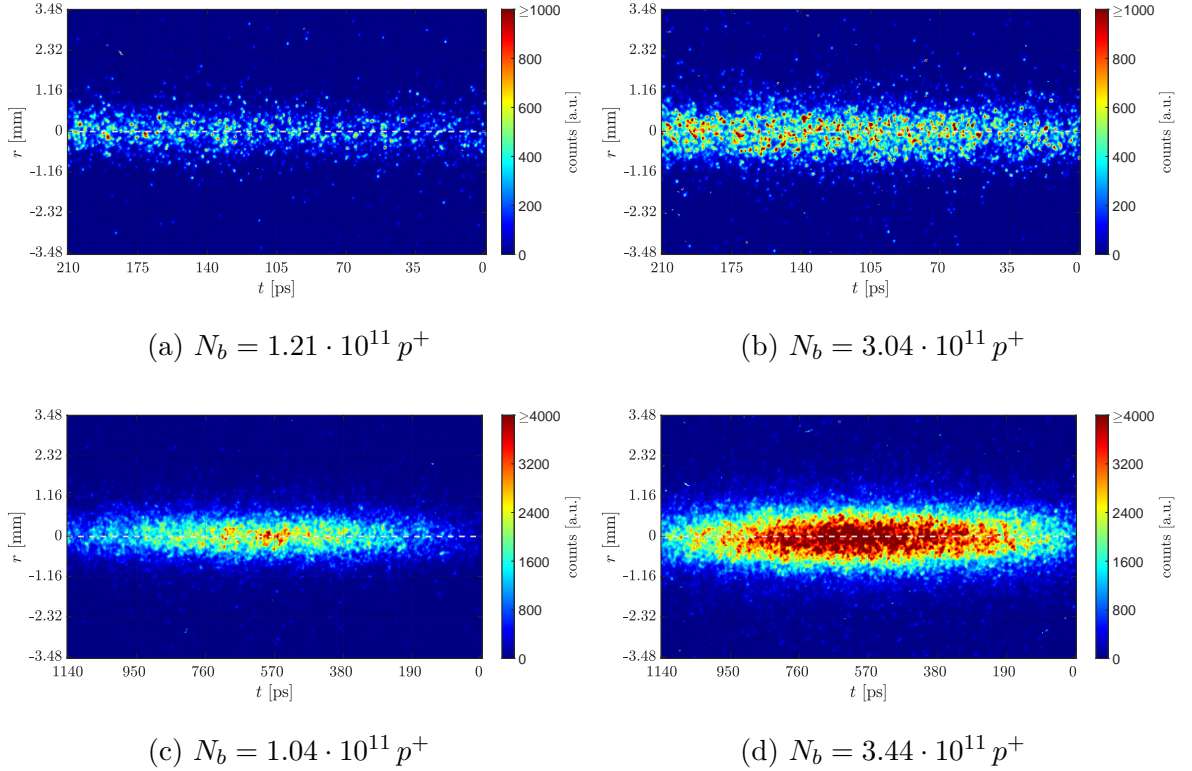


Figure 44: Plasma off events in the 211 ps and 1134 ps SC time window of p^+ -bunches with low and high bunch population. The bunch rotation mechanism is switched off. For all images, the MCP gain is 30, the slit width 20 μm . In (a) and (b), the streaking sequence starts ~ 100 ps, in (c) and (d) ~ 550 ps before the centre of the p^+ -bunch. The white dashed lines mark the trajectories of the p^+ -bunches. Note, for a better comparability, the colour maps are set to equal upper limits for images (a), (b) and for (c), (d), respectively.

Figure 44 shows SC images of p^+ -bunches with low and high bunch population propagating through Rb vapour in the 211 ps (Figures 44a and 44b) and 1134 ps SC time window (Figures 44c and 44d)⁴. Note, in all SC images shown in this thesis, the bunch is propagating from left to right, i.e. the front of the p^+ -bunch is on the right-hand side of the image.

The comparison between images with low and high bunch population shows that the pixel counts of the images are scaling about linearly with the bunch population. On the 211 ps images, the streaking sequence starts ~ 100 ps before the centre of the p^+ -bunch. Here, only a part of the bunch is visible, but the resolution of the image allows to resolve a potential modulation (SMI/SSM) or oscillation (HI) of the bunch. On the images gathered in the 1134 ps time window, however, the streaking sequence starts already ~ 550 ps before the centre of the p^+ -bunch and almost the entire bunch is visible.

It is important to note that the SC images appear very pixelated, even though the

⁴In this section, we do not discuss SC images in the 509 ps time window as there would be only little additional information gained in doing so.

p^+ -bunches contain on the order of 10^{11} protons. As inside the SC the incoming OTR-photons are converted into a number of electrons, the demand of electrons to create a signal is rather low, but leads to a much larger pixelation on the SC images compared to fluctuations in the incoming signal. A too high intensity of the signal sent to the SC slit also reduces the temporal resolution of the SC images.

The plasma off events now allow for a characterisation of the size of the incoming p^+ -bunches. Gaussian fits to the longitudinal and radial bunch size σ_z and σ_r

$$f(z) = cst \cdot \exp\left(-\frac{1}{2} \left(\frac{z - z_0}{2\sigma_z}\right)^2\right) \quad (6.2)$$

and

$$f(r) = cst \cdot \exp\left(-\frac{1}{2} \left(\frac{r - r_0}{2\sigma_r}\right)^2\right) \quad (6.3)$$

are applied to the bunch charge distribution of $N_{P,off}$ acquired images under similar experimental conditions.

As an example, Figure 45a shows the Gaussian fit to the p^+ -bunch charge distribution in Figure 44d (1134 ps SC time window). Even though the time window is too small to fully cover the entire bunch length, the Gaussian shape of the bunch is clearly visible. We can determine the FWHM (and therefore also σ_z) as well as the position of the bunch centre from the fit. In the 211 ps time window, however, the time window is too short to perform a reasonable longitudinal Gaussian fit, therefore, we only use images in the 1134 ps time window for the longitudinal fits. This ensures to have a large part of the bunch on the image and reduces the extrapolation length at the edges of the image.

The radial Gaussian fit of the p^+ -bunch charge distribution is shown in Figure 45b. As the radial dimension of the streak image is independent of the time window, we are able to perform radial Gaussian fits for both the 211 ps (not shown in the figure) and the 1134 ps time window. The radial p^+ -bunch charge distribution is nearly Gaussian with a peak close to the bunch centre axis determined from the SC image ($r = 0$ mm) and has wings in the range $r = \pm (1 - 2)$ mm.

Table VI gives an overview of the averaged longitudinal and radial bunch sizes σ_z and σ_r determined by Gaussian fits to the integrated signal of $N_{P,off}$ SC images (as shown in Figure 45) for p^+ -bunches with and without bunch rotation mechanism enabled (see Section 3.1.2).

We can conclude that the radial fits give the same values within the error margin for the 211 ps and 1134 ps time windows and that the bunch rotation mechanism reduces the σ_z of the bunch by about a factor of 25% while keeping σ_r almost constant. The radial bunch size is proportional to the bunch population and decreases by about 15 – 20 % for the low bunch population events compared to high bunch population events. Thus, for the same N_b , the local charge density, i.e. the bunch charge per volume, is higher in events with bunch rotation on compared to events with bunch rotation off. Therefore, the initial seed wakefields in these events should lead to stronger defocusing forces and to higher centroid oscillation amplitudes.

For all calculations and fits to experimental data, we use the values for σ_r and σ_z

6 Experimental Results – Part 1

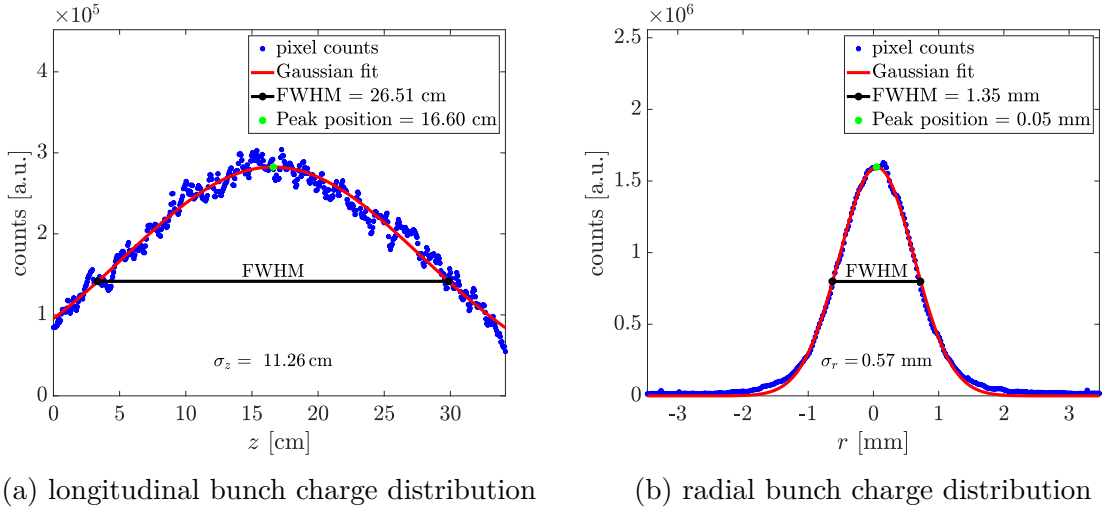


Figure 45: Gaussian fits of the longitudinal (a) and radial (b) bunch charge distribution of the proton bunch shown in Figure 44d (1134 ps time window).

determined in this section.

To visualize the effect of the bunch rotation mechanism on the incoming p^+ -bunches, Figure 46 shows two events with similar bunch populations ($N_b = 2.7 \cdot 10^{11} p^+$) and with equal colour map, slit width and MCP gain. The bunch rotation mechanism is switched off in Figure 46a and turned on in Figure 46b. The p^+ -bunch in the event with bunch

SC window [ps]	N_b [$10^{11} p^+$]	Bunch rot.	σ_r [mm]	σ_z [cm]	$N_{P,off}$
1134	2.67 ± 0.14	off	0.54 ± 0.02	9.75 ± 0.22	52
211	2.77 ± 0.37	off	0.54 ± 0.03	—	30
1134	3.21 ± 0.31	on	0.56 ± 0.03	7.70 ± 0.27	52
211	3.21 ± 0.25	on	0.55 ± 0.04	—	29
1134	1.17 ± 0.10	off	0.45 ± 0.02	9.83 ± 0.20	5
211	1.20 ± 0.05	off	0.45 ± 0.01	—	7
1134	0.91 ± 0.04	on	0.47 ± 0.01	7.12 ± 0.14	3
211	1.11 ± 0.09	on	0.45 ± 0.02	—	8

Table VI: Longitudinal and radial p^+ -bunch sizes for different SPS beams determined from Gaussian fits

rotation off appears longitudinally more elongated than the event with bunch rotation on, which is consistent with the results in Table VI. It is, moreover, remarkable that the sum of the pixel counts of the SC image $\sum I_{pix}$ in events with no bunch rotation is by a factor of about 1.5–2.5 higher than in events with bunch rotation on. This is most likely caused by the fact that due to the bunch rotation mechanism the beam gets steered slightly off the SC slit as the OTR transport line was aligned and optimized for bunches with bunch rotation mechanism off. This assumption is also supported by the readings of the BPMs in the SPS beam line (see Section 3.1.6).

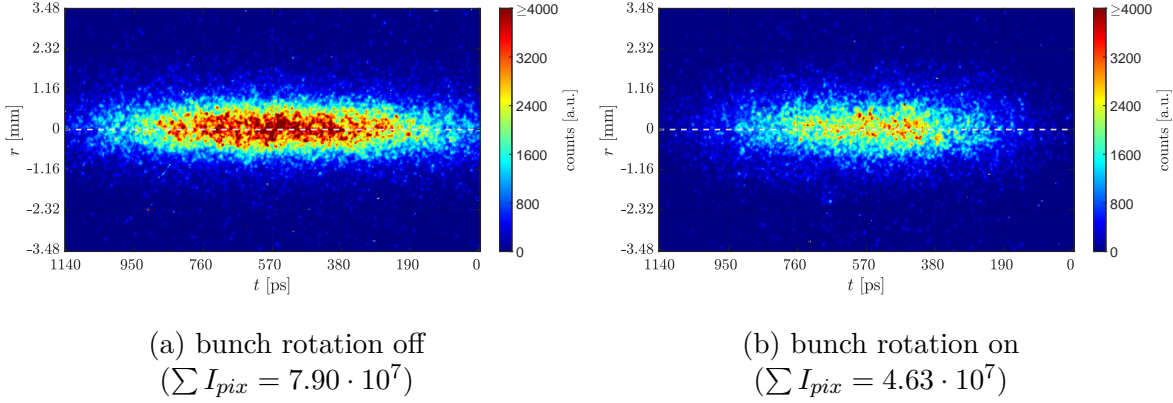


Figure 46: Events with similar bunch populations ($N_b = 2.7 \cdot 10^{11} p^+$) and bunch rotation mechanism off (a) and on (b). For both images, the MCP gain is 30, the slit width $20 \mu\text{m}$. Note, for a better comparability, the colour maps are equal for both images.

6.3 Characterisation of Hosing and Self-Modulation

Having all images centered on the bunch propagation axis of their corresponding plasma off events and the background subtracted, we are now able to analyze events where the plasma is turned on. In this section, we compare the characteristics between events with HI and SSM based on a typical event for each process and for low and high p^+ -bunch populations. The SM process is seeded about 100 ps ahead of the p^+ -bunch centre. Moreover, we establish the methods to determine the position of the bunch centroid and to calculate the frequency of the bunch centroid oscillation.

Figure 47 shows as an example one SC image of a typical HI event and one of a typical SSM event for low and high p^+ -bunch populations each at $n_{pe} \sim 0.5 \cdot 10^{14} \text{cm}^{-3}$. We choose this plasma density because in this density regime we are able to observe both SM and HI events. Above $n_{pe} \sim 0.7 \cdot 10^{14} \text{cm}^{-3}$ no signs for any occurrence of the HI are observed. For all SC images shown in this section, the chosen time window has a duration of 211 ps.

In Figure 47a, a typical HI event at low p^+ -bunch population can be seen. After the seed position (at a time of $t \sim 5$ ps on the image), the charge distribution is no longer axi-symmetric and the bunch centroid starts to oscillate around the bunch propagation axis with growing amplitude along the bunch. Figure 47b presents an event where only the SSM develops. The transverse charge distribution of the bunch is symmetric with respect to the bunch propagation axis and gets periodically focused and defocused along the bunch turning into a train of short micro-bunches (as described in [31]). The distance of the defocused protons from the bunch propagation axis is also growing along the bunch (see [30]). Figures 47c and 47d show similar effects at high bunch population.

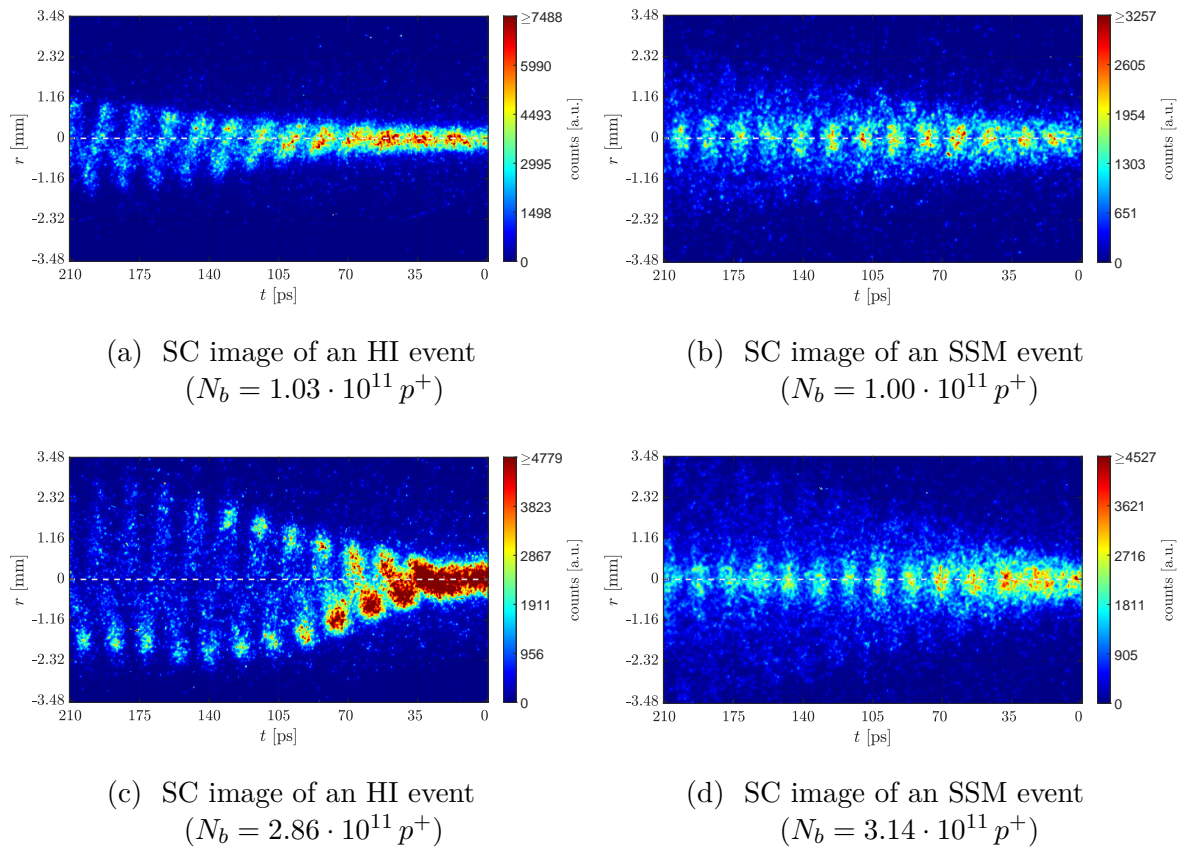


Figure 47: SC images of HI and SSM events under similar experimental conditions with low and high p^+ -bunch population. The ionizing laser pulse is 100 ps ahead of the bunch centre. The seed points in (a), (b), (d) are at $t \sim 5$ ps and in (c) at $t \sim 30$ ps. In (a) and (c), the MCP gain is 35 and the slit width $20 \mu\text{m}$, in (b) and (d) the MCP gain is 30 and the slit width $50 \mu\text{m}$. The white dashed lines mark the reference p^+ -bunch trajectories determined from corresponding plasma off events.

Contrary to the other three events in Figure 47, the seed point of the SM process⁵ for the HI event with high bunch population (Figure 47c) is at $t \sim 30$ ps. In the high bunch population events, the amplitude of the centroid oscillation (of the HI event) and the defocusing amplitude (of the SSM event) are clearly higher than in case of low bunch population. This is consistent with the expectation of a higher bunch population driving larger wakefields in the plasma.

In the next section, we analyze the centroid of the p^+ -bunch more closely in order to quantify the oscillation and to describe its symmetry with respect to the bunch propagation axis.

6.3.1 Integrated Signal and Bunch Centroid Position

First, we calculate the integrated signal on the SC images by summing all pixels in every column of the temporal axis along the bunch. The results for the bunches with low population are shown in Figure 48a for the HI event (Figure 47a) and in Figure 48b for the SSM event (Figure 47b). Moreover, for both images, we compute the position of the centroids for every column along the bunch using Equation 6.1. The resulting positions of the centroids are plotted in Figures 48c and 48d. For a better comparability of the centroid distributions to the fit results in Section 6.6, we convert in all centroid plots the time scale into a length scale in the co-moving frame⁶.

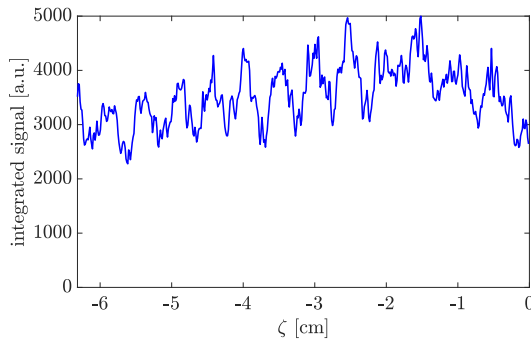
The integrated signals for both events (Figures 48a and 48b) show a periodic modulation of the charge density of the p^+ -bunch, whereas Figure 45a shows a uniform profile when the plasma is off. As the streak image shows the projection of a slice along the p^+ -bunch on the slit (see Figure 49) less defocused protons are captured than focused ones. Therefore, the periodical focusing and defocusing of the protons in the bunch leads to a periodic modulation of the summed pixel counts on the image. Moreover, the SC has a threshold below which charge is not recorded, i.e. a limited signal to detection level. This effect needs to be considered when calculating the bunch charge as a function of time (see [86]). For late times along the bunch (in most cases > 211 ps), due to the aperture in the transport line, parts of the OTR-light from the defocused protons are cut off and can no longer be transmitted to the SC slit. For the SC time windows discussed here, however, this effect is negligible.

The envelope of the bunch is increasing up to $\zeta \lesssim -1.5$ cm due to the Gaussian shape of the bunches. The integrated signal of the bunch in the HI event (Figure 48a) is higher than for the bunch in the SSM event (Figure 48b) due to different choices of the SC MCP gain and slit width between the two events (MCP gain = 35, slit width = 20 μm

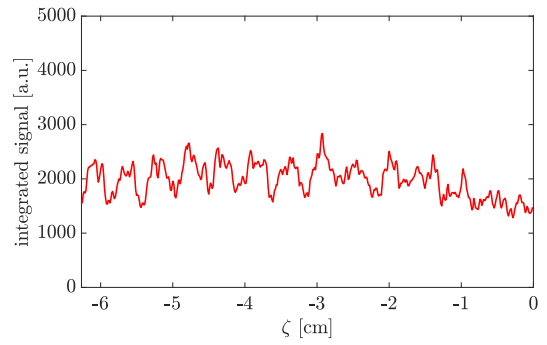
⁵The seed point is estimated by the delay between the high-power laser pulse to the p^+ -bunch extraction from the SPS and the position of the streak window in time, i.e. the start of the streaking with respect to the bunch position. The uncertainty is estimated to be about ± 5 ps in the 211 ps time window. To get a better information on the position of the seed point on the streak image, the marker laser line (see Section 3.1.3) was installed by end of 2017.

⁶In Figure 48, we only present the integrated signals and the centroid displacements for the p^+ -bunches with low bunch population. The procedure for the analysis is identical for the events with high bunch population.

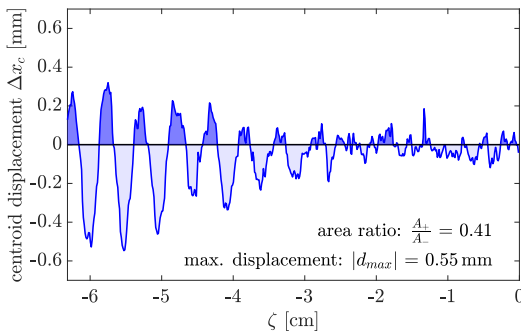
6 Experimental Results – Part 1



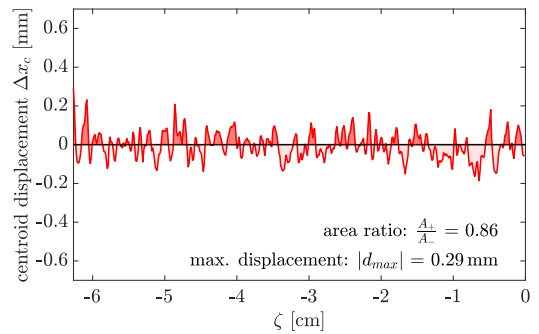
(a) Integrated signal of the HI event shown in Figure 47a



(b) Integrated signal of the SSM event shown in Figure 47b



(c) Bunch centroid displacement of the HI event shown in Figure 47a



(d) Bunch centroid displacement of the SSM event shown in Figure 47b

Figure 48: Integrated signals and bunch centroid displacements for the low bunch population events shown in Figures 47a and 47b. While the integrated signals show a modulation for both the HI and the SSM events, it is a key feature of the HI that bunch centroid is oscillating along the bunch and the plasma as opposed to the SSM event, where the bunch centroid remains on the bunch propagation axis.

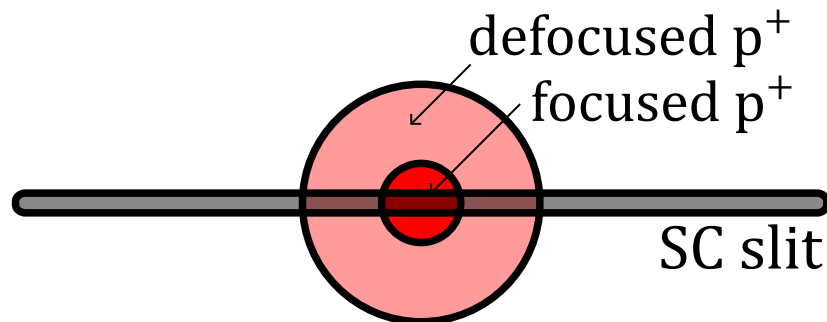


Figure 49: Projection of focused and defocused protons on the SC slit

for the HI events and MCP gain = 30, slit width = 50 μm for the SSM events). This does not effect the centroid calculation.

The bunch centroid of the p^+ -bunch in the HI event (Figure 48c) starts to oscillate periodically with growing amplitude along the bunch and the plasma, as already visible on Figure 47a. This oscillation is a key feature of the HI as opposed to the SM process (Figure 48d) for which it can be clearly seen that the centroid of the bunch remains on the bunch propagation axis ($A_+/A_- = 0.86$) and is mainly fluctuating because of noise in the image. Moreover, the oscillation of the bunch centroid in the HI case is non-axisymmetric with respect to the bunch propagation axis as the amplitude is higher on one side compared to the other. This asymmetry ($A_+/A_- = 0.41$) is already a strong sign for the appearance of the coupling to the SM process (CBH), theoretically explained in Section 2.3.4 and has also been observed in the results of the OSIRIS simulations (see Figures 29a and 29b).

The area ratio A_+/A_- (defined in Section 2.3.4) is illustrated by the coloured areas in Figures 48c and 48d. It is discussed in more detail in a statistical analysis on the symmetry of events with respect to their bunch propagation axes in Section 6.4.2.

Note that the displacement of the bunch centroid in the HI event (see Figure 48c) is smaller than it appears on the SC image (Figure 47a). To visualize this effect, we overlay in Figure 50 the SC image of Figure 47a with the positions of its centroid along the bunch, indicated by white symbols. The amplitude of the oscillation of the beam envelope is about a factor of three higher than the amplitude of the bunch centroid oscillation.

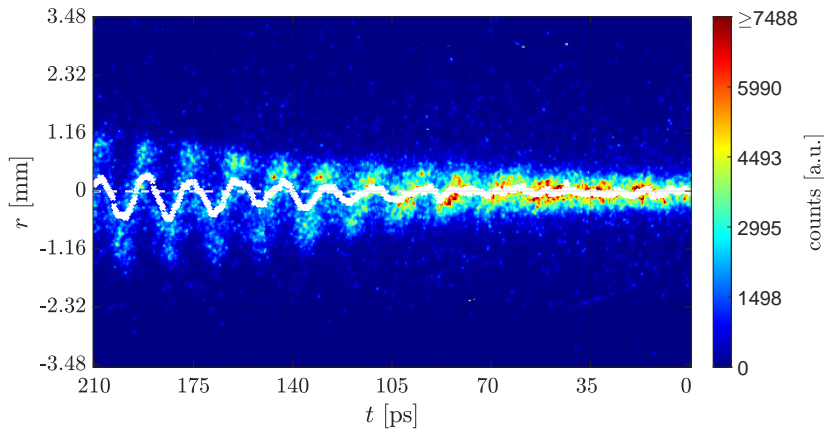


Figure 50: SC image of the HI event shown in Figure 47a and the bunch centroid positions (white symbols).

6.3.2 The Fourier Transform of Streak Camera Data

The Choice of the Streak Camera Time Window

Table VII shows the frequency resolution Δf for different SC time windows used in AWAKE and their maximum theoretically achievable bandwidth f_{max} in case of a sinusoidal signal (see Section 2.3.4). The ability to resolve high frequency signals up to

T_{streak} [ps]	Δf [GHz]	$f_{max,sin}$ [GHz]
73.00	13.70	3506.8
210.63	4.75	1215.4
508.60	1.97	503.3
1134.29	0.88	225.7

Table VII: Frequency resolution Δf and maximum bandwidth for a purely sinusoidal signal $f_{max,ideal}$ at different SC time windows T_{streak} used in AWAKE.

450 GHz with the SC installed in AWAKE in a single measurement was shown by Rieger et al. [67]. Our measurements at low densities ($f_{pe}(0.5 \cdot 10^{14} \text{ cm}^{-3}) = 63.44 \text{ GHz}$) fall well within the detectable limit of the SC.

For the frequencies expected in our experiment, we choose events in the 211 ps and the 509 ps SC time windows. The 211 ps time window has the advantage that the modulation or oscillation of the bunch is directly visible on the image without further analysis. At the chosen plasma density approximately 12–14 periods along the bunch can be acquired on the image. It has, however, the disadvantage that its frequency resolution (see Table VII) is about a factor of 2.4 lower than the frequency resolution of the 509 ps time window, in which ~ 30 oscillations occur within the frame of the SC image. This fact makes it much harder to identify the oscillation of the bunch centroid directly on the SC image and to distinguish it from a modulation of the bunch (as an example see Figure 52 in Section 6.4).

Therefore, for the determination of the oscillation frequency, we analyze images from both time windows, but we restrict ourselves for the illustrative explanations of the HI, the SSM and the fits to the bunch centroid displacements to events in the 211 ps window. The 73 ps window, however, would have an even higher temporal resolution of the modulation than the 211 ps window, but the frequency resolution is substantially worse ($\Delta f = 13.7 \text{ GHz}$) as the number of periods acquired on the image is less.

Discrete Fourier Transform of Hosing and Self-Modulation Events

According to theory (see Section 2.3.3), $f_{osc}(n_{pe})$, the bunch centroid oscillation frequency due to the HI, should be equal to $f_{pe}(n_{pe})$. We now compute the DFT of the two signals shown in Figure 48, the integrated charge along the bunch and the displacement

of the bunch centroid⁷, similarly to what is applied to the centroid oscillation signals obtained from the simulations (see Figures 29a and 29b). Figure 51 gives the resulting power spectra of the DFT in a range between 0–150 GHz for the integrated charge signal (Figures 51a and 51b) and the bunch centroid displacement (Figures 51c and 51d) of the HI and SSM events shown in Figures 47a and 47b, respectively, both obtained at the same n_{Rb} . The signals are zero padded (see Section 2.3.4 and Equation 2.34) to $n = 14$, i.e. to a sample length of 16384 pixels, an appropriate padding length for our purposes. To neglect the low frequency noise in the DFT spectra, which originates from the re-

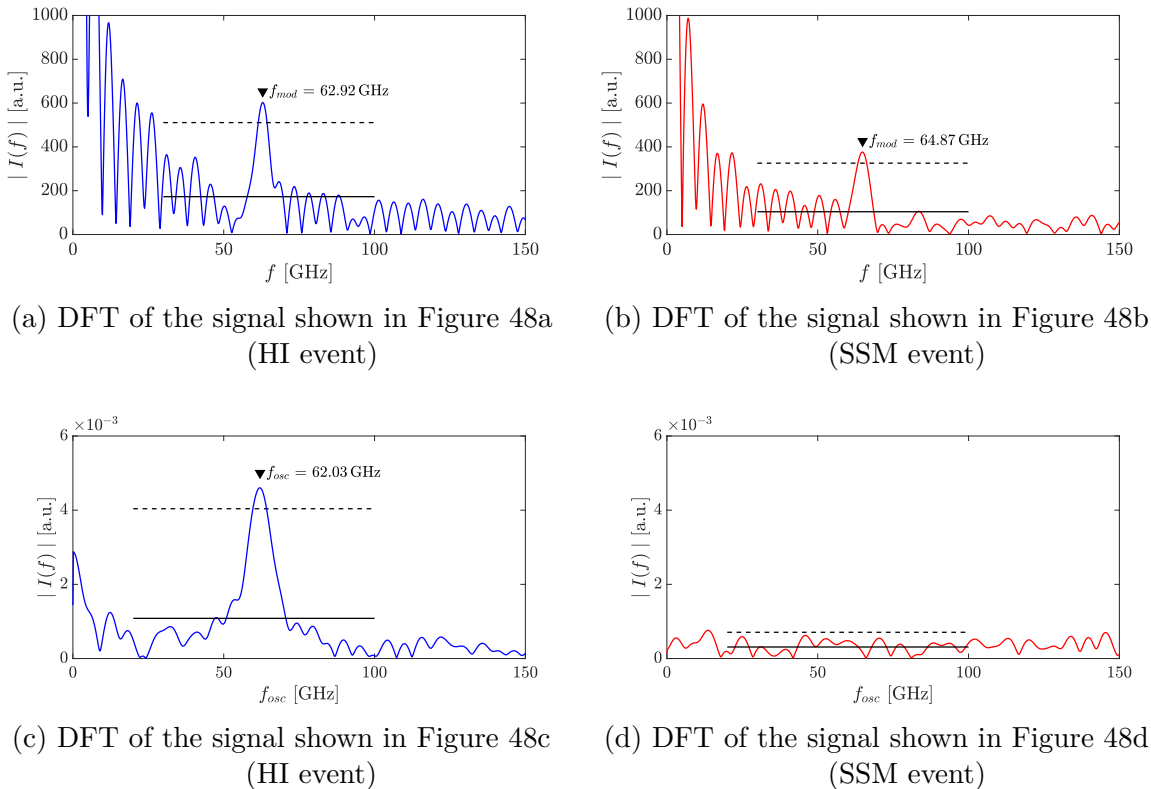


Figure 51: DFTs of the integrated signals and the centroid displacements for the HI and the SSM events shown in Figure 48. The black solid lines give the mean value of $|I(f)|$ in the range of 30–100 GHz for the integrated signals and 20–100 GHz for the centroid displacements. A peak exceeding the black dashed line (2.576σ of $|I(f)|$) is defined as a distinct peak in the DFT power spectrum as it originates with a probability of less than 1% from noise in the spectrum.

maining background and which does not contain information on the frequency of the bunch modulation or centroid oscillation, we determine the frequency of the intensity maximum in the DFT spectra above 30 GHz for the integrated signals and above 20 GHz for the centroids.

⁷The displacement of the centroid is only an one-dimensional signal, so we can only apply an 1D-DFT of the oscillation curve. To apply the same analysis method for the bunch modulation and the centroid oscillation, we use also an 1D-DFT of for the determination of the bunch modulation frequency even though also a 2D-DFT could be applied. The determination of f_{mod} using the 2D-DFT of SC images is topic of [31].

It can be seen that the DFT of the integrated signal shows a clear frequency peak for both the HI event (Figure 51a) and the SSM event (Figure 51b). It has already been shown in [31] that for a fully ionized plasma with density n_{pe} the frequency of the p^+ -bunch modulation due to the SM process, associated with f_{mod} , occurs at the cold e^- -plasma frequency, i.e. $f_{mod}(n_{pe}) = f_{pe}(n_{pe})$.

The DFT of the centroid position along the bunch shows a distinctly defined peak for the HI event (Figure 51c) at a centroid oscillation frequency f_{osc} , whereas there is no apparent peak in the frequency spectrum of the self-modulated bunch (Figure 51d) as the bunch is symmetrically focused and defocused with respect to its propagation axis. It shows no features of the HI (see Figure 47d).

Hence, the plots from Figure 51 show that calculating the DFT of the bunch centroid position is not only resolving the centroid oscillation frequency, but also allows for a simple numerical way to distinguish between an HI and an SSM event. Only if there is a clear peak in the DFT spectrum in the signal of the bunch centroid position, the bunch is oscillating along its propagation axis. Hence, when computing the DFT of the bunch centroids, we identify the highest peak in the frequency spectrum in the range above 30 GHz for the integrated signals and above 20 GHz for the centroids. Only if its height exceeds at least 2.576σ of the mean value of the spectrum in this range (see dashed lines in Figure 51), i.e. the probability that the peak originates from noise is less than 1%, we define the peak as being significantly above background and the event as an HI event. In Section 6.4, we discuss in more detail the bunch centroid oscillation frequency and analyze based on a statistical analysis of HI events, whether we can also state from the experimental data that f_{osc} is equal to f_{pe} .

6.4 Analysis of Hosing Instability Events with Seed of the Self-Modulation Process

So far, we showed a single pair of HI and SSM events as an example to introduce the basic concept of the analysis. For the discussion of the appearance of the HI, where the SM process is seeded 100 ps ahead of the p^+ -bunch centre, we analyze two different data sets. The first one consists of 29 consecutive events at low p^+ -bunch population and 44 events⁸ at high bunch population, all in the 211 ps time window. The second one consists of 97 events (34 consecutive events at low, 48 consecutive events at medium and 15 consecutive events at high p^+ -bunch population) in the 509 ps time window and is only analyzed for determination of the bunch centroid oscillation frequency due to the reasons explained in Section 6.3.1. An example of a SC image from this data set is presented in Figure 52. The experimental conditions are kept unchanged in and between all data sets, only the settings of the SC are varied between different data sets: For the low bunch population events in the 211 ps window, the MCP gain on the SC is set to 35 and the chosen slit width is 20 μm . For high bunch population events, the MCP gain on the SC is set to 30, the chosen slit width is 50 μm . All events in the 509 ps time window

⁸12 and 32 consecutive events

6.4 Analysis of Hosing Instability Events with Seed of the Self-Modulation Process

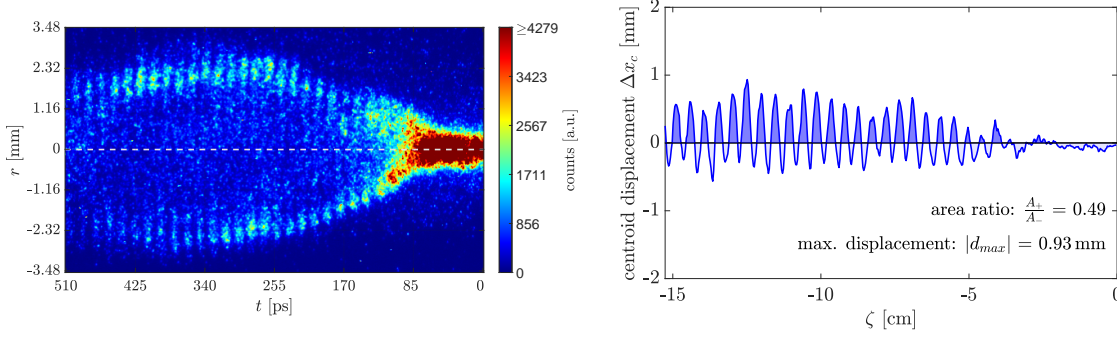


Figure 52: SC image (left-hand side) and bunch centroid (right-hand side) of an HI event ($N_b = 1.78 \cdot 10^{11} p^+$) from the data set acquired in the 509 ps SC time window.

are gathered with MCP gain 30 and slit with 20. For all events, the bunch rotation mechanism is enabled.

In order to select the events in the data sets where the HI develops, we perform DFTs of the bunch centroids and select all events where a distinct peak in the power spectrum according to the method described in Section 6.3.2 can be determined. All these events are akin to the events shown in Figures 47 and 52. The experimental parameters of the selected events are listed in Table VIII. The events, for which no growth of the HI is

211 ps SC time window:

bunch population	low	high
events in data set	29	44
events with HI detected	28 (96.6 %)	43 (97.7 %)
bunch population N_b [$10^{11} p^+$]	1.06 ± 0.05	2.80 ± 0.12
Rb vapour density n_{Rb} [10^{14}cm^{-3}]	0.504 ± 0.003	0.507 ± 0.005
Pulse energy E_{las} [mJ]	257 ± 6	258 ± 5

509 ps SC time window:

bunch population	low	medium	high
events in data set	34	48	15
events with HI detected	34 (100 %)	48 (100 %)	15 (100 %)
bunch population N_b [$10^{11} p^+$]	1.07 ± 0.05	1.79 ± 0.14	2.77 ± 0.16
Rb vapour density n_{Rb} [10^{14}cm^{-3}]	0.504 ± 0.003	0.504 ± 0.003	0.506 ± 0.003
Pulse energy E_{las} [mJ]	258 ± 5	248 ± 5	256 ± 6

Table VIII: Overview of the experimental parameters of the data sets for the HI characterisation with seed of the SM process

detected, could in principle be events, where the CBH develops in the plane perpendicular to the slit so that it only appears as pure SSM event on the SC images (similarly to the bunch charge distribution in the plane perpendicular to the HI seed in the simulation,

Figure 26). The symmetry of the time-integrated radial bunch profiles, however, supports the assumption that only the SM process grows in these events.

6.4.1 Dependence of the Hosing Instability Growth on the Bunch Population

For all events from the data sets in the 211 ps SC time window, we calculate the position of the centroid along the bunch similarly to Figure 48c and determine its maximum deviation from the bunch propagation axis. For this, we neglect whether the maximum centroid displacement is above or below the plasma off trajectory, i.e. we only take the absolute value $|x_{c,max}|$. According to Equation 2.27, $x_{c,max}$ correlates with the p^+ -bunch population. For the same initial seed level δ_c (and all other parameters equal, including the noise level), the maximum deviation from the plasma off trajectory due to the HI at $\zeta = -6.2$ cm (i.e. at the end of the 211 ps SC time window) should be about three times higher for bunches with high population than for bunches with low population (see Figure 3b).

This expectation is supported by our experimental results presented in Table IX and by the histograms in Figure 53, which show that the displacement of the bunch centroid from the plasma off trajectory caused by the growth of the HI is about 2.3 times larger for bunches with high population than for the ones with lower population. The maxi-

bunch population	low	high
event with max. value for $ x_{c,max} $ [mm]	0.60	1.68
event with min. value for $ x_{c,max} $ [mm]	0.35	0.67
$ \bar{x}_{c,max} \pm \Delta \bar{x}_{c,max} $ [mm]	0.47 ± 0.06	1.09 ± 0.23

Table IX: Maximum displacements $|x_{c,max}|$ of the bunch centroid from the plasma off trajectory for the data sets with low and high p^+ -bunch population in the 211 ps SC time window.

mum measured $|x_{c,max}|$ out of all events is 1.68 mm, whereas it is only 0.67 mm for the events with low bunch population resulting in an about 2.8 times higher $|x_{c,max}|$ for the high bunch population event⁹. Moreover, the smallest value measured for $|x_{c,max}|$ in the data set of high bunch population events is about the same as the highest $|x_{c,max}|$ from the low bunch population events. Taking all this into account, these results confirm the theoretical expectation of the dependence of the number of exponentiations N_{HI} on N_b (see Equation 2.28), $N_{HI} \propto N_b^{1/3}$.

⁹In this context, it is suitable to compare the ratio of the highest values for $|x_{c,max}|$ to theory as the model in Figure 3b does not take into account the saturation of the HI growth.

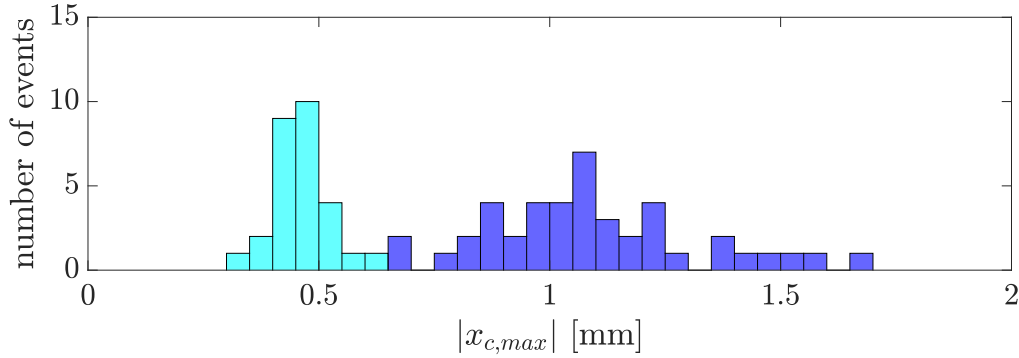


Figure 53: Histogram of the maximum displacements $|x_{c,max}|$ of the bunch centroid from the plasma off trajectory for the data sets with low-bunch population (cyan) and high p^+ -bunch population (dark blue) in the 211 ps SC time window.

6.4.2 Symmetry of the Events with Respect to the Bunch Propagation Axis

As described in Section 6.3, in case there is a coupling between the HI and the SM process, the centroids of a p^+ -bunch are not oscillating symmetrically with respect to the bunch propagation axis. Therefore, we try to quantify this effect for the events in the 211 ps SC time window by calculating the areas above and below the bunch propagation axis, i.e. the area ratio A_+/A_- and compare the results to the predictions by the PIC simulations (inset of Figure 29a, left-hand side). As mentioned in Section 2.3.4, the area ratio is defined in a way that it neglects whether the event is more asymmetric up- or downwards with respect to the center line, i.e. for area ratios larger than one, we take the inverse value (A_-/A_+) so that $A_+/A_- \in [0, 1]$. Table X and the histograms in

bunch population	low	high
A_+/A_- in the most symmetric event	0.988	0.995
A_+/A_- in the most asymmetric event	0.067	0.014
average A_+/A_-	0.487 ± 0.268	0.506 ± 0.241

Table X: Area ratios A_+/A_- determined from the centroid displacements for the data sets with low and high p^+ -bunch population the in 211 ps SC time window.

Figure 54 give an overview of A_+/A_- for high and low p^+ -bunch populations. The data set contains a range of almost symmetric events ($A_+/A_- = 0.995$) to very asymmetric events ($A_+/A_- = 0.014$). The average area ratio is about 0.50 ± 0.25 regardless of the bunch population. This means that on average about two third of the bunch charge captured on the SC image is displaced above the center axis and one third below (or vice versa).

These experimental observations give again strong evidence for the coupling of the HI to the growth of the SSM, i.e. for the appearance of CBH, as explained in Section 2.3.4. However, it important to note that, contrary to the simulation, the strength of the coupling cannot be directly determined from the area ratio of an event as in general

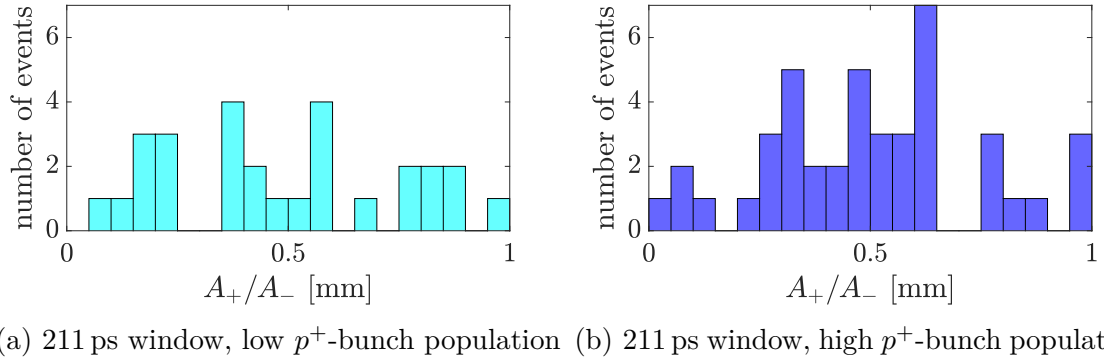


Figure 54: Histograms of the maximum displacements A_+/A_- of the bunch centroid from the plasma off trajectory for the data sets with low and high p^+ -bunch population in the 211 ps SC time window.

the plane of the SC slit does not coincide with the plane in which the HI grows (see Sections 5.3.3 and 6.5). According to the results in Section 5.3.3, however, the coupling constant ε is independent from the angle α between the planes of the SC slit and the HI growth. Therefore, in Section 6.6, we determine the strength of the coupling from the fit parameter ε in the fits of the bunch centroid displacement (Equation 2.30) to the experimental data.

6.4.3 Bunch Centroid Oscillation Frequency

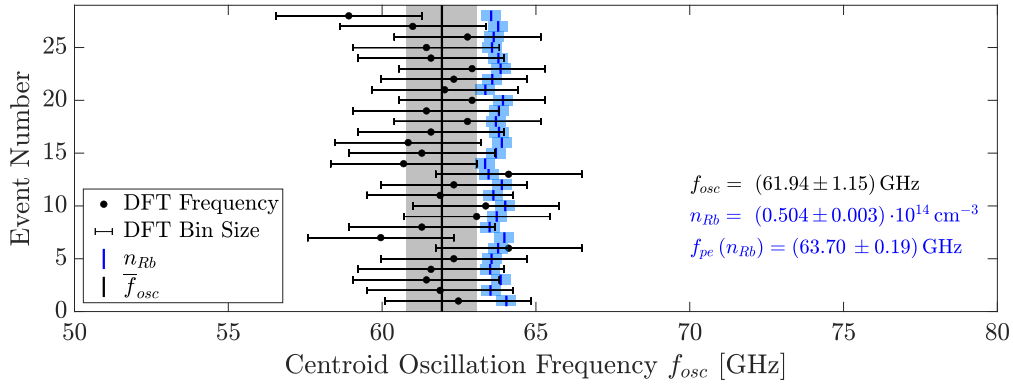
To determine the bunch centroid oscillation frequency at a certain n_{pe} , we compute the DFT of the bunch centroid modulation (similarly to Figure 51c) for all events introduced above, i.e. all events acquired in both the 211 ps and the 509 ps SC time window.

The peak frequencies of the DFT are plotted in Figure 55. Note, the bars at the data points correspond to the frequency resolution given by the bin discretisation of the DFT. For each event, the corresponding plasma frequencies inferred from the Rb vapour density measurements are shown as blue lines. According to [63], the uncertainty of the vapour measurement is about 0.5% (light-blue error bars). The solid black line and its gray uncertainty region indicate the average measured bunch centroid oscillation frequency and its error of the mean.

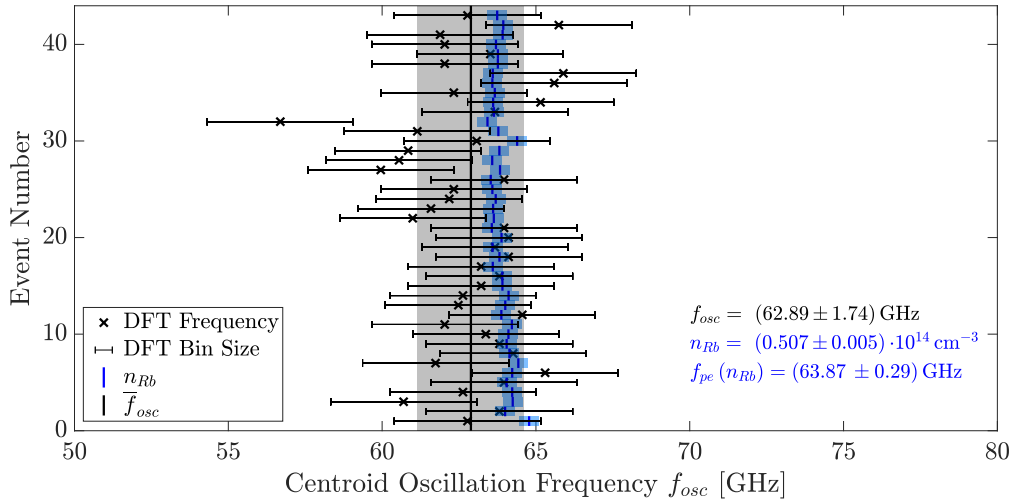
In the 211 ps time window, for both p^+ -bunch populations, the oscillation frequency of the bunch centroid is close to the plasma frequency at n_{Rb} , but slightly lower. For the low p^+ -bunch population events (Figure 55a), the mean measured frequency is (61.9 ± 1.4) GHz and hence about 1.8 GHz less than expected from the measured Rb vapour density. This frequency corresponds to a period of (16.2 ± 0.4) ps. For the high bunch population data set (Figure 55b), f_{osc} is measured to be (62.9 ± 1.7) GHz and differs by only 0.85 GHz from f_{pe} , i.e. f_{osc} is consistent with f_{pe} . The corresponding period is (15.9 ± 0.4) ps. The error of the mean is larger for the high bunch population events than for the events with lower one, even though about 60% more events are analysed there. Therefore, f_{pe} lies within the range of measured frequencies for the events with

6.4 Analysis of Hosing Instability Events with Seed of the Self-Modulation Process

high bunch population, whereas it is slightly outside for the events with lower one. The DFT of the events in the 509 ps time window gives oscillation frequencies of (63.3 ± 1.1) GHz, (63.8 ± 0.9) GHz and (63.4 ± 0.6) GHz for the low, medium and high p^+ -bunch population data sets, respectively (see Figures 55c–55e). This corresponds to periods of (15.8 ± 0.3) ps, (15.7 ± 0.2) ps and (15.8 ± 0.2) ps. Due to the 2.4 times smaller DFT bin size in the 509 ps time window, as expected, the error of the mean is smaller than for the events in the 211 ps time window.

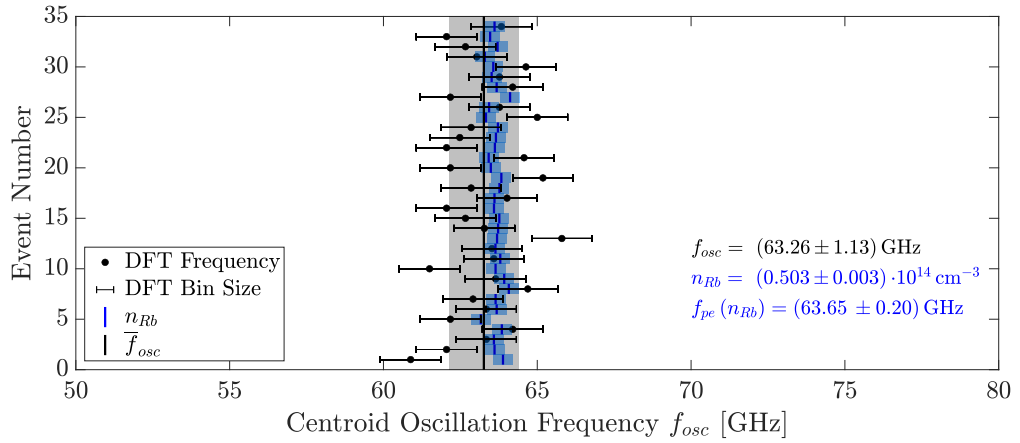


(a) 211 ps window, low p^+ -bunch population

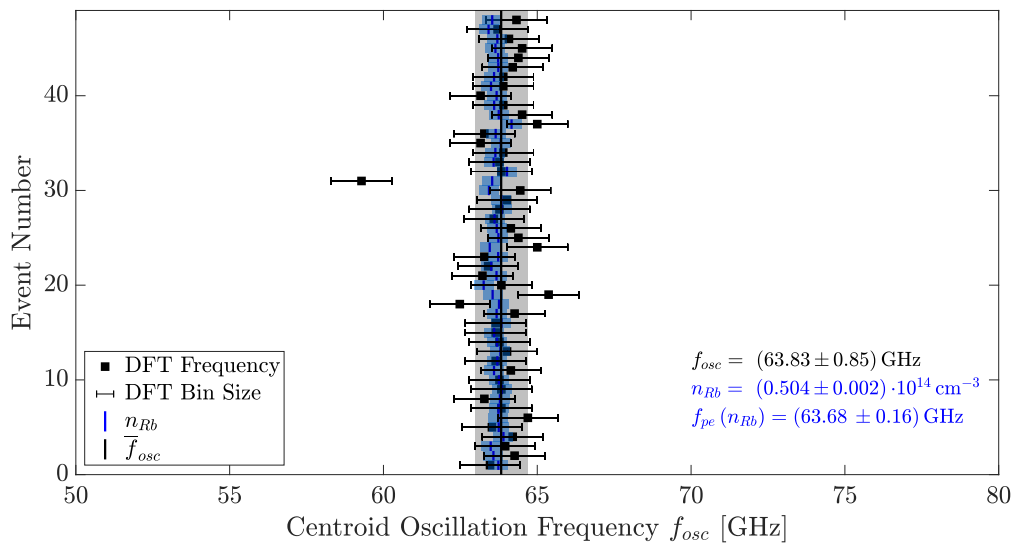


(b) 211 ps window, high p^+ -bunch population

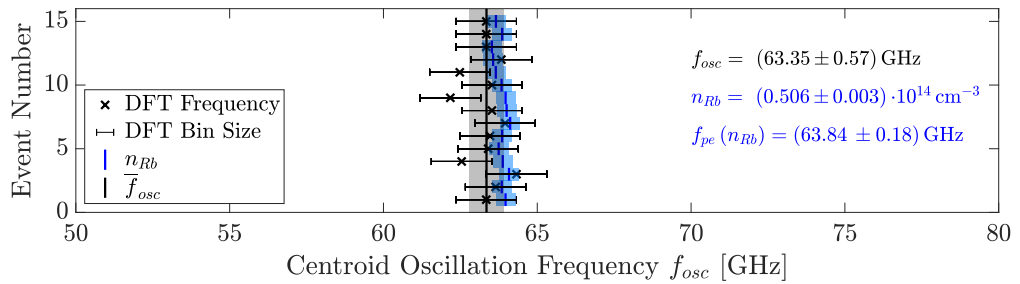
6 Experimental Results – Part 1



(c) 509 ps window, low p^+ -bunch population



(d) 509 ps window, medium p^+ -bunch population



(e) 509 ps window, high p^+ -bunch population

Figure 55: DFT of the bunch centroid displacements for the different data sets.

The black bars indicate the bin size of the DFT bin discretisation. The black solid line shows the average measured centroid modulation frequency and its uncertainty (gray). The corresponding plasma frequencies at measured neutral Rb densities n_{Rb} are depicted in blue (incl. their uncertainty of 0.5%).

As the measured Rb vapour density inside the vapour source is slightly varying from event to event, for a better comparability on the event-to-event basis, we normalize the centroid oscillation frequency f_{osc} to the plasma frequency $f_{pe}(n_{Rb})$ at the measured Rb vapour density n_{Rb} .

The events shown in Figure 55a and 55b are combined in Figure 56a and the normalized oscillation frequency $f_{osc}/f_{pe}(n_{Rb})$ for the two data sets gives $f_{osc}/f_{pe}(n_{Rb}) = 0.980 \pm 0.025$. The normalized DFT of the 97 further bunch centroid displacements calculated from the events in the 509 ps time window are shown in Figure 56b. Here, we can observe a similar result than in the 211 ps window. The averaged bunch centroid oscillation frequencies give $f_{osc}(n_{Rb})/f_{pe}(n_{Rb}) = 0.998 \pm 0.015$.

For both data sets, considering the uncertainty of measurements, the normalized oscillation frequencies confirm the theoretical expectation

$$f_{osc}(n_{Rb}) = f_{pe}(n_{Rb}) \quad (6.4)$$

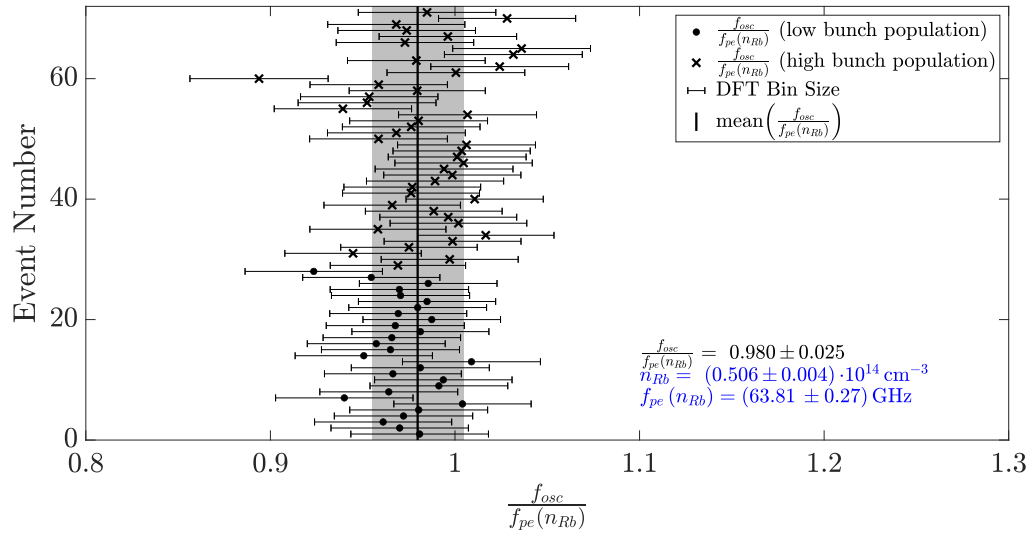
also observed in the PIC simulations.

It has been shown in [31] over the broad range of $1.3 \cdot 10^{14} \text{ cm}^{-3} \leq n_{Rb} \leq 10.5 \cdot 10^{14} \text{ cm}^{-3}$ that the frequency of the transverse self-modulation f_{mod} of a relativistic p^+ -bunch propagating through a fully ionized plasma is equal to the plasma frequency, i.e. $f_{mod}(n_{Rb}) = f_{pe}(n_{Rb})$. Their resolution limit for the frequency determination is 4 GHz (given by half of the 3 dB bandwidth of the interpolation kernel function).

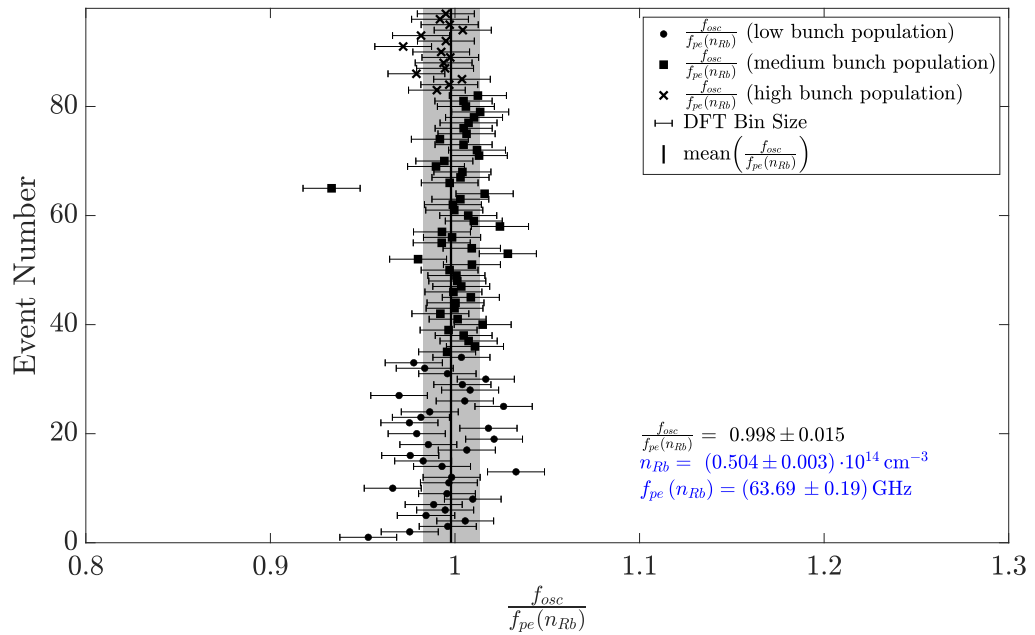
As already mentioned, they determine the bunch modulation frequency by a 2D-DFT of the SC data and use a wide range of different Rb densities, while we only Fourier transform the one-dimensional signal of the bunch centroid oscillation at a fixed Rb vapour density. Hence, the precision of the results in our DFT calculations is smaller. This might in general lead to a higher uncertainty in the frequency determination, especially for events where the plane of the HI growth is poorly resolved due to the SC slit orientation or for events where the growth of the SSM clearly dominates over the growth of the HI.

We observe a small deviation between the bunch oscillation frequencies from events gathered in the 211 ps ($f_{osc} = 0.980 f_{pe}$) and the 509 ps ($f_{mod} = 0.998 f_{pe}$) SC time windows, even though the theoretically expected result $f_{osc} = f_{pe}$ lies for both cases still within the uncertainty margin. This is not only caused by the lower frequency resolution in the 211 ps time window but also by a second effect: The SC images in both time windows include the seed point from where the instability and thus the oscillation starts to develop. In this regime the oscillation frequency is lower than later in the bunch. This effect has a larger impact on the determination of f_{osc} within a shorter SC time window than within a longer one and is sufficient to explain the observed deviation. The effect was also observed in the analysis of the bunch modulation frequency f_{mod} of SC images, which cover the bunch in a range close to the seed point of the SM process [87].

There is no other physical explanation, like e.g. a non fully ionized plasma or a phase drift due to the relativistic motion of the plasma electrons along the bunch, which would cause the centroid to oscillate with lower frequency ($f_{osc} = 0.980 f_{pe}$), while f_{mod} is nearly equal to the plasma frequency ($f_{mod} = 0.998 f_{pe}$) measured later in the bunch excluding



(a) centroid oscillation frequencies of events gathered in the 211 ps SC time window



(b) centroid oscillation frequencies of events gathered in the 509 ps SC time window

Figure 56: Normalized centroid oscillation frequencies for the events shown in Figure 55. The black solid line shows the average measured ratio $f_{osc}/f_{pe}(n_{Rb})$ and its uncertainty (gray).

the first modulation periods. Moreover, also the simulation results shown in Chapter 5 strongly support an equality between the bunch oscillation and the plasma frequency at a certain n_{pe} .

We thus conclude this section with the key result of this measurement

$$\boxed{f_{osc}(n_{Rb}) = f_{mod}(n_{Rb}) = f_{pe}(n_{Rb})}. \quad (6.5)$$

6.5 Radial Diagnostic of the Hosing Instability

The Imaging Stations IS1 and IS2 (see Section 3.1.6) allow for an analysis of the time-integrated radial charge distribution of the p^+ -bunch. When the p^+ -bunch propagates through the Chromox screen of an IS, the scintillation light emitted by the screen is detected by CMOS cameras. Between IS1 (~ 2 m from the plasma exit) and IS2 (~ 10 m from the plasma exit), the p^+ -bunch propagates ballistically over a distance of approximately 8 m through vacuum. Protons, which are radially displaced from the bunch propagation axis either due to the defocusing wakefields inside the plasma or due to an oscillation of the bunch centroid are further diverging during this ballistic propagation between the two IS. A detailed analysis of this phenomenon regarding the SSM is subject of [88]. In the case of an HI event, the specific plane, in which the oscillation takes place, should then appear as an elongation of the charge distribution on the time-integrated radial bunch profiles both on IS1 and IS2.

The images of the CMOS cameras have a 12-bit depth and a size of 1200×1600 pixels. The Chromox screens in the IS have an imprinted scale so that a conversion from pixels to a length scale is possible. For IS1, the conversion factor is given by 0.0333 mm/pixel, for IS2 by 0.0396 mm/pixel [88]. In order to crop the images to their region of interest and to equalize the length scales of both images, they are centered to the average p^+ -bunch trajectory of the corresponding plasma off events akin to the procedure applied on the SC images. The cropped images of IS1 have eventually a size of 400×400 pixels, the images of IS2 a size of 330×330 pixels.¹⁰

In Figure 57a, the time integrated radial bunch profile of a plasma off event on IS1 (left-hand side) and IS2 (right-hand side) can be seen. As the bunch is propagating entirely through Rb vapour (no plasma), the profiles are narrow as no protons are defocused or displaced by plasma wakefields. The increase of the bunch radius between IS1 and IS2 is caused by the bunch diverging from its waist due to its emittance and by the absence of focusing optics in the p^+ -beamline in between the two IS, i.e. by the purely ballistic propagation over a distance of ~ 8 m. It is important to mention that the images are gathered above the saturation level on the cameras in order to be able to resolve weak features in the radial charge distribution near the bunch edges.

Figure 57b shows the time-integrated radial p^+ -bunch profiles on both IS of the HI event

¹⁰Note, at the time when the images were gathered only the core cameras of the imaging stations were installed (see Section 3.1.6).

with low bunch population shown in Figure 47a, Figure 57c the profiles of the event with high bunch population shown in Figure 47c. Figure 57d visualizes as a comparison the profile of the high-bunch population SSM event (Figure 47b).

It can be understood from the bunch shapes on the two IS that the radial momentum of the protons defocused by the SM process leads to a broadening of the entire time-integrated bunch distribution. It has been shown by [30] that for a p^+ -bunch with seeded SM process the protons are defocused radially symmetric and therefore the time-integrated radial p^+ -bunch distribution is growing symmetrically from the plasma exit to IS1 and IS2.

For the HI events, however, the charge distribution appears oval and elongated along one axis. The presence of a privileged plane (marked by a white line in Figures 57b and 57c) gives strong evidence for the beam hosing along this axis. The orientation of this privileged HI plane remains almost constant between IS1 and IS2 in both events. As the HI process is an instability, the orientation of the HI plane should be defined by the initial noise and therefore change from event to event (see Section 6.5.1).

To determine the orientation of this privileged plane, i.e. of the white lines in Figures 57b and 57c and to define the eccentricity \mathcal{E} of a profile, we apply the same algorithm already applied to the radial profiles of the simulated bunches described in Section 5.3.4. From a comparison to SM events (akin to the event shown in Figure 57d), we see that events with SM have usually eccentricities below $\mathcal{E} \sim 0.5$, events with growth of the HI usually above $\mathcal{E} \sim 0.5$.

Moreover, we observe that radially defocused protons get on average further displaced from the bunch centre in the events with high bunch population than for events with low bunch population, consistent with plasma wakefield theory and as experimentally observed in [30, 31].

On IS2 in Figure 57c, the asymmetric charge distribution along the HI plane (i.e. a higher charge density on the lower right-hand side of the profile than on the upper left-hand side) reveals the asymmetry of the centroid modulation with respect to the bunch propagation axis and is another indication for CBH. In the experiment, however, the effect appears to be less distinct when compared to the simulation results.

We discuss the orientation of the planes in which the HI grows in more detail in the following section and in Chapter 7 when we analyze the growth of the HI without seed of the SM process.

6.5.1 Determination of the Plane of the Hosing Instability Growth

Now, we determine the privileged planes for all events from the data sets in the 211 ps SC time window using the method described above. In Figure 58 the orientation of these privileged planes is plotted at IS1 for all 29 events with low bunch population and 44 events with high bunch population (Figures 58a and 58b).

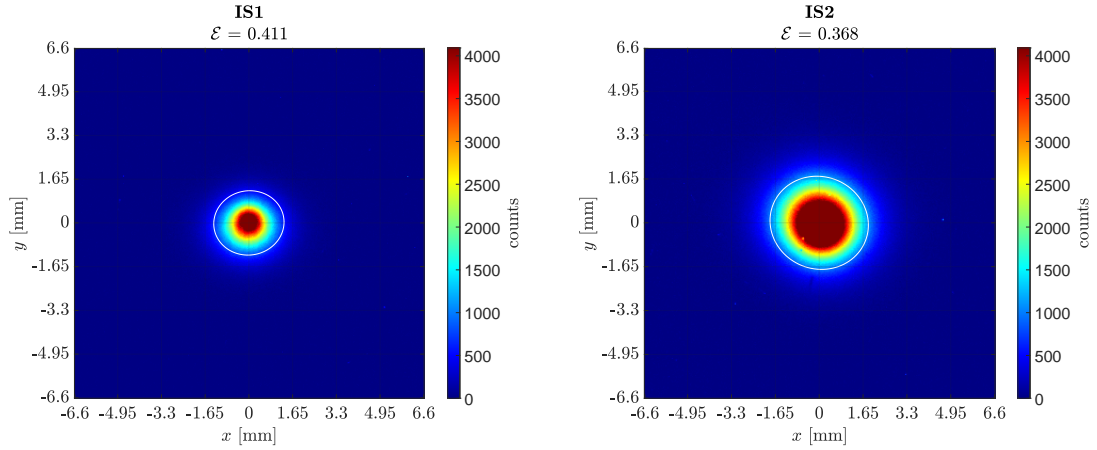
It can be observed that there is no preferred direction in the orientation of the HI planes on an event-to-event basis. This is a strong indication that the HI is growing from a random noise in the bunch structure and that there is no sign for a systematic initial

seed in the delivered SPS p^+ -bunches or from a misalignment between the p^+ -bunch and the high-power laser pulse creating the plasma column (as introduced in Section 7.3). Moreover, we would like to emphasise that even though there is a jitter in the alignment of the ionizing laser pulse with respect to the p^+ -bunch trajectory, there is no correlation between the direction of the alignment jitter and the orientation of the HI plane (as there is in the events discussed in Section 7.3). Moreover, the series of pure SSM events discussed in [30, 31] are gathered with a similar laser alignment jitter and do not show any signs for a growth of the HI.

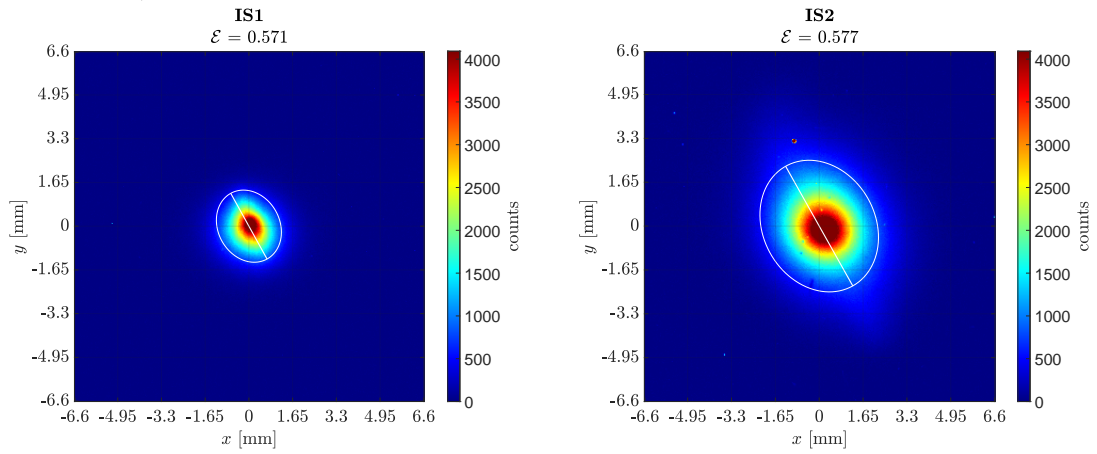
The fact that the randomly distributed HI planes can be easily detected from the time-integrated radial bunch profiles gives also evidence that the SSM events observed in the experiment are actual SSM events and that on SC images we do not mainly record the projections along the SM plane of CBH events.

In Section 7.3, we discuss in more detail the effects of a deliberate laser misalignment on the orientation of the HI plane.

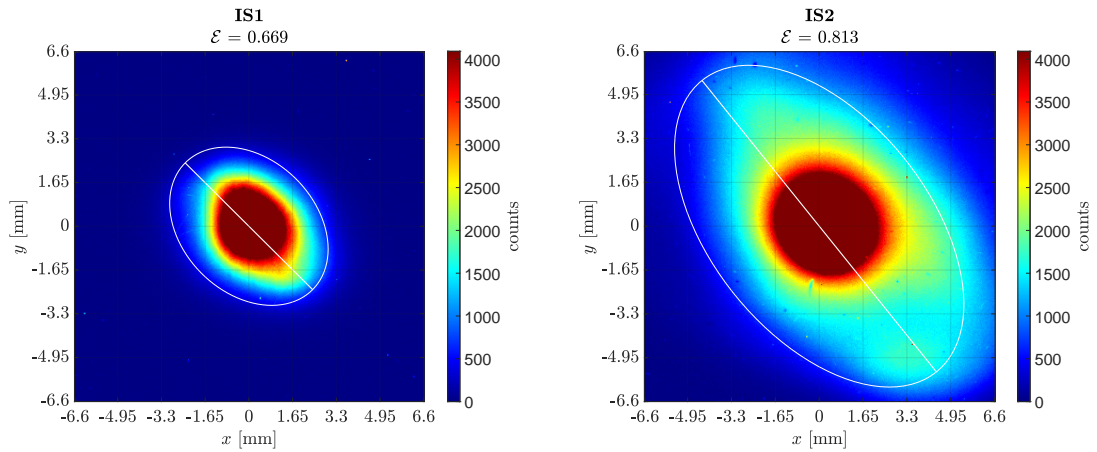
6 Experimental Results – Part 1



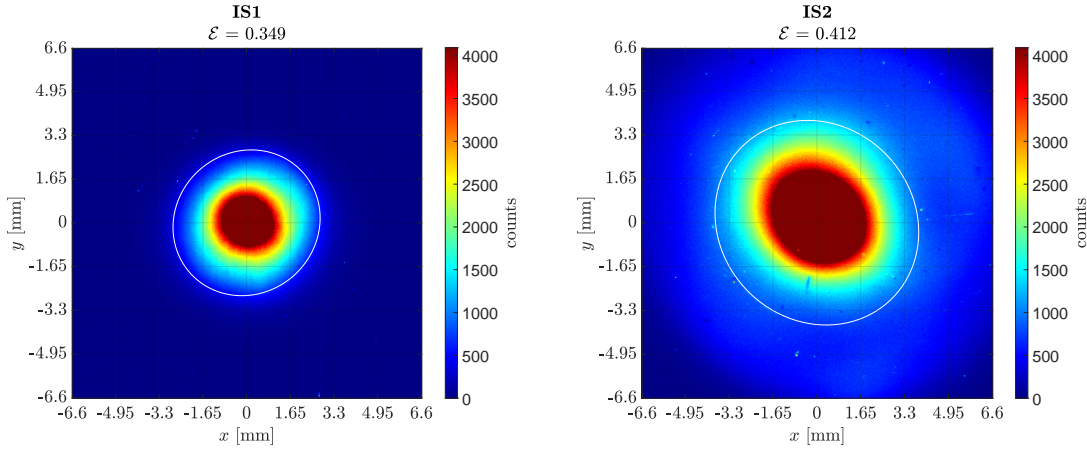
(a) Time-integrated radial bunch profile of a p^+ -bunch propagating through Rb vapour (plasma off event)



(b) Time-integrated radial bunch profile of the HI event with low p^+ -bunch population shown in Figure 47a

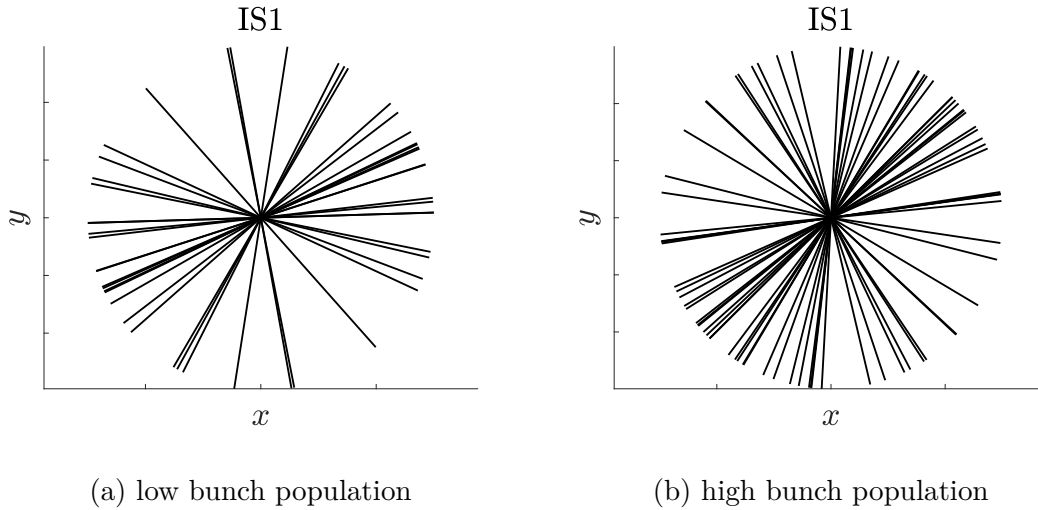


(c) Time-integrated radial bunch profile of the HI event with high p^+ -bunch population shown in Figure 47c.



(d) Time-integrated radial bunch profile of the SSM event with high p^+ -bunch population shown in Figure 47d.

Figure 57: Time-integrated radial p^+ -bunch profiles at IS1 (left-hand side) and IS2 (right-hand side) of a plasma off event (a), an HI event at low bunch population (b), an HI event at high bunch population (c) and an SSM event at high bunch population (d). The white lines (major axes of the ellipses) in (b) and (c) indicate the plane in which the HI is growing. For a better comparability, the colour scales and the filter settings are equal for all events on IS1 and for all events on IS2 (but differ between IS1 and IS2).



(a) low bunch population

(b) high bunch population

Figure 58: Orientation of the plane of the HI growth for the events gathered in the 211 ps SC time window with low (a) and high p^+ -bunch population (b).

6.6 Fit of the Bunch Centroid Displacement Equation to the Experimental Data

In the next part of our analysis, we fit the equation of the centroid position (Equation 2.30) to the experimental data in the same way as it is done in Section 5.3.2 to the centroids of the simulation data.

We perform again three different fits with the trust-region algorithm. Contrary to the simulation, the initial seed level is an unknown parameter in the experiment. Therefore, we use δ_c as independent fit parameter in all fits. The first of the three fits is then performed with two independent fit parameters (δ_c, ζ_0), i.e. the equation describes only a symmetric centroid oscillation and no coupling between the growth of the HI and the SM process. The second fit with three independent fit parameters ($\delta_c, \zeta_0, \varepsilon$) then considers the possibility of a coupling, whereas the third fit with four independent fit parameters ($\delta_c, \zeta_0, \varepsilon, p$) aims to check the power law in N_{HI} also for the experimental results. An overview of all fit parameters including the start points as well as the upper and lower limits for the trust regions are given in Table XI. As already mentioned in Section 6.3,

fit parameter	δ_c	ζ_0	ε	p
start point	0.01	$\zeta(t_{seed})$	0	0.333
upper limit	—	—	—	1
lower limit	—	0	—	0

Table XI: Initial parameters for the fit of Equation 2.27 to the experimentally determined centroid oscillation: Start points, upper and lower limits for the trust regions.

the seed points t_{seed} for the HI events with low and high bunch population are different. For the low bunch population events, it is approximately around $t \sim 5$ ps, for the high bunch population events around ~ 25 – 40 ps. Thus, we estimate the seed point from the SC images and remove the corresponding number of data points before the seed point from the centroid distribution used for the fit.

In each subfigure of Figure 59, the estimated seed points are marked by a red vertical line. In the fits, we then take $\zeta(t_{seed})$ as initial parameter for the start point of ζ_0 . This procedure is necessary to determine the right start point within one period of the centroid oscillation.

It is important to mention that k_{pe} is not an independent fit parameter. In general, there are two different ways to determine k_{pe} in the experiment: From the DFT of the centroid oscillation or from the measurement of the neutral Rb vapour density (see Section 6.4.3). The first one uses the result $f_{osc}(n_{pe}) = f_{pe}(n_{pe})$, i.e. k_{pe} is determined from the bunch centroid on the SC image. For the second method, we assume fully ionization of the plasma, i.e. $n_{Rb} = n_{pe}$. This method has the advantage that k_{pe} is determined from an independent measurement. Moreover, the uncertainty of the density measurement is less than the uncertainty introduced by the DFT bin discretisation. Therefore, we select the

second method for the determination of k_{pe} in this Chapter.¹¹ We checked based on a few events that the choice of the method to determining k_{pe} does not change the conclusions.

We begin with the symmetric centroid oscillation without coupling of the HI to the growth of the SM process ($\varepsilon = 0$) by fitting only two independent fit parameters: The amplitude of the oscillation δ_c , which corresponds to the initial strength of the HI seed due to noise in the bunch or the plasma and the seed position along the bunch ζ_0 , which is in general equal to the position of the ionizing laser pulse. Figure 59a shows as examples the result of the fits to the centroids from the events with low and high bunch population presented in Figures 47a and 47c.

As the fit function is axi-symmetric, it cannot reflect the asymmetry in the bunch centroid modulation, but the fits match well the periodicity of the oscillation. The goodness of the fit is about $R^2 = 0.7$ for both events.

Now, we add the coupling term in Equation 2.30 to our fit function with the additional free fit parameter ε . The result of these fits with three parameters is given in Figure 59b. The fits are now able to take into account the asymmetry of the bunch centroid oscillation due to the coupling of the HI to the SM of the bunch. The fits show a much better agreement with the data than the fits with only two fit parameters ($R^2 = 0.84$ and $R^2 = 0.77$ for the low and high bunch population event, respectively). The value for $|\varepsilon| \sim 0.3 - 0.5$ shows that the event is clearly asymmetric and proves the coupling of the SM process to the HI in experiment.

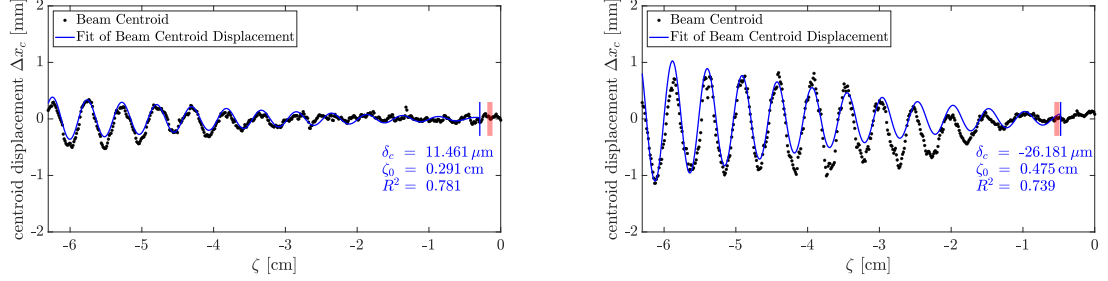
To check the power law for $(k_{pe}^3 \zeta z^2)^{1/3}$ in N_{HI} (Equation 2.28), we perform a third fit, where we introduce additionally the exponent p as a fourth fit parameter. The fits are presented in Figure 59c and deviate only slightly from the theoretically expected result $p = 1/3$. Due to the introduction of an additional fit parameter, the *GoF* is increasing to $R^2 = 0.85$ and $R^2 = 0.81$ for the low and high bunch population event, respectively. A fit value $p < 1/3$ can be interpreted as an indication that at least over some range late in ζ the growth of the HI has reached its saturation.

Note that for the derivation of Equation 2.27 (and thus Equation 2.30) a number of prerequisites stated in Section 2.3.3 are assumed. One of these assumptions of the model is that the centroid oscillation is small when compared to the bunch radius, i.e. $x_c \ll \sigma_r$, which is obviously no longer valid for the events shown in this chapter. Nevertheless, the results show that some of the main characteristics of the linear regime persist in the non-linear regime.

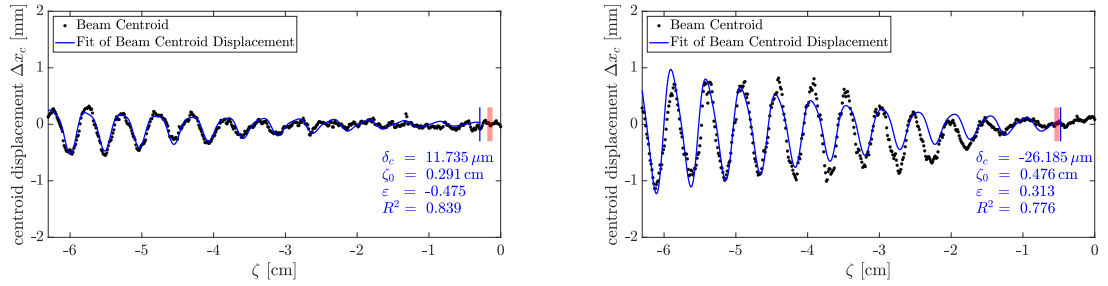
The same kind of fits are now performed for all events with low and high p^+ -bunch population in the data set of the 211 ps SC time window. The averaged fit parameters are summed up in Table XII. As for some parameters the averaged values alone are not very meaningful, we give not only the standard deviations but show also an example event for low and high values of the fit parameters ε and p in Figures 60 and 61.

¹¹To determine k_{pe} for events with a long delay between the ionizing laser pulse and the p^+ -bunch (see Chapter 7), we have to rely on the DFT of the centroid displacement. For the timescales of the delays discussed there, the actual plasma density does no longer correspond to the measured neutral Rb vapour density as the plasma already starts to decay.

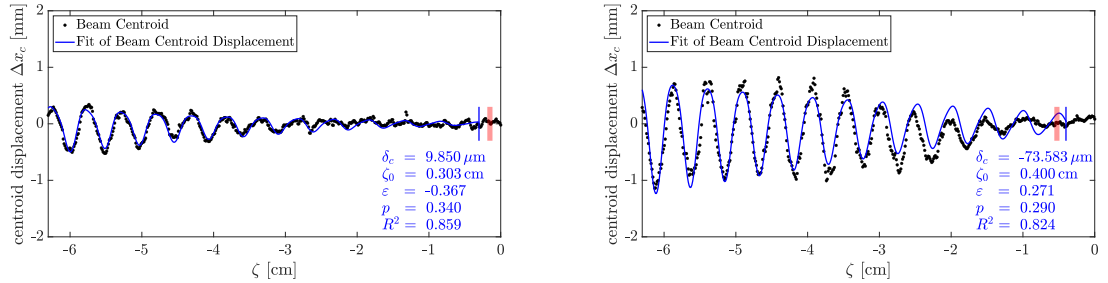
6 Experimental Results – Part 1



(a) two fit parameters δ_c, ζ_0 ($\varepsilon = 0, p = 0.333$)



(b) three fit parameters $\delta_c, \zeta_0, \varepsilon$ ($p = 0.333$)



(c) four fit parameters $\delta_c, \zeta_0, \varepsilon, p$

Figure 59: Fits of the bunch centroid equation (Equation 2.30) to the experimentally determined centroids for the low (left-hand side) and high (right-hand side) bunch population events shown in Figures 47a and 47c, respectively.

6.6 Fit of the Bunch Centroid Displacement Equation to the Experimental Data

Two fit parameters (δ_c, ζ_0):

bunch population	low	high
$ \delta_c \pm \Delta \delta_c $ [μm]	10.0 ± 3.3	15.1 ± 4.6
$\xi \pm \Delta\xi$ [cm]	0.06 ± 0.04	0.31 ± 0.24
event with best GoF	0.87	0.83
average GoF	0.58 ± 0.24	0.42 ± 0.37
	incl. 1 event with $GoF < 0$	incl. 3 events with $GoF < 0$

Three fit parameters ($\delta_c, \zeta_0, \varepsilon$):

bunch population	low	high
$ \delta_c \pm \Delta \delta_c $ [μm]	10.0 ± 3.2	15.1 ± 4.5
$\xi \pm \Delta\xi$ [cm]	0.06 ± 0.04	0.30 ± 0.24
$ \varepsilon \pm \Delta \varepsilon $	0.34 ± 0.28	0.46 ± 0.44
event with best GoF	0.88	0.83
average GoF	0.64 ± 0.18	0.49 ± 0.25
	no events with $GoF < 0$	incl. 1 event with $GoF < 0$

Four fit parameters ($\delta_c, \zeta_0, \varepsilon, p$):

bunch population	low	high
$ \delta_c \pm \Delta \delta_c $ [μm]	10.6 ± 7.2	49.8 ± 95.5
$\xi \pm \Delta\xi$ [cm]	0.08 ± 0.06	0.33 ± 0.26
$ \varepsilon \pm \Delta \varepsilon $	0.35 ± 0.29	0.49 ± 0.39
$p \pm \Delta p$	0.33 ± 0.04	0.31 ± 0.07
event with best GoF	0.88	0.85
average GoF	0.66 ± 0.18	0.57 ± 0.20
	no events with $GoF < 0$	incl. 1 event with $GoF < 0$

Table XII: Resulting fit parameters of the fits to the bunch centroid oscillation according to Equation 2.27.

In general, δ_c depends on the angle of the SC slit to the HI plane, which is random (see Section 6.5.1), thus for the same initial seed level δ_c can vary accordingly and the absolute values are not comparable amongst themselves. From Table XII, however, we can deduce that the average $|\delta_c|$ is higher for the fits with two and three parameters than in the fit with four parameters. This can be explained by the introduction of the additional fit parameter p , which allows for adapting the fit to the amplitude at the beginning of the oscillation at higher ζ and thus leads to an artificially lower amplitude here. The effect is already observed in Section 5.3.2.

In all events, the seed point ζ_0 is within one period of the centroid oscillation to the estimated start point $\zeta(t_{start})$, but the difference between estimated seed point and seed point inferred by the fit $\xi = |\zeta - \zeta_0|$ is about five times higher for the high bunch popula-

tion events than for the low bunch population events. The higher variation in the events with high bunch population is caused by the estimation of the seed point from event to event and has no effect on general conclusions based on the fit results.

As expected, the lower the values for $|\varepsilon|$, i.e. the less coupling between SM and HI occurs, the more symmetric the centroid oscillation of the event. From the angle scan of the simulation results (Section 5.3.3), we know that ε is (almost) independent from the angle between the HI plane and the orientation of the SC slit. The absolute value of $|\varepsilon|$, however, is difficult to be interpreted due to the high variance between the events. Especially events with $R^2 < 0$ result in high values of $|\varepsilon|$ which are non-physical. Figure 60 compares events with high and low values for $|\varepsilon|$ from the high bunch population data set, where $R^2 > 0$. The event in Figure 60a ($|\varepsilon| = 0.03$) has a very symmetric centroid oscillation around the bunch propagation axis and also an area ratio close to 1 (see Table X). The event in Figure 60b ($|\varepsilon| = 0.72$), however, shows an asymmetric bunch centroid oscillation. The distinct asymmetry of the event leads to a high value of $|\varepsilon|$ in the fit. This asymmetric behaviour, where the bunch centroid envelope shows a profile bent towards the direction of the higher oscillation amplitude, is also observed in the fits to the simulation results in Section 5.3.2, i.e. it is not caused by misalignment of the plasma column with respect to the bunch propagation axis. The *GoF* is still high for these events ($R^2 = 0.67$ in the example).

The average value for the exponent is $p = 0.35 \pm 0.03$ for the low and $p = 0.31 \pm 0.05$ for the high bunch population events. Therefore, the fit results are consistent with the expected value of $p = 1/3$ and thus prove the power law of N_{HI} . Similarly to the events with low and high $|\varepsilon|$, in Figure 61, we compare events with low and high fit results for p from the high bunch population data set. The event with the lowest exponent in the data set, $p = 0.14$ (Figure 61a), is a relatively symmetric event ($|\varepsilon| = 0.12$). The growth of the HI saturates around $\zeta \sim -3$ cm, which leads to a rather small $x_{c,max}$. Contrary to that, the event with the highest value $p = 0.38$ (Figure 61b) shows a strong growth of the HI along the bunch which does not saturate within the frame of the SC image. Even though it is not very asymmetric ($|\varepsilon| = 0.32$), its $x_{c,max}$ is the highest in the entire data set (see Table IX). The difference in the events can be covered by using four fit parameters and the R^2 is similar for both events ($R^2 = 0.78$ for the low- p event and $R^2 = 0.79$ for the high- p event). However, the fit results for δ_c become meaningless in case of large fluctuations in p due to an over-compensation by the fit routine, e.g. $\delta_c = 337 \mu\text{m}$ vs. $\delta_c = 1 \mu\text{m}$ for the low and high- p events, respectively. Therefore, we should only compare the initial seed levels δ_c for events with p fixed to $1/3$.

Figure 62 shows an event where the R^2 of the fit is negative ($R^2 = -0.40$). The fit matches well the period and the amplitude of the oscillation. The bunch centroid is, however, not oscillating across the plasma off trajectory. The entire charge distribution is kicked radially away from the initial bunch propagation axis and oscillates so that the upper turning point of the oscillation is close to the bunch propagation axis or even below. Our model of CBH is not capable to describe events of this kind. Explanations for these events could be either a misalignment between the plasma column and the plasma off trajectory or more likely the long-wavelength mode of the HI (see Chapter 8). The fit cannot take into account the strong kick and over-compensates the coupling

6.6 Fit of the Bunch Centroid Displacement Equation to the Experimental Data

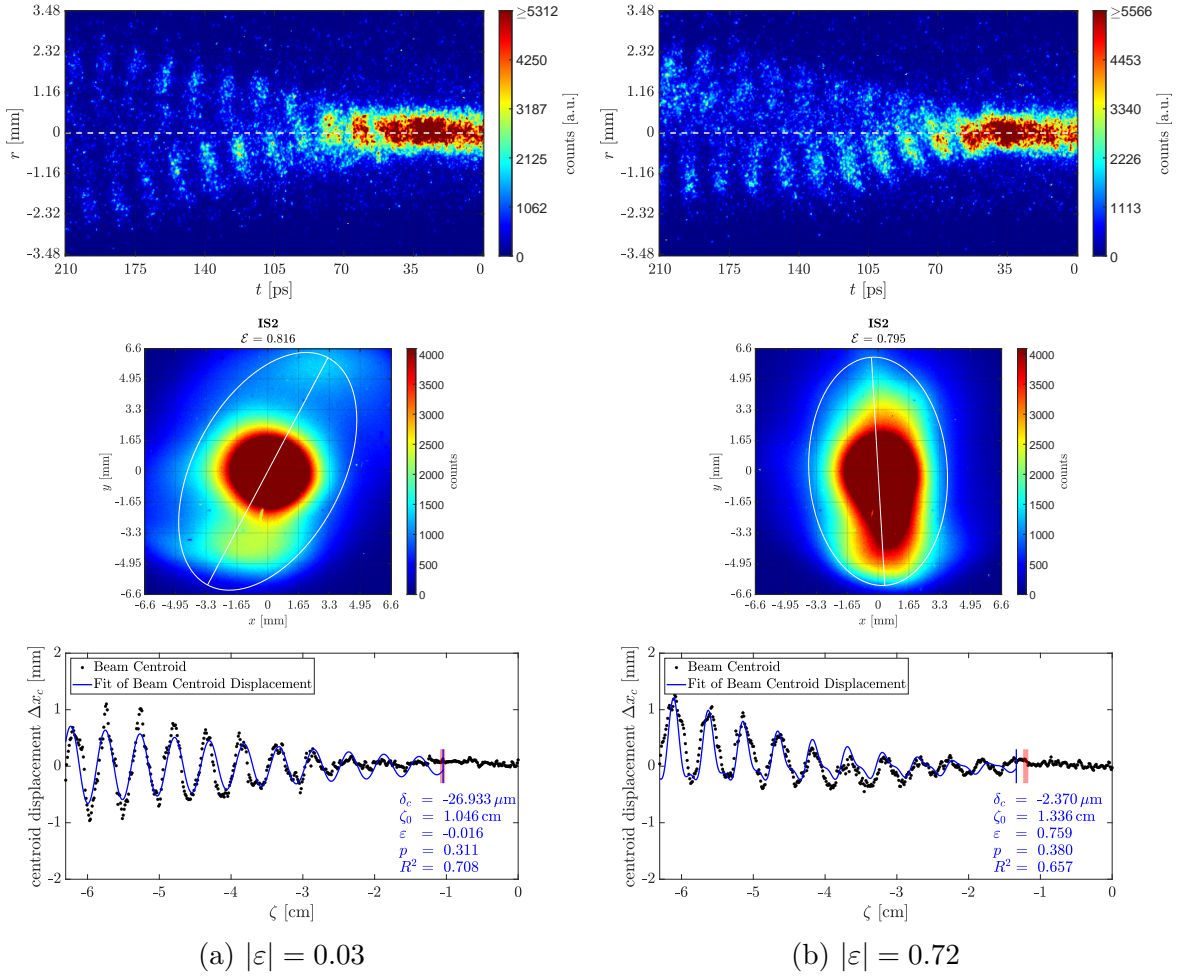


Figure 60: Events with low and high $|\varepsilon|$ from the high bunch population data set and fits of Equation 2.30 to their centroid oscillations.

6 Experimental Results – Part 1

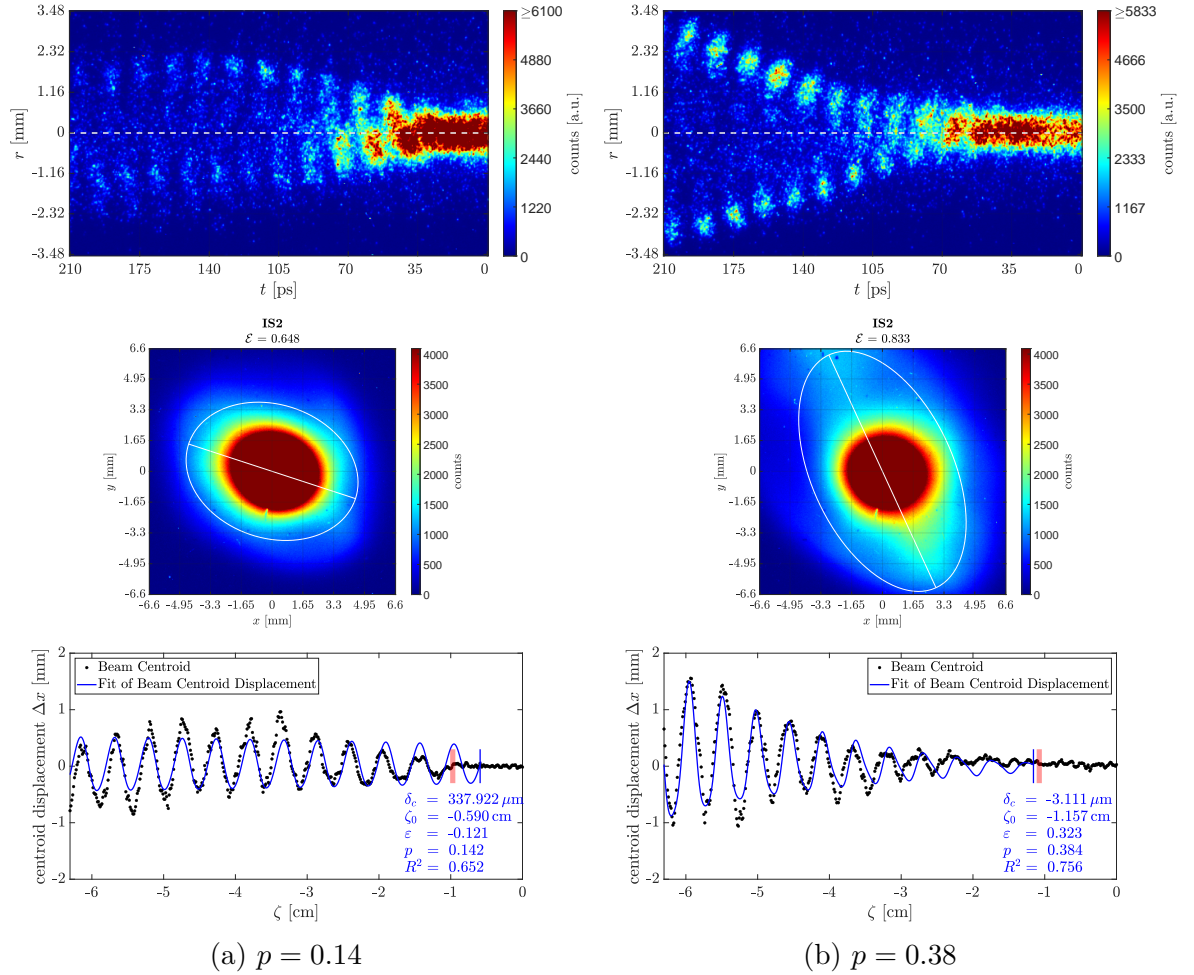


Figure 61: Events with lowest and highest p from the high bunch population data set and fits of Equation 2.30 to their centroid oscillations.

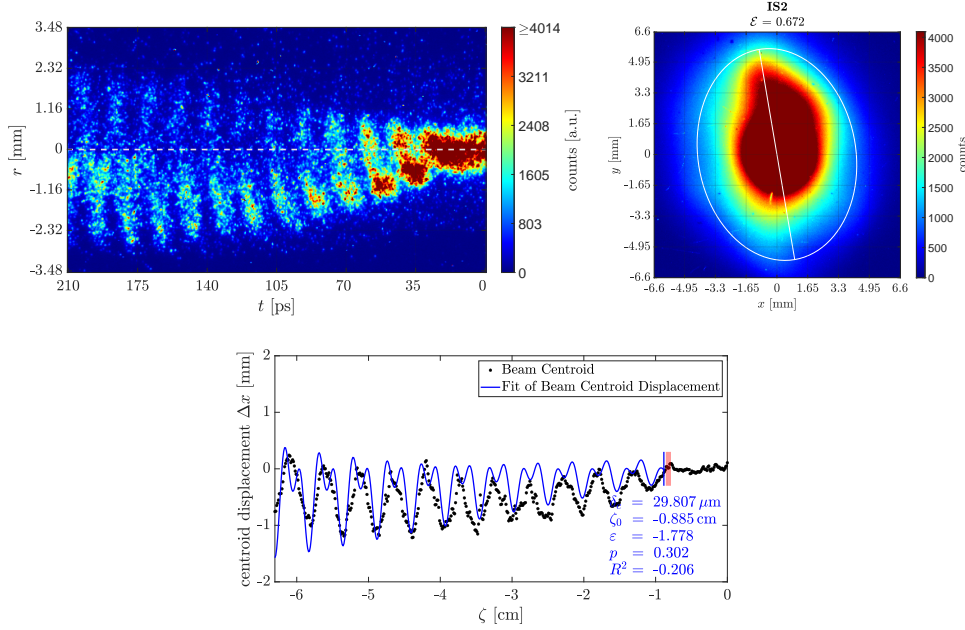


Figure 62: Event with negative R^2 from the high bunch population data set ($R^2 = -0.21$) and fit of Equation 2.30 to the centroid oscillation

constant ε to drag down the upper turning point of the fit. This leads to the appearance of presumably non-physical minima in between the upper turning points, which are never observed in the experimentally determined p^+ -bunch centroids but also received in the fits to the simulation results for large Δx_1 (see Figures 31b and 31c). The number of events where $R^2 < 0$, are noted in Table XII and are a reason for the high observed variances of R^2 .

6.7 Comparison of the Experimental Results to the Simulation Results

The experimental data with seed of the HI and the SM process show good agreement with the simulation results of the HI events shown in Chapter 5. Even though, the asymmetry in the bunch centroid oscillation observed in the simulation after 10.10 m of plasma is more distinct than for most events in the experimental data sets, the comparison to the simulation gives evidence that the experimentally observed oscillation of the bunch centroid grows from an HI seed initially present in the bunch or the plasma. For all events analyzed, the initial noise level in the bunch serving as HI seed seems to be lower than the seed level chosen in the simulation. Therefore, it is suitable to compare our experimental results to simulation distances around $\Delta x_1 \sim 6$ m. In this range, the maximum displacement of the bunch centroid $x_{c,max}$ and the ratio $\Delta x_c/\sigma_r$ is about equal to the parameters of the HI events observed in the experiment.

6 *Experimental Results – Part 1*

Moreover, getting the best fit results by adding the coupling term to the fit formula and for $p \sim 0.33$ in both simulations and experimental data establishes that the asymmetric oscillation is caused by a coupling of the HI to the SM process, as theoretically predicted by [36].

7 Experimental Results – Part 2

Observation of the Hosing Instability without Seed of the Self-Modulation Process

In the following chapter, we discuss the appearance of the HI when the SM process is not seeded and the entire p^+ -bunch is propagating through a preformed Rb plasma. As a consequence, the SMI and the HI can grow exclusively from noise in the bunch or in the plasma and the two instabilities compete with each other. This configuration is experimentally realized by introducing a delay between the ionizing laser pulse and the p^+ -bunch. We analyze delays between 1000 ns and 6000 ns and show that for shorter delays the SMI dominates over the growth of the HI, whereas for longer delays the HI becomes the dominant instability.

Furthermore, we give evidence that a deliberate misalignment of the plasma column with respect to the p^+ -bunch trajectory can induce the growth of the HI. By analyzing the time-integrated radial bunch distribution (similarly to Section 6.5), we show that the plane in which the HI grows depends on the direction of the misalignment.

All events shown in this chapter are gathered in scientific run periods of AWAKE between May and November 2018.

7.1 Effects of the Delay between Ionizing Laser Pulse and Proton Bunch

As mentioned in Chapter 6, no signs for the HI are found above a plasma density of $n_{pe} \gtrsim 0.7 \cdot 10^{14} \text{ cm}^{-3}$ for the experimental situation, where the SM process is seeded by an ionisation front close to the centre of the p^+ -bunch. For a bunch propagating through a preformed plasma (ionizing laser pulse about 10 ns ahead of the p^+ -bunch), no signs for the HI are observed above or around a plasma density of $n_{pe} \approx 0.5 \cdot 10^{14} \text{ cm}^{-3}$, the density, where we describe the regime of CBH in Chapter 6.

Therefore, to determine the transition region between the dominance of the SMI and the HI, we have to lower the plasma densities below $n_{pe} \sim 0.5 \cdot 10^{14} \text{ cm}^{-3}$, which is below the limit of a stable vapour source operation. Thus, to have even lower plasma densities, we have to set the Rb vapour density inside the vapour source to $n_{Rb} = 0.5 \cdot 10^{14} \text{ cm}^{-3}$ and introduce a delay Δt_{lp^+} between the high-power laser pulse and the arrival of the p^+ -bunch from the SPS. As in the previous chapters, the Rb vapour is assumed to be fully ionized within the plasma column at the moment of the ionization. Afterwards, the plasma density decays due to different processes: Expansion or diffusion of the plasma

7 Experimental Results – Part 2

into the Rb vapour (same ionization fraction but larger volume) and recombination of Rb ions to neutral Rb atoms by capturing a free electron of the plasma (same volume but lower ionization fraction).

These processes lead to a decay of the plasma density versus time below $n_{pe} \sim 0.5 \cdot 10^{14} \text{ cm}^{-3}$, but also to a possibly different size or shape of the plasma channel compared to very short Δt_{lp^+} . Thus, the plasma may develop inhomogeneously and obtain a radial density profile. A detailed study on the plasma density as a function of the delay Δt_{lp^+} by analyzing the SMI of p^+ -bunches in AWAKE is subject of [89].

Figure 63 shows SC images for p^+ -bunches with high bunch population at four different delays Δt_{lp^+} (1000 ns, 2000 ns, 4000 ns and 6000 ns). For all events, the density inside the vapour source is set to $n_{pe} = 0.5 \cdot 10^{14} \text{ cm}^{-3}$ (similarly to the events analyzed in Chapter 6). It can be seen directly on the SC images that the number of oscillation periods is decreasing for increasing Δt_{lp^+} . Note, as mentioned in Section 3.1.5, the den-

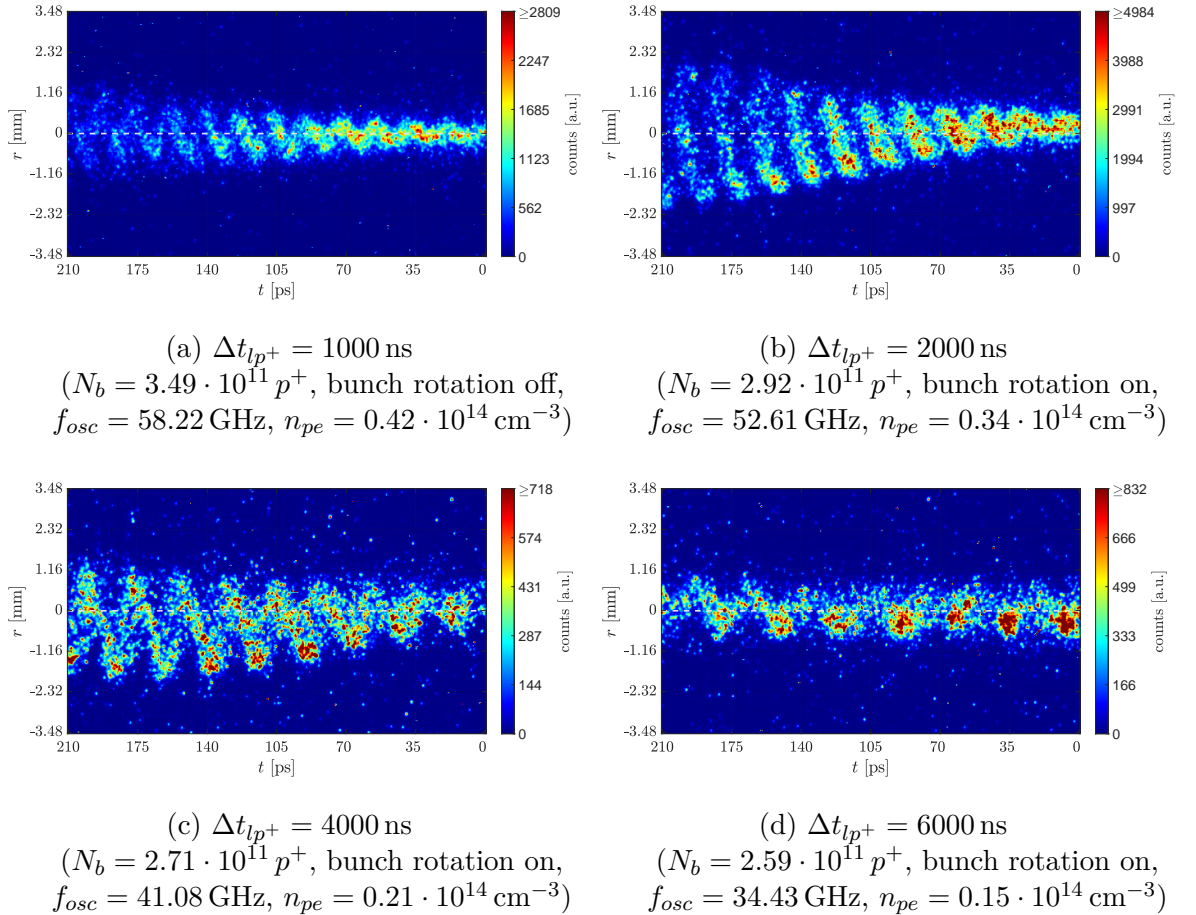


Figure 63: Events with HI at different delays Δt_{lp^+} between ionizing laser pulse and p^+ -bunch. The decreasing number of centroid oscillation periods per time range, and thus the decreasing bunch oscillation frequency f_{osc} for increasing Δt_{lp^+} , is clearly visible on the SC images.

sity measurement is only measuring the neutral density of the Rb vapour n_{Rb} and not the plasma density n_{pe} . Therefore, we have to rely on the results of the DFT of the modulation or oscillation frequency of the p^+ -bunches (see Section 6.3.2) to determine the plasma frequency at the time of the p^+ -bunch passage. The plasma density in the four events shown in Figure 63 is decreasing from $n_{pe} = 0.42 \cdot 10^{14} \text{ cm}^{-3}$ ($f_{osc} = 58.22 \text{ GHz}$) at $\Delta t_{lp^+} = 1000 \text{ ns}$ to $n_{pe} = 0.15 \cdot 10^{14} \text{ cm}^{-3}$ ($f_{osc} = 34.43 \text{ GHz}$) at $\Delta t_{lp^+} = 6000 \text{ ns}$.

7.2 Analysis of Hosing Instability Events without Seed of the Self-Modulation Process

In the following, we analyze events at different Δt_{lp^+} and discuss the likelihood of the growth of the HI compared to the SMI and the coupling of the instabilities to each other. For $\Delta t_{lp^+} = 1000 \text{ ns}$ and 4000 ns , we analyse a sequence of low/medium and high bunch population events, for $\Delta t_{lp^+} = 2000 \text{ ns}$ and 6000 ns , however, we only analyze events with high bunch population. In between all sequences of events, all experimental settings are kept constant and no parameters are deliberately changed. For $\Delta t_{lp^+} = 6000 \text{ ns}$, besides SC images in the 211 ps time window, also events in the 509 ps time window are analyzed. Moreover, the energy of the laser pulses is reduced to about 50% of the pulse energy of the events discussed in Chapter 6, i.e. to about $E_{las} \sim 120 \text{ mJ}$, due to the installation of the Pockels cells in the laser pulse cleaner of the high-power laser system in August 2017 (see Section 3.1.3). The parameters of all analyzed events can be found in Table XIII.

In order to select the events where the HI develops among all events analyzed, we apply a DFT to the bunch centroids positions determined from the SC images similar to Section 6.4. In the remaining events either only the SMI grows (symmetric time-integrated p -bunch profiles) or both the SMI and HI are developing, whereas the SMI is clearly dominating. For all Δt_{lp^+} , the average of the DFT frequency spectrum to calculate the 2.576σ threshold is taken in the range between 30 GHz and 100 GHz. The frequency ranges in which the peaks are determined vary for the different delays and are listed in Table XIV.

The resulting ratios f_{osc}/f_{pe} received from the DFT for all events where a clear peak above the threshold is found are shown in Figure 64. We observe a decreasing ratio f_{osc}/f_{pe} for increasing delays Δt_{lp^+} : From $f_{osc}/f_{pe} = 0.958$ at $\Delta t_{lp^+} = 1000 \text{ ns}$ to $f_{osc}/f_{pe} = 0.539$ at $\Delta t_{lp^+} = 6000 \text{ ns}$. The different sizes of the DFT bins result from the analysis of events in the 211 ps and 509 ps SC time windows (see Table VII).

We can conclude from the data shown in Table XIII that the fraction of events, where the HI develops, is in general the higher, the lower the plasma density. Moreover, for high p^+ -bunch population the percentage of HI events is higher than for a low p^+ -bunch population. These results are consistent with the theoretical expectations in Figures 3 and 4.

In the following, we analyze in more detail examples of events at $\Delta t_{lp^+} = 1000 \text{ ns}$ in order to focus on the transition regime between the occurrence of the SMI and the HI.

7 Experimental Results – Part 2

$\Delta t_{lp^+} = 1000$ ns:

bunch population (SC time window)	low (211 ps)	high (211 ps)
events in data set	14	41
events with HI	5 (35.7%)	31 (75.6%)
bunch population N_b [$10^{11} p^+$]	1.10 ± 0.08	3.22 ± 0.25
Rb vapour density n_{Rb} [10^{14} cm^{-3}]	0.448 ± 0.004	0.446 ± 0.006
Pulse energy E_{las} [mJ]	120.2 ± 1.4	119.8 ± 1.3
bunch rotation mechanism	off	off

$\Delta t_{lp^+} = 2000$ ns:

bunch population (SC time window)	medium (211 ps)
events in data set	21
events with HI	18 (85.7%)
bunch population N_b [$10^{11} p^+$]	1.845 ± 0.119
Rb vapour density n_{Rb} [10^{14} cm^{-3}]	0.537 ± 0.002
Pulse energy E_{las} [mJ]	116.3 ± 1.5
bunch rotation mechanism	on

$\Delta t_{lp^+} = 4000$ ns:

bunch population (SC time window)	medium (211 ps)	high (211 ps)
events in data set	43	111
events with HI	32 (74.4%)	105 (94.6%)
bunch population N_b [$10^{11} p^+$]	1.88 ± 0.12	2.64 ± 0.08
Rb vapour density n_{Rb} [10^{14} cm^{-3}]	0.537 ± 0.003	0.537 ± 0.002
Pulse energy E_{las} [mJ]	115.8 ± 1.5	115.6 ± 1.6
bunch rotation mechanism	on	on

$\Delta t_{lp^+} = 6000$ ns:

bunch population (SC time window)	high (211 ps)	high (509 ps)
events in data set	9	18
events with HI	9 (100%)	18 (100%)
bunch population N_b [$10^{11} p^+$]	2.70 ± 0.07	2.69 ± 0.07
Rb vapour density n_{Rb} [10^{14} cm^{-3}]	0.539 ± 0.002	0.540 ± 0.002
Pulse energy E_{las} [mJ]	115.6 ± 1.4	116.2 ± 1.0
bunch rotation mechanism	on	on

Table XIII: Overview of the experimental parameters of the data sets for the HI characterisation without seed of the SM process at different delays Δt_{lp^+} .

7.2 Analysis of HI Events without Seed of the SM Process

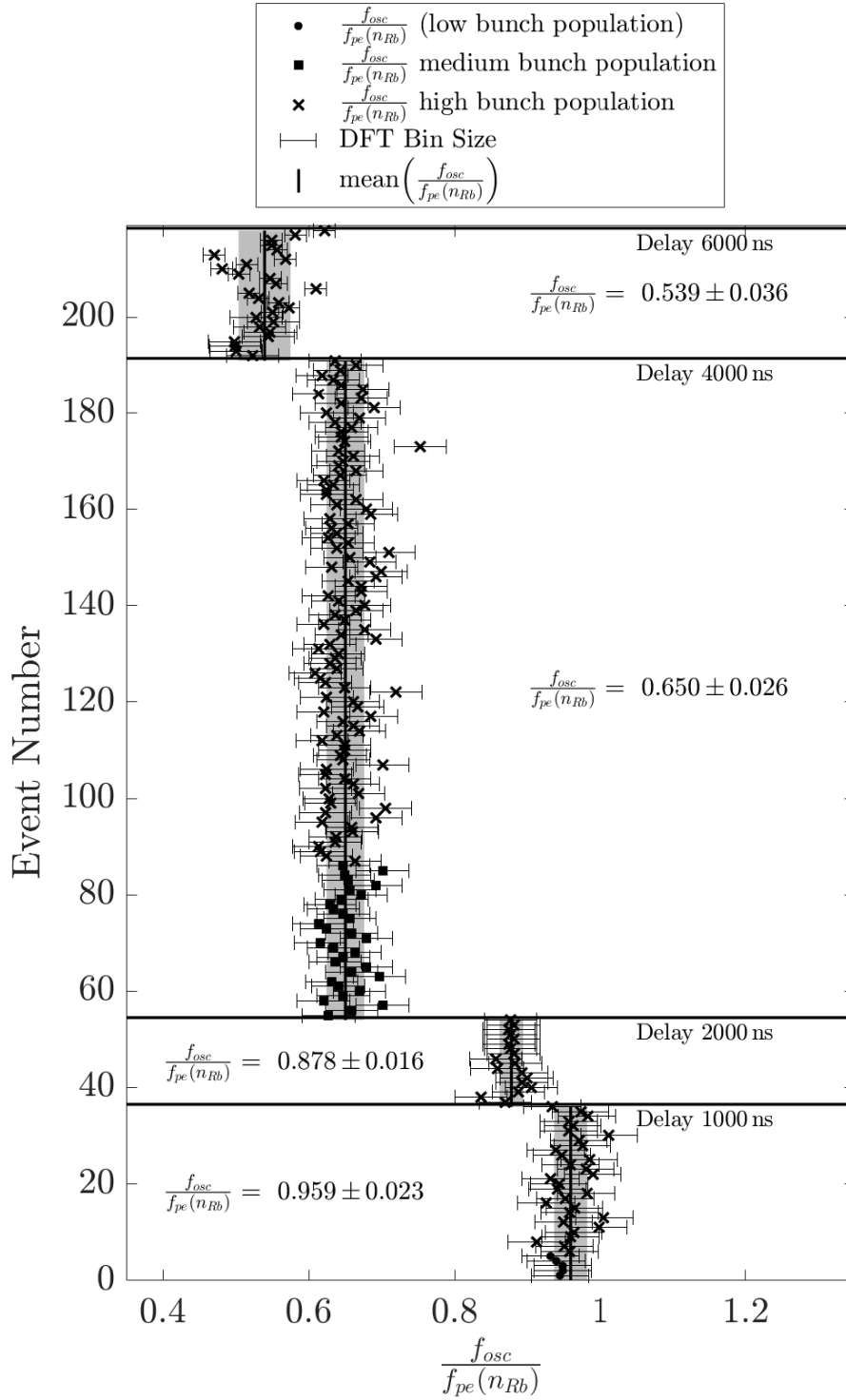


Figure 64: Normalized centroid oscillation frequencies for HI events at different delays Δt_{lp+} .

Δt_{lp^+} [ns]	Δf [GHz]
1000	55 – 75
2000	55 – 75
4000	40 – 60
6000	30 – 50

Table XIV: Frequency ranges for the determination of the DFT peaks at different delays Δt_{lp^+} .

The analysis of the events (DFT of HI events see first block in Figure 64) shows that in about 75% of the events with high bunch population the HI develops, whereas it develops in only about 35% of the low bunch population events. In most of the remaining events, the SMI develops.

Figure 65a presents as an example the SC image of an SMI event from the data set. The figure shows in addition the centroid displacement along the p^+ -bunch and the time-integrated radial bunch profiles at IS2 (core and halo camera, see Section 3.1.6). The orientation of the HI plane is determined from the core cameras as described in Section 6.5 and additionally marked in the images of the halo camera. As we discuss the position of the plasma column with respect to the bunch propagation axis in Section 7.3, the figures show also the position of the ionizing laser pulse determined from the virtual laser line (see Section 3.1.3) at the entry and the exit of the plasma.

We observe that the bunch starts to self-modulate at its head and that the SMI grows symmetrically with respect to the bunch propagation axis. The bunch centroid stays on the plasma off trajectory and shows no oscillation along the bunch and the plasma column. The ionizing laser pulse is aligned between the plasma entry and exit within ± 0.5 mm to the centre of the plasma off trajectory (radial size of the plasma column 1 – 2 mm).

The integrated radial bunch profiles have a radially symmetric bunch shape with no elongation along a specific direction as expected for events where only the SM process grows.¹ As in Chapter 6, the profiles acquired with the core camera are saturated in order to better recognize features in the profile near their edges.

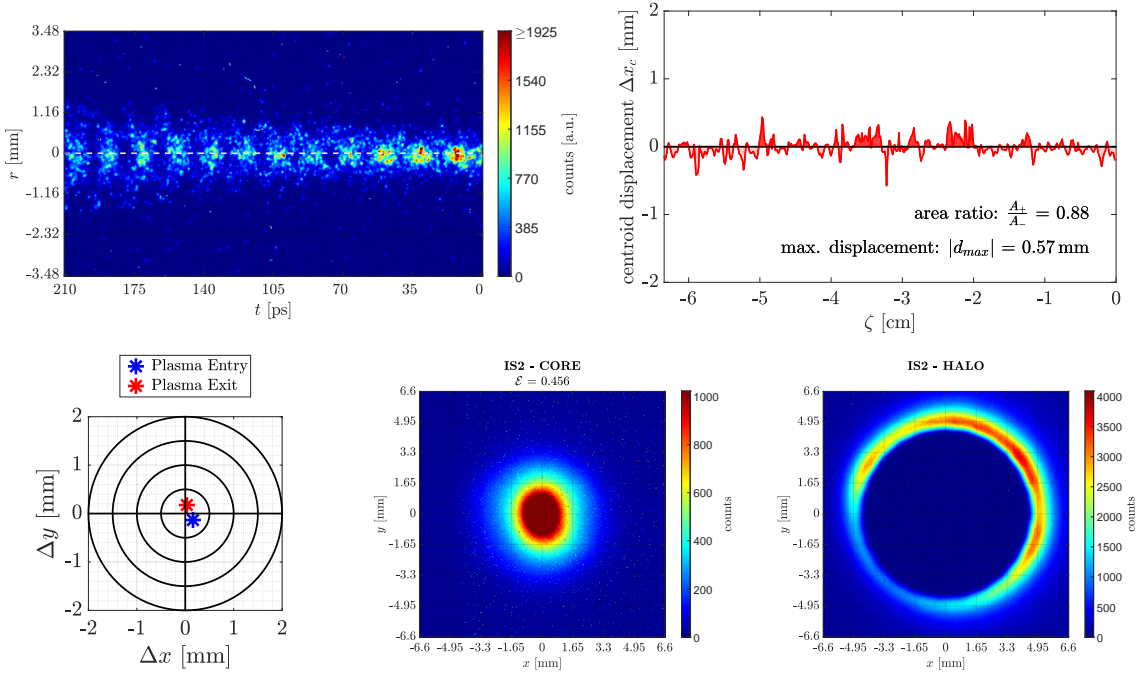
For a comparison with f_{osc} , in the following subfigures, we determine the bunch modulation frequency to be $f_{mod} = 56.89 \pm 4.75$ GHz.

Contrary to that, Figure 65b shows an event from the same data set where the HI develops. Similar to the HI events described in Section 6.4, we observe that the centroid of the p^+ -bunch starts to oscillate along the bunch. Also the time-integrated radial bunch profiles show an elongation in one plane, the HI plane. The oscillation in this event is rather symmetric with respect to the bunch propagation axis ($A_+/A_- = 0.86$).

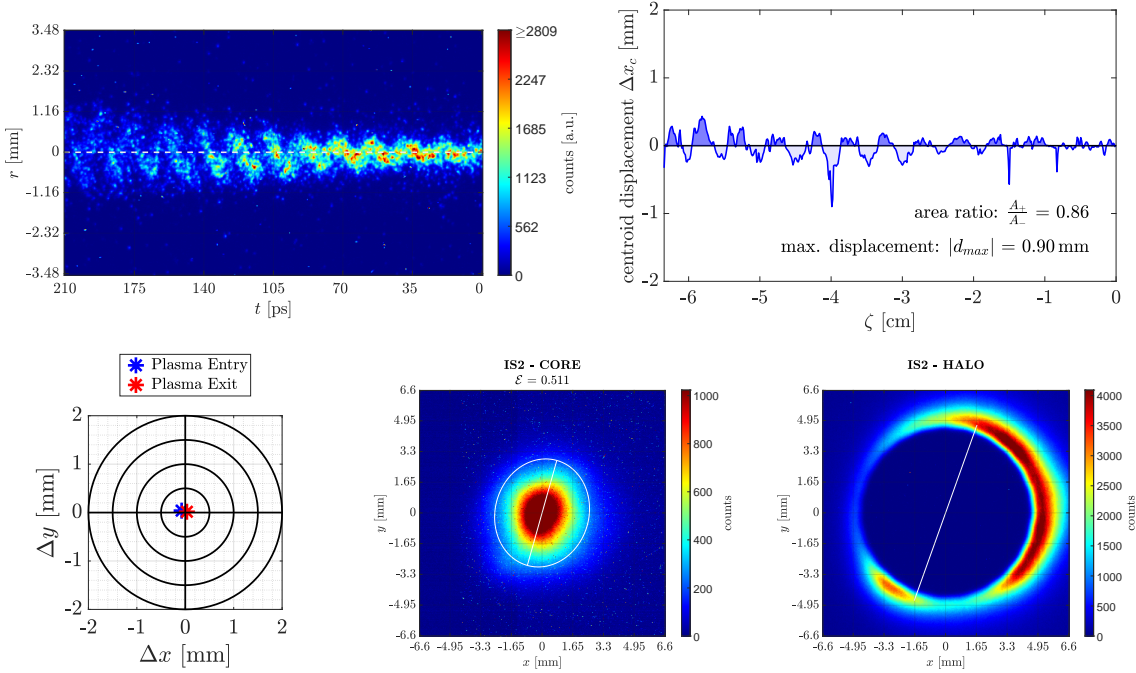
Figure 65c shows another event from the same data set that also contains clear signs for the growth of the HI. Contrary to the event in Figure 65b, the bunch centroid is

¹Note, on all halo camera profiles shown in this section, the mask blocking out the OTR light from the inner part of the bunch distribution is slightly misaligned to the lower left side. This results in a higher signal on the upper right side of the mask on all images. Therefore, we determine the orientation of the major axes indicating the plane of the HI growth exclusively from the core cameras (and only mark this orientation in the profiles of the halo cameras).

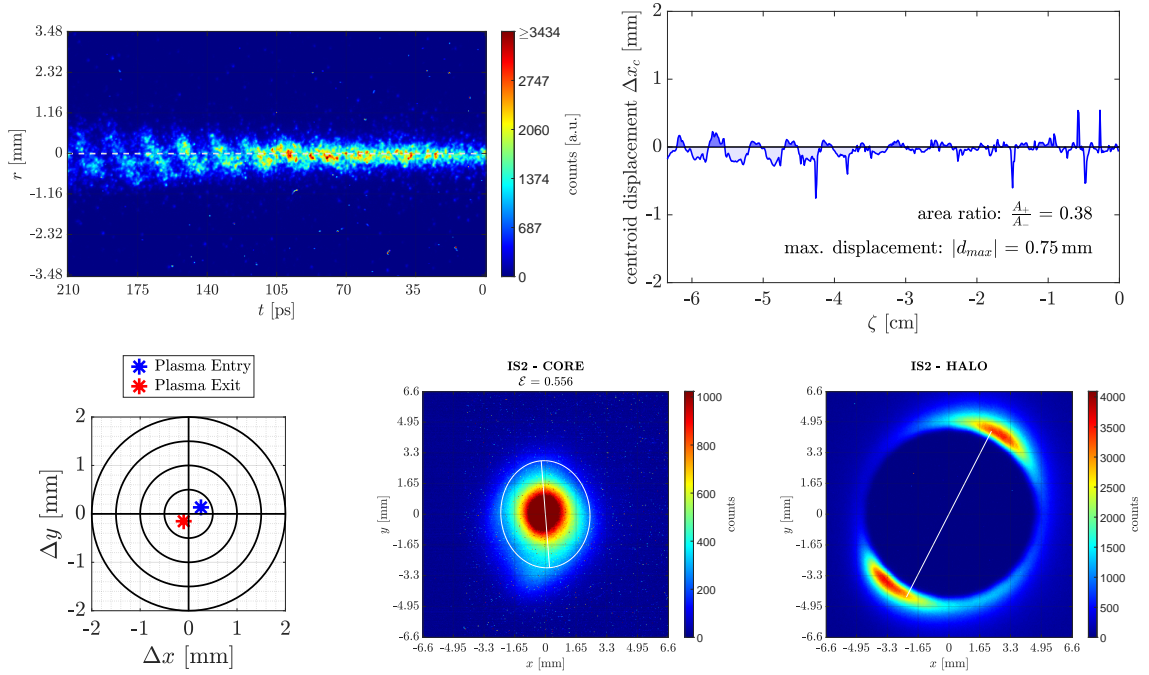
7.2 Analysis of HI Events without Seed of the SM Process



(a) SMI event at $\Delta t_{lp^+} = 1000$ ns
 $(N_b = 3.34 \cdot 10^{11} p^+, E_{las} = 121.2$ mJ, $f_{mod} = 56.89$ GHz, $n_{pe} = 0.40 \cdot 10^{14}$ cm $^{-3}$)



(b) axi-symmetric HI event at $\Delta t_{lp^+} = 1000$ ns
 $(N_b = 3.49 \cdot 10^{11} p^+, E_{las} = 120.8$ mJ, $f_{osc} = 59.41$ GHz, $n_{pe} = 0.44 \cdot 10^{14}$ cm $^{-3}$)



(c) non-axi-symmetric HI event at $\Delta t_{lp^+} = 1000$ ns
 $(N_b = 3.14 \cdot 10^{11} p^+, E_{las} = 118.9$ mJ, $f_{osc} = 59.26$ GHz, $n_{pe} = 0.44 \cdot 10^{14}$ cm $^{-3}$)

Figure 65: SC image, centroid displacement, laser alignment and time-integrated radial p^+ -bunch profiles for different events at $\Delta t_{lp^+} = 1000$ ns.

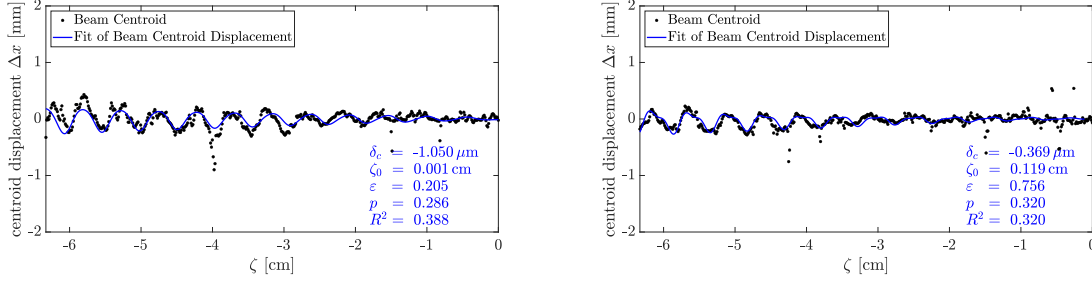


Figure 66: Fits of the bunch centroid displacements (Equation 2.30) to the experimentally determined centroids for the events shown in Figure 65b (left-hand side) and Figure 65c (right-hand side). Note, the lower centroid oscillation amplitude and thus the lower signal to noise ratio is caused by the fact that the bunch rotation mechanism is switched off in these events.

oscillating non-axi-symmetrically with respect to the bunch propagation axis. The ratio $A_+/A_- = 0.38$ (more charge above the plasma off trajectory), a value which is also observed for events with CBH described in Chapter 6.4.

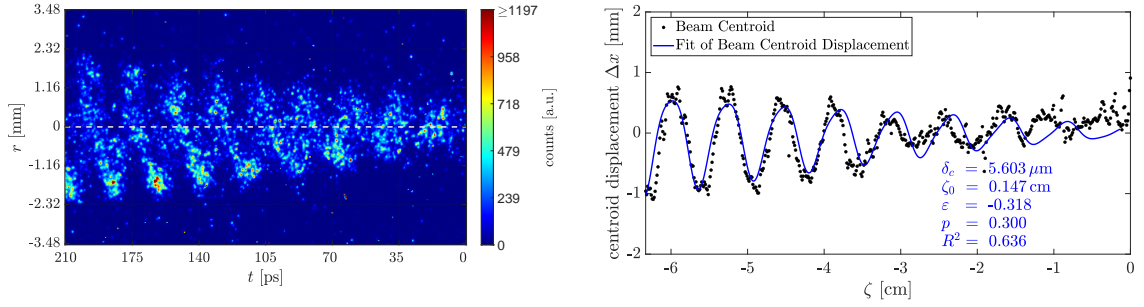
Figure 66 shows on the left-hand side the fits of Equation 2.30 to the p^+ -bunch centroid of the symmetric HI event presented in Figure 65b and on the right-hand side the fits to the asymmetric HI event from Figure 65c. Similarly to Chapter 6, we apply for each event a fit with four independent fit parameters.

As in this experimental configuration the HI grows entirely from noise, the start point ζ_0 of the HI growth is unknown since the plasma is preformed before the arrival of the p^+ -bunch, whereas in the experimental configuration in Chapter 6, the interaction starts at the time of the ionizing laser pulse close to the centre of the p^+ -bunch. Thus, we use the same trust regions as in Table XI but set the start point for the fit to $\zeta_0(1\text{ ps})$. It is important to mention that as for the experimental situation discussed in this section there is no well defined seed point for the start of the SM process, ζ_0 does only define a start point for the process to adapt the oscillation phase of the fit curve to the phase of the bunch centroid oscillation. Therefore, ζ_0 is always close to $\zeta = 0$.

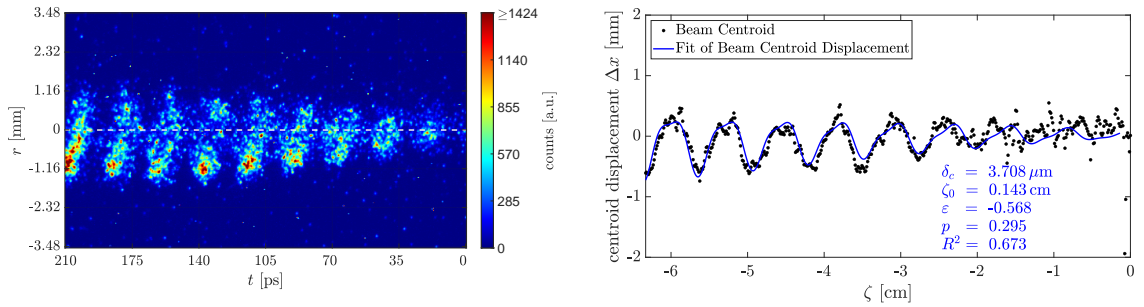
Moreover, in this chapter, k_{pe} has to be calculated from the average of the oscillation frequency f_{osc} determined from the DFT of the bunch centroid oscillation at Δt_{lp^+} (see Figure 64).

For the symmetric event (left-hand side of Figure 66), the fit gives $R^2 = 0.39$, a coupling strength $\varepsilon = 0.205$ and $p = 0.286$. For the asymmetric event (right-hand side of Figure 66) the result gives $R^2 = 0.32$, $\varepsilon = 0.756$ and $p = 0.32$. Hence, the values for p are close to the theoretical expectation of CBH, $p = 1/3$. Note, the values for R^2 for events with bunch rotation mechanism switched off (events with $\Delta t_{lp^+} = 1000\text{ ns}$) are in general lower than for fits to the experimental data with bunch rotation on (events in Chapter 6 and with $\Delta t_{lp^+} = 4000\text{ ns}$). This is caused by the lower signal to noise level of the bunch centroid on the SC images caused by the smaller oscillation amplitude of the HI due to the lower local charge density (see Section 6.2).

In Figure 67, we give two examples for HI events with $\Delta t_{lp^+} = 4000\text{ ns}$ and the corresponding fits with four independent fit parameters. At this delay, we observe in general



(a) HI event with weak coupling and high oscillation amplitude
 $(N_b = 2.66 \cdot 10^{11} p^+, E_{las} = 118.5 \text{ mJ}, f_{osc} = 42.71 \text{ GHz}, n_{pe} = 0.23 \cdot 10^{14} \text{ cm}^{-3})$



(b) HI event with strong coupling and low oscillation amplitude
 $(N_b = 2.82 \cdot 10^{11} p^+, E_{las} = 116.2 \text{ mJ}, f_{osc} = 42.26 \text{ GHz}, n_{pe} = 0.22 \cdot 10^{14} \text{ cm}^{-3})$

Figure 67: SC images (left-hand side) and fits to the bunch centroid oscillation (right-hand side) for two different HI events with $\Delta t_{lp^+} = 4000 \text{ ns}$

7.3 HI Induced by a Misalignment of the p^+ -Bunch with Respect to the Plasma Column

the same features of the HI as at $\Delta t_{lp^+} = 1000$ ns. The fit model shows again a very good agreement with the experimentally determined centroids, even though the number of oscillation periods on the SC images is less due to the lower plasma frequency. The event in Figure 67a is an event with large oscillation amplitude and less coupling ($|\varepsilon| = 0.32$), whereas the event presented in Figure 67b is more asymmetric ($|\varepsilon| = 0.59$), but with a slower growth of the HI resulting in a smaller centroid oscillation amplitude.

Hence, we can conclude that these examples of events give evidence that also in this regime, both the growth of the SMI and the HI compete with each other. The initial noise levels, which are different on an event-to-event basis and cannot be determined in the experiment, are presumably the reason why eventually the growth of one instability dominates over the growth of the other. Also in this regime a coupling of the SMI to the HI, resulting in an asymmetric centroid oscillation with respect to the bunch propagation axis, seems possible and the model of CBH can also be applied to this regime.

7.3 Hosing Instability Induced by a Misalignment of the Proton Bunch with Respect to the Plasma Column

Moreover, at a delay $\Delta t_{lp^+} = 1000$ ns, we try to induce the HI by deliberately misaligning the plasma column with respect to the p^+ -bunch trajectory. This is done by changing the alignment of the ionizing laser pulse parallel to the bunch propagation trajectory. As the plasma column is finite, the resulting plasma density (or ionization rate) becomes radially non-homogeneously distributed. The size of the plasma wakefields might therefore become larger than the plasma skin depth, which leads to radially asymmetric focusing and defocusing forces inside the plasma. These asymmetric forces could then induce the growth of the HI.

The centre of the plasma column, i.e. the position of the laser beam centroid is determined from the centre of gravity of the laser pulse profile as recorded by the virtual line cameras VLCAM3 and VLCAM5 (see Section 3.1.3) corresponding to the pulse profile at the plasma entry and exit, respectively.

In the case of such a deliberate misalignment between plasma column and p^+ -bunch trajectory, the asymmetry of the set-up should be reflected by the direction of the HI growth. The wakefields feel the lower (or even zero) density of the plasma when they touch the edges of the plasma column or get even beyond. This creates an asymmetry in the transverse force that can act on the development of the HI.

In this section, a comparison between events with well aligned p^+ -bunch trajectories (see Section 7.2) and deliberately misaligned trajectories (shifted parallelly 1–2 mm in horizontal or vertical direction with respect to the plasma column) is presented. Even though, the set-up is rotationally symmetric and there should be no difference for the HI growth for horizontal and vertical misalignment, the projection on the SC slit is not. Thus, the HI events show different features on the SC images, depending on the direction

of the misalignment with respect to the orientation of the SC slit. When inducing the HI in different planes with respect to the SC slit orientation, we should see planes where the p^+ -bunch trajectory is oscillating parallel or perpendicular to the slit orientation and thus the oscillation should be visible in a more or less distinct manner.

Figure 68 presents four examples of events where the bunch centroid is deliberately misaligned with respect to the plasma column in four directions perpendicular to each other. For a laser misalignment by about 1–2 mm along the y -direction (Figures 68a and 68b), the HI is growing in a plane almost parallel to the SC slit and the bunch can be observed to oscillate across the bunch propagating axis and the characteristic "zig-zag" pattern of the HI is visible ($A_+/A_- \sim 0.5$ for both events). The time-integrated radial p^+ -bunch profiles on the IS show an oval elongation of the charge distribution which follows the general direction of the misalignment (see orientation of white lines). These asymmetric profiles also prove the growth of the HI (see Section 6.5).

Furthermore, for a misalignment of the plasma column along the x -direction, the events appear to be much more asymmetric and we even observe a reversal of the asymmetry between the event shown in Figure 68c and the event shown in Figure 68d: The beamlets appear tilted from the upper left to the lower right side for an misalignment in the positive x -direction, whereas the beamlets appear tilted from the lower left to the upper right side of the SC image for a misalignment in negative x -direction. This infers that the HI is growing in a plane almost perpendicular to the SC slit as the projection of the bunch centroid on the slit moves away from the bunch propagation axis ($A_+/A_- \leq 0.10$). The elongation in the time-integrated radial bunch profiles on the IS follow again the direction of the laser misalignment.

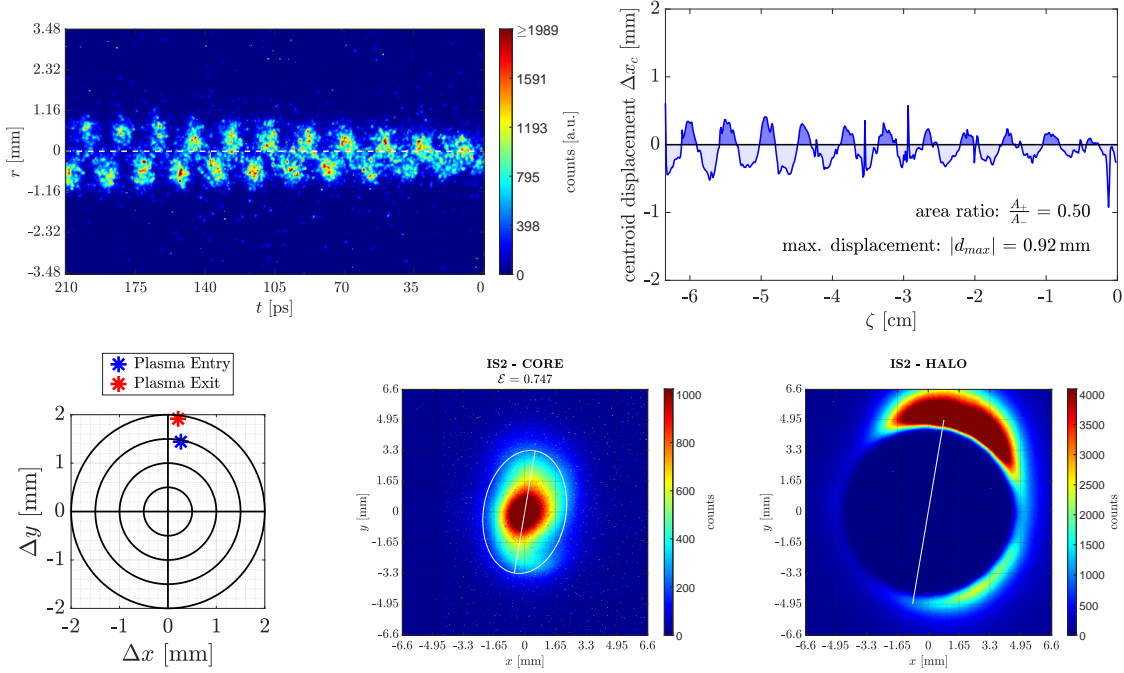
For the events in this section, we only describe the asymmetry by A_+/A_- and do not perform fits in order to get a value for ε as the fits do not give reasonable results when the bunch centroid is no longer oscillating across the plasma off trajectory (see Figure 62).

We want to emphasize that the events presented here are not selected events, but that nearly all events, where the misalignment between plasma column and p^+ -bunch trajectory is on this order, show the features described above. Therefore, in the following, we analyze 13 consecutive events at high bunch population and bunch rotation mechanism on (see Table XV), where in all events the plasma column is deliberately misaligned with respect to the bunch propagation axis by about 1–2 mm in the same direction.

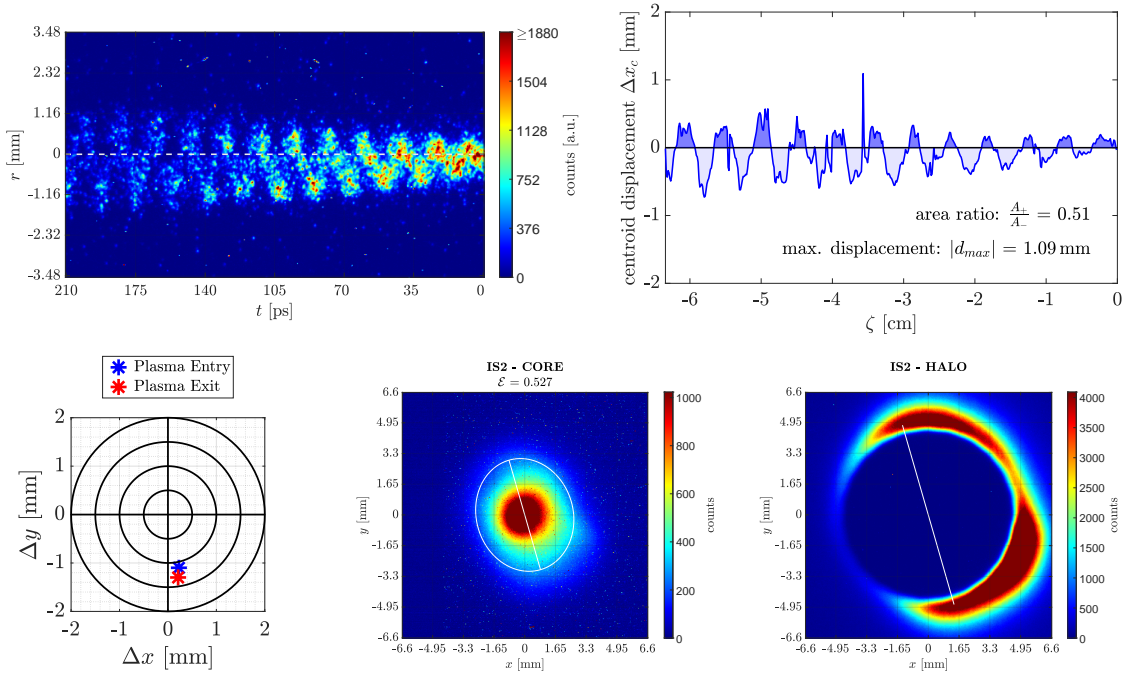
Figure 69 shows the orientation of the HI planes determined from the major axes of the time-integrated radial bunch profiles at IS1 (Figure 69a) and IS2 (Figure 69b). We observe that the plane of the HI growth is no longer randomly distributed as it is the case for events with well-aligned SSM (Figure 58). The orientation of the HI plane is pointing (with a deviation of less than $\sim 25^\circ$ in all analyzed events) in the direction of the laser misalignment.

Finally, we can conclude that the SC images of the events in this section show different features (e.g. tilted micro-bunches) than the well aligned events or the results of the angle scan through different planes of the simulation (see Section 5.3.3). We can

7.3 HI Induced by a Misalignment of the p^+ -Bunch with Respect to the Plasma Column

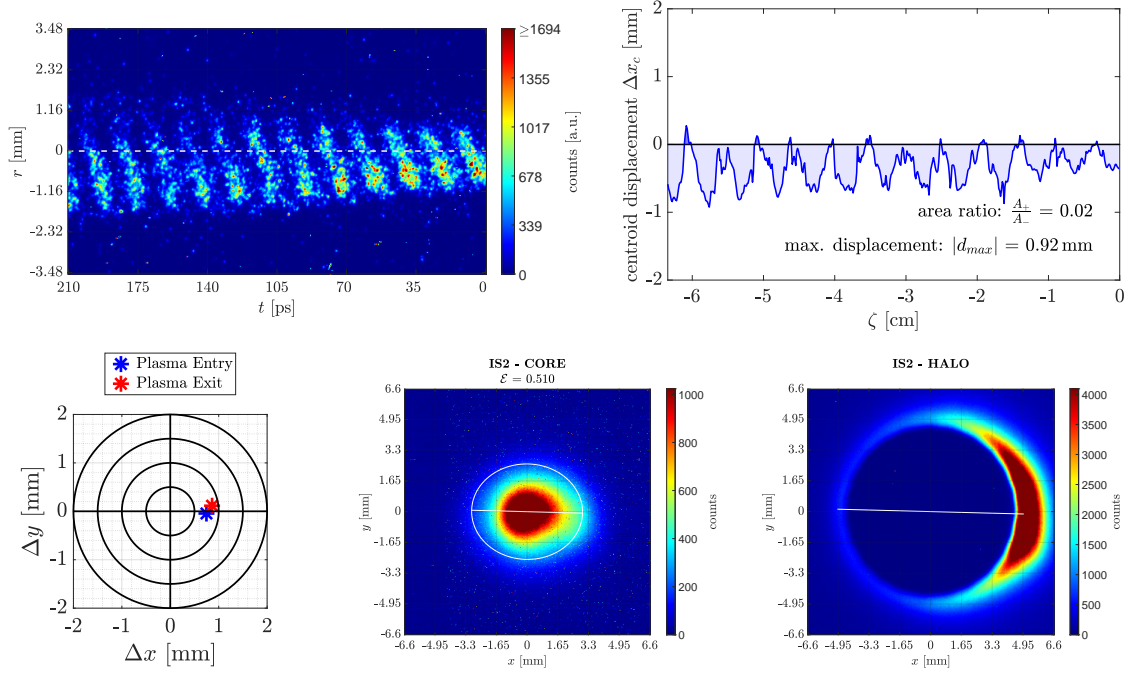


(a) event with plasma column shifted by $\sim 1\text{--}2$ mm in $+y$ -direction
 $(N_b = 3.18 \cdot 10^{11} p^+, E_{las} = 120.1$ mJ, $f_{osc} = 53.35$ GHz, $n_{pe} = 0.35 \cdot 10^{14} \text{ cm}^{-3}$)

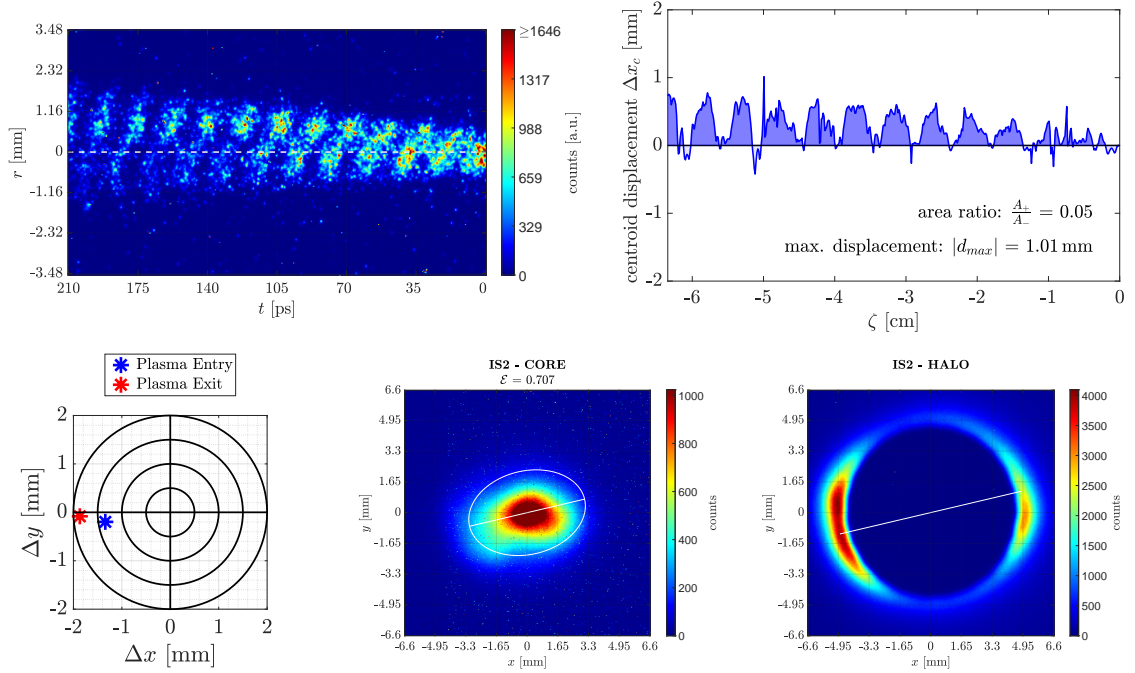


(b) event with plasma column shifted by $\sim 1\text{--}2$ mm in $-y$ -direction
 $(N_b = 3.66 \cdot 10^{11} p^+, E_{las} = 119.0$ mJ, $f_{osc} = 56.60$ GHz, $n_{pe} = 0.40 \cdot 10^{14} \text{ cm}^{-3}$)

7 Experimental Results – Part 2



(c) event with plasma column shifted by $\sim 1\text{--}2$ mm in $+x$ -direction
 $(N_b = 3.59 \cdot 10^{11} p^+, E_{las} = 119.3$ mJ, $f_{osc} = 58.22$ GHz, $n_{pe} = 0.41 \cdot 10^{14} \text{ cm}^{-3}$)



(d) event with plasma column shifted by $\sim 1\text{--}2$ mm in $-x$ -direction
 $(N_b = 2.91 \cdot 10^{11} p^+, E_{las} = 120.5$ mJ, $f_{osc} = 50.61$ GHz, $n_{pe} = 0.39 \cdot 10^{14} \text{ cm}^{-3}$)

Figure 68: Effects of plasma column position on the development of the HI.

7.3 HI Induced by a Misalignment of the p^+ -Bunch with Respect to the Plasma Column

bunch population	high
events in data set	13
bunch population N_b [$10^{11} p^+$]	3.21 ± 0.25
Rb vapour density n_{Rb} [10^{14} cm^{-3}]	0.448 ± 0.008
Pulse energy E_{las} [mJ]	120.0 ± 1.2

Table XV: Overview of the experimental parameters of the data set for the study of the HI seed by a deliberate misalignment of the p^+ -bunch with respect to the plasma column.

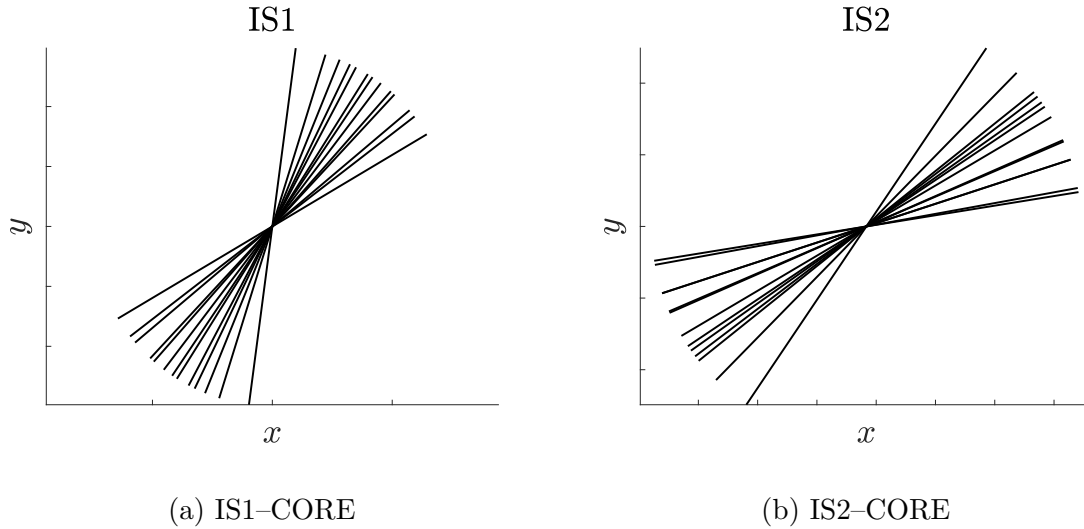


Figure 69: Orientation of the planes of the HI growth determined from the time-integrated radial p^+ -bunch profiles for events with deliberately misaligned laser position in one direction.

no longer fully resolve the HI as the axis of the oscillation is no longer equal to the bunch propagation axis, so that the time-integrated radial bunch profiles are the more convincing diagnostics to detect the growth of the HI. The asymmetric beam-wakefield strengths and thus the different forces acting on both sides of the bunch due to a parallelly shifted plasma column with respect to the p^+ -bunch propagation axis are capable to induce the growth of the HI. As the effect starts to be visible above a misalignment of ~ 1.5 mm, we can assume that the size of the plasma column is on this order, which is also in agreement with the specifications in the AWAKE design report [51]. Moreover, around $n_{pe} \sim 0.15 \cdot 10^{-14} \text{ cm}^{-3}$, the plasma skin depth and thus the radius of the plasma wakefields gets larger than the size of the plasma column (see Figure 70).

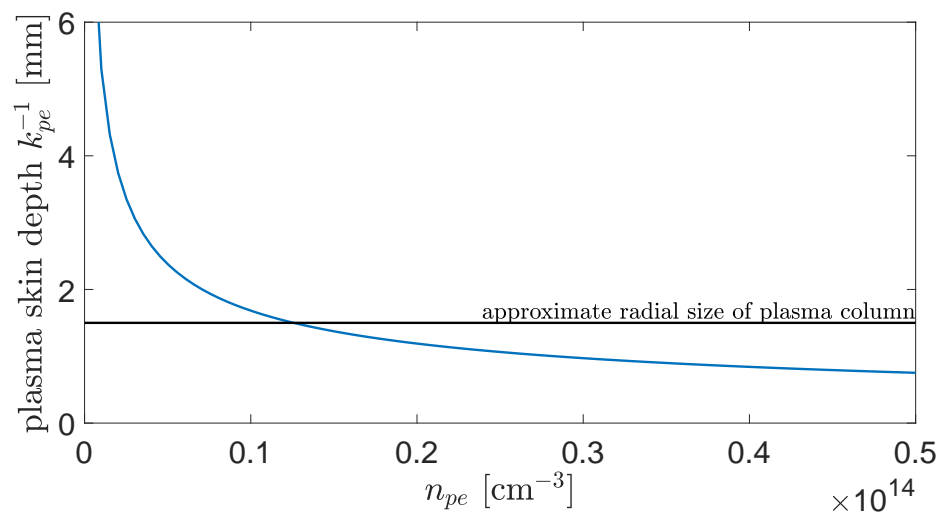


Figure 70: Plasma skin depth k_{pe}^{-1} in dependence on plasma density n_{pe}

8 Conclusions and Outlook

In this thesis, we described the observation of a characteristic centroid oscillation of a long relativistic p^+ -bunch propagating through plasma in the AWAKE experiment at CERN, both with and without seed of the Self-Modulation (SM) process. This represents the first conclusive observation of the Hosing Instability (HI) of a long, relativistic, charged particle bunch in a plasma.

We could confirm that the HI grows along the p^+ -bunch and the plasma and that the growth rate of the oscillation amplitude depends on the p^+ -bunch population. Furthermore, we established that the oscillation frequency is equal to the cold electron plasma frequency and that the oscillation couples to the growth of the Seeded Self-Modulation (SSM) of the p^+ -bunch with varying strength on an event-to-event basis. This coupling leads to an asymmetry in the oscillation with respect to the bunch propagation axis and was theoretically predicted by Schroeder et al. in [36]. The coupling can be appropriately described by introducing a term to the initially axi-symmetric oscillation term in the bunch centroid motion equation. This approach could be verified by performing fits to the experimentally determined bunch centroid displacements and by comparison to the theory of the HI.

The experimental results could be supported by three dimensional PIC simulations with similar parameters. These simulations were utilized to gain a better understanding of the three-dimensional processes that cause the coupling: Periodical focusing and defocusing phases acting on the oscillating bunch charge. Moreover, by means of the simulations, we could show that the coupling strength is a unique property of HI events that can in general be determined independently from the angle at which the SC image was gathered. Furthermore, the simulations showed that some of the features described by the linear theory of Coupled Beam Hosing (CBH) persist also into a highly non-linear regime that was not fully reached over the plasma length of 10 m in our experiment.

As the streak camera (SC) images only show the plane along the SC slit, we additionally used time-integrated radial bunch profiles from two imaging stations to identify the plane of the HI growth that manifests itself as an elongation of the bunch profile along a specific plane. This approach is also supported by the results of the PIC simulations in which we also showed that the HI is only growing in the plane of the HI seed and that the radial bunch profile appears elongated along this HI plane. In the experiment, the HI is usually not seeded and its growth can happen in any plane changing from event-to-event.

In the final chapter, we showed that under the experimental conditions, where the SM process is not seeded and the p^+ -bunch is propagating entirely through a pre-formed plasma, both the SMI and the HI can grow from noise along the bunch and the plasma, and that the two instabilities can also couple to each other in this regime, similarly to

the case where the SM process is seeded. The HI can also be deliberately induced by a radial misalignment of the plasma column with respect to the bunch propagation axis when the misalignment is at least on the order of the plasma skin depth. The orientation of the HI plane then follows the general direction of the misalignment.

Of course, there remain many interesting and important topics to be studied in the context of the HI for which no further data could be taken before LS2 at CERN. These topics could therefore not be answered in the scope of this thesis and could be subject of further research during the upcoming AWAKE Run 2 (see Section 3.2). The most critical question for the experiments will be the investigation whether the HI appears more distinct over much longer plasma lengths and how it could be possibly mitigated. The fact that the HI was only observed at low plasma densities, however, is very encouraging for further plasma wakefield acceleration (PWFA) experiments. The growth of the SM seems to be the predominant process at AWAKE baseline parameters and therefore the HI at λ_{pe} -scale should not be a major limitation for such experiments.

Nevertheless, more studies are needed to answer the question why a lower plasma density supports the growth of the HI. In the following, we make some conjectures to solve this question that could serve as a possible base for future experimental studies:

1. A first hint why the appearance of the HI is more likely at lower densities is already given in the model by Schroeder et. al. (see Figure 4). The figure infers that for a similar seed level the SMI is always dominant compared to the HI. The lower the plasma density, however, the smaller the difference between N_{HI} and N_{SMI} . This means that it is more likely at low plasma densities that the HI becomes the dominant instability in case both instabilities grow purely from noise and compete with each other. This does, however, not yet take into consideration the possibility of a coupling between the two instabilities. Moreover, it can not explain why in AWAKE the transition region between the dominance of the SMI and the HI is observed around $n_{pe} = 0.5 \cdot 10^{14} \text{ cm}^{-3}$.
2. An intrinsic frequency component in the spectrum of the incoming p^+ -bunches from the SPS on the order of $\sim 40\text{--}70 \text{ GHz}$ could act as a seed for the HI. Hence, an oscillation frequency f_{osc} close to this intrinsic frequency component could lead to a higher rate of HI events. Fourier studies of plasma off events, i.e of a possible centroid displacement in the incoming p^+ -bunches, have been conducted by [90,91]. Their results do not indicate such intrinsic frequency components in the incoming spectrum close to the particular frequencies presented in our HI studies. The measured amplitudes are dominated by noise in the SC images.
3. Furthermore, the appearance of pre-bunches before the main p^+ -bunch from the SPS could also lead to a potential seed of the HI growth in the main p^+ -bunch, but only for the experimental situation described in Chapter 7, where the ionizing laser pulse is ahead of the p^+ -bunch. Similarly to the concept of seeding with a short electron bunch (see Section 2.4), such pre-bunches could provide small initial seed wakefields that could eventually lead to a slight oscillation of the pre-bunch

centroid, which could then act as a seed for the HI.

Pre-bunches before the main p^+ -bunch have been observed in the AWAKE experiment. Figure 71 shows a SC image of such a pre-bunch (at $t \sim 30000$ ps) before the

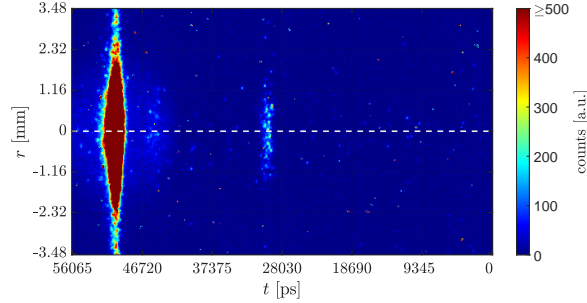


Figure 71: Appearance and temporal distribution of pre-bunches (faint signal at $t \sim 30000$ ps) before the main p^+ -bunch (saturated signal at $t \sim 50000$ ps). For a better visibility of the pre-bunch, the upper limit of the colour map is set to 500.

main p^+ -bunch (at $t \sim 50000$ ps). No signs for additional pre-bunches are found further ahead. The temporal distance between the main bunch and the pre-bunch (~ 20 ns), however, is too short to explain the observation of HI events that starts mainly for delays $\Delta t_{lp^+} \gtrsim 1000$ ns in case of no SM seed.

4. To improve the quality of the SSM events, a major laser upgrade has taken place in August 2017: A laser pulse cleaner consisting of two additional Pockels cells was installed in the laser beam-line after the regenerative amplifier (see Section 3.1.3) in order to remove laser pre-pulses, which were measured up to a few ps before the main high-power laser pulse [92]. These pre-pulses are mostly caused by laser pulses which are coupled out of the regenerative amplifier earlier than the main pulse and further amplified in the following amplification stages. Such pulses are able to (at least partially) ionize the Rb vapour before the main high-power laser pulse, especially at lower vapour densities, i.e. at the density regimes where the HI is observed.

The upgrade reduced the intensity of the pre-pulses and led to an increase of the quality of the SSM events. The time scales, however, on which the pre-pulses occurred before, cannot explain the increase of the observation of the HI for delays Δt_{lp^+} in case no SM process is seeded.

Another main effect, which has the potential for further studies and which is not addressed in the scope of this thesis, is the appearance of a bunch centroid oscillation on much longer time scales, referred to as long wavelength hosing. Figure 72a shows a SC image of such an event in the 509 ps time window. The long-wavelength hosing leads to a “helix”-like structure of the bunch. The centroid calculated from the SC image (see Figure 72b) clearly shows a slower oscillation superimposed onto the oscillation of the bunch centroid at the λ_{pe} -scale of the HI described in this thesis.

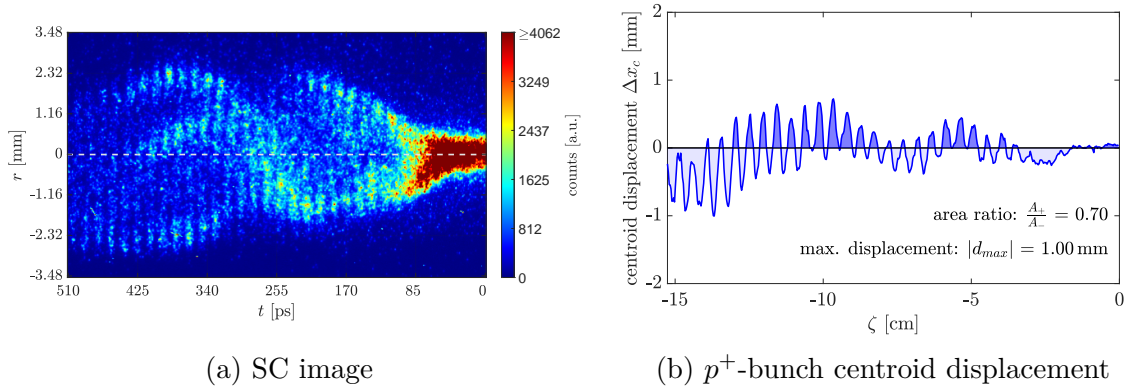


Figure 72: Appearance of the long-wavelength mode of the HI, i.e. an oscillation of the p^+ -bunch centroid with a superimposed longer wavelength than the oscillation on the λ_{pe} -scale.

Hence, a lot of interesting and important topics concerning the HI still remain to be discussed, e.g. during AWAKE Run 2, especially the development of the long-wavelength mode of the HI.

Moreover, in a plasma longer than 10 m the HI could grow to a more non-linear regime, comparable to what is observed in our simulations at $\Delta x_1 = 10.10$ m. After these propagation distances, the long wavelength mode of the HI could also play a more important role and potentially would even need to be mitigated in experiments.

Finally, we should always keep in mind that contrary to the SSM desired for PWFA, where the bunch modulation process is seeded and thus the conditions for its growth are stable and well defined on an event-to-event basis (in case of a well-aligned system), the HI is an unwanted instability that can grow purely from noise. This makes it by far harder to predict its behaviour on the event-to-event level and to forecast its occurrence over the much longer plasma length envisaged for future experiments and for an actual accelerator.

Glossary

ACC	AWAKE Control Centre	
Al	Aluminium	
α	angle of plane across the bunch charge distribution	
A_{min}	peak intensity of the cos-shaped electron bunch	see Figure 7
A_{Spot}	Laser spot size area	
a.u.	arbitrary units	
AWAKE	Advanced Wakefield Experiment	
A_0	peak intensity of the cos-shaped proton bunch	see Figure 7
A_1	constant for wakefield calculation	see Equation 2.43
A_2	constant for wakefield calculation	see Equation 2.44
A_+/A_-	area ratio of the bunch centroid displacement	$A_+/A_- \in [0; 1]$
BBO	β -Barium borate	
BBU	Beam Break-Up (Instability)	
BELLA	Berkeley Lab Laser Accelerator	
BPM	Beam Position Monitor	
c	speed of light in vacuum	$c = 2.998 \cdot 10^8$ m/s
C	Courant condition	see Equation 5.1
CBH	Coupled Beam Hosing	see Section 2.3.4
CERN	European Centre of Nuclear Research	
CFI	Current Filamentation Instability	see Section 2.3.1
CLIC	Compact Linear Collider	
CNGS	CERN Neutrinos to Gran Sasso	
CPA	Chirped Pulse Amplification	
cst	constant	
CTR	Coherent Transition Radiation	
C_{\pm}	constant for wakefield calculation	see Equation 2.45
d	current hole depth of the foil for ablation studies	
D	thickness of the foil for ablation studies	
δ_c	initial seed amplitude of the centroid oscillation	
DFT	Discrete Fourier Transform	
D_{\pm}	constant for wakefield calculation	see Equation 2.46

Glossary

e	elementary charge	$e = 1.602 \cdot 10^{19} \text{ C}$
E	electric field	
\mathcal{E}	eccentricity of ellipse	$\mathcal{E} \in [0; 1]$
E_{las}	laser pulse energy	
ε	coupling constant of CBH	
ϵ_0	vacuum permittivity	$\epsilon_0 = 8.854 \cdot 10^{-12} \frac{\text{As}}{\text{Vm}}$
E_S	energy loss per synchrotron turn	see Equation 1.1
η	plasma refractive index	
E_{wb}	non-relativistic cold wave-braking field	see Equation 2.10
E_0	maximum acceleration gradient in plasma	see Equation 2.11
e^-	electron	
FCC	Future Circular Collider	
f_{mod}	frequency of the bunch density modulation	due to SMI/SSM
f_{osc}	frequency of the bunch centroid oscillation	due to HI
f_{pe}	cold electron plasma frequency	
FWHM	full width at half maximum	
f_1	focal length of UV beamline lens	
f_2	focal length of UV beamline lens	
γ	Lorentz factor	
γ_L	Littrow angle	
GoF	Goodness of fit (R^2)	
$G1$	first grating of the grating compressor set-up	see Figure 19
$G2$	second grating of the grating compressor set-up	see Figure 19
h	Planck constant	$h = 6.626 \cdot 10^{-34} \text{ Js}$
HI	Hosing Instability	see Section 2.3.3
ILC	International Linear Collider	
IS	Imaging Station	see Section 3.1.6
IST	Instituto Superior Técnico, Lisbon	
I_{TR}	intensity of transition radiation	see Equation 3.3
I_0	zeroth order modified Bessel function of the first kind	
I_1	first order modified Bessel function of the first kind	
κ	exponent in λ_z	see Equation 3.1
k_b	wave number of beam particle	see Equation 2.8
k_B	Boltzmann constant	$k_B = 1.380 \cdot 10^{23} \text{ J/K}$
k_β	beam betatron wave number	
k_{pe}	plasma wave number	

k_{pe}^{-1}	collisionless plasma skin depth	
K_0	zeroth order modified Bessel function of the second kind	
K_1	first order modified Bessel function of the second kind	
L	half of the length of the cos-shaped proton bunch	see Figure 7
λ_D	Debye length	see Equation 2.3
λ_{max}	maximum wavelength in THG generation	
λ_{pe}	plasma wavelength	
λ_{SH}	wavelength of the second harmonic	
λ_{TH}	wavelength of the third harmonic	
λ_0	wavelength of the main laser pulse	
LBDP	Laser Beam Dump	see Section 3.1.4
LEP	Large Electron-Positron Collider	
LHC	Large Hadron Collider	
L_i	length of simulation box in i -th dimension	
LINAC	Linear Accelerator	
L_p	plasma length in simulation	
LS2	Long Shutdown 2 of the CERN Accelerator Complex	
LVDT	Linear Variable Differential Transformer	
LWFA	Laser Wakefield Acceleration	see Section 1.2.1
MCP	multi-channel plate	
m_e	electron rest mass	$m_e = 9.109 \cdot 10^{31}$ kg
MO	out-coupling mirror of grating compressor	see Figure 19
MPP	Max Planck Institute for Physics, Munich	
m_{sp}	rest mass of particle of certain species	
μ	term describing effect of plasma return current	for the HI
m_0	particle rest mass	
N	number of pulses shot on foil	
N_b	bunch population	
n_{b0}	initial bunch charge density	
N_D	number of particles inside the Debye sphere	
Nd:YAG	Neodymium-doped Yttrium Aluminium Garnet	
N_{HI}	number of exponentiations of the HI	see Equation 2.28
N_{it}	number of iterations in simulation	
n_{pe}	cold electron plasma density	
$N_{P,off}$	number of plasma off events for Gaussian fits	
n_{Rb}	Rubidium vapour density	
N_{SMI}	number of exponentiations of the SMI	see Equation 2.22

Glossary

ν	term describing effect of plasma return current	for the SMI
n_0	gas density	
ω_{pe}	plasma angular frequency	
$\omega_{pe,metal}$	metal equivalent electron plasma frequency	
OTR	Optical Transition Radiation	
p	exponent in the number of exponentiations N_{HI}	
P	periscope in the grating compressor set-up	see Figure 19
Φ_W	work function	
PIC	Particle-in-cell	
p_{r-b}	distance between red and blue wavelength components inside the compressor	see Figure 19
PSF	Point Spread Function	
PS	Proton Synchrotron	
PWFA	Plasma Wakefield Acceleration	see Section 1.2.2
p^+	proton	
QE	quantum efficiency of the e^- -gun cathode	
R	transverse component of plasma wakefield	see Equation 2.15
R_A	ablation rate	
Rb	Rubidium	
R_{Bessel}	ratio of Bessel functions	
RF	radio-frequency	
RM	roof mirror of grating compressor	see Figure 19
RMS	root mean square	
r_s	radius of synchrotron	
R^2	Goodness of fit (GoF)	$R^2 \in [-\infty; 1]$
SC	streak camera	
SHG	second harmonic generation	
σ_r	radial bunch size	
σ_x	bunch size in x -direction	
σ_y	bunch size in y -direction	
σ_z	longitudinal bunch size	
SLAC	Stanford Linear Accelerator Center	
SLC	Stanford Linear Collider	
SM	Self-Modulation	
SMI	Self-Modulation Instability	see Section 2.3.2
SPS	Super Proton Synchrotron	
$S_{S,reg}$	sum-of-squares of the regression model	see Equation 5.6
$S_{S,tot}$	sum-of-squares of the total error	see Equation 5.5
SUSY	Supersymmetry	

t	time in lab frame	
T	temperature of Rb vapour inside the vapour source	
Θ	Heaviside step function	
THG	third harmonic generation	
Ti:Sa	Titanium Sapphire	
t_{max}	maximum number of iterations in simulation	
t_{start}	estimated position of the seed laser pulse	
U	half of the length of the cos-shaped bunch	see Figure 7
v	velocity	
v_{gr}	group velocity	see Equation 2.7
VL	virtual (laser) line	
VLCAM3	virtual laser line camera at distance of plasma entry	
VLCAM5	virtual laser line camera at distance of plasma exit	
v_{ph}	phase velocity	see Equation 2.6
$v_{th,e}$	thermal velocity of electron	
W_r	radial wakefield	see Equation 2.14
W_z	longitudinal wakefield	see Equation 2.13
x_c	bunch centroid position	
$x_{c,max}$	maximum displacement of the bunch centroid	
ξ	difference between estimated seed point and seed point inferred by the fit	$\xi = \zeta - \zeta_0 $
y	set of data points for regression analysis	
y_{reg}	data points obtained by regression	
ζ	spatial coordinate in the co-moving bunch frame	$\zeta = ct - z$
ζ_0	seed position in ζ	

Acknowledgements

A doctoral thesis like this would not be possible without the enormous help and support of many people. Hereby, I would like to thank sincerely everybody who contributed to the realization of this theses.

My particular gratitude for

- Dr. Patric Muggli, for integrating me in the AWAKE team, for introducing me to the world of Plasma Wakefield Acceleration and for his enormous advise, motivation and support.
- Prof. Dr. Allen Caldwell for his kind support as my PhD supervisor.
- Dr. Bela Majorovits for his grateful effort as my third IMPRS Advisory Panel Member.
- my post-doc colleagues from MPP, Dr. Falk Braunmüller, Dr. Mikhail Martyanov, Dr. Josh Moody and Dr. Erdem Öz. They always lent a sympathetic ear to all my questions.
- my colleagues as PhD-candidates from MPP, Anna-Maria Bachmann, Fabian Batsch and Karl Rieger, with all of whom I spent countless hours in the AWAKE tunnel and control room. We always were a good team in mostly successfully solving all the smaller and bigger problems and challenges of such a large experiment.
- Mariana Moreira and Jorge Vieira for their extremely helpful support with the OSIRIS simulations. Their simulations are an essential aspect for a better understanding of the experimental results.
- Dr. Marlene Turner and Dr. Spencer Gessner from CERN for their support concerning various practical questions around the experiment.
- my office mate Felipe Peña for our fruitful discussions about all kinds of physical and non-physical topics as well as all the table tennis matches at the institute.
- Thomas Haubold from the MPP design workshop for the technical drawings and the fabrication of the laser beam dumps as well as Krzysztof Szczurek from CERN for their integration into the CERN front-end software architecture.
- Markus Lippert from the MPP workshop at CERN, who was always my first address in Geneva for various technical and practical problems.
- everybody else from the AWAKE team at MPP and at CERN, who directly or indirectly contributed to make this work possible.
- my family and friends for their support and for always listening patiently to all my stories and latest news from the lab.

Bibliography

- [1] F. Braun. Über ein Verfahren zur Demonstration und zum Studium des zeitlichen Verlaufes variabler Ströme. *Annalen der Physik*, 296(3):552–559, 1897.
- [2] J. Cockcroft and E. Walton. Experiments with High Velocity Positive Ions. *Proc. R. Soc. Lond. A*, 129(811):477–489, 1930.
- [3] R. van de Graaff. A 1,500,000 Volt Electrostatic Generator. *Phys. Rev*, 38:1919, 1931.
- [4] J. Seeman. The Stanford Linear Collider. In *AIP Conference Proceedings*, volume 249, pages 2035–2081. AIP, 1992.
- [5] S. Myers. The LEP collider, from design to approval and commissioning. In *CERN Yellow Reports: Monographs*, 1991.
- [6] P. Bryant. A Brief history and review of accelerators. In *CAS-CERN Accelerator School: 5th general accelerator physics course, Jyväskylä, Finland, 7-18 Sep 1992: Proceedings. 2 vol.*, pages 1–16, 1992.
- [7] M. Aicheler et al. A Multi-TeV linear collider based on CLIC technology: CLIC Conceptual Design Report. Technical report, SLAC National Accelerator Lab., Menlo Park, CA (United States), 2014.
- [8] P. Burrows et al. Updated baseline for a staged Compact Linear Collider. Technical report, CERN, 2016.
- [9] ILC: The International Linear Collider. <https://ilchome.web.cern.ch/ilc/facts-and-figures>. Accessed: 2020-04-14.
- [10] M. Benedikt and F. Zimmermann. Towards future circular colliders. *Journal of the Korean Physical Society*, 69(6):893–902, 2016.
- [11] T. Tajima and J. Dawson. Laser Electron Accelerator. *Phys. Rev. Lett.*, 43:267–270, 1979.
- [12] D. Strickland and G. Mourou. Compression of amplified chirped optical pulses. *Optics Communications*, 55(6):447 – 449, 1985.
- [13] F. Amiranoff et al. Observation of modulational instability in Nd-laser beat-wave experiments. *Phys. Rev. Lett.*, 68(25):3710, 1992.

Bibliography

- [14] Y. Kitagawa et al. Beat-wave excitation of plasma wave and observation of accelerated electrons. *Phys. Rev. Lett.*, 68(1):48, 1992.
- [15] C. Clayton et al. Ultrahigh-gradient acceleration of injected electrons by laser-excited relativistic electron plasma waves. *Phys. Rev. Lett.*, 70(1):37, 1993.
- [16] A. Modena et al. Electron acceleration from the breaking of relativistic plasma waves. *Nature*, 377(6550):606, 1995.
- [17] S. Mangles et al. Monoenergetic beams of relativistic electrons from intense laser-plasma interactions. *Nature*, 431(7008):535, 2004.
- [18] C. Geddes et al. High-quality electron beams from a laser wakefield accelerator using plasma-channel guiding. *Nature*, 431(7008):538, 2004.
- [19] J. Faure et al. A laser-plasma accelerator producing monoenergetic electron beams. *Nature*, 431(7008):541, 2004.
- [20] R. Weingartner et al. Ultralow emittance electron beams from a laser-wakefield accelerator. *Phys. Rev. ST Accel. Beams*, 15(11):111302, 2012.
- [21] A. Gonsalves et al. Petawatt laser guiding and electron beam acceleration to 8 GeV in a laser-heated capillary discharge waveguide. *Phys. Rev. Lett.*, 122(8):084801, 2019.
- [22] N. Zamfir. Nuclear physics with 10 PW laser beams at extreme light infrastructure—nuclear physics (ELI-NP). *The European Physical Journal Special Topics*, 223(6):1221–1227, 2014.
- [23] P. Chen and J. Dawson. The plasma wake field accelerator. *AIP Conference Proceedings*, 130(1):201–212, 1985.
- [24] J. Rosenzweig et al. Experimental Observation of Plasma Wake-Field Acceleration. *Phys. Rev. Lett.*, 61(1):98, 1988.
- [25] I. Blumenfeld et al. Energy doubling of 42 GeV electrons in a metre-scale plasma wakefield accelerator. *Nature*, 445(7129):741, 2007.
- [26] A. Caldwell et al. Proton-driven plasma-wakefield acceleration. *Nature Physics*, 5(5):363, 2009.
- [27] L. Evans and P. Bryant. LHC Machine. *JINST*, 3(08):S08001, 2008.
- [28] N. Kumar et al. Self-Modulation Instability of a Long Proton Bunch in Plasmas. *Phys. Rev. Lett.*, 104(25):255003, Jun 2010.
- [29] P. Muggli et al. (AWAKE Collaboration). AWAKE readiness for the study of the seeded self-modulation of a 400 GeV proton bunch. *Plasma Physics and Controlled Fusion*, 60(1):014046, 2017.

- [30] M. Turner et al. (AWAKE Collaboration). Experimental Observation of Plasma Wakefield Growth Driven by the Seeded Self-Modulation of a Proton Bunch. *Phys. Rev. Lett.*, 122(5):054801, 2019.
- [31] E. Adli et al. (AWAKE Collaboration). Experimental Observation of Proton Bunch Modulation in a Plasma at Varying Plasma Densities. *Phys. Rev. Lett.*, 122(5):054802, 2019.
- [32] F. Batsch et al. (AWAKE Collaboration). Transition between instability and seeded self-modulation of a relativistic particle bunch in plasma. To be published.
- [33] E. Adli et al. (AWAKE Collaboration). Acceleration of electrons in the plasma wakefield of a proton bunch. *Nature*, 561(7723):363, 2018.
- [34] J. Vieira et al. Hosing Instability Suppression in Self-Modulated Plasma Wakefields. *Phys. Rev. Lett.*, 112(20):205001, 2014.
- [35] P. Sprangle et al. Hose-Modulation Instability of Laser Pulses in Plasmas. *Phys. Rev. Lett.*, 73(26):3544, 1994.
- [36] C. Schroeder et al. Coupled beam hose and self-modulation instabilities in overdense plasma. *Phys. Rev. E*, 86(2):026402, 2012.
- [37] P. Gibbon. Introduction to Plasma Physics. In *CERN Accelerator School Plasma Wake Acceleration, 23–29 November 2014, Geneva, Switzerland*, 2014.
- [38] J. Dawson. Nonlinear Electron Oscillations in a Cold Plasma. *Physical Review*, 113(2):383, 1959.
- [39] J. Su et al. Stability of the Driving Bunch in the Plasma Wakefield Accelerator. *IEEE Transactions on Plasma Science*, 15(2):192–198, 1987.
- [40] Y. Fang. Resonant excitation of plasma wakefield. *PhD Thesis, University of Southern California*, 2014.
- [41] W. Lu et al. Limits of linear plasma wakefield theory for electron or positron beams. *Physics of Plasmas*, 12(6):063101, 2005.
- [42] R. Lee and M. Lampe. Electromagnetic Instabilities, Filamentation, and Focusing of Relativistic Electron Beams. *Phys. Rev. Lett.*, 31(23):1390, 1973.
- [43] B. Allen et al. Experimental Study of Current Filamentation Instability. *Phys. Rev. Lett.*, 109(18):185007, 2012.
- [44] M. Hüther and P. Muggli. Seeding of the self-modulation in a long proton bunch by charge cancellation with a short electron bunch. *Nuclear Instruments and Methods in Physics Research Section A: Accelerators, Spectrometers, Detectors and Associated Equipment*, 909:67–70, 2018.

Bibliography

- [45] C. Schroeder et al. Growth and Phase Velocity of Self-Modulated Beam-Driven Plasma Waves. *Phys. Rev. Lett.*, 107(14):145002, 2011.
- [46] D. Whittum et al. Electron-Hose Instability in the Ion-Focused Regime. *Phys. Rev. Lett.*, 67(8):991, 1991.
- [47] C. Huang et al. Hosing Instability in the Blow-Out Regime for Plasma-Wakefield Acceleration. *Phys. Rev. Lett.*, 99(25):255001, 2007.
- [48] T. Mehrling et al. Mitigation of the Hose Instability in Plasma-Wakefield Accelerators. *Phys. Rev. Lett.*, 118(17):174801, 2017.
- [49] J. Smith. *Mathematics of the Discrete Fourier Transform (DFT)*. Julius Smith, 2007.
- [50] K. Lotov et al. Natural noise and external wakefield seeding in a proton-driven plasma accelerator. *Physical Review Special Topics-Accelerators and Beams*, 16(4):041301, 2013.
- [51] A. Caldwell et al. (AWAKE Collaboration). AWAKE Design Report: A Proton-Driven Plasma Wakefield Acceleration Experiment at CERN. Technical report, CERN, 2013.
- [52] C. Bracco et al. Beam studies and experimental facility for the AWAKE experiment at CERN. *Nuclear Instruments and Methods in Physics Research Section A: Accelerators, Spectrometers, Detectors and Associated Equipment*, 740:48–53, 2014.
- [53] Linear accelerator 2. <https://home.cern/science/accelerators/linear-accelerator-2>. Accessed: 2020-04-14.
- [54] The Proton Synchrotron Booster. <https://home.cern/science/accelerators/proton-synchrotron-booster>. Accessed: 2020-04-14.
- [55] The Proton Synchrotron. <https://home.cern/science/accelerators/proton-synchrotron>. Accessed: 2020-04-14.
- [56] SPS Basic Super Cycles 2018. <https://op-webtools.web.cern.ch/SuperCycle/2018/2018-BasicSuperCycles.pdf>. Accessed: 2020-04-14.
- [57] W. Höfle et al. SPS beam for run II and beyond. In *AWAKE Collaboration Meeting, 8–12 March 2017, Novosibirsk, Russia*, 2017.
- [58] Awake laser. <https://edms.cern.ch/ui/file/1506630/1.0/AWK-TO-ES-0001-10-00.pdf>. 2016-11-08.
- [59] Fabian Batsch. Setup and Characteristics of a Timing Reference Signal with sub-ps Accuracy for AWAKE. *arXiv preprint arXiv:1911.12201*, 2019.

- [60] V. Fedosseev et al. Integration of a Terawatt Laser at the CERN SPS Beam for the AWAKE Experiment on Proton-Driven Plasma Wake Acceleration. Technical report, CERN, 2016.
- [61] A. Caldwell et al. (AWAKE Collaboration). AWAKE status report 2015. Technical report, CERN, 2015.
- [62] E. Öz and P. Muggli. A novel Rb vapor plasma source for plasma wakefield accelerators. *Nuclear Instruments and Methods in Physics Research Section A: Accelerators, Spectrometers, Detectors and Associated Equipment*, 740:197–202, 2014.
- [63] E. Öz et al. An accurate Rb density measurement method for a plasma wakefield accelerator experiment using a novel Rb reservoir. *Nuclear Instruments and Methods in Physics Research Section A: Accelerators, Spectrometers, Detectors and Associated Equipment*, 829:321–325, 2016.
- [64] V. Ginsburg and I. Frank. Radiation from a uniformly moving electron passing from one medium to another. *Journ. of Experimental and Theoretical Physics (JETP)* V, 16:15–26, 1946.
- [65] P. Goldsmith and J. Jelley. Optical transition radiation from protons entering metal surfaces. *Philosophical Magazine*, 4(43):836–844, 1959.
- [66] J. Jackson. *Classical electrodynamics*. Wiley, 1999.
- [67] K. Rieger et al. GHz modulation detection using a streak camera: Suitability of streak cameras in the AWAKE experiment. *Review of Scientific Instruments*, 88(2):025110, 2017.
- [68] M. Martyanov. Personal communication.
- [69] Hamamatsu Photonics K.K. Guide to streak cameras. https://www.hamamatsu.com/resources/pdf/sys/SHSS0006E_STREAK.pdf, 2008.
- [70] M. Turner et al. The two-screen measurement setup to indirectly measure proton beam self-modulation in AWAKE. *Nuclear Instruments and Methods in Physics Research Section A: Accelerators, Spectrometers, Detectors and Associated Equipment*, 854:100–106, 2017.
- [71] F. Braunmüller et al. Novel diagnostic for precise measurement of the modulation frequency of Seeded Self-Modulation via Coherent Transition Radiation in AWAKE. *Nuclear Instruments and Methods in Physics Research Section A: Accelerators, Spectrometers, Detectors and Associated Equipment*, 909:76–79, 2018.
- [72] Forck P. et al. Beam position monitors, 2009.
- [73] Alkaline photocathodes. http://photoinjector.web.cern.ch/photoinjector/cathodes_alcalines.htm. Accessed: 2020-02-23.

Bibliography

- [74] V. Fedosseev et al. Generation and Delivery of an Ultraviolet Laser Beam for the RF-Photoinjector of the Awake Electron Beam. In *10th Int. Particle Accelerator Conf. (IPAC'19), Melbourne, Australia, 19-24 May 2019*, pages 3709–3712. JACOW Publishing, Geneva, Switzerland, 2019.
- [75] Femtokits for third harmonic generation of femtosecond ti:sapphire laser. http://eksmaoptics.com/out/media/EKSMA_Optics_Femtokits.pdf. Accessed: 2020-02-22.
- [76] K. Pepitone et al. The electron accelerator for the AWAKE experiment at CERN. *Nuclear Instruments and Methods in Physics Research Section A: Accelerators, Spectrometers, Detectors and Associated Equipment*, 829:73–75, 2016.
- [77] M. Wing et al. The AWAKE electron spectrometer. In *Proceedings of the 9th International Particle Accelerator Conference (IPAC2018), 29 April – 4 May 2018, Vancouver, BC, Canada*. JACoW Publishing, 2018.
- [78] D. Cooke et al. Calibration of the AWAKE electron spectrometer with electrons derived from a partially stripped ion beam. In *Proceedings of the 10th International Particle Accelerator Conference (IPAC2019): Melbourne, Australia, May 19-24, 2019*, page WEPGW089, 2019.
- [79] P. Muggli et al. (AWAKE Collaboration). Physics to plan AWAKE Run 2. Preprint on arXiv:1911.07534, 2019, 2019.
- [80] A. Wynne and B. Stuart. Rate dependence of short-pulse laser ablation of metals in air and vacuum. *Applied physics A*, 76(3):373–378, 2003.
- [81] R. Fonseca et al. OSIRIS: A three-dimensional, fully relativistic particle in cell code for modeling plasma based accelerators. In *International Conference on Computational Science*, pages 342–351. Springer, 2002.
- [82] R. Fonseca et al. Exploiting multi-scale parallelism for large scale numerical modelling of laser wakefield accelerators. *Plasma Physics and Controlled Fusion*, 55(12):124011, 2013.
- [83] M. Moreira. Personal communication.
- [84] What Is R Squared And Negative R Squared. <http://www.fairlynerdy.com/what-is-r-squared/>. Accessed: 2019-12-13.
- [85] CCD Glossary. <http://starlink.eao.hawaii.edu/devdocs/sun139.htx/sun139se21.html>. Accessed: 2019-12-19.
- [86] A.-M. Bachmann and P. Muggli. Determination of the Charge per Micro-Bunch of a Self-Modulated Proton Bunch using a Streak Camera. In *4th European Advanced Accelerator Concepts Workshop*, 12 2019. Preprint on arXiv:1912.02162.

- [87] A.-M. Bachmann et al. (AWAKE Collaboration). To be published.
- [88] M. Turner. First Observation of the Seeded Proton Bunch Self-Modulation in Plasma. *PhD Thesis, Graz University of Technology*, 2017.
- [89] S. Gessner et al. (AWAKE Collaboration). Measurement of the evolution of a plasma column by modulation of a high-energy proton beam. To be published.
- [90] E. Senes. Personal communication.
- [91] J. Pucek. Personal communication.
- [92] J. Moody. Personal communication.

Appendix A: Publications



Contents lists available at ScienceDirect

Nuclear Inst. and Methods in Physics Research, A

journal homepage: www.elsevier.com/locate/nima

Seeding of the self-modulation in a long proton bunch by charge cancellation with a short electron bunch

Mathias Hüther^{a,b,*}, Patric Muggli^{a,c}^a Max Planck Institute for Physics, Munich, Germany^b Technical University of Munich, Garching b. München, Germany^c CERN, Geneva, Switzerland

ARTICLE INFO

Keywords:

AWAKE

Seeding of proton bunch self-modulation

Plasma wakefield acceleration

Electron injection

ABSTRACT

In plasma wakefield accelerators (e.g. AWAKE) the proton bunch self-modulation is seeded by the ionization front of a high-power laser pulse ionizing a vapour and by the resulting steep edge of the driving bunch profile inside the created plasma.

In this paper, we present calculations in 2D linear theory for a concept of a different self-modulation seeding mechanism based on electron injection. The whole proton bunch propagates through a preformed plasma and the effective beam current is modulated by the external injection of a short electron bunch at the centre of the proton beam. The resulting sharp edge in the effective beam current in the trailing part of the proton bunch is driving large wakefields that can lead to a growth of the seeded self-modulation (SSM).

Furthermore, we discuss the feasibility for applications in AWAKE Run 2.

1. Introduction

The proton bunch self-modulation in plasma wakefield accelerators (e.g. the Advanced Wakefield Experiment (AWAKE) located at CERN [1,2]) is usually seeded by using a high-power laser pulse co-propagating in the centre of the proton bunch (see Fig. 1(a)). The laser ionizes a vapour and creates a plasma, resulting in a sharp relativistic ionization front separating vapour and plasma. Due to this ionization front, the proton bunch self-modulation is seeded and consequently growing within a distance of a few metres before reaching its saturation level [3,4]. The long proton bunch is split into a train of micro-bunches with a period on the order of the plasma wavelength [5]. This modulation is caused by the self-modulation instability (SMI), a transverse beam–plasma instability. A witness electron bunch can thus deterministically be injected into one of the buckets between the micro-bunches and accelerated.

The seeding concept presented in this paper gives another approach to reach this goal: A high-power laser pulse is ionizing the plasma some time ahead of the proton bunch, so that the proton bunch is propagating through a preformed plasma (see Fig. 1(b)). Hence, there is no seeding from the ionization process. A short electron bunch is injected at the centre or somewhere along the long proton bunch. The resulting local charge cancellation leads to a distinct drop in the effective charge density distribution — and is therefore driving wakefields in the rear part of the proton bunch. The front of the bunch

is still long with a smoothly increasing density and thus drives much lower amplitude wakefields. Thanks to the seeding process [6], the wakefield phase and amplitude is determined and weakly dependent on initial beam parameters [7]. The witness electrons to be accelerated are again injected a number of buckets behind the seeding, as in the usual injection scheme. An overview of the different self-modulation seeding approaches using a short electron bunch is given in Fig. 1. A variation of the approach described in this paper, where a seed electron bunch is put ahead of the proton bunch, is shown in Fig. 1(c) and will be explained later.

AWAKE is the world's first proton-driven plasma wakefield accelerator aiming for acceleration of externally injected electrons in gradients up to the GV/m scale. It uses a 8–12 cm long proton bunch from CERN's Super Proton Synchrotron (SPS) that propagates through a 10 m long Rubidium plasma (with a density of $(1 - 10) \cdot 10^{14} \text{ cm}^{-3}$), induced by a high-power, short laser pulse (duration $\tau = 120 \text{ fs}$, energy $E = 450 \text{ mJ}$).

2. A simplified model in linear theory

For a more quantitative understanding of the approach towards seeding, we introduce the following simplified model: The proton and electron bunch longitudinal density distribution is described by a *cos*-profile, whereas their radial profiles are Gaussian. We use 2D-linear

* Corresponding author at: Max Planck Institute for Physics, Munich, Germany.
E-mail address: huethe@mpp.mpg.de (M. Hüther).

<https://doi.org/10.1016/j.nima.2018.02.084>

Received 1 December 2017; Received in revised form 9 February 2018; Accepted 19 February 2018

Available online 22 February 2018

0168-9002/© 2019 The Authors. Published by Elsevier B.V. This is an open access article under the CC BY-NC-ND license (<http://creativecommons.org/licenses/by-nc-nd/4.0/>).

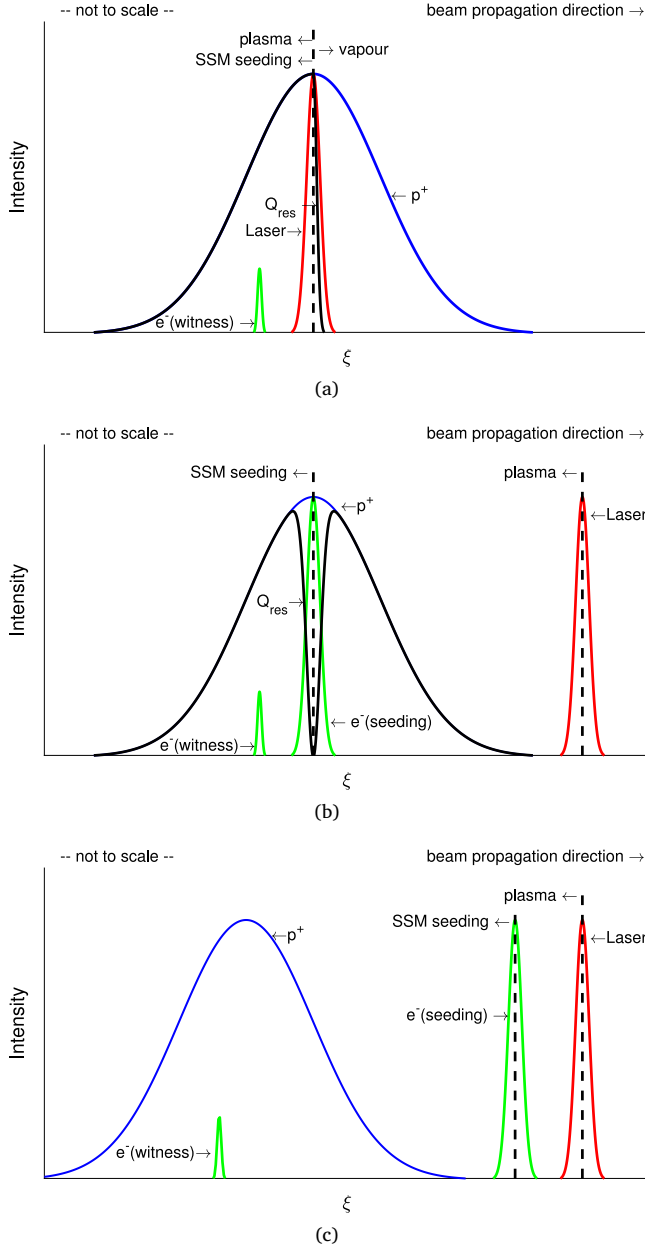


Fig. 1. Self-modulation seeding and electron injection schemes. (a) Current seeding concept with wakefields seeded by a vapour–plasma transition front created by a high-power laser pulse in the centre of the proton beam. (b) Novel seeding scheme with an electron bunch injected in the centre of the long proton bunch and resulting in a dip in the effective charge density. The laser pulse is ionizing the vapour ahead of the proton bunch. (c) Laser pulse and electron bunch ahead of the proton bunch. Seeding of SM process due to wakefields driven by the electron bunch.

plasma wakefield theory [8] to describe the seeding effect by calculating the initial wakefields. The total (proton and electron) longitudinal charge distribution $n_{b\parallel}$ (see Fig. 2) is given by

$$n_{b\parallel}(\xi') = \begin{cases} A_0 \cdot \sin\left(\frac{\pi \cdot (\xi' + L)}{2(L-U)}\right) & \xi' \in [-L, -U] \\ \frac{A_{min} - A_0}{2} \cdot \cos\left(\frac{\pi \xi'}{U}\right) + \frac{A_{min} + A_0}{2} & \xi' \in [-U, U] \\ A_0 \cdot \cos\left(\frac{\pi \cdot (\xi' - U)}{2(L-U)}\right) & \xi' \in [U, L] \\ 0 & \text{elsewhere,} \end{cases} \quad (1)$$

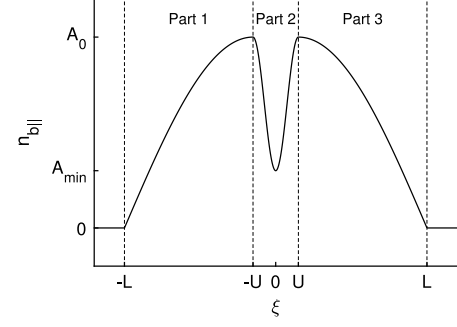


Fig. 2. cos-approximation of the longitudinal proton bunch density $n_{b\parallel}$ as described by Eq. (1).

where $\xi = ct - z$ is the spatial coordinate in the co-moving bunch frame, $2L$ the longitudinal size of the proton bunch and $2U$ the longitudinal size of the electron bunch. Outside $[-L, L]$ the bunch charge density is assumed to be zero. The amplitude of the proton charge density is A_0 and the amplitude of the electron charge density is $A_0 - A_{min}$. The absolute number of charges in one bunch for our model is given by $N = 8A_0 L n_b \sigma_{r,p}^2 \cdot 0.683$. For comparison in case of a Gaussian longitudinal bunch profile N is given by $N = (2\pi)^{\frac{3}{2}} n_b \sigma_{z,p} \sigma_{r,p}^2$. According to [8] the parallel and perpendicular wakefields $W_z(\xi, r)$ and $W_r(\xi, r)$ are given by

$$W_z(\xi, r) = \frac{e}{\epsilon_0} \int_{-\infty}^{\xi} n_{b\parallel}(\xi') \cos(k_{pe}(\xi - \xi')) d\xi' \cdot R(r) \quad (2)$$

and

$$W_r(\xi, r) = \frac{e}{k_{pe} \epsilon_0} \int_{-\infty}^{\xi} n_{b\parallel}(\xi') \sin(k_{pe}(\xi - \xi')) d\xi' \cdot \frac{dR(r)}{dr}, \quad (3)$$

where e is the elementary charge, ϵ_0 the vacuum permittivity and $k_{pe} = \omega_{pe}/v_b \approx \omega_{pe}/c$ the plasma wave number in case of a relativistic particle bunch with bunch velocity $v_b \approx c$. The plasma electron angular frequency ω_{pe} is

$$\omega_{pe} = \sqrt{\frac{n_{pe} e^2}{\epsilon_0 m_e}}, \quad (4)$$

where m_e is the electron mass and n_{pe} the plasma charge density. The transverse component $R(r)$ in Eqs. (2) and (3) is given by

$$R(r) = k_{pe}^2 K_0(k_{pe} r) \int_0^r r' n_{b\perp}(r') I_0(k_{pe} r') dr' + k_{pe}^2 I_0(k_{pe} r) \int_r^\infty r' n_{b\perp}(r') K_0(k_{pe} r') dr', \quad (5)$$

with I_0 and K_0 the modified Bessel functions of the first and second kind, respectively. Assuming the radial profile and the radial size of the electron and proton bunch are the same, $R(r)$ and $\frac{dR}{dr}$ are just multiplying factors. Considering different radii is trivial.

Piecewise integration of the separate bunch parts of Eqs. (2) and (3) along ξ (see Fig. 2) gives the contribution of each single part to the resulting wakefields.

The wakefields driven by the leading part of the proton bunch ($-L < \xi < -U$) are described by

$$E_{1,\parallel}(\xi) = \begin{cases} 0 & \xi < -L \\ \frac{A_0}{2k_{pe}} \left[-(C_+ + C_-) \left[\cos\left(\frac{\pi(\xi + L)}{2(L-U)}\right) + \cos(k_{pe}(\xi + L)) \right] \right] & -L < \xi < -U \\ \frac{A_0}{2k_{pe}} \left[-(C_+ - C_-) \sin(k_{pe}(\xi + U)) + (C_+ + C_-) \cos(k_{pe}(\xi + L)) \right] & -U < \xi < U \\ 0 & \xi > U \end{cases} \quad (6)$$

and

$$E_{1,\perp}(\xi) = \begin{cases} 0 \\ \frac{A_0}{2} \left[(C_+ - C_-) \sin\left(\frac{\pi(\xi + L)}{2(L - U)}\right) + (C_+ + C_-) \sin(k_{pe}(\xi + L)) \right] \\ \frac{A_0}{2} \left[(C_+ - C_-) \cos(k_{pe}(\xi + U)) + (C_+ + C_-) \sin(k_{pe}(\xi + L)) \right], \end{cases} \quad (7)$$

where the first term is valid for $\xi < -L$, the second term for $-L \leq \xi \leq -U$ and the third term for $\xi > -U$. The parallel and perpendicular wakefields in the part where the electrons are injected and therefore cause a drop in the effective charge density are given by

$$E_{2,\parallel}(\xi) = \begin{cases} 0 \\ \frac{A_1}{2k_{pe}} \left[(D_+ + D_-) \sin\left(\frac{\pi\xi}{U}\right) - (D_+ - D_-) \sin(k_{pe}(\xi + U)) \right] \\ + \frac{A_2}{k_{pe}^2} \sin(k_{pe}(\xi + U)) \\ \frac{A_1}{2k_{pe}} \left[(D_+ - D_-) \sin(k_{pe}(\xi - U)) - (D_+ - D_-) \sin(k_{pe}(\xi + U)) \right] \\ - \frac{A_2}{k_{pe}^2} \left[\sin(k_{pe}(\xi - U)) - \sin(k_{pe}(\xi + U)) \right] \end{cases} \quad (8)$$

and

$$E_{2,\perp}(\xi) = \begin{cases} 0 \\ \frac{A_1}{2} \left[(D_+ + D_-) \cos\left(\frac{\pi\xi}{U}\right) - (D_+ - D_-) \cos(k_{pe}(\xi + U)) \right] \\ + \frac{A_2}{k_{pe}} [1 - \cos(k_{pe}(\xi + U))] \\ \frac{A_1}{2} \left[(-D_+ + D_-) \cos(k_{pe}(\xi - U)) + (D_+ - D_-) \cos(k_{pe}(\xi + U)) \right] \\ - \frac{A_2}{k_{pe}} [\cos(k_{pe}(\xi + U)) - \cos(k_{pe}(\xi - U))]. \end{cases} \quad (9)$$

Here, the first term is valid for $\xi < -U$, the second for $-U \leq \xi \leq U$ and the third for $\xi > U$.

The wakefields caused by bunch section between U and L are described by

$$E_{3,\parallel}(\xi) = \begin{cases} 0 \\ \frac{A_0}{2k_{pe}} \left[(C_+ + C_-) \sin\left(\frac{\pi(\xi - U)}{2(L - U)}\right) + (C_+ - C_-) \sin(k_{pe}(\xi - U)) \right] \\ \frac{A_0}{2k_{pe}} \left[(C_+ + C_-) \cos(k_{pe}(\xi - L)) + (C_+ - C_-) \sin(k_{pe}(\xi - U)) \right] \end{cases} \quad (10)$$

and

$$E_{3,\perp}(\xi) = \begin{cases} 0 \\ \frac{A_0}{2} \left[(C_+ - C_-) \cos\left(\frac{\pi(\xi - U)}{2(L - U)}\right) + (-C_+ + C_-) \cos(k_{pe}(\xi - U)) \right] \\ \frac{A_0}{2} \left[(C_+ + C_-) \sin(k_{pe}(\xi - L)) + (-C_+ + C_-) \cos(k_{pe}(\xi - U)) \right]. \end{cases} \quad (11)$$

For this case, the first line is valid for $\xi < U$, the second for the interval $U \leq \xi \leq L$ and the third line for $\xi > L$.

The constants in Eqs. (6) to (11) are given by $A_1 = \frac{A_{min} - A_0}{2}$, $A_2 = \frac{A_{min} + A_0}{2}$, $C_{\pm} = \frac{1}{2(L-U) \pm k_{pe}}$ and $D_{\pm} = \frac{1}{\frac{\pi}{U} \pm k_{pe}}$.

Making use of the superposition theorem of waves in linear theory, the final wakefield distribution can be determined by adding the different contributions of the bunch segments in every region. Hence, the

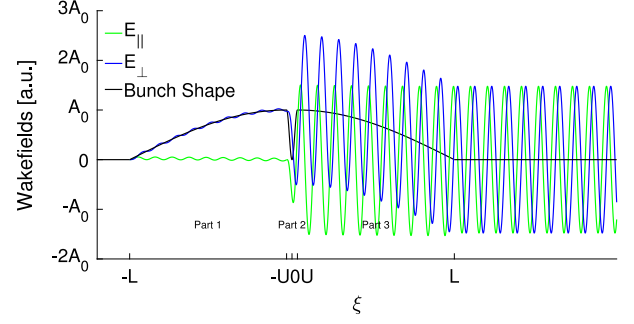


Fig. 3. Parallel and perpendicular wakefields $E_{\parallel}(\xi)$ and $E_{\perp}(\xi)$ for a bunch shape with $\sigma_{z,p} = 12$ cm, $\sigma_{z,e} = 4$ mm, $\frac{U}{L} = \frac{1}{30}$, $\frac{U}{\lambda_{pe}} = 1.6$, peak currents $|Q_{p^+,peak}| = |Q_{e^-,peak}|$.

resulting wakefields are described by

$$E(\xi) = \begin{cases} 0 & \xi < -L \\ E_1(\xi) \Big|_{\xi \in [-L; -U]} & \xi \in [-L; -U] \\ E_1(\xi) \Big|_{\xi \in [-U; U]} + E_2(\xi) \Big|_{\xi \in [-U; U]} & \xi \in [-U; U] \\ E_1(\xi) \Big|_{\xi \in [U; L]} + E_2(\xi) \Big|_{\xi \in [U; L]} + E_3(\xi) \Big|_{\xi \in [U; L]} & \xi \in [U; L] \\ E_1(\xi) \Big|_{\xi > L} + E_2(\xi) \Big|_{\xi > L} + E_3(\xi) \Big|_{\xi > L} & \xi > L. \end{cases} \quad (12)$$

Fig. 3 shows the longitudinal and perpendicular wakefields (Eq. (12)) for a ratio $\frac{U}{L} = \frac{1}{30}$ and $\frac{U}{\lambda_{pe}} = 1.6$. The front of the proton bunch ($\xi < -U$) propagates in a preformed plasma where its length is very long when compared to the plasma wavelength λ_{pe} and its profile is smooth. It is therefore not effective at driving wakefields, but still drives a low amplitude fields that could lead to development of the SMI process over long plasma distances. The adiabatic response of the plasma generates a globally focussing force by charge neutralization that, upon propagation, can lead to an increase in bunch density and thus also of the wakefield response. This effect could also lead to SMI growth (as opposed to SSM) over long plasma distances. From the position of the electron bunch ($\xi > U$) and all along the second half of the proton bunch, much larger wakefields are driven, which subsequently provide the strong seed for the SM process.

For bunch parameters similar to AWAKE ($L = 6$ cm, $U = 2$ mm, $\frac{U}{L} = \frac{1}{30}$, $\frac{U}{\lambda_{pe}} = 1.6$, peak currents $|Q_{p^+,peak}| = |Q_{e^-,peak}|$ (see **Fig. 3**) and $k_{pe} = 5000 \text{ m}^{-1}$, $n_p = 7 \cdot 10^{14} \text{ cm}^{-3}$, $\sigma_r = 200 \mu\text{m}$) the wakefields in the trailing part of the bunch could reach values up to the GV/m scale.

It can be easily seen from Eqs. (6)–(11) that the amplitudes of the wakefields in the trailing part of the bunch are scaling linearly with the electron bunch charge Q_e , i.e. the depth of the gap in the effective charge density $A_0 - A_{min}$.

Furthermore, the wakefields are strongly depending on the width of the gap in the effective charge density $2U$, corresponding to the longitudinal size of the injected electron bunch $\sigma_{z,e}$. The amplitude of the wakefields can be maximized for a given configuration of A_{min} and L and follow the distribution shown in **Fig. 4**. For an electron bunch length U on the order of λ_{pe} , the peak wakefields are the highest (see **Fig. 4**).

3. Discussion of the method

The seeding method described above could be an interesting approach for a seeding concept for the planned extension of the AWAKE experiment after 2021, called AWAKE Run 2 [9]. Current design studies for the plasma accelerator consist of a split plasma, a short one (~ 4 m) for the seeding of the SSM and a second, longer one (~ 10 m) driven by

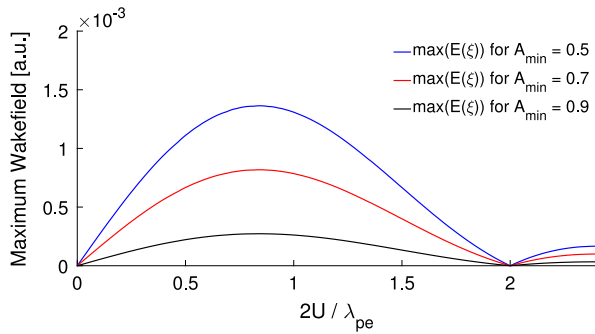


Fig. 4. Maximum wakefields for different ratios of $2U/\lambda_{pe}$.

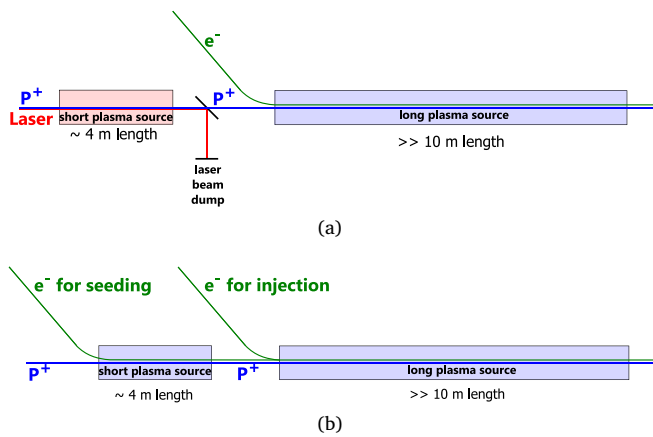


Fig. 5. Maximum wakefields for different ratios of $2U/\lambda_{pe}$.

the modulated proton bunch for the acceleration of the electrons (see Fig. 5). The injection point for the witness electron bunch is foreseen to be between the two plasmas. The short plasma source is similar to the one used in AWAKE Run 1, whereas the long plasma cell could be either a Helicon or a discharge source [10].

By seeding the SMI with an electron bunch, as described here, the ionization front is not necessary for seeding and thus the first plasma could also be preformed in one of these two types of sources. Hence, there would be no longer need for a maintenance-intensive high-power laser system nor for the complicated Rubidium handling and storage procedures required by a Rubidium based vapour source.

The major uncertainty concerning the feasibility of this approach is the effect of the first part of the proton bunch. Even though, according to the simulations of Kumar et al. [5] and according to the wakefields described in Eq. (12), there is no strong seeding of the SMI expected by the leading part of the bunch, the weak amplitude wakefields or those from noise may grow. Subsequently, wakefields in the front of the bunch

would interfere with the seeded wakefields in the trailing part of the bunch. Hence, a phase-stable seeding of the SSM would no longer be possible.

First preliminary experimental results from the AWAKE-experiment show some evidence for a growth of wakefields along the bunch on a scale of a few metres as well as micro-bunching even without seeding, i.e. propagation in a preformed plasma.

In case the unseeded SM-growth in the leading part of the proton bunch is too high for a seeding with an electron bunch in the centre of the beam, another option would be to shift the electron bunch to an earlier position with respect to the proton bunch or even ahead of it (see Fig. 1(c)). With this, the full proton bunch charge could be used for driving wakefields, while removing the risk of growth of SMI ahead of the seeding point.

4. Conclusions

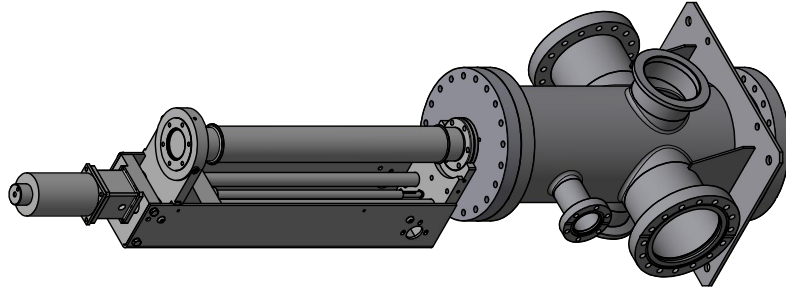
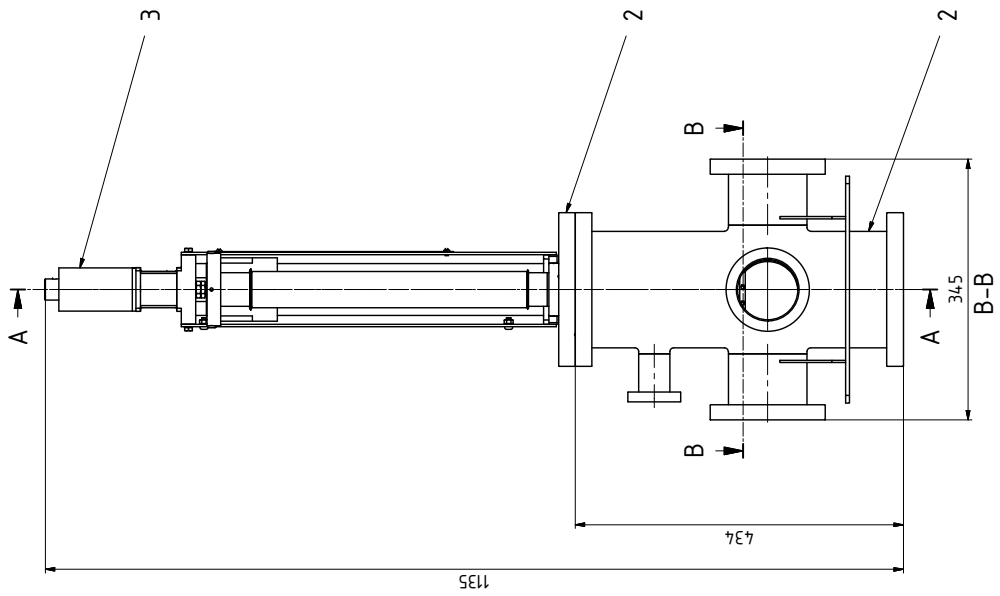
We presented an alternative concept for the seeding of the SSM in plasma-wakefield accelerators. Instead of seeding by an ionization front created by a high-power laser pulse, the seeding is archived by the injection of a short electron bunch in the centre of a long proton bunch propagating through a preformed plasma. Calculations in 2D linear theory show that the resulting steep rising edge in the effective charge density of the proton bunch drives large amplitude wakefields that seed the SSM. Although the approach is very promising and could simplify the design for AWAKE Run 2, first experimental results from the latest AWAKE Runs give evidence that wakefields do grow from noise in the front of the proton bunch, when the bunch propagates in a preformed plasma and no seeding is provided.

References

- [1] P. Muggli, et al., Physics of the AWAKE project, in: IPAC 2013: Proceedings of the 4th International Particle Accelerator Conference, 2013, pp. 1179–1181.
- [2] E. Gschwendtner, et al., AWAKE, the advanced proton driven plasma wakefield acceleration experiment at CERN, Nucl. Instrum. Methods Phys. Res. A 829 (2016) 76–82.
- [3] K.V. Lotov, A.P. Sosedkin, A.V. Petrenko, Long-term evolution of broken wakefields in finite-radius plasmas, Phys. Rev. Lett. 112 (2014) 194801. <http://dx.doi.org/10.1103/PhysRevLett.112.194801>.
- [4] A. Caldwell, et al., Path to AWAKE: Evolution of the concept, Nucl. Instrum. Methods Phys. Res. A 829 (2016) 3–16.
- [5] N. Kumar, A. Pukhov, K. Lotov, Self-modulation instability of a long proton bunch in plasmas, Phys. Rev. Lett. 104 (25) (2010) 255003.
- [6] K. Lotov, et al., Natural noise and external wakefield seeding in a proton-driven plasma accelerator, Phys. Rev. ST Accel. Beams 16 (4) (2013) 041301.
- [7] N. Savard, P. Muggli, J. Vieira, Effect of proton bunch parameter variation on awake, in: North American Particle Accelerator Conf., NAPAC'16, Chicago, IL, USA, October 9–14, 2016, JACOW, Geneva, Switzerland, 2017, pp. 684–686.
- [8] P. Chen, et al., Plasma focusing for high-energy beams, IEEE Trans. Plasma Sci. 15 (2) (1987) 218–225.
- [9] E. Adli, Towards AWAKE applications: Electron beam acceleration in a proton driven plasma wake, in: 7th Int. Particle Accelerator Conf., IPAC'16, Busan, Korea, May 8–13, 2016, JACOW, Geneva, Switzerland, 2016, pp. 2557–2560.
- [10] AWAKE Collaboration, AWAKE status report 2016, SPSC-SR-194.

Appendix B: Technical Drawings

A-A



Revisionsverlauf

Nr.	Beschreibung	Datum	Name
A	Schubstange 2 durch Austauschhalter ersetzt	14.07.2016	Haubold



Hauptprojektion



gezeichnet	Tag	Name
19.04.2016	P. Tscharas	
geprüft		
geplant		

Max-Planck-Institut für Physik
(Werner-Heisenberg-Institut)
München

AWAKE
OTR-CTR

Gewicht: 20,109 kg
Dimensionen: mm
Maße ohne Fertigungstoleranzen nach
DIN ISO 2768 m K

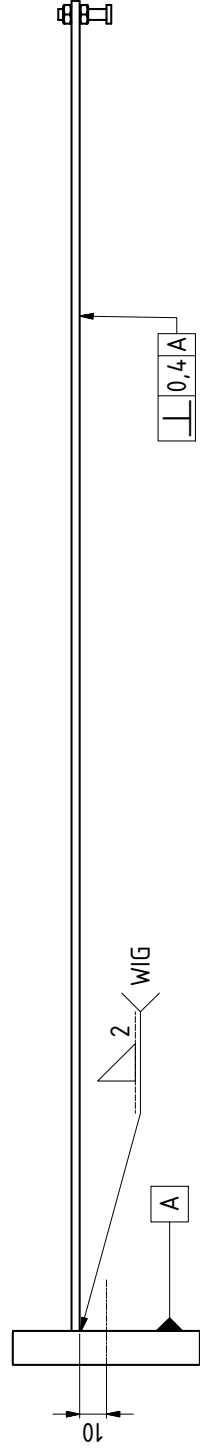
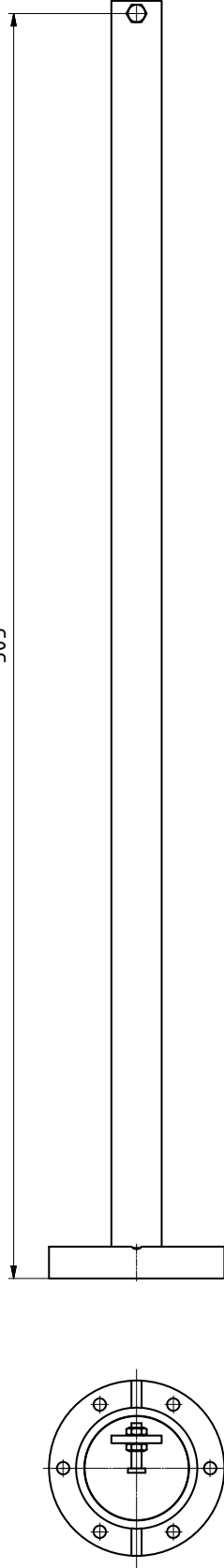
Werkstoff

Zeichnungsnummer / EDV Nr.:
110-011100-010.iw

Schwarz... Inventor: 20.06.
Blatt: 1 Gesamtzahl: 1
V6.c
DIN EN 20 216 - A2 (20 x 594)

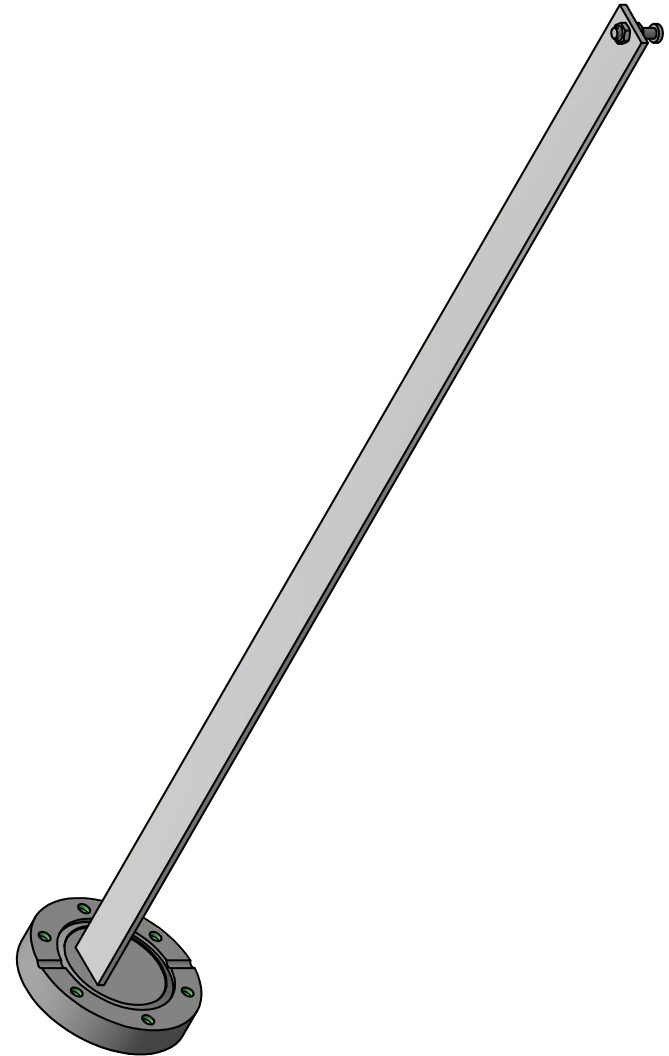
15	19	Zyl.-Schr. m. Schlitz	-	A2-70	M3x6	ISO 1207	
13	1	Austauschhalter	110-011100-013.iam				
12	1	Schubstange 2	110-011100-012.iam				
8	1	Druckrahmen	110-011154.ipf	1.4-301 X5CrNi18-10			vorhanden
7	1	Folie	Folie.ipf	Alu-Leg			vorhanden
3	1	Folienhalter	110-011153.ipf	1.4-301 X5CrNi18-10			vorhanden
3	1	Z-Manipulator	Z1R3070W.ipf			Fa. vargen	vorhanden
2	1	Vakuumkammern	110-011100.iam				vorhanden
2	1	Reduzierflansch	ZL1540-304.ipf				vorhanden
Teil	St.	Benennung	Zeichn. Nr. / EDV Nr.	Werkstoff	Abmessungen / Art. Nr.	Norm	Bemerkung
				Stückliste			

505



$\perp_{0,4A}$

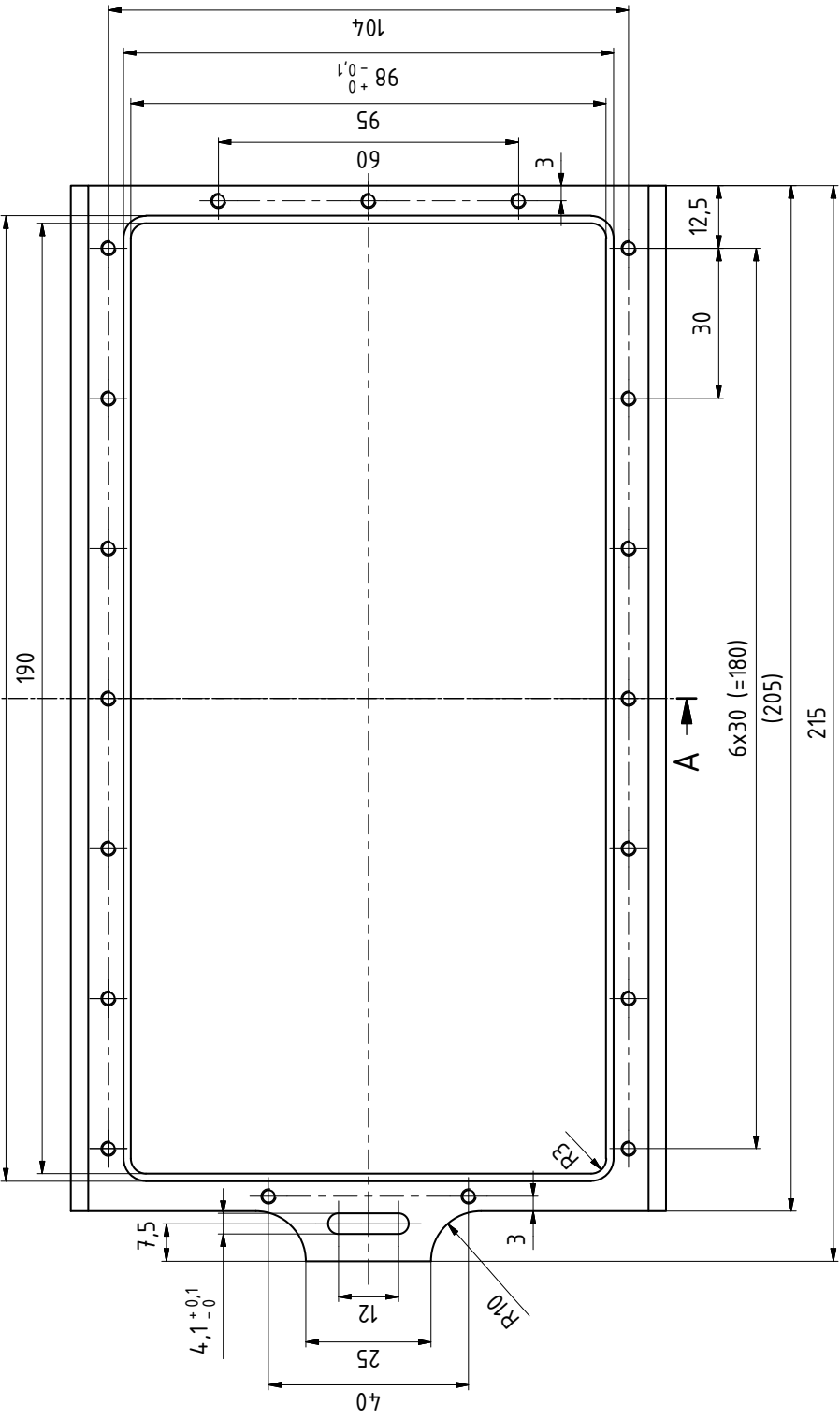
Hauptprojektion
 $\perp_{-0,1}$ $\perp_{+0,1}$



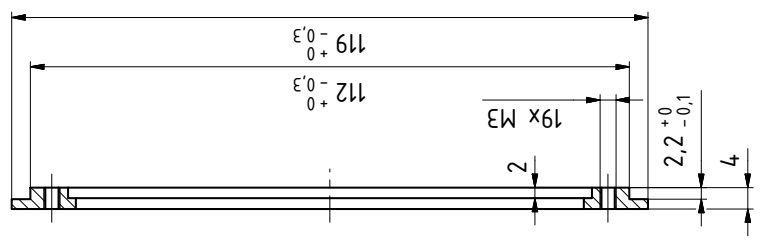
1	1	Drehflansch	20151217 - CF 40 Fl dr.iam
2	1	Platte, schmal	110-011156.ipt
3	1	Schraube	110-011157.ipt
4	2	Mutter, 6kt	-
Teil	St.	Benennung	Zeichn. Nr. / EDV Nr., Stückliste
			Werkstoff
			1.4.301 X5CrNi18-10
			A2-50
			A2-70

		Gewicht.....: 0.459 kg Dimensionen : mm Maße ohne Toleranzangabe nach DIN ISO 2768 m K	
Max-Planck-Institut für Physik (Werner-Heisenberg-Institut) München		Werkstoff	
Tag Name T. Haubold		Projekt AWAKE OTR-CTR	
gezeichnet	14.07.2016	Zeichnungsnummer / EDV Nr.: 110-011100-013.idw	
geprüft		Software.....: Inventor 2016	
geplottet		Blatt: 1 Gesamtzahl: 1 V16.a	
Maßstab 1:2		Teil: DIN EN 20 216 - A3 (297 x 420)	

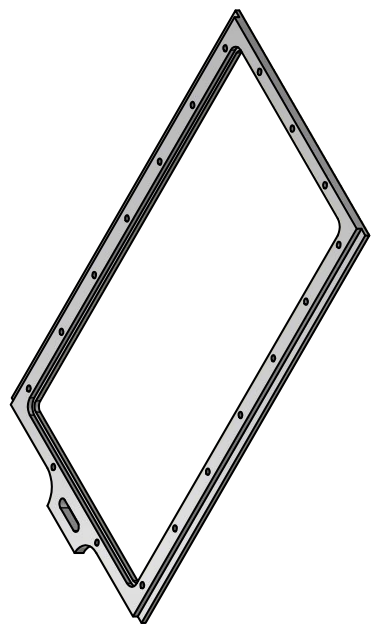
A → 193⁺⁰_{-0,1}



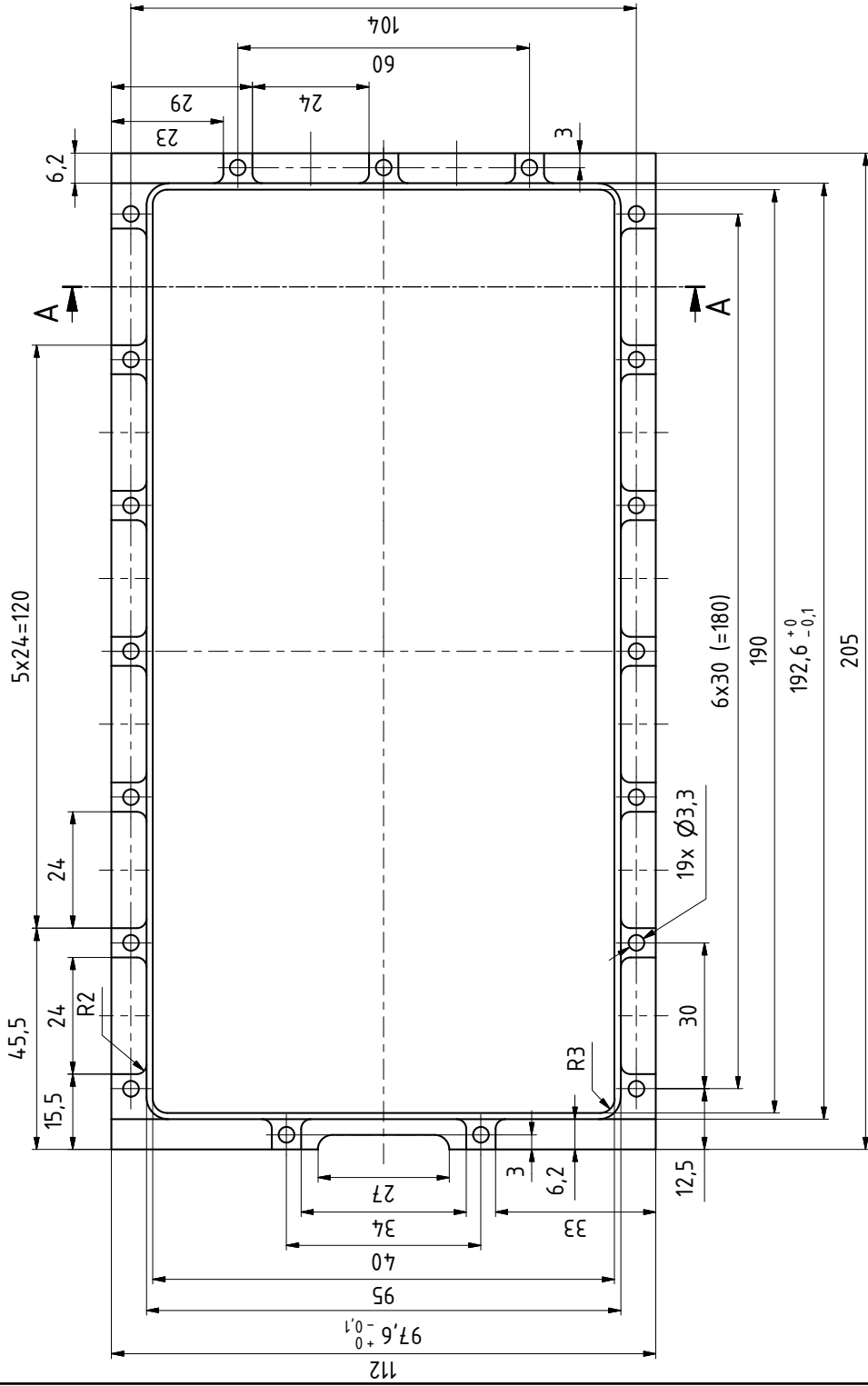
A-A



Rz 25

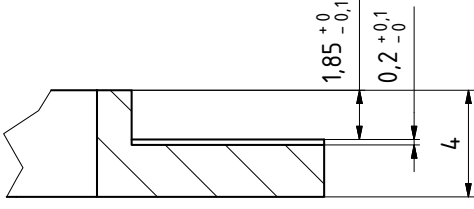


<p>Hauptprojektion</p>		<p>Tag</p> <p>18.04.2016</p>		<p>Name</p> <p>P. Tsiantas</p>		<p>Projekt</p> <p>AWAKE OTR-CTR</p>		<p>Werkstoff</p> <p>1.4.301 X5CrNi18-10</p>		<p>Gewicht.....: 0,167 kg</p> <p>Dimensionen : mm</p> <p>Maße ohne Toleranzangabe nach DIN ISO 2768 m K</p>	
<p>gezeichnet</p> <p>18.04.2016</p>		<p>geprüft</p>		<p>geplottet</p>		<p>Max-Planck-Institut für Physik (Werner-Heisenberg-Institut) München</p>		<p>1.4.301 X5CrNi18-10</p>		<p>Zeichnungsnummer / EDV Nr.: 110-011153.idw</p>	
<p>Maßstab</p> <p>1:1 (1:2)</p>		<p>Folienhalter</p>		<p>Teil:</p>		<p>Software.....: Inventor 2016</p> <p>Blatt: 1 Gesamtzahl: 1</p>		<p>DIN EN 20 216 - A3 (297 x 420)</p>		<p>V16.c</p>	

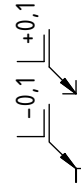
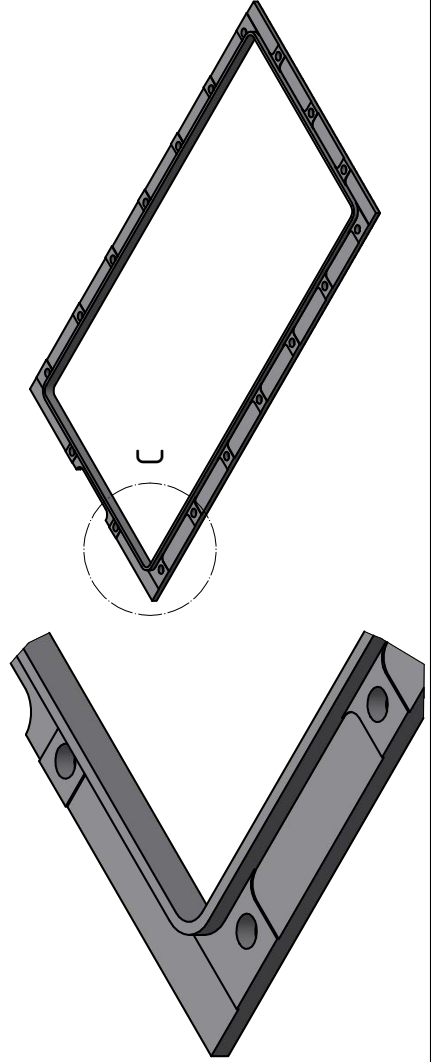


A-A

Z (5:1)



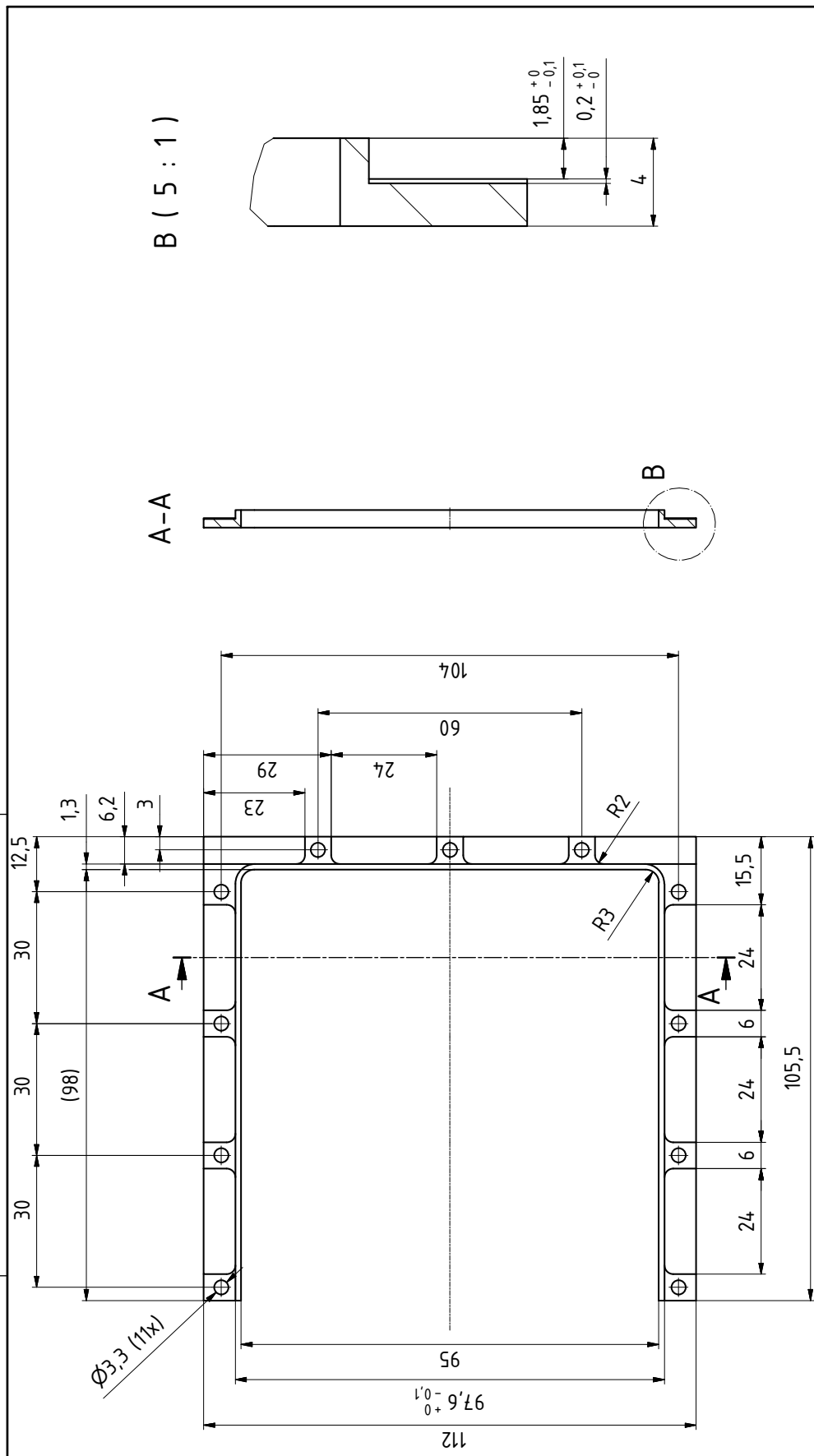
C (2:1)



Rz 25

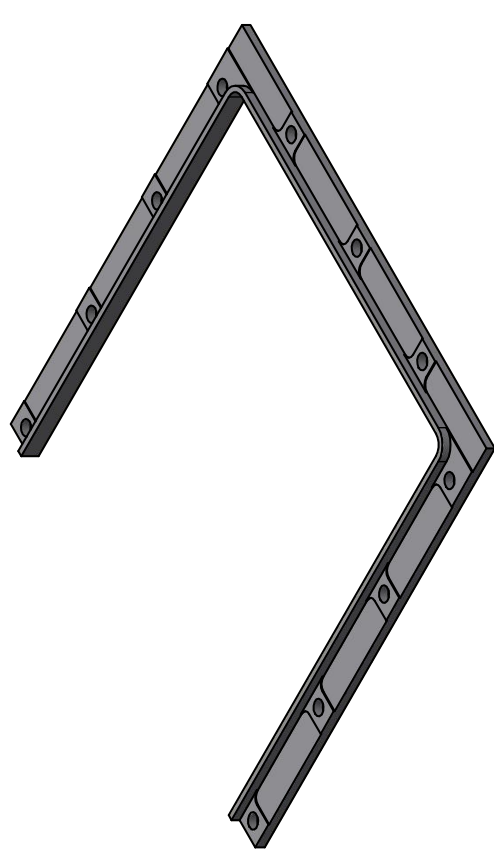
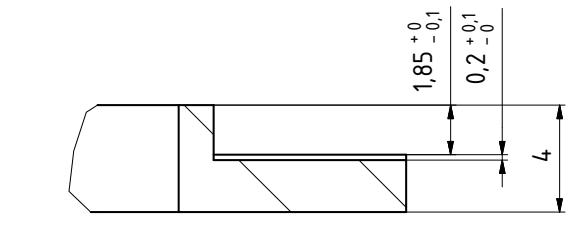
Max-Planck-Institut für Physik (Werner-Heisenberg-Institut) München	Projekt Name P.Tsiantas	Tag 18.04.2016	gezeichnet geprüfert geplottet	Gewicht.....: 0,085 kg
				Dimensionen : mm Maße ohne Toleranzangabe nach DIN ISO 2768 m K
Werkstoff 1.4301 X5CrNi18-10		Zeichnungsnummer / EDV Nr.: 110-011154.idw		
Druckrahmen		Software.....: Inventor 2016 Blatt: 1 Gesamtzahl: 1 V16.c DIN EN 20 216 - A3 (297 x 420)		

Teil:



B (5 : 1)

A-A



Hauptprojektion 		Max-Planck-Institut für Physik (Werner-Heisenberg-Institut) München	
gezeichnet 18.04.2017 T. Haubold geprüfert geplottet		Projekt Name T. Haubold	
Maßstab 1:1; 5:1		Werkstoff 1.4301 X5CrNi18-10	
Zeichnungsnummer / EDV Nr.: 110-011174.idw		Zeichnungsnummer / EDV Nr.: 110-011174.idw	
Software..... Inventor 2016 Blatt: 1 Gesamtzahl: 1 V16.a		Blatt: 1 Gesamtzahl: 1 V16.a	
Teil:		Teil:	